DISSERTATION / DOCTORAL THESIS

Titel der Dissertation /Title of the Doctoral Thesis

„Vanadium-based Misfit Layer Compounds – A study on their phase diagrams and properties“

verfasst von / submitted by

Gabriel R. Reisinger, BSc MSc

angestrebter akademischer Grad / in partial fulfilment of the requirements for the degree of

Doktor der Naturwissenschaften (Dr. rer. nat.)

Wien, 2020 / Vienna 2020

Studienkennzahl lt. Studienblatt / degree programme code as it appears on the student record sheet:	A 796 605 419
Dissertationsgebiet lt. Studienblatt / field of study as it appears on the student record sheet:	Chemie
Betreut von / Supervisor:	ao. Univ.-Prof. Mag. Dr. Klaus Richter

Acknowledgements

I would like to express my deepest gratitude to:

- Klaus Richter for his advice, help, and support – personally and professionally.
- Patric Berger, Hans Flandorfer, Siegfried Fürthauer, Herbert Ipser, Peter Kainzbauer, Martin Marker, Klaus Richter, Clemens Schmetterer, Stephan Solé, and Andriy Yakymovych for the valuable discussions and the pleasant working atmosphere they created.
- Anna Lebhard, Martin Pack, Anto Puljic, Claudia Rabijasz, and Katharina Rauchenwald for providing the possibility to mutually learn and profit from one another.
- Herta Effenberger and Alexander Roller for their help with single crystal XRD measurements, their advice and the professional collaboration.
- Stephan Puchegger his help with SEM measurements, his advice and the professional collaboration.
- Antonin Dlouhy, Kenan Elibol, and Jani Kotakoski their help with TEM measurements, their advice and the professional collaboration.
- Philipp Baloh, Dieter Baurecht, and Hinrich Grothe their help with Raman measurements, their advice and the professional collaboration.
- Ernst Bauer his help with resistivity measurements, his advice and the professional collaboration.
- Patricia Jenner for her tireless efforts towards proof-reading and error correction of this work.
- My family and my friends for their constant support and encouragement, even in difficult times.

Without the help of these people, it would not have been possible to complete this thesis.

Table of Contents

List of Figures

List of Tables

List of Abbreviations

CCD	Charge-coupled device
CDW	Charge density wave
DSC	Differential scanning calorimetry
DTA	Differential thermal analysis
EDX/EDS	Energy-dispersive X-ray spectroscopy
EPMA	Electron probe microanalysis
MLC	Misfit layer compound
PXRD	Powder X-ray diffraction
SAED	Selected area electron diffraction
SCXRD	Single crystal X-ray diffraction
SEM	Scanning electron microscopy
STEM	Scanning transmission electron microscopy
TEM	Transmission electron microscopy
TMD	Transition metal dichalcogenide
XRD	X-ray diffraction

Abstract

Misfit layer compounds (MLCs) are a widely studied research topic. These compounds are low-dimensional materials with strongly anisotropic properties, which makes them attractive for basic research as well as potential applications in industry. Little is reported in literature on the phase equilibria and/or the phase diagrams of systems containing such MLCs, despite the numerous publications that have appeared on such compounds.

The current work focuses on the exploration of the three ternary phase diagrams Pb-Se-V, Sb-Se-V and Se-Sn-V. Due to the strongly differing physical and chemical properties of the elements sample preparation is challenging. The phase equilibria in these systems are also difficult to interpret, especially those involving the MLCs. The data is presented by utilising isothermal sections.

In addition to the phase diagrams, the optimal synthesis conditions for vanadium-selenium-based MLCs and the morphology of these compounds are investigated. The structural properties of the, up to now unknown, $(PbSe)_{1+\delta}VSe_2$ MLC are examined in detail and compared to the literature.

A systematised literature review in this thesis summarises the whole literature on vanadium-based MLCs' synthesis and crystal structures, including the present data. It standardises the available data to a common scheme and compares them to the closely related *fere*crystalline compounds, which can aid future investigations in this field of study.

Zusammenfassung

Zum Themenbereich der niedrigdimensionalen Materialien gehören auch die sogenannten Misfit-Layer-Compounds (MLCs). Sie wurden bereits vielfach untersucht, da ihre stark anisotropen Eigenschaften sowohl für die Grundlagenforschung als auch für potenzielle industrielle Anwendungen von Interesse sind. Ungeachtet der zahlreichen Veröffentlichungen, die zu solchen Verbindungen erschienen sind, wird in der Literatur wenig über die Phasengleichgewichte und/oder die Phasendiagramme der zugehörigen Systeme berichtet.

Daher liegt der Hauptfokus der aktuellen Arbeit auf der Erforschung der drei ternären Phasendiagramme Pb-Se-V, Sb-Se-V und Se-Sn-V, in deren Systemen die stark unterschiedlichen physikalischen und chemischen Eigenschaften der Elemente eine besondere präparatorische Herausforderung darstellen. Die teilweise schwierig zu ermittelnden Phasengleichgewichte werden anhand von Isothermen dargestellt. Neben der Phasendiagramme werden auch die optimalen Synthesebedingungen für Vanadium-Selen-basierte MLCs und die Morphologie dieser Verbindungen diskutiert, sowie die strukturellen Eigenschaften von $(PbSe)_{1+\delta}VSe_2$, einem bisher unbekannten MLC, mit der Literatur verglichen.

Eine systematisierte Literaturrezension in der vorliegenden Arbeit fasst die gesamte Literatur, einschließlich der Daten dieser Arbeit, zur Synthese und Kristallstruktur von MLCs auf Vanadiumbasis zusammen. Hierbei werden nicht nur die Daten zusammengeführt, sondern auch auf ein gemeinsames Schema gebracht, um sie besser untereinander, sowie zu den eng verwandten Ferecrystals, vergleichen zu können. Dies soll etwaige zukünftige Untersuchungen auf diesem Gebiet unterstützen.

1. Introduction

The digital revolution is just beginning and already has an impact on every aspect of society. Manifestations of these transformations can be observed in the government (“government 4.0” [1]) and industrial sector (“industry 4.0” [2]), as well as private life [3]. The main driving forces for the former two are either motivated by reduction in costs (e.g. digitalised administration services, automatised production processes, and automated logistics) [4] or by implementing completely new digital business models in order to gain market share (e.g. cloud computing, artificial intelligence, and end-to-end traceability in the chain of custody) [5]. Private customers, on the other hand, adopt digital technologies (e.g. smart home, autonomously driving vehicles, and wearables) according to the technology acceptance model. Especially the two factors of perceived ease-of-use and perceived usefulness are important in their decision making process [6].

However, the so-called “internet of things”, which are interrelated systems and devices that do not require human interaction to function, comes at a price. Not only that overall power consumption is increased and high demands are required regarding the cellular infrastructure [7], but all these connected devices need some computing capacity, too. In the ideal case, the power consumption and size of the circuits in these devices are low, whereas the computational power of all these devices is high.

According to the empirical observation of Moore (“Moore's Law”), the processing power of computers is growing exponentially. A doubling of transistors per area can be observed in an interval of one to two years, depending on the literature and period considered [8, 9]. Nevertheless, advances in technology are required in order to meet the targets “set” by Moore's Law. In the past, such advances were basically achieved by narrowing down the structure size in semiconductors. Nowadays new solutions are needed desperately, as the physical boundary of the semiconductor scale is approaching (e.g. tunnelling-based of source-to-drain leakage [10] or wavelength in optical lithography [11]). Exotic solutions, such as low-temperature, superconducting, optical or quantum computing, might be difficult to implement in small devices in near future. Besides them, two- (e.g. Graphene [12]) and other low-dimensional materials (e.g. layered compounds [13]) are promising candidates for increases in computing capacity. Not only that low-dimensional materials exhibit new properties, but the stacking of transistors would add another dimension to manufacturing transistors. Instead of limiting the density of integrated circuits to the area, they would be limited to the volume and, hence, increase the possible number of transistors per area, too.

Misfit layer compounds are such low dimensional materials. They comprise two different crystal structures with differing physical properties. The thicknesses of each slab equal the unit cell thicknesses, which are just two or three atomic layers, respectively. Misfit layer compounds incorporate these 2D materials' properties in large crystals, they hold the potential to be utilised in the semiconductor industry.

1.1. Research questions

Aim of this thesis is the investigation of several vanadium-based ternary systems relevant for misfit layer compounds (MLCs). Special focus will be on the systems of M-Se-V, where M are bismuth, lead, antimony, and tin. In those systems the existence of ternary phases, including MLCs, is suspected. Those compounds shall be synthesised and investigated regarding their properties. Additional experiments regarding possible ternary phases or misfit layer compounds in the systems of M-Te-V shall be employed in order to reveal a possible existence of MLCs there.

1.2. Structure of this thesis

The results of this thesis are presented in a cumulative way. Published and submitted papers are presented as well as yet unpublished manuscripts and data. Chapter 2 gives a short excursus on nanomaterials and their unique properties compared to bulk materials. Chapter 3 (unpublished manuscript) discusses the existing literature on MLCs, the different synthesis methods, and the phase equilibria in such ternary systems in a systematised review. As it will be submitted for publication after all other manuscripts, it readily contains data of the chapters 4 to 7. Chapters 4, 5 (both published papers), and 6 (submitted manuscript) present evaluations of the ternary phase diagrams of Sb-Se-V, Pb-Se-V, and Se-Sn-V, respectively. Chapter 7 (unpublished manuscript) presents data on the morphology and crystal structure of MLCs. It also discusses the different synthesis approaches for MLCs including that via microwave-induced plasmas. Chapter 8 presents further unpublished data on the Raman spectra and electrical conductivity of the synthesised MLCs. In chapter 9 the cumulated results are discussed. chapters 10 and 11 draw final conclusions and give an outlook on further research questions in this field of study in English and German language, respectively.

2. Excursus – Nanomaterials

In this chapter, a brief introduction into the topics of nanomaterials and two-dimensional materials is presented. However, the literature on misfit layer compounds (MLCs) and *fere*crystalline compounds, with particular focus on the different synthesis methods and the structural properties of those closely related compounds, is discussed in detail in chapter 3.

Metallic and oxidic nanomaterials are utilised since ancient times in applications such as colourant for ceramics or glasses (e.g. *Lycurgus cup*), as additives in steel production (e.g. *Damascus steel*) [14], and as hair dyes (e.g. PbS) [15]. Nevertheless, nanomaterials are lacking a common and internationally acknowledged definition to the present day. Depending on the area of application (e.g. foods, cosmetics, and biocides) different legislative provisions with differing classifications of nanomaterials are in order. In general, the definitions are consistent with regard to the scale. At least one of the dimensions of the material requires to be in the size range of 1 to 100 nm [15, 16], but in some cases, materials that are smaller than 1 nm (e.g. graphene, fullerenes, and carbon nanotubes) are regarded as nanomaterials, too [17].

Nanomaterials can be classified by their origin and in doing so the natural and synthetic materials can be differentiated. However, more frequently a classification by type of chemical compounds or the nanomaterials dimensions is utilised. Former differentiates between carbon-based (e.g. graphene, fullerene, and carbon nanotubes), organic-based (e.g. dendrimers, micelles, and liposomes), composite-based (e.g. hybrid-perovskite, functionalised graphene, and metal-organic frameworks), and inorganic-based nanomaterials (e.g. metallic and oxidic nanoparticles, silica aerogel, and mesoporous silica) [15]. Misfit layer compounds are inorganic composites and, hence, be either regarded as composite-based or inorganic-based nanomaterials. This shows the limitations of this system. The latter classification is trivial when just the particle sizes are considered. First considerations were proposed by Siegel on this topic [18]. Basically, nanomaterials can have the dimensionalities zero, one, two, or three. This dimensionality reflects the possibility for electrons to move along an axis in a Cartesian coordinate system.

Whereas in a 0D system (e.g. quantum dots) the charge carriers are confined in all directions, the charge carriers can move in one, two or all three directions in 1D (e.g. nanorods), 2D (e.g. nanosheets) or 3D systems (e.g. nanocrystalline bulk), respectively [15, 19-21]. In order to fully describe composite-based nanomaterials, the dimensionalities of the individual elementary units need to be added to the overall dimensionality of the system. Misfit layer compounds are structures of heterolayers. Hence, they are classified as 3D22 structures, which reflects a three-dimensional bulk that comprises of two different substructures of nanosheets [22].

The unique properties of nanomaterials are influenced by internal (e.g. surface-to-bulk-ratio, defect concentration, and degree of movability restrictions of the charge carriers) and external factors (e.g. chemical nature of the surroundings and interaction of the nanomaterial with the surroundings). Changes in properties can be observed in the diffusivity as well as chemical, catalytical, mechanical, elastic, thermal, optical, magnetic, and electrical properties, when compared to a similar non-nanomaterial (e.g. graphene compared to graphite) [21].

The activation energy for diffusion is lower on surfaces, grain boundaries, and dislocation sites, compared to the activation energy required for lattice diffusion. In general, nanocrystalline materials exhibit high defect concentrations (e.g. grain boundaries, vacancies, and dislocations). Thus, the diffusivity in nanocrystalline materials is several magnitudes higher than in non-nanomaterials, which would require much higher temperatures in order to reach similar diffusivities and compensate for the difference of activation energies. A major disadvantage, however, is that grain boundaries have high free energies. Hence, nanocrystalline materials will tend to coarsen when heat treated, making them unsuitable for high-temperature applications [21].

The high defect concentrations influence the thermal behaviour, too. On the one hand, when loosely bonded atoms are subjected to strong lattice vibrations, as a result of an increase in temperature, they are more likely to liquefy, since they are less constrained compared to the bulk lattice. Hence, crystals with smaller radii and higher defect concentrations will exhibit lower melting points. However, in cases when the nanocrystalline material is embedded in a matrix with a higher melting point, the strong confinement can result in elevated melting points of the nanomaterial, too. On the other hand, grain boundaries will result in phonon scattering phenomena as well as phonon-phonon interactions. Thus, nanomaterials, with except from nanotubes, exhibit significantly reduced thermal conductivity. 1D and 2D, especially multi-layer compounds with a lattice mismatch, will have anisotropic thermal transport properties and altered phonon dispersion relations [21]. For instance, the thermal conductivities at room temperature of 2D *fere*crystals are reported to be lower than the theoretical minimum thermal conductivities of bulk materials and even lower than thermal conductivities of amorphous materials [23].

For nanoparticles, the ratio between bulk volume and surface area is shifted towards high values for the specific area per unit volume of the grains. This ratio influences the coercivity and saturation magnetisation. Both values are increased upon a decrease in grain size. For soft magnetic alloys the reason is that the grain sizes in nanomaterials are smaller than the domain wall withs and, thus, the grains and their orientations average the magnetic anisotropy. Also, effects such as a giant magnetoresistance in thin-film multilayer compounds [21] or a change of magnetic behaviour (e.g. bulk VSe_2 is paramagnetic but ferromagnetic when the number of layers is reduced to a few [24]) are reported.

Nanomaterials' surface area is large compared to the bulk. Hence, these materials are capable to hold more energy, which may be utilised in energy storage applications. Phenomena, such as alloys with metallic properties in bulk can be converted into semiconductors when prepared as nanoquasicrystalline phase [21], or that 2D materials are strongly anisotropic for the electrical resistivity (e.g. of electrical resistivities' temperature coefficients of vanadium-based MLCs and *fere*crystals indicate that they are metallic along *c* and semiconducting in the *ab* plane [25-28]), are not well understood.

Synthesis routes can be categorised in physical and chemical approaches or in top-down and bottom-up methods [20, 21]. Top-down techniques originate from a macro- or microcrystalline material that is broken up into nanocrystalline material (e.g. mechanical alloying and nanolithography). This method should be favoured in inexpensive and robust applications, as the size distribution is broader. Bottom-up processes (e.g. Spray pyrolysis, Sol-Gel, and chemical or physical vapour deposition) utilise plasmas, gases or liquids. They allow more variation in procedures and, hence, have better controllability but are difficult to scale up [21]. Similar physical and chemical approaches have their distinct advantages. Whereas users of chemical methods enjoy the advantage of good chemical homogeneity and versatility, physical methods are economically appealing due to the lack of by-products and solvents [20]. Misfit layer compounds and ferecrystals are synthesised via different bottom-up techniques [29] as it will be shown in chapter 3. However, typical sample preparation for the investigation of these van der Waals heterostructures are usually top-down approaches (e.g. scotch tape method).

3. Manuscript 1: Review of V-based layered compounds

3.1. Authorship Statement

Chapter 3 describes material that will be submitted to *Journal of Materials Science* in 2021. The co-author is Klaus W. Richter, who is my advisor and I am the primary author of the manuscript.

Reisinger: Conceptualisation, Investigation, Writing - Original Draft, Visualisation

Richter: Writing - Review & Editing, Supervision, Project administration

3.2. Abstract

In this systematised review, we present a bibliographic analysis of the literature available on vanadium-based layered compounds. The keywords are not entirely standardised for all publications and topics covered. Numerous different synthesis approaches are presented in literature. The most common approaches involve mineralisers and annealing conditions above 800 °C for several days or weeks in the case of misfit layer compounds and below 60 minutes and below 650 °C for *fere*crystals. We standardise all available structural data regarding the (sub-/super-)lattice parameters, misfit parameters and stacking, and compare them to each other. Furthermore, we show research possibilities for further investigations in this field of study (e.g. templated growth mechanism, phase equilibria, twelvefold symmetry).

3.3. Keywords

Misfit layer compound, *Fere*crystal, Synthesis, Phase equilibria, Crystal Structure

3.4. Prime novelty statement

Systematised review of the literature on vanadium-based layered compounds with special consideration of synthesis conditions, compositions, and crystal structures.

3.5. Highlights

- Bibliographic analysis of the entire literature on vanadium-based misfit layer compounds and *fere*crystals
- Synthesis conditions are compared

- All structural parameters are summarised in a standardised form
- Discussion of structural parameters and further research possibilities

3.6. Introduction

Over the last decades, nanomaterials gained increasingly more attention from researchers. 2D heterostructures, such as *fere*crystals and misfit layer compounds, were investigated by members from various research disciplines in order to replace expensive/inefficient materials in established applications or to investigate exotic properties. Those compounds both comprise of two different crystal structures that are loosely bonded via van der Waals forces and are incommensurate in at least one crystallographic direction (refer to Figure 1) but differ in their synthesis approach and thermodynamic stability. As a topic evolves over time and broadens in a more

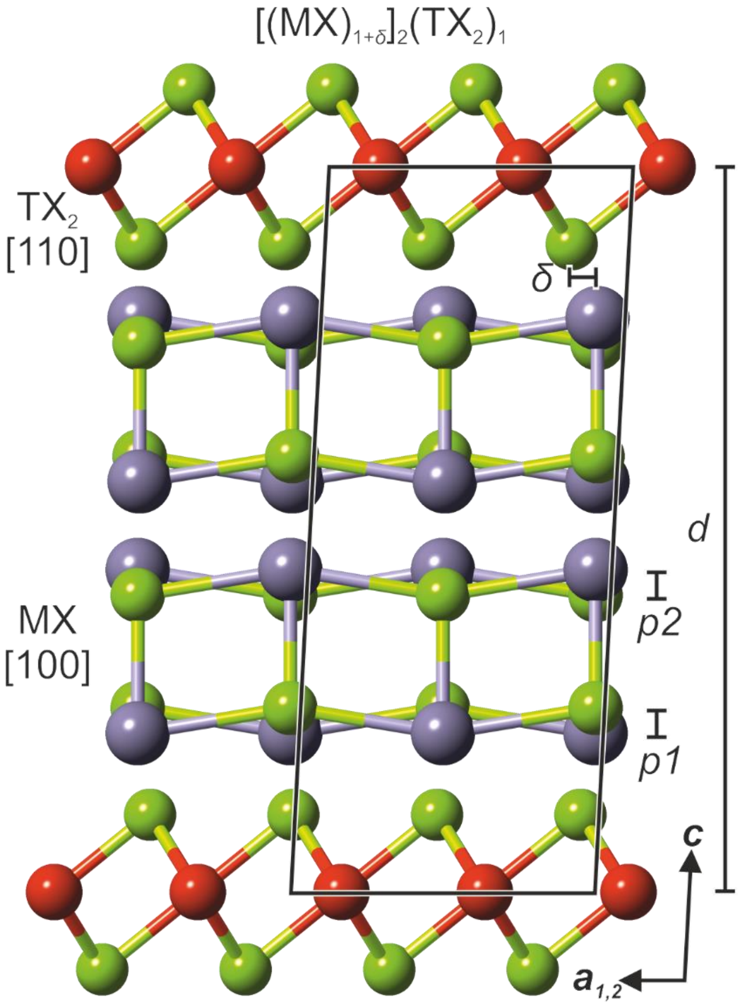

Figure 1: Schematic structure of a $[(MX)_{1+\delta}]_2(TX_2)_1$ type ferecrystal or misfit layer compound; the structure shows a monoclinic distortion in β; the misfit parameter (δ), the puckering of MX layers (p1 and p2), and the interlayer distance (d) are indicated.

interdisciplinary direction, the number of different authors increases. By this, different styles of writing (e.g. commonly used terms in language, styles of presenting data) as well as citation and publication cultures (e.g. utilisation of preprints) are introduced. The increasingly diverging literature becomes more difficult to comprehend and, hence, intersecting sets are reduced. In the worst case, the same topic is investigated multiple times by various researchers from different disciplines without a direct comparison and proper co-citation. Also, the topics of *fere*crystals and misfit layer compounds to some extend drifted apart in the last decades, despite the close structural relationship. The literature on vanadium-based layered compounds are exemplary for such an alienation.

This systematised review [30] aims to reduce the barriers that arise from different research topics, research collaborations, and/or terminologies. We present a complete bibliographic overview of all publications available on vanadium-based *fere*crystalline and misfit layer compounds. The established synthesis conditions for preparing those compounds as well as their structural features are summarised. We also briefly comment on the topics of crystal composition, morphology, and the phase equilibria in such intermetallic systems. However, a review of the physical properties, such as the magnetic susceptibility, the electrical transport, or charge density waves, will be published separately due to the extent of available publications.

3.7. Bibliographic overview

Vanadium-based layered compounds of the formula $[(MX)_{1+\delta}]_m(VX_2)_n$ (M = Bi, Pb, RE, or Sn; X = S, or Se) are known since the investigation of Donohue in 1975 [31]. More than 50 publications on vanadium-based misfit layer compounds published between 1988 and 1999 are available. Thereafter, only few works on those compounds were published each year. The interest revived again in 2011, as Atkins *et al.* [32] first synthesised vanadium-based *fere*crystals. This second wave of publications includes over 30 items, with most being published on the topic of *fere*crystals in 2015.

The topics of those publications [23, 25-28, 31-122] cover different aspects of vanadium-based layered compounds: synthesis and composition, crystal structures and superstructures, intercalation of foreign atomic species and compounds, electronic structures and physical properties, electronic transport and superconductivity, as well as magnetic properties. The keywords chosen for the respective publications as well as their temporal evolution was analysed in detail by utilising data available from the Web of Science Core Collection database and the VOSviewer software [123]. As illustrated in Figure 2, working groups choose different terms for those vanadium-based layered compounds depending on the topic. For example, “misfit compound” is chosen for theoretical investigations, “misfit-layer compound” is chosen for investigations on physical properties, and

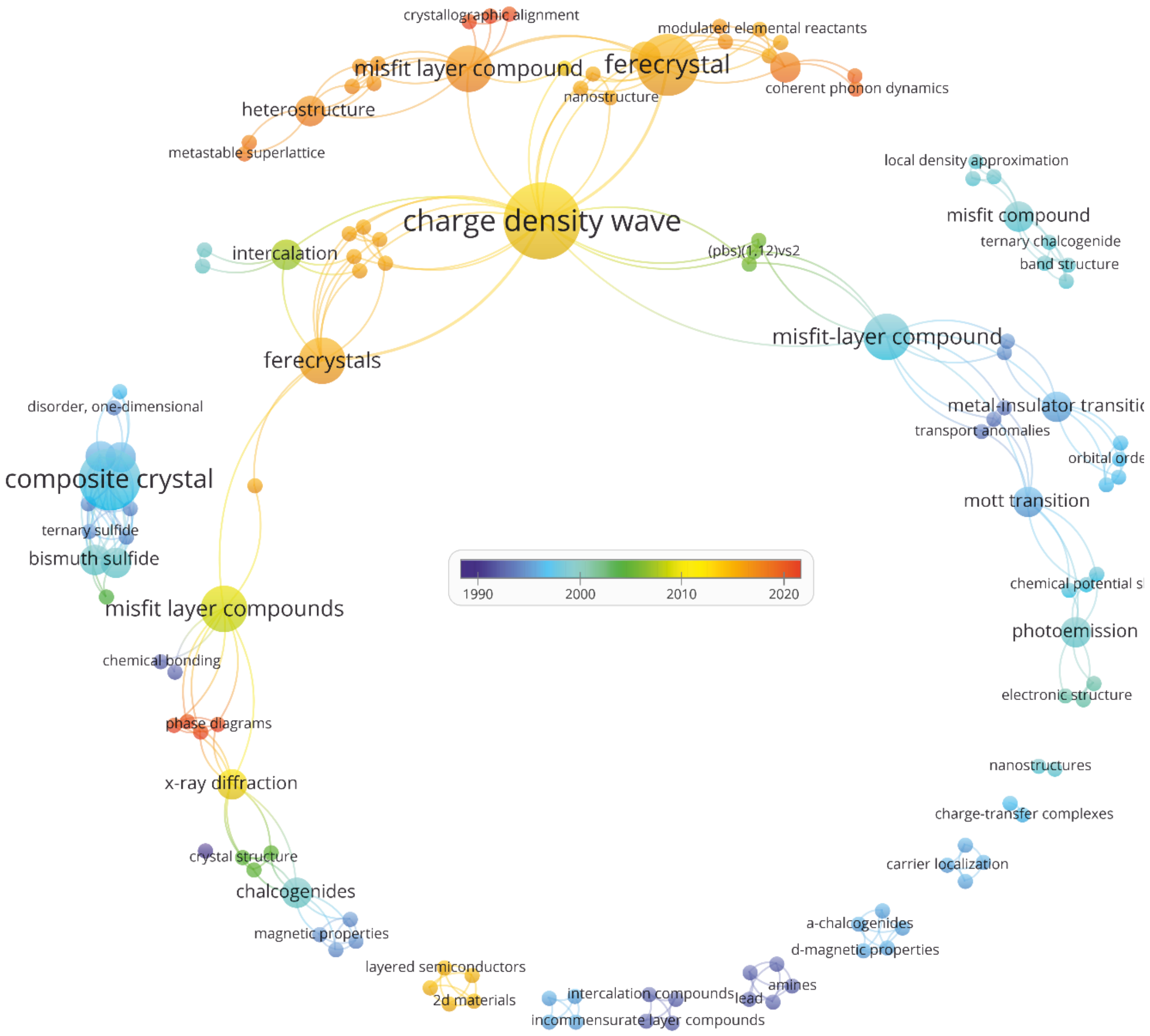

Figure 2: Temporal evolution and relation of keywords of the publications featured in this review

"misfit layer compound(s)" for phase diagrams and crystallographic investigations. Detailed investigations on superstructures and the incommensurate modulations of the crystal structures are grouped around the keyword "composite crystal". For *fere*crystalline compounds "*fere*crystal" and "*fere*crystals" are both commonly employed keywords and frequently used together with "charge density wave". No noticeable tendencies can be observed, for choosing the singular or plural term of "*fere*crystal" for different research topics. The fact that no standardisation of keywords can be found, may be the result of isolated working groups. The miscellaneous denotations different authors choose for the layered compounds they investigate, complicate literature research and can in result hamper the exchange of knowledge.

This is also visible in the co-authorship of publications (refer to Figure 3). Apart from different generations of researchers in that field which evidently prevents a co-authorship, some personal and/or topical aspects (e.g. MLCs and *fere*crystals) might have hindered collaboration. The main collaborations on vanadium-based layered compounds are grouped around several researchers leading the field. However, we observed little collaborations between these topical leaders. The leaders are:

- J. Morales (University of Cordoba),
- Y. Gotoh (National Institute of Advanced Industrial Science and Technology) and M. Onoda (National Institute for Material Science),
- T. Nishikawa (Nagoya University) and A. Fujimori (University of Tokyo),
- K. Suzuki (Yokohama National University) and T. Enoki (Tokyo Insitute of Technology),
- G. Wiegers (University of Groningen), A. Meerschaut, and L. Cario (both University of Nantes),
- and D. C. Johnson and M. Falmbigl (both University of Oregon).

Citation analysis not only demonstrates how collaborations evolved over time, particularly for that of G. Wiegers, A. Meerschaut, and L. Cario, but also how the field is drifting apart due to different preparation procedures, especially for the research networks around D.C. Johnson. The working groups around L. Cario and

D. C. Johnson cite similar sources (e.g. J. Rouxel, J. Morales G. Wiegers, A. Meerschaut, and Y. Gotoh) but cite each other only to a limited extend (refer to Figure 4).

The main publications in the field of vanadium-based layered compounds are the reviews of Rouxel *et al.* [121] and Wiegers [122]. Often cited publications on synthesis, crystal structures, and properties are the works of Onoda *et al.* [45], Kondo *et al.* [47], and Atkins *et al.* [67]. Additionally, the works of Kato *et al.* [124] and Wiegers *et al.* [125] are cited frequently. Those two publications, however, are not about vanadium-based compounds but about structurally related compounds.

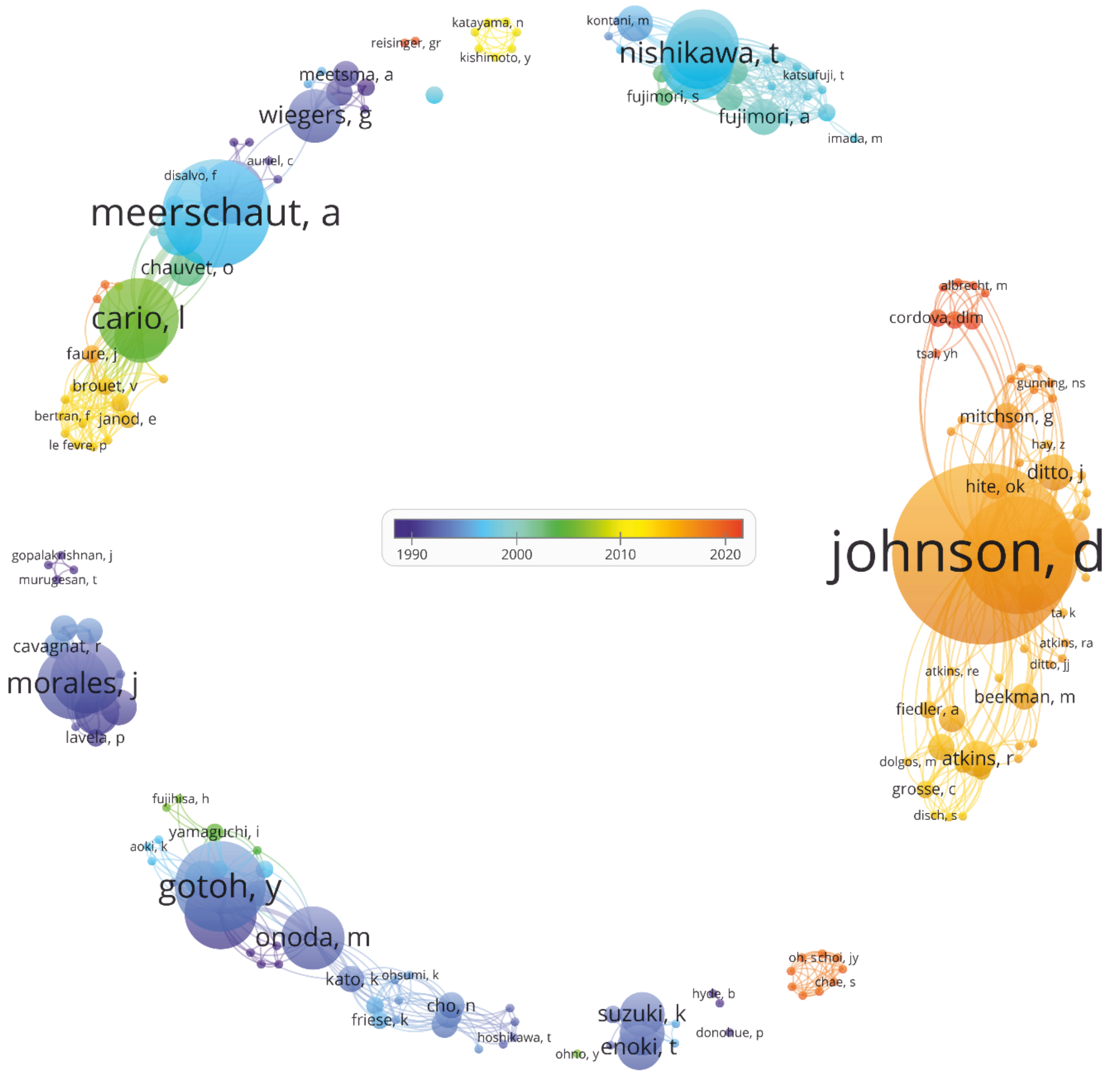

Figure 3: Temporal evolution and relationship of co-authors of the publications featured in this review

3.8. Synthesis, crystal growth, preparation and phase equilibria

3.8.1. Synthesis

Misfit layer compounds and *fere*crystalline compounds differ regarding their synthesis technique. The former, are obtainable via standard solid-state synthesis approaches [109, 122], the latter, via the modulated element reactant method [126]. A third synthesis procedure attempts to employ microwave-induced plasmas to synthesise vanadium-based layered compounds. This synthesis approach was unsuccessful up to now [109].

a. *Misfit layer compounds*

Three different starting materials can be used to produce the desired vanadium-based layered compounds:

- the pure elements, in form of powders, rods or ingots

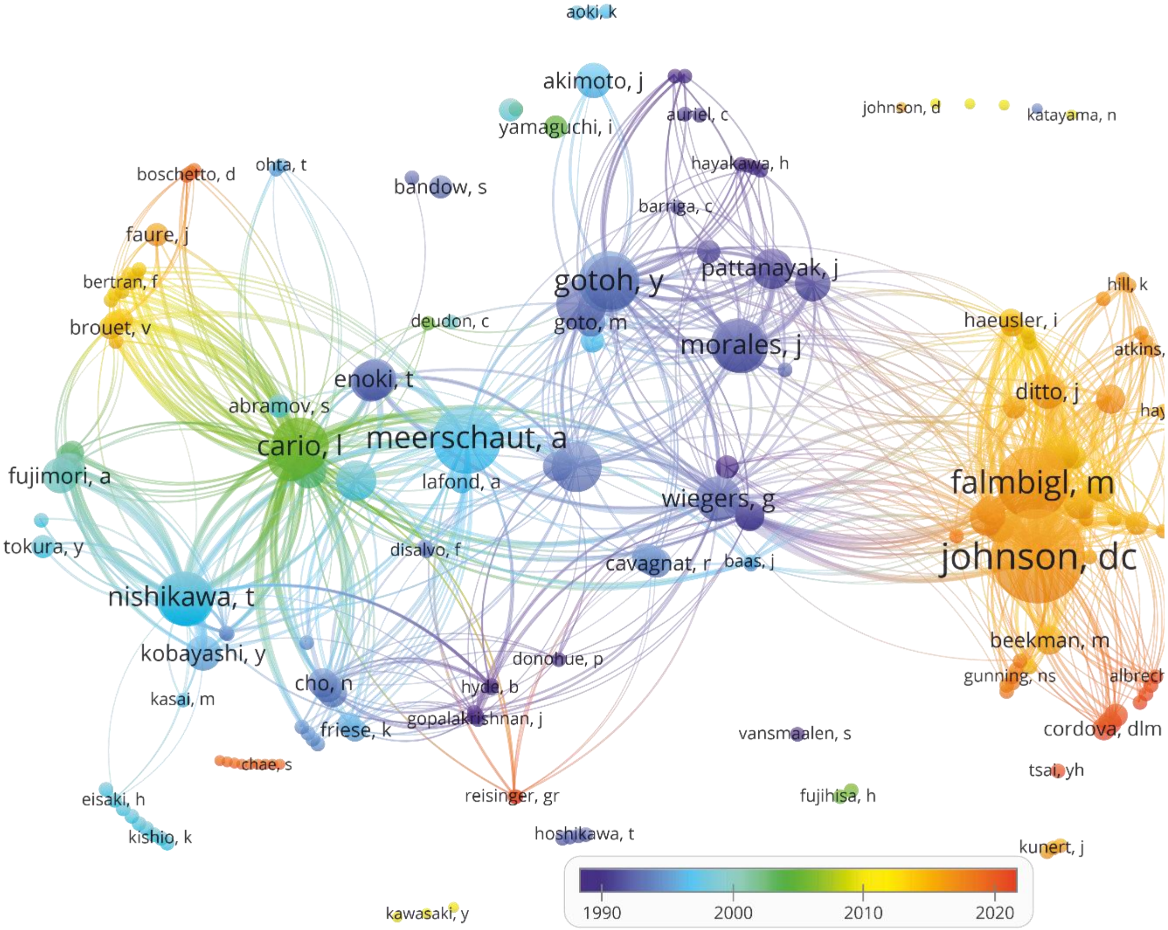

Figure 4: Temporal evolution and relationship between citation networks of the publications featured in this review

- the adjacent binary compounds, in form of powders or small crystals (e.g. MX, VX_2, V_8X_5)
- oxidic powders of the binary constituent analogs (e.g. MO, VO_2) or the ternary stoichiometric composition (e.g. MVO_3) in combination with a H_2X or CX_2 gas flow.

As some of the pure elements and binary compounds are be prone to oxidation, especially those based on rare earth elements, precautionary measures (e.g. glovebox) have to be taken [107, 122].

Weighed-out compositions typically range from stoichiometric compositions of the formula MVX_3 (M = Bi, Pb, RE, or Sn; X = S, or Se), in older literature, to compositions of the formula $[(MX)_{1+\delta}]_m(VX_2)_n$, in more recent literature. In some works, an off-stoichiometric composition is chosen for synthesis, yet, for different reasons. First, when eventual losses of chalcogen are to be compensated. Kikkawa *et al.* added up to 10 wt.% S to their starting composition [41]. For selenium-based compounds no addition of chalcogen, to compensate losses is reported. Second, when the formula $[(MX)_{1+\delta}]_m(VX_2)_n$ appears not to be well-fitting due to vacancies and/or other defects [36, 66, 75]. Finally, when the synthesis of misfit layer compounds is only feasible for off-stoichiometric compositions [107-109].

The annealing procedure is usually executed in multiple steps. The first heat-treatment is different for each type of source material. Oxidic powders are heated at high temperatures in an H_2S or CS_2 gas flow. For the pure elements, a lower annealing temperature or a steadily increasing temperature ramp is chosen, to maintain the chalcogen vapour pressure in the closed silica ampoule low. When starting from the binary compounds, the first annealing step can be skipped for vanadium-based misfit layer compounds. After this first annealing cycle, the resulting powder and/or crystals may be re-grounded. Furthermore, some chalcogen, to compensate losses (e.g. 1.1 wt.% S [41]), and/or some mineraliser, to facilitate crystallisation processes, can be added. Mineralisers utilised in previous investigations to synthesise vanadium-based misfit layer compounds are iodine, chlorine, NH_4Cl, $LaCl_3$, $PbCl_2$, $(NH_4)_2PbCl_6$, or the salt flux of a LiCl/KCl eutectic. The second step of heat-treatment is employed regardless of the type of source material. Either an isothermal annealing procedure or heating within a temperature gradient, where the source is hotter than the sink due to an endothermic transport reaction, can be chosen. The temperatures used depend on the “M” element of the compound; misfit layer compounds based on a rare earth element require higher temperatures than those based on bismuth, lead, or tin. Detailed synthesis procedures of all published data on vanadium-based misfit layer compounds are shown in Table 1.

The resulting plate-like crystals exhibit grey [26] to black metallic lustre [31, 95] and are up to several millimetres in diameter and several ten micrometres in thickness. Not only plate-like crystals but also tubes are reported [109]. Vanadium-based misfit layer compounds tend to oxidise, similar to the source materials. However, the oxidic surface can be easily removed by cleavage/exfoliation [33].

Altering the preparation technique greatly influences the resulting compounds. Cario *et al.* observed different sulphur levels in their misfit layer compounds. Prolonged treatment of oxide mixtures under a constant gas flow of H_2S raised excess sulphur levels in the compound [33]. Additionally, the crystal dimensions and the degree of twinning depend on the choice of mineraliser, as observed by Kikkawa *et al.* [41]. This might be also the reason why the synthesis and/or characterisation of some compounds is challenging [107-109].

b. Ferecrystalline compounds

Specimens created by the modulated elemental reactant technique are synthesised in a high vacuum chamber (~10^{-7} mbar). The pure elements are either evaporated in an effusion cell, as in case of selenium, or by an electron beam gun. Only high purity elements are used as source materials [32, 67]. Thin films of the desired elements are deposited on (100) oriented polished silicon substrates or silicon with thermally grown oxide layers of thicknesses around 100 nm [69].

Deposition rates are controlled by shutter movements and monitored by a quartz crystal monitoring system. Before determining the ideal deposition parameters for a $[(MSe)_{1+\delta}]_m(VSe_2)_n$-type precursor (M = Bi, Eu, La, Pb, or Sn), the two binary compounds need to be calibrated separately. The result is a linear relationship of

Table 1: Preparation procedures of vanadium-based MLCs

MLC	Source + mineraliser	Temperature program	Source
$[(BiS)_{1+\delta}]_m(VS_2)_n$	pure elements	500°C 12h → 800°C 2d → crushed → 700-800°C 2-4d	[60]
	pure elements	500°C 1d → 800°C 1d → 700°C 3d and cooled to RT	[90]
	pure elements	500°C → 800°C	[59, 61, 106]
	pure elements + NH_4Cl	source 850-900°C / sink 800-850°C	[93]
	pure elements + NH_4Cl	source 850°C / sink 700°C	[90]
$[(BiSe)_{1+\delta}]_m(VSe_2)_n$	pure elements	500°C 12h → 800°C 2d → crushed → 700-800°C 2-4d	[60]
	pure elements	500°C → 800°C	[59, 106]
	pure elements / binary compounds + NH_4Cl	560°C 56d	[109]
	pure elements / binary compounds + NH_4Cl	650°C 18m	[109]
$[(LaSe)_{1+\delta}]_m(VSe_2)_n$	pure elements + I_2	400-600°C 2d → 800°C 1d → 1000-1200°C 1-3d	[31]
	pure elements + I_2	400°C 1d → 1100°C 14d → 1100°C 7d	[35]
$[(PbS)_{1+\delta}]_m(VS_2)_n$	pure elements + Cl_2	850°C → source 840°C / sink 770°C	[62, 63]
	pure elements	300°C ?h → 900°C 15d	[63]
	pure elements	500°C 1d → 800°C 4d	[45, 64, 92]
	pure elements	500°C 1d → 800°C ?d	[25, 63]
	pure elements	500°C → 800°C	[106, 111]
	pure elements / binary compounds + $PbCl_2$	source 840°C / sink 730°C 40d	[26]
	pure elements / binary compounds + I_2	900-1100°C	[48]
	ternary oxides + I_2	1300-1400°C CS_2 or H_2S vapour	[48]
	pure elements + $(NH_4)_2PbCl_6$	800°C 1-14d	[118]
$[(PbSe)_{1+\delta}]_m(VSe_2)_n$	pure elements / binary compounds + NH_4Cl	550°C 28d	[107]
	pure elements / binary compounds + NH_4Cl	550°C 56d	[109]
$[(RES)_{1+\delta}]_m(VS_2)_n$	mixture of oxides + I_2	1200°C 6h H_2S vapour → source 950°C / sink 850°C 10d	[49]
	pure elements + I_2	400°C ?d → source 950°C / sink 850°C	[47]
	mixture of oxides + I_2	1200°C 6h H_2S vapour → 950°C 10d	[43]
	pure elements / binary compounds	475°C 5h → 900°C 10h → crushed → 1080°C 20h	[42, 57, 58]
	pure elements / binary compounds	400°C12h → 800-900°C 40h and slowly cooled → crushed → 800-900°C 40h and slowly cooled	[40, 99]
	pure elements + I_2	400-600°C 2d → 800°C 1d → 1000-1200°C 1-3d	[31]
	pure elements / binary compounds	400°C 5h → 1130°C 40h	[54, 57, 58]
	pure elements / binary compounds	400°C12h → 1050-1150°C 40h and slowly cooled → crushed → 1050-1150°C 40h and slowly cooled	[40, 57, 58, 99]
	pure elements / binary compounds + $LaCl_3$	1000°C → crushed → 1000°C → crushed → 1000°C	[34, 83]
	mixture of oxides + I_2	1300°C 6h H_2S vapour	[33, 76, 77]
	pure elements	source 1000°C / sink 950°C 7d	[41]
	pure elements + $LaCl_3$ / I_2	1000°C 7d	[41]
	pure elements / binary compounds	source 950°C / sink 850°C	[53]

	ternary oxides	1200°C 150h H_2S vapour	[105]
$[(SnSe)_{1+\delta}]_m(VSe_2)_n$	pure elements	300°C ?h → 900°C 15d	[95]
	pure elements	500°C 1d → 800°C 7d	[95]
	pure elements / binary compounds + NH_4Cl	550°C 28d	[108]
	pure elements / binary compounds + NH_4Cl	700°C 28d	[108]
	pure elements / binary compounds	550°C 28d	[108]
	pure elements / binary compounds	700°C 28d	[108]
	pure elements / binary compounds + NH_4Cl / I_2 / NaCl+KCl	550°C 28d	[109]
$[(SnS)_{1+\delta}]_m(VS_2)_n$	pure elements / binary compounds + I_2 /NH_4Cl	870°C 5h → source 870°C / sink 730°C 5h	[78]

between opening duration of the shutter time and the element ratio of the binary compound (e.g. M/Se or V/Se). The ratio of the MSe/VSe_2 as a function of shutter times is determined in a second calibration step, while the previously calibrated binary ratios are kept constant. After this second step the shutter opening times and the ratios of the binaries in the newly created compound are plotted and interpolated linearly. When choosing the ideal ratio of MSe/VSe_2 for experimentally preparing *fere*crystals it is the misfit parameter $1+\delta$ rather than the the exact stoichiometric composition [32]. The "average" misfit parameter, calculated by Falmbigl *et al.*, lies close to 1+0.16 [86]. The as-deposited precursor $[(MSe)_{1+\delta}]_m(VSe_2)_n$ is an amorphous material with a total thickness of 400 Å to 600 Å. It mimics the approximate composition and lattice parameter *c* of the final product [32].

Annealing conditions are mild compared to the synthesis of misfit layer compounds [32]. The most suitable temperature range for annealing vanadium-based *fere*crystals is determined by the smallest FWHM of diffraction peaks in X-Ray diffraction. Similar as for misfit layer compounds the optimal temperatures depend on the "M" element of the *fere*crystal. Bismuth- and lanthanum-based compounds need higher temperatures (500 °C and 650 °C) compared to europium-, lead-, and tin-based *fere*crystals (300 °C to 400 °C). Typically, the duration of annealing is between 20 and 30 minutes, as diffusion distances in the precursor are sufficiently short. However, in one study already 10 minutes are observed to be sufficient [71] and two other publications, report one hour to be necessary for satisfying annealing results [27, 28]. A comprehensive list of the published annealing conditions is shown in Table 2.

Table 2: Impact of annealing conditions on the formation of vanadium-based ferecrystals

“M” element	Crystallisation	Annealing	Decomposition	Source
Bi		500 °C 20 min	~550 °C	[96]
Bi/Sn		400 °C 20 min	>500 °C	[74]
Eu	200-300 °C	300 °C 10 min		[71]
La		650 °C 20 min	~700 °C	[71]
Pb		250 °C 60 min		[27]
		300 °C 60 min	300-400 °C	[28]
		400 °C 30 min		[84]
Sn		350 °C 30 min		[32]
	<300 °C	400 °C	400-600 °C	[67]
		400 °C 20 min		[37, 68-70, 114]
	~130 °C	400 °C	>400 °C	[85]
	150-300 °C	400 °C 20 min	>450 °C	[38]
		400 °C		[120]
	~145 °C	400 °C 20 min		[87]

Nucleation of the crystals appears to occur below 300 °C for vanadium-based *fere*crystals (refer to Table 2). Häusler *et al.* [70] investigated the underlying crystallisation process. Determining the orientation of the individual layers, they observed that these layers exhibit a preferred orientation, yet, in a random stacking sequence. Based on that, they suggest a templated growth mechanism for the nucleation process. In this scenario, one layer nucleates first (e.g. VSe_2) and serves as a template for the second layer (e.g. MSe) during growth. This excludes the other two possible nucleation mechanisms of either independent subsequent nucleations or independent nucleations at the same time [70]. The mechanism of templated growth is also assumed by other authors [71, 72]. Evidence such as the relative orientation of layers at a fixed angle of 30°, which equals a twelvefold symmetry [73], or the random orientation of SnSe building blocks, whereas the isostructural layers $SnSe_2$ and VSe_2 are oriented in the same direction [87], could support their assumption.

Prolonged annealing and/or high temperatures not only result in severe oxidation (e.g. ~18 % [87] or ~23 % [38]) but also in the decomposition of the *fere*crystalline precursor into the binary constituents in a disproportionation reaction [28] or in the sublimation of readily formed oxides [38]. Additionally, evaporation effects of selenium require consideration. This decrease in selenium proceeds incrementally and starts even below the optimal annealing temperatures (e.g. 300 °C [87] or 450 °C to 550 °C [71]). It can be detected by shifts of X-Ray diffraction peaks. Generally, precursors are prepared with up to 5 % excess chalcogen to compensate losses during annealing [126], but also amounts of up to 9 % selenium are reported

[87]. Interestingly, not only a loss of selenium is observed but also an accompanying increase in oxygen [38, 87], which might also contribute to off-stoichiometry effects [87]. Häusler *et al.* suggest that rapid thermal annealing and/or annealing in controlled chalcogenide overpressure might result in ordered supercells [70].

3.8.2. Composition and phase equilibria

The exact compositions of the synthesised vanadium-based layered compounds are not mentioned in most works; instead of measured compositions and experimentally determined misfit parameters $1+\delta$, only the ideal values according to the formula $[(MX)_{1+\delta}]_m(VX_2)_n$ with calculated misfit parameters are stated.

For misfit layer compounds no solid solution studies are reported as there are difficulties in synthesis and analysis [120]. Nevertheless, some investigations indicate that the composition might be close to, but not exactly at the ideal stoichiometry. Kikkawa *et al.* investigated sulphur deficiency in the compound $(LaS)_{1+\delta}VS_2$. They observed that the lattice parameter c is not constant, but can be varied by the amount of excess sulphur. Up to an excess sulphur level of 1.1 wt. %, the unit cell expands in c. For sulphur levels above this 1.1. wt. % the c parameter remains constant. For the sublattices, the common lattice parameter b remains constant when the sulphur content is increased, but the individual a parameter of VS_2 shrinks and expands for LaS [41]. This indicates the filling of sulphur vacancies and, hence, some solid solubility. Also, the “M” elements’ lattice position can host significant vacancies (e.g. for Sm [75] or for La [33-36]). Ren *et al.* were able to refine the $(LaSe)_{1+\delta}VSe_2$ compound in X-Ray diffraction in a stoichiometric structure model and a structure model including vacancies. The difference between $(LaSe)_{1.16}VSe_2$ and $(La_{0.95}Se)_{1.21}VSe_2$ equals a solid solubility of ~0.4 at.% [35]. Cario *et al.* [33], who state an exact chemical composition of serval untreated batches and also cleaved batches, observe different compositions of the $(LaS)_{1+\delta}VS_2$ compound that vary by ~0.5 at.%. They confirm a systematic shift towards lanthanum vacancies, yet, not up to the theoretical maximum of $\delta/3$ (i.e. 0.06) proposed by Rouxel and Meerschaut [75]. These vacancies are a result of the existing charge balance between the three elements [35, 88]. In a later investigation, Cario *et al.* even observed a lack in vanadium and a surplus of sulphur [43].

Recent investigations on misfit layer compounds indicate an off-stoichiometric composition measured by EDX for compounds in the ternary systems Bi-Se-V [109], Pb-Se-V [107, 109], and Se-Sn-V [108, 109]. These off-stoichiometric compositions are most likely matrix effects of the EDX measurements rather than results of defects in the crystal structure [109], such as the antisites where $M_{MSe}^{2+} + T_{TSe_2}^{4+}$ are replaced by $T_{MSe}^{3+} + T_{TSe_2}^{3+}$ [127, 128], interstitial layers between VSe_2 slabs [122], or vacancies.

Due to the manifold synthesis possibilities of the modulated elemental reactant technique used for *fere*crystalline compounds, vanadium-rich [37-39] and tin-rich [37] crystals can be synthesised. In several studies, a varying ratio between “M” and vanadium was observed, which cannot be explained by a correlating misfit parameter 1+δ [37, 38, 69, 74]. Furthermore, annealing procedures are reported to reduce selenium contents [87], especially in the layer of VSe_2 [39, 71]. Gunning *et al.* observed local fluctuations of the composition in the VSe_2 layer. They concluded that energy differences within the solubility range between VSe and VSe_2 are rather small and, similar to the ones in bulk, depend on the starting compositions of the precursors [39]. All these reports indicate that *fere*crystals permit larger solubility ranges than expected from the stoichiometric formula $[(MX)_{1+\delta}]_m(VX_2)_n$ and that the amount of all elements can be altered by different defect mechanisms (i.e. substitutions, interstitials, oxides, and vacancies).

Concerning the phase equilibria and/or phase diagrams in systems containing vanadium-based layered compounds only little is known. Due to the metastable nature of *fere*crystalline compounds, only studies on the thermodynamically stable misfit layer compounds should be considered for interpreting the phase equilibria. Some of the equilibria can be obtained by gathering information on impurity phases. Oosawa *et al.* suspected some impurities in the prepared powder pellets of $(BiS)_{1+\delta}VS_2$ and $(BiSe)_{1+\delta}VSe_2$ but did not investigate further on that matter [106]. Three other works that comment on impurities are on $(LaS)_{1+\delta}VS_2$ and/or $(La_{1-x}Sr_xS)_{1+\delta}VS_2$ [40-42]. The authors observed impurities of V_5S_8 and $LaS_{1.75-1.8}$ at 1050 °C to 1150 °C [40], of V_5S_8 at 1000 °C [41], of V_5S_8 and V_3S_4 at 1080 °C [42]. These results require some interpretation. The phase V_5S_8 is a result of the quenching process, as the high-temperature composition of it appears to be not quenchable [129]. Subject to the condition that the misfit layer compound $(LaS)_{1+\delta}VS_2$ is stoichiometric, the ternary phase equilibria are VS_2 + V_3S_4 + $(LaS)_{1+\delta}VS_2$ and LaS + $LaS_{1.75\text{-}1.8}$ + $(LaS)_{1+\delta}VS_2$. Also, the equilibria VS_2 + $LaS_{1.75\text{-}1.8}$ + $(LaS)_{1+\delta}VS_2$ and LaS + V_3S_4 + $(LaS)_{1+\delta}VS_2$ may be proposed for the La-S-V system, provided that the situation is similar to the isothermal section at 700 °C in the Se-Sn-V system. In that section, all ternary phase equilibria between VSe_2, V_3Se_4, SnSe, and a selenium-rich liquid are radially connected to the misfit layer compounds [108]. At 500 °C, where several misfit layer compounds are reported, the phase equilibria are more complicated. For the selenium-rich side, all misfit layer compounds' compositions connect to $SnSe_2$, but for the vanadium-rich side, no clear pattern is visible [108]. For the Pb-Se-V system, the phase equilibria are reported to be uncertain, as the composition was off-stoichiometric and the misfit layer compound could only be obtained by the addition of NH_4Cl [107].

3.9. Crystal structures

3.9.1. General structural features of vanadium-based misfit layer compounds

Similar to all other misfit layer compounds described in detail by Wiegers [122], all vanadium-based misfit layer compounds comprise two subsystems that are bonded via van der Waals forces (refer to Figure 1). The MX and VX_2 subsystem may comprise the "M" elements tin, lanthanum, cerium, praseodymium, neodymium, samarium, gadolinium, bismuth, and/or lead, and the "X" chalcogen elements sulphur or selenium. Studies with antimony and/or tellurium were unsuccessful in preparing the desired compounds [109, 130].

The in-plane lattice parameter *a* is incommensurate, whereas, the *b* and *c* axis are common, or at least a multiple, for both subsystems. All available published structural data were normed to this scheme and are shown in Table 3, Table 4, and Table 5. Noteworthy, only certain lattice parameters and/or crystallographic angles are stated in literature and no space groups are available in most studies. The ratio between the length of the two incommensurate *a* axes (a_{MX}/a_{VX_2}) is between 1.65 [35, 122] and 1.78 [25, 122]. In the ideal case of a non-defective structure this ratio defines the composition. Several authors pointed out, that this ratio is close to rational ratios such as 5/3 [34, 35, 43, 44], 34/20 [44], and 7/4 [25]. Such rational ratios indicate periodicities for a superstructure setting.

As the *a* axis in vanadium-based misfit layer compounds should be the only incommensurate axis, the ratio of length between the two incommensurate *a* axes of the sublattices is used as a basis for the calculation of the misfit parameter 1+δ (refer to Figure 1). However, different methods of calculation are employed for determining the misfit parameter, which all yield slightly different results; particularly, on the third decimal. Wiegers [122] suggests to generally calculate of the misfit parameter by the formula $1+\delta=\frac{Z_{MX}*a_{VX_2}}{Z_{VX_2}*a_{MX}}$, utilising only the *a* parameters and the formula units per unit cell *Z*. Some authors (e.g. Onoda *et al.* [45], Gotoh *et al.* [90]) work with the volume ratio in the rather similar formula $1+\delta=\frac{Z_{MX}*V_{VX_2}}{Z_{VX_2}*V_{MX}}$. These authors probably used this method due to slight deviations in the common *b* axis. Wiegers [122] points out that this approach is less precise. Merril *et al.* suggest employing the square basal plane in the formula $1+\delta=\frac{Z_{MX}*a_{VX_2}*b_{VX_2}}{Z_{VX_2}*a_{MX}*b_{MX}}$, in order to compare the results to *fere*crystals [126]. As both *b* axes are commensurate in vanadium-based misfit layer compounds, this method reduces the accuracy, just as the volume ratio does. The misfit parameters stated in some publications, are slightly different from our calculations. We suspect that the authors either refered to another crystal in the same work (e.g. Gotoh *et al.* [25]), or to results of earlier works (e.g. Gotoh *et al.* [90]) or that they rounded their results more generously (e.g. Gotoh *et al.* [92]). In other works some generalised misfit parameter is estimated [83] or the stated misfit parameters cannot be verified, as the respective lattice parameters are missing [26, 33, 40, 41, 44-58]. Generally, misfit parameters 1+δ of vanadium-based misfit layer compounds range from 1.12 for lead-based [45] to 1.25 for samarium-based or gadolinium-based compounds [53] (refer to Table 3).

For vanadium-based misfit layer compounds, three different crystal systems are reported in literature. The lattices are described by orthorhombic, monoclinic or triclinic lattices. It is noteworthy that in all reported structures the angle γ is equal to 90° or at least equal to that value within the standard deviation. Angles for α and/or β are within 90° ± 10°, but most common ~90°, ~95°, or ~99° (refer to Figure 1,

Table 3: All reported misfit parameters δ and lattice distances d of vanadium-based misfit layer compounds as well as our calculations, when possible; indices given in the table denote our calculations (*), approximations in the literature (a), our approximations from graphs in the literature (g), d parameters that are equal to the overall c axis (c), the c axis of the VX_2 lattice (c1), and the c axis of the MX lattice (c2).

Compound	Comment	δ	d [Å]	Lit.
$(BiS)_{1+\delta}VS_2$ and intercalate			11.250	[59]
			11.270	[60]
	0 Li/unit		22.440	[61]
	0.07 Li/unit		22.470	
	0.13 Li/unit		22.540	
		0.16/0.15*	11.311*/11.311*	[90]
		0.160	11.310	
		0.160	11.310	[46]
		0.16/0.156*	11.311*/11.314*	[93]
			11.310	[91]
$(BiSe)_{1+\delta}VSe_2$			11.920	[59]
			11.920	[60]
		-0.12	11.885	[109]
$(CeS)_{1+\delta}VS_2$		0.190	11.060	[47]
		0.2^{a}/0.177*	11.105^{c1}/11.105^{c2}	[83]^{g}
		0.190		[52]
		0.190		[51]
		0.190		[53]
$(GdS)_{1+\delta}VS_2$			10.865*	[105]
		0.2^{a}/0.17*	10.922^{c1}/10.922^{c2}	[83]^{g}
		0.250		[53]
$(La_{0.95}S)_{1+\delta}VS_2$		0.18/0.18*	44.59^{c1}/66.89^{c2}	[88]
	3D space group	0.196	11.108*	[43]
	3+1D space group	0.196	11.1*	
		0.196/0.196*	11.103*/11.095*	
		0.180	22.36^{c}	[33]
$(LaS)_{1+\delta}VS_2$			11.158*	[105]
		0.176		[44]
		0.160	11.156	[47]
		0.2^{a}/0.171*		[83]
		0.2^{a}/0.176*	11.135^{c1}/11.135^{c2}	[83]^{g}
		0.150		[51]
		0.18/0.18*	22.32^{c1}/22.32^{c2}	[34]
		0.180	22.35^{c}	[41]
		0.160		[55]
		0.180	22.21^{c}	[33]
		0.196		[77]
		0.196		[50]
		0.196		[49]
$(LaS_x)_{1+\delta}VS_2$	initial composition +x wt.% S	0.180	22.175^{c}	[41]
	initial composition +0.7 wt.% S	0.18/0.183*	22.2682^{c1}/22.2682^{c2}	[41]^{g}
	initial composition +0.8 wt.% S	0.18/0.18*	22.2937^{c1}/22.2937^{c2}	
	initial composition +0.9 wt.% S	0.18/0.178*	22.3109^{c1}/22.3109^{c2}	
	initial composition +1 wt.% S	0.18/0.176*	22.3282^{c1}/22.3282^{c2}	
	initial composition +1.1 wt.% S	0.18/0.175*	22.3628^{c1}/22.3628^{c2}	
	initial composition +1.4 wt.% S	0.180	22.3724^{c1}/22.3724^{c2}	
	initial composition +2 wt.% S	0.180	22.3724^{c1}/22.3724^{c2}	
	initial composition +11 wt.% S	0.180	22.3802^{c1}/22.3802^{c2}	
$(La_{1-x}Pb_xS)_{1+\delta}VS_2$	x=0	0.170	22.5701^{c}	[40]^{g}
	x=0.04	0.170	22.6167^{c}	
	x=0.08	0.170	22.6493^{c}	
	x=0.13	0.170	22.6866^{c}	
	x=0.14	0.170	22.7644^{c}	
	x=0.21	0.170	22.8421^{c}	

	x=0.25	0.170	22.8747[c]	
	x=0.29	0.170	22.9509[c]	
	x=0.56	0.170	23.2406[c]	
	x=0.64	0.170	23.3915[c]	
	x=0.73	0.170	23.5455[c]	
	x=0.82	0.170	23.7805[c]	
	x=0.86	0.170	23.8232[c]	
	x=0.91	0.170	23.8597[c]	
	x=0.95	0.170	23.8977[c]	
	x=1	0.170	23.9957[c]	
$(La_{1-x}Sr_xS)_{1+\delta}VS_2$	x=0	0.170	11.157[c]	[54][g]
	x=0.17	0.170	11.22[c]	
	x=0.22	0.170	11.236[c]	
	x=0.25	0.170	11.268[c]	
	x=0.28	0.170	11.281[c]	
	x=0.3	0.170	11.279[c]	
	x=0.32	0.170	11.304[c]	
	x=0.35	0.170	11.311[c]	
	x=0.4	0.170	11.353[c]	
	x=0	0.170	22.5701[c]	[40][g]
	x=0.04	0.170	22.6167[c]	
	x=0.06	0.170	22.6346[c]	
	x=0.08	0.170	22.6711[c]	
	x=0.12	0.170	22.7115[c]	
	x=0.14	0.170	22.7512[c]	
	x=0.18	0.170	22.7892[c]	
	x=0.21	0.170	22.8421[c]	
	x=0.23	0.170	22.867[c]	
	x=0.25	0.170	22.863[c]	
	x=0.27	0.170	22.9159[c]	
	x=0.29	0.170	22.9299[c]	
	x=0.32	0.170	23.0272[c]	
	x=0.34	0.170	23.0264[c]	
	x=0.38	0.170	23.048[c]	
	x=0.42	0.170	23.0728[c]	
	$0 \leq x \leq 0.4$	0.170		[56]
	$0 \leq x \leq 0.3$	0.170		[57]
	$0 \leq x \leq 0.35$	0.170		[58]
$(La_{0.95}Se)_{1+\delta}VSe_2$		0.210		[35]
		0.21/0.21*	11.614*/11.606*	
$(LaSe)_{1+\delta}VSe_2$		0.21/0.21*	11.614*/11.602*	[122]
		0.210		[86]
$(NdS)_{1+\delta}VS_2$			10.957*	[105]
		0.230	10.972	[47]
		0.2[a]/0.181*	11.031[c1]/11.031[c2]	[83][g]
		0.230		[53]
$(PbS)_{1+\delta}VS_2$ and intercalate		0.1/0.138*	23.608*/23.608*	[92]
		0.13/0.129*	23.503*/11.768*	[118]
		0.13/0.132*	23.533*/11.771*	[118]
		0.12/0.135*	23.663*/23.608*	[25]
		0.12/0.125*	23.655*/23.648*	
		0.12/0.125*	11.824*/23.649*	[122]
		0.120		[45]
		0.120		[45]
	0 Li/unit		23.64*	[62]
	0.89 Li/unit		23.619*	
	2.4 Li/unit		amorphous	
	delithiated		23.632*	
				[104]
		0.130		[48]
		0.131*	23.539*/11.769*	[111]

		0.120	11.830	[46]
		0.120/0.125*	23.648*/23.648*	[26]
$(PbSe)_{1+\delta}VSe_2$		0.10/0.15	12.208	[109]
$(PrS)_{1+\delta}VS_2$		0.2[a]/0.178*	11.039[c1]/11.039[c2]	[83][g]
$(SmS)_{1+\delta}VS_2$		0.230	10.902	[47]
		0.250	10.866	
		0.2[a]/0.169*	10.96[c1]/10.96[c2]	[83][g]
		0.250		[53]
$(SnSe)_{1+\delta}VSe_2$ and intercalate			24.2[c]	[95]
	0 Li/unit		24.2[c]	[61]
	0.05 Li/unit		24.4[c]	
		0.17	12.066	[108, 109]
$[(SnSe)_{1+\delta}]_2VSe_2$		0.17	17.866	[108, 109]
$[(SnSe)_{1+\delta}]_3VSe_2$		0.15	23.71*	[109]
$[(SnSe)_{1+\delta}]_4VSe_2$		0.15	29.549	[108, 109]
$[(SnSe)_{1+\delta}]_5VSe_2$		0.15	35.35*	[109]
$[(SnSe)_{1+\delta}]_6VSe_2$		0.16	41.16*	[109]

Table 4 and Table 5). The monoclinic distortion can also be estimated by the empirical relation $\alpha = 90 + \arcsin\frac{b}{6*c}$ [118]. Due to these angular distortions, the *c* axes are not comparable for all compounds. The interlayer distance *d*, which is the surface normal to the layers, is corrected for these distortions and may be compared easily. The interlayer distance *d* is reported when the remaining lattice parameters are not determined [46, 47, 59-61]. Lattice parameters and interlayer distances of misfit layer compounds in a quaternary solid-solution model [40, 54] or in a model with sulphur deficiency [41] obey Vegard's law. All published data on this interlayer distance as well as our calculated values are shown in Table 3.

Only for some of the reported vanadium-based misfit layer compounds the space groups and/or super-space groups are published. All of them are either *C* or *F* centred. Of the four possible types of stackings described by Wiegers (e.g. *CC* type – $c_{MX} \approx c_{VX2}$, *CF* type – $2c_{MX} \approx c_{VX2}$, *FC* type – $c_{MX} \approx 2c_{VX2}$, and *FF* type – $2c_{MX} \approx 2c_{VX2}$) [122], all types are observed. However, the fact that different stacking types are reported for the same misfit layer compound features the ambiguity of results and also the difficulties in the interpretation of results. $(PbS)_{1+\delta}VS_2$ for example is reported in a *CF* [25, 111, 118], a *FC* [122], and a *FF* [92] type of setting. For vanadium-based systems, the stacking parameters *m* and *n* are equal to one in most cases. Due to that reason, the interlayer distance *d* for one layer of each sublattice of the compounds is between 10.866 Å [105] and 12.2 Å [61] in a *C* centred setting.

Table 4: All reported superstructures of vanadium-based misfit layer compounds normalised to an incommensurate a axis; indices given in the table denote our approximations from graphs in the literature (g).

Lit.	Compound	Comment	δ	S.G.	a [Å]	b [Å]	c [Å]	α [°]	β [°]	γ [°]
[90]	$(BiS)_{1+\delta}VS_2$		0.16	2/m						
[105]	$(GdS)_{1+\delta}VS_2$				5.847	16.37	10.866		89.4	
[43]	$(La_{0.95}S)_{1+\delta}VS_2$	3D	0.196	C	17.1	5.9	11.2	95.1	84.7	90
	$(La_{0.95}S)_{1+\delta}VS_2$	3+1D	0.196		3.41	5.845	11.191	95.15	84.79	89.98
[33]	$(La_{0.96}S)_{1+\delta}VS_2$		0.18		5.7	5.814	22.36			
[40][g]	$(La_{1-x}Pb_xS)_{1+\delta}VS_2$	x=0	0.17		5.697	5.865	22.57			
		x=0.04	0.17		5.686	5.86	22.617			
		x=0.08	0.17		5.686	5.851	22.649			
		x=0.13	0.17		5.689	5.848	22.687			
		x=0.14	0.17		5.718	5.841	22.764			
		x=0.21	0.17		5.722	5.824	22.842			
		x=0.25	0.17		5.74	5.825	22.875			
		x=0.29	0.17		5.727	5.821	22.951			
		x=0.56	0.17		5.776	5.796	23.241			
		x=0.64	0.17		5.769	5.788	23.392			
		x=0.73	0.17		5.805	5.768	23.546			
		x=0.82	0.17		5.817	5.758	23.781			
		x=0.86	0.17		5.787	5.76	23.823			
		x=0.91	0.17		5.809	5.756	23.86			
		x=0.95	0.17		5.805	5.737	23.898			
		x=1	0.17		5.817	5.748	23.996			
[40][g]	$(La_{1-x}Sr_xS)_{1+\delta}VS_2$	x=0	0.17		5.697	5.865	22.57			
		x=0.04	0.17		5.701	5.863	22.617			
		x=0.06	0.17		5.686	5.864	22.635			
		x=0.08	0.17		5.704	5.858	22.671			
		x=0.12	0.17		5.704	5.858	22.712			
		x=0.14	0.17		5.711	5.849	22.751			
		x=0.18	0.17		5.743	5.854	22.789			
		x=0.21	0.17		5.711	5.843	22.842			
		x=0.23	0.17		5.729	5.842	22.867			
		x=0.25	0.17		5.727	5.836	22.863			
		x=0.27	0.17		5.738	5.831	22.916			
		x=0.29	0.17		5.738	5.823	22.93			
		x=0.32	0.17		5.751	5.827	23.027			
		x=0.34	0.17		5.749	5.823	23.026			
		x=0.38	0.17		5.758	5.828	23.048			
		x=0.42	0.17		5.74	5.817	23.073			
[105]	$(LaS)_{1+\delta}VS_2$				5.985	16.854	11.158		89.7	
[33]	$(LaS)_{1+\delta}VS_2$		0.18		5.722	5.818	22.21			
[35]	$(La_{0.95}Se)_{1+\delta}VSe_2$		0.21	C-1						
[105]	$(NdS)_{1+\delta}VS_2$				5.886	16.8	10.958		89.3	
[45]	$(PbS)_{1+\delta}VS_2$		0.12	PC2/m1-1						
[62]	$(PbS)_{1+\delta}VS_2$	0 Li/unit			5.719	5.76	23.924		98.83	
		0.89 Li/unit			5.72	5.74	23.9		98.8	
		delithiated			5.67	5.67	23.92		98.9	

For the *F* centred setting this value is doubled compared to the *C* centred setting. Two exceptions are reported. Friese *et al.* report an ordered superstructure in which the lattice parameters for the *c* axis are quadruple and sextuple for the VS2 and LaS sublattices, respectively [88]. In a study of Reisinger and Richter [108, 109] stacking sequence values *m* of up to six are reported for $[(SnSe)_{1+\delta}]_m VSe_2$. Generally, it is uncommon for misfit layer compounds to show stacking sequences with *m* or *n* values larger than one [122]. Kikkawa *et al.* also attempted to synthesise different stacking sequences for $(LaS)_{1+\delta}(VS_2)_n$. They observed that only $n = 1$ was feasible, but $2 \leq n \leq 5$ were not [41].

Tin-based compounds show different stacking sequences whereas for lanthanum-based compounds only one stacking is observed. This may be attributed to the electron donation of the MX to the VX_2 layer. For lanthanide-based and bismuth-based misfit layer compounds the vanadium and the "M" element are both trivalent. This results in a stronger covalent interlayer interaction and a larger charge transfer from MX to VX_2 [122]. Assuming a constant charge transfer, increasingly higher defect concentrations may be required to permit increasing stacking values (e.g. m and/or n larger than one). Although lanthanide-based misfit layer compounds such as samarium are reported to permit high vacancy densities [75], various effects have to be considered. On the one hand, the effect of defect concentrations was reported to be significant in the structural coherence of *fere*crystalline compounds [67], where slight deviations in composition resulted in defect-filled structures (e.g. partial layers, interstitials, vacancies) and large deviations resulted in the decomposition of the whole compound into individual crystals of MX and VX_2 [28]. On the other hand, the stabilising influence of substitution of "M" sites was reported for misfit layer compounds, as the charge transfer is altered and, due to the different cationic radii, the interfacial energies are reduced [66].

Intercalation studies of several vanadium-based misfit layer compounds are available in literature. $(SnSe)_{1+\delta}VSe_2$ [61, 62] as well as sulphur-based compounds with the "M" elements tin [66, 78], lanthanum [36], lead [36, 61-66], and bismuth [61] were intercalated. The intercalated cation is integrated into the van der Waals gap of the host's crystal structure. In the process of intercalation, the host unit cell expands along the *c* axes. Intercalation attempts were undertaken with lithium, either electrochemically [63] or with n-butyl-lithium [61, 62, 64], and with different n-alkylamines (n = 1 to 10 carbon atoms) [61, 64]. Lithiation of the compounds allowed the development of a twelvefold symmetry. Since the "M" ions interact with the lithium ions, three energetically equivalent orientations are observed for the MX layer. This is in contrast to the VX_2 sublattice, where the orientation is maintained [61, 62]. Prolonged lithiation leads to the disappearance of

Table 5: All reported structures of sublattices in vanadium-based misfit layer compounds normalised to an incommensurate a axis; indices given in the table denote our calculations (*), approximations in the literature (a), and our approximations from graphs in the literature (g).

Lit.	Compound	Comment	δ	lattice	S.G.	a [Å]	b [Å]	c [Å]	α [°]	β [°]	γ [°]
[90]	$(BiS)_{1+\delta}VS_2$		0.16/ 0.15*	VS_2	C	3.261	5.67	11.354	94.97		
				BiS	C	5.67	5.643	11.354	94.97		
[93]	$(BiS)_{1+\delta}VS_2$		0.16/ 0.156*	VS_2	C-1	3.2605	5.6701	11.354	94.97	90.5	89.975
				BiS	C-1	5.6425	5.669	11.357	94.97	90	90.02
[83]^{g}	$(CeS)_{1+\delta}VS_2$		0.2^{a}/ 0.177*	VS_2		3.29	5.916	11.105			
				CeS		5.592	5.916	11.105			
[83]^{g}	$(GdS)_{1+\delta}VS_2$		0.2^{a}/ 0.17*	VS_2		3.16	5.848	10.922			
				GdS		5.4	5.848	10.922			
[88]	$(La_{0.95}S)_{1+\delta}VS_2$		0.18/ 0.18*	VS_2	C2/m1(1)	3.366	5.83	44.59			
				$La_{0.95}S$	Cmm(a)	5.705	5.83	66.89			
[43]	$(La_{0.95}S)_{1+\delta}VS_2$		0.196/ 0.196*	VS_2		3.41	5.85	11.196	95.12	84.69	90
				$La_{0.95}S$		5.703	5.844	11.19	95.18	84.61	90.03
[83]	$(LaS)_{1+\delta}VS_2$		0.2^{a}/ 0.171*	VS_2		3.32	5.9				
				LaS		5.67	5.9				
[83]^{g}	$(LaS)_{1+\delta}VS_2$		0.2^{a}/ 0.176*	VS_2		3.325	5.929	11.135			
				LaS		5.654	5.929	11.135			
[34]	$(LaS)_{1+\delta}VS_2$		0.18/ 0.18*	VS_2	C2/m1(1)	3.366	5.828	22.32			
				LaS	Cm2(a)	5.705	5.828	22.32			
[41]^{g}	$(LaS_x)_{1+\delta}VS_2$	+0.7 wt.% S	0.18/ 0.183*	VS_2		3.36	5.809	22.268			
				LaS_x		5.681	5.809	22.268			
		+0.8 wt.% S	0.18/ 0.18*	VS_2		3.357	5.804	22.294			
				LaS_x		5.69	5.804	22.294			
		+0.9 wt.% S	0.18/ 0.178*	VS_2		3.354	5.806	22.311			
				LaS_x		5.697	5.806	22.311			
		+1 wt.% S	0.18/ 0.176*	VS_2		3.352	5.816	22.328			
				LaS_x		5.703	5.816	22.328			
		+1.1 wt.% S	0.18/ 0.175*	VS_2		3.352	5.81	22.363			
				LaS_x		5.707	5.81	22.363			
[35]	$(La_{0.95}Se)_{1+\delta}VSe_2$		0.21/ 0.21*	VSe_2	C-1	3.576	6.1	11.69	95.12	85.96	89.91
				$La_{0.95}Se$	C-1	5.911	6.101	11.684	95.07	85.76	90.02
[122]	$(LaSe)_{1+\delta}VSe_2$		0.21/ 0.21*	VSe_2	C-1	3.576	6.102	11.69	95.12	85.96	
				LaSe	C-1	5.911	6.101	11.68	95.07	85.76	
[83]^{g}	$(NdS)_{1+\delta}VS_2$		0.2^{a}/ 0.181*	VS_2		3.24	5.888	11.031			
				NdS		5.487	5.888	11.031			
[92]	$(PbS)_{1+\delta}VS_2$		0.1/ 0.138*	VS_2		3.28	5.72	23.896	98.91		
				PbS		5.766	5.72	23.896	98.91		
[118]	$(PbS)_{1+\delta}VS_2$		0.13/ 0.129*	VS_2	F^{a}	3.279	5.718	23.579	94.61	90	90.4
				PbS	C	5.807	5.736	11.809	94.76	89.97	89.97
			0.13/ 0.132*	VS_2	F^{a}	3.289	5.727	23.618	94.87	89.9	89.5
				PbS	C	5.81	5.735	11.812	94.79	89.97	90.05
[25]	$(PbS)_{1+\delta}VS_2$		0.12/ 0.135*	VS_2		3.272	5.718	23.93	98.56		
				PbS		5.766	5.72	23.896	98.91		
			0.12/ 0.125*	VS_2		3.256	5.73	23.948	98.97		
				PbS		5.789	5.728	23.939	98.95		
[122]	$(PbS)_{1+\delta}VS_2$		0.12/ 0.125*	VS_2	C2	3.256	5.727	11.97	98.95		
				PbS	F2	5.789	5.728	23.94	98.95		
[26]	$(PbS)_{1+\delta}VS_2$		0.120/ 0.125*	VS_2		3.256	5.7279	23.939		98.947	
				PbS		5.7886	5.7279	23.939		98.947	
[45]	$(PbS)_{1+\delta}VS_2$		0.12	VS_2	C2						
				PbS	C2						
[111]	$(PbS)_{1+\delta}VS_2$		0.131*	VS_2	F2	3.284	5.729	23.62		94.76	
				PbS	C2	5.808	5.729	11.81		94.76	
[109]	$(PbSe)_{1+\delta}VSe_2$		0.10	VSe_2		3.26	5.69			$90\text{-}99^{a}$	
				PbSe		5.93	5.69			$90\text{-}99^{a}$	
[83]^{g}	$(PrS)_{1+\delta}VS_2$		0.2^{a}/ 0.178*	VS_2		3.26	5.905	11.039			
				PrS		5.536	5.905	11.039			
[83]^{g}	$(SmS)_{1+\delta}VS_2$		0.2^{a}/ 0.169*	VS_2		3.175	5.868	10.96			
				SmS		5.43	5.868	10.96			

the MX sublattice [61] and finally amorphisation of the whole compound [61-63]. Amorphisation is reversible by delithiation via I_2/CH_3CN [62]. Intercalated n-alkyl-amines, with chain lengths of up to ten carbon atoms, form bilayers of chains that adopt an angel of approximately 60 ° with the host lattice [64]. In contrast to these results, another study reported that n-hexyl-amine cannot be intercalated without prior lithiation. Hernan *et al.* suspect that an increased interlayer spacing is required for the successful intercalation of long n-alkyl-amines [61].

3.9.2. General structural features of vanadium-based *fere*crystals

The number of different vanadium-based *fere*crystalline compounds is lower than for the misfit layer compounds. For the chalcogen elements “X” only selenium is reported and for the “M” elements tin, lanthanum, europium, lead, and/or bismuth were investigated. Albeit, *fere*crystals comprise of MSe and VSe_2 building blocks (refer to Figure 1), which is similar to misfit layer compounds, some significant structural differences can be observed.

The most striking difference is observed for the common interface of the two constituent structures. For misfit layer compounds the constituent structures distort in a rectangular manner. This distortion results in one of the two in-plane lattice parameters being common, whereas the other is incommensurate. Furthermore, some distortions for α and/or β but not in γ are observed. Vanadium-based *fere*crystals, on the other hand, exhibit hexagonal and square basal planes for the VSe_2 and the MSe layer, respectively. The in-plane lattice parameters are very closely related to the bulk materials and are insensitive to the stacking sequence [23]. Only one exception is reported by Gunning for a lanthanum-based *fere*crystal [39], where two orthorhombic unit cells are utilised to describe the lattices.

Hence, the calculation of the misfit parameter δ on an interface is different from that proposed by Wiegers [122] and described above. For *fere*crystals it is generally calculated by the formula $1+\delta=\frac{Z_{MSe}*a_{VSe_2}*b_{VSe_2}}{Z_{VSe_2}*a_{MSe}*b_{MSe}}$ [126]. For the setting of hexagonal ($a_{VSe_2}*\sqrt{3}=b_{VSe_2}$) and square basal planes ($a_{MSe}=b_{MSe}$) it simplifies to $1+\delta=\frac{Z_{MSe}*a_{VSe_2}^2*\sqrt{3}}{Z_{VSe_2}*a_{MSe}^2}$. We recalculated all misfit parameters, when in-plane structural parameters were available. The difference between the method of Wiegers [122] and that of Merrill *et al.* [126] is up to $\delta = \pm 0.04$. But besides that, there are also some differences between the reported and our calculated misfit parameters (method of Merrill *et al.* [126]; refer to Table 6), which may be attributed to three reasons. First, similar to the misfit layer compounds, in many cases, only two decimals are reported, although, the propagation of error would allow three decimals in many cases. Hence, rounding might explain some slight differences. Second, regardless of the actual calculated values, a fixed value (e.g. $\delta = 0.15$) is stated especially on tin-bases *fere*crystals. Presumably, a misfit parameter of previous investigations or an "average" misfit parameter was used, which is empirically found to be around $\delta = 0.16(1)$ for *fere*crystals except for the trivalent cations M = Bi and La [86]. The error here is up to $\delta = \pm 0.033$ [87]. Third, some publications state misfit parameters that are determined by the M/V-ratio in EPMA and contrast them with the values determined by the ratio of basal planes [67-70]. For those, the largest differences, of up to $\delta = \pm 0.198$, are observed [69].

In contrast to vanadium-based misfit layer compounds, no angular distortion of the sublattices for *fere*crystals is reported. Hence, regarding the interlayer distances the lattice parameters *c* do not require correction in order to compare them for different *fere*crystals. For a compound, where *m* and *n* are both equal to one, the *c* axis ranges from 11.22 Å to 12.73 Å (refer to Table 6), which is about 0.5 Å larger than for vanadium-based misfit layer compounds. We suspect that the larger lattice spacing may be either attributed to higher defect contractions or to the rotational disorder, the resulting lattice mismatch and the, therefore, weaker interlayer interactions.

In most of the literature on *fere*crystals no information on the utilised space groups is given. When available only the trigonal space group *P*-3*m*1 is reported, which is used to explain the distances between atomic layers in the superstructure along the *c* axis [37, 69-71]. Unfortunately, albeit hypothetically possible, no two-dimensional layer groups are used which would be favourable in two ways. Vanadium-based *fere*crystals show almost no observable superstructures and if only for large unit cells [68, 70] due to the rotational disorder of the layers. Layer groups, On the one hand, reflect the two-dimensional nature of *fere*crystals and, on the other hand, resolve the issue that such disordered structures cannot be described properly.

Rotational disorder along the *c* axis, or also turbostratic disorder, is reported for multiple vanadium-based *fere*crystals [28, 32, 38, 39, 67-69, 71-74]. This layer-to-layer rotational misregistration alters the visible faces in STEM imaging. As a result, not only the zone axes [100] of the MX layer and [110] of the VX_2 layer, are visible [126]. Nevertheless, Hite *et al.* also report on aligned layers in a $[(BiSe)_{1+\delta}]_1(VSe)_1$ *fere*crystal over the majority of the sample [96], as common for misfit layer compounds. Häusler *et al.* suggest, those may be the ordered supercells synthesised by rapid thermal annealing [70].

The subsequent publication by Rudin and Johnson [73] also investigated the relative rotation between domains. They observed that the arrangement is not random. Moreover, they report on a most favourable angle of 15 ° to minimise total energies (i.e. -13 meV per ion) whereas the least favourable one is at 0 °. Minima and maxima oscillate with a 30 ° periodicity [73], which explains the twelvefold symmetry observed earlier [70]. Rudin and Johnson also calculated the relative offset between layers. It is most favourable for the SnSe-“dimer” to be centred over a selenium triangle and in line with the vanadium ion. The least favourable offset for the “dimer” is to be in line with a selenium ion and centred over a vanadium triangle [73]. Albeit, the results are calculated for a $[(SnSe)_{1+\delta}]_1(VSe)_1$ *fere*crystal only, these results might be generally applicable to other vanadium-based *fere*crystals, too.

In contrast to most misfit layer compounds, where most stacking sequences reported are $m = n = 1$ compounds, the *fere*crystals were investigated for values up to $m \leq 4$ and $n = 1$ or $m = 1$ and $n \leq 6$. However, no investigations on *fere*crystalline heterostructures with $m \geq 2$ and $n \geq 2$ at the same time are available. Such stacking sequences are in general energetically less stable than ratios where either $m = 1$ or $n = 1$ [101]. For the *fere*crystals in these series, a linear relationship between the stacking parameters *m* or *n* and the length of *c* axes is observed. This allows the extrapolation of the layer thicknesses of each building block. Vegard’s law can be also applied to the lattice parameter *c* in solid solution models (e.g. Sn for Bi [74], V for Ta [114, 120]). For these multicomponent systems, ordered (i.e. ACBC) and

Table 6: All reported misfit parameters δ and lattice distances d of vanadium-based ferecrystals as well as our calculations, when possible; indices given in the table denote our calculations (*), our approximations from graphs in the literature (g), and values determined experimentally by EPMA (e).

Lit.	Compound	Comment	δ	S.G.	a_{VSe2}/b_{VSe2} [Å]	a_{MSe}/b_{MSe} [Å]	c [Å]
[96]	$[(BiSe)_{1+\delta}]_1(VSe_2)_1$						11.80
	$[(BiSe)_{1+\delta}]_1(VSe_2)_1$						11.86
	$[(Bi_xSe)_{1+\delta}]_1(VSe_2)_1$						11.78
[71]	$[(EuSe)_{1+\delta}]_1(VSe_2)_1$		-0.04				11.22
	$[(EuSe)_{1+\delta}]_1(VSe_2)_2$		-0.04				17.37
	$[(EuSe)_{1+\delta}]_1(VSe_2)_3$		-0.04				23.46
[39]	$[(LaSe)_{1+\delta}]_1(V_{n(1+y)+1}Se_{2n+2})$	n=1 y=0.5	0.17/0.167*	P-3m1	a=3.56/ b=6.06	a=6.14/ b=6.02	17.50
	$[(LaSe)_{1+\delta}]_1(V_{n(1+y)+1}Se_{2n+2})$	n=2 y=0.5	0.17/0.17*	P-3m1	a=3.54/ b=6.02	a=6.09/ b=5.98	23.40
	$[(LaSe)_{1+\delta}]_1(V_{n(1+y)+1}Se_{2n+2})$	n=3 y=0.5	0.17/0.171*	P-3m1	a=3.57/ b=6.03	a=6.11/ b=6.02	29.30
[71]	$[(LaSe_{1-x})_{1+\delta}]_1(VSe_2)_1$		0.17				11.70
	$[(LaSe_{1-x})_{1+\delta}]_1(VSe_2)_2$		0.17				17.50
	$[(LaSe_{1-x})_{1+\delta}]_1(VSe_2)_3$		0.17				23.40
	$[(LaSe_{1-x})_{1+\delta}]_1(VSe_2)_4$		0.17				29.30
[84]	$[(PbSe)_{1+\delta}]_1(VSe_2)_1$	AD	0.11				12.28
		100 °C	0.11				12.38
		200 °C	0.11				12.38
		250 °C	0.11				12.36
		300 °C	0.11/0.121*		3.43	6.03	12.31
		350 °C	0.11				12.25
		400 °C	0.11				12.17
[27]	$[(PbSe)_{1+\delta}]_1(VSe_2)_1$		0.11/0.113*		3.43	6.05	12.25
	$[(PbSe)_{1+\delta}]_1(VSe_2)_2$		0.14/0.137*		3.46	6.04	18.35
	$[(PbSe)_{1+\delta}]_1(VSe_2)_3$		0.08/0.08*		3.39	6.07	24.45
[28]	$[(PbSe)_{1+\delta}]_1(VSe_2)_1$		0.12/0.118*		3.425	6.03	12.730
	$[(PbSe)_{1+\delta}]_2(VSe_2)_1$		0.1/0.1*		3.447	6.116	18.343
	$[(PbSe)_{1+\delta}]_3(VSe_2)_1$		0.08/0.077*		3.404	6.106	24.486
	$[(PbSe)_{1+\delta}]_4(VSe_2)_1$		0.07/0.071*		3.408	6.13	30.617
[74]	$[(Sn_{1-y}Bi_ySe)_{1+\delta}]_1(V_{1+x}Se_2)_1$	y=0	0.143/0.146*		3.414	5.935	12.030
		y=0.06	0.127/0.126*		3.434	6.022	12.008
		y=0.23	0.15/0.15*		3.456	5.999	11.946
		y=0.42	0.157/0.157*		3.466	5.997	11.889
		y=0.57	0.164/0.164*		3.475	5.996	11.856
[38]	$[(SnSe)_{1+\delta}]_1(V_{1+x}Se_2)_1$	x=0.23	0.15/0.145*		3.4082	5.9273	12.030
	$[(SnSe)_{1+\delta}]_1(V_{1+x}Se_2)_2$	x=0.14	0.15/0.15*		3.424	5.9419	18.014
	$[(SnSe)_{1+\delta}]_1(V_{1+x}Se_2)_3$	x=0.22	0.15/0.153*		3.4335	5.9514	24.000
	$[(SnSe)_{1+\delta}]_1(V_{1+x}Se_2)_4$	x=0.24	0.15/0.146*		3.4037	5.917	30.120
	$[(SnSe)_{1+\delta}]_1(V_{1+x}Se_2)_5$	x=0.38	0.15/0.146*		3.3985	5.908	36.180
	$[(SnSe)_{1+\delta}]_1(V_{1+x}Se_2)_6$	x=0.28	0.15/0.153*		3.4273	5.9412	42.280
[120]^g	$[(SnSe)_{1+\delta}]_1(V_{1-x}Ta_xSe_2)_1$	x=0	0.15/0.147*		3.415	5.935	12.020
		x=0.28	0.15/0.155*		3.455	5.984	12.108
		x=0.48	0.15/0.16*		3.482	6.018	12.152
		x=0.65	0.15/0.171*		3.501	6.022	12.199
		x=1	0.15/0.143*		3.456	6.015	12.321
[114] ^g	$[(SnSe)_{1+\delta}]_1(V_{1-x}Ta_xSe_2)_1$	x=0	0.15/0.14*		3.409	5.943	12.056
		x=0.04	0.15/0.14*		3.411	5.945	12.064
		x=0.06	0.15/0.143*		3.416	5.946	12.062
		x=0.07	0.15/0.144*		3.422	5.954	12.063
		x=0.09	0.15/0.148*		3.428	5.956	12.065
[32]	$[(SnSe)_{1+\delta}]_1(VSe_2)_1$		0.09/0.145*		3.415	5.94	12.02
[67]	$[(SnSe)_{1+\delta}]_1(VSe_2)_1$		0.15/0.146*		3.414	5.935	12.03
[85]	$[(SnSe)_{1+\delta}]_1(VSe_2)_1$		0.15				
[80]	$[(SnSe)_{1+\delta}]_1(VSe_2)_1$		0.15				
[70]	$[(SnSe)_{1+\delta}]_1(VSe_2)_1$		0.11/0.12^e	P-3m1			12.01
		supercell					26.90
[37]	$[(SnSe)_{1+\delta}]_1(VSe_2)_1$	Sn/V=0.89	0.14/0.142*	P-3m1	3.402	5.924	12.0446
		Sn/V=0.95		P-3m1			12.0449
		Sn/V=1.07		P-3m1			12.0036
		Sn/V=1.11		P-3m1			11.9730
		Sn/V=1.17	0.15/0.145*	P-3m1	3.408	5.927	11.9890

		Sn/V=1.23		P-3m1			11.9900
		Sn/V=1.32		P-3m1			11.9410
		Sn/V=1.37	a_1 0.12/0.123* a_2 0.14/0.144*	P-3m1	3.413	a_1=5.995/ a_2=5.94	11.9540
[87]	$[(SnSe)_{1+\delta}]_1(VSe_2)_1$	100 °C	0.15/0.183*		a_{VSe2}=3.46/ a_{SnSe2}=3.78	5.92	12.40
		200 °C	0.15/0.175*		a_{VSe2}=3.46/ a_{SnSe2}=3.78	5.94	12.33
		300 °C	0.15/0.131*		a_{VSe2}=3.4/ a_{SnSe2}=3.79	5.95	12.31
		400 °C	0.15/0.132*		3.39	5.93	12.01
[69]	$[(SnSe)_{1+\delta}]_1(VSe_2)_1$		$0.15/0.06^e$				12.03
	$[(SnSe)_{1+\delta}]_1(VSe_2)_2$		$0.15/0.08^e$	P-3m1			17.98
	$[(SnSe)_{1+\delta}]_1(VSe_2)_3$		$0.15/0.08^e$/0.158*	P-3m1	3.44	5.95	23.92
	$[(SnSe)_{1+\delta}]_1(VSe_2)_4$		$0.15/-0.04^e$	P-3m1			29.90
[68]	$[(SnSe)_{1+\delta}]_1(VSe_2)_1$		$0.15/0.164^e$/0.151*		3.414	5.923	12.034
	$[(SnSe)_{1+\delta}]_2(VSe_2)_1$		$0.15/0.164^e$/0.15*		3.4564	5.9976	17.828
	$[(SnSe)_{1+\delta}]_3(VSe_2)_1$		$0.15/0.164^e$/0.157*		3.463	5.9923	23.640
	$[(SnSe)_{1+\delta}]_4(VSe_2)_1$						29.300

disordered/random (i.e. (A,B)C) stacking variants are reported [120].In several cases, the in-plane lattice parameters are more volatile [28, 38, 39] or plateau at some point [74, 120] and are, hence, not easily interpretable. On the one hand, effects such as an altered charge transfer are assumed [120]. On the other hand, even though *fere*crystals basically comprise the very same two subsystems as misfit layer compounds, the composition of building blocks is much more flexible as the general formula $[(MSe)_{1+\delta}]_m(VSe_2)_n$ suggests. As a matter of fact, Falmbigl *et al.* reported that small alterations of the Sn/V ratio significantly influence the unit cell dimensions [37]. Additionally, various defect mechanisms that support off-compositions (i.e. extra layers on the surface [84], extra layers in the crystal [84], partial replacement of layers [28, 37, 84], substitutions of atom positions [120], substitutions by foreign $SnSe_2$ layers [85, 87], interstitial vanadium [38, 71], and vacancies [28, 39, 71]) are described in literature. In general, volume defects are more likely than intercalates [38, 114]. Interaction of several of these effects, complicates the determination of the relationship of stacking sequence or composition and in-plane axes.

3.9.3. Special structural features of the layers

In principle, the sublayers adopt two different crystal structures. The VX_2 triple layer is a slightly distorted CdI_2-type sandwich and the MX double layer is a distorted NaCl-type slice [122]. A direct comparison of the building blocks of vanadium-based misfit layer compounds and *fere*crystals is difficult; not only due to the above-described differences in structural features but also due to the lack of data. Detailed structural data on the individual sublayers is mainly available for sulphur-based misfit layer compounds, but only selenium-based *fere*crystals were synthesised. Only for $(La_xSe)_{1+\delta}(V_ySe_2)_n$ the respective misfit layer compounds [35, 122] and *fere*crystals [39] are comparable (refer to Table 5 and Table 6). All other substructures of vanadium-based misfit layer compounds can only be compared to the constituent bulk materials; the same is valid for the vanadium-based *fere*crystals.

The basal lattice parameters of vanadium-based *fere*crystals are insensitive to alterations of m and n and very closely related to the bulk materials [23]. The thicknesses of the layers can be easily estimated by a linear plot of the stacking sequence m or n versus the lattice parameter c. The layer thicknesses of one individual MSe layer and one VSe_2 layer are determined by the slope and the intercept when m is varied. When n is varied the layer thicknesses are determined *vice versa* (slope for VSe_2 and intercept for MSe). As shown in Table 7, the layer thicknesses vary significantly, even for the same “M” element despite R^2-values of the fit above 0.995. Explaining this phenomenon is complex as the following contradiction illustrates. On the one hand, interstitial vanadium is observed to decrease the c axis length [38, 69]. On the other hand, samples with high tin/vanadium-ratio were reported to have smaller c axes than samples with lower ratios [37] (refer to Table 6). We suspect that differences in defect concentrations and/or compositions may alter charge transfer and/or van der Waals gap between adjacent layers and, hence, the estimated layer thicknesses.

Interestingly, the same evaluation approach can be applied for estimating the layer thickness of misfit layer compounds, too. As shown for the values of $[(SnSe)_{1+\delta}]_m(VSe_2)_1$ in Table 7, the results are comparable, when the calculations are based on the lattice distances d instead of the lattice parameter c [109].

Concerning the intralayer distances, several effects are noteworthy: the puckering of layers, the periodic anti-phase boundaries, the modulation of V-V interatomic distances, and the asymmetric distortion of layers.

First, the transformation of the 3D crystal structure unit into a 2D lattice results in a change of the local environment (e.g. coordination number). The electrostatic interlayer interactions in combination with the lattice mismatch results in an anharmonic puckering of the MX layers that is approximately perpendicular to the in-plane surface [126] (refer to Figure 1). The displacement of the VX_2 layer's chalcogen atom, in contrast, is less affected by alterations of the local environment. All available (average) puckering values are collected in Table 8. The puckering is stronger for lanthanide-based compounds than for bismuth-, lead-, and tin-compounds. The effect of puckering can be modulated by altering the composition. Falmbigl *et al.* observed, that the exchange of tin for bismuth reduces the overall puckering to zero in their synthesised *fere*crystals. They attribute this effect to weaker interlayer interactions, which are a result of changes of the electronic structure. Those changes probably arise, just as for lithium-intercalated VSe_2, from enhanced Coulomb repulsions of the V 3d-band [74]. Presumably, due to the altered charge transfer to the VSe_2 sheets, different stacking sequences influence the puckering strength, too. The puckering of exterior layers is more pronounced than that of interior layers [68].

Second, for bismuth-based *fere*crystalline [74, 96] and misfit layer compounds [61, 122] periodic anti-phase boundaries are observed perpendicular to the *a* axis of the BiX layer. Although the intensity of reflections is not affected by the presence of these misorientations, satellite reflections are observed [61]. Unfortunately, no interatomic distances or site locations are reported. For a similar tantalum-based misfit layer compound with anti-phase boundaries, the Bi-Bi distances at the boundary are about the same as in metallic bismuth and the S-S distances indicate non-bonding interaction [122]. The HAADF-STEM images of the vanadium-based *fere*crystal show similar interatomic distances [96].

Third, the V-V interatomic distances appear to be modulated for several vanadium-based misfit layer compounds [26, 35, 36, 43, 49, 50, 66, 75-77]. The modulation amplitude is relatively large for both the sulphur-based (e.g. up to 0.7 Å [43]) and the selenium-based (e.g. up to 0.6 Å [35]) misfit layer compounds. Regardless of that amplitude, the reported distances are typical for metallic properties. For instance, in bulk $LiVSe_2$, which is metallic, the reported V-V distances are 3.52 Å [36]. Also, for bulk VS_2 intercalated by Na, the V-V distances indicate whether it is

Table 7: Thicknesses of layers estimated by a linear fit; indices given in the table denote the slope (s) and intercept (i) in our calculations.

Lit.	Compound	MSe [Å]	VSe_2 [Å]
[71]	$[(EuSe)_{1+\delta}]_1(VSe_2)_n$	6.120^s	5.110^i
[39]	$[(LaSe)_{1+\delta}]_1V_{n(1+y)+1}Se_{2n+2}$	5.900^s	5.700^i
[71]	$[(LaSe_{1-x})_{1+\delta}]_1(VSe_2)_n$	5.870^s	5.800^i
[28]	$[(PbSe)_{1+\delta}]_m(VSe_2)_1$	5.980^i	6.593^s
[27]	$[(PbSe)_{1+\delta}]_1(VSe_2)_n$	6.100^s	6.150^i
[109]	$[(SnSe)_{1+\delta}]_m(VSe_2)_1$	5.818^i	6.255^s
[68]	$[(SnSe)_{1+\delta}]_m(VSe_2)_1$	5.761^i	6.298^s
[38]	$[(SnSe)_{1+\delta}]_1(V_{1+x}Se_2)_n$	6.053^s	5.917^i
[69]	$[(SnSe)_{1+\delta}]_1(VSe_2)_n$	5.955^s	6.070^i

Table 8: Puckering of the MX layer; indices given in the table denote our calculations (*), our approximations from graphs in the literature (g), the puckering of MSe layers are (p1) for the most exterior layer and (pn) for the most interior layer (compare Figure 1).

Lit.	Compound	Comment	Puckering [Å]
[88]	$(La_{0.95}S)_{1+\delta}VS_2$	MLC	0.68*
[43]	$(La_{0.95}S)_{1+\delta}VS_2$	MLC	0.69*
[34]	$(LaS)_{1+\delta}VS_2$	MLC	0.69*
[35]	$(La_{0.95}Se)_{1+\delta}VSe_2$	MLC	0.73*
[39]	$[(LaSe)_{1+\delta}]_1V_{n(1+y)+1}Se_{2n+2}$	$n=2$	0.62
		$n=3$	0.76
[71]	$[(LaSe_{1-x})_{1+\delta}]_1(VSe_2)_1$		0.44
	$[(EuSe)_{1+\delta}]_1(VSe_2)_1$		0.63
[27]	$[(PbSe)_{1+\delta}]_1(VSe_2)_1$		0.367
[28]	$[(PbSe)_{1+\delta}]_3(VSe_2)_1$		$0.6^{p1}/0.5^{p2}/0.4^{p3}$
[109]	$(PbSe)_{1+\delta}V_{1+x}Se_2$	MLC	0.41
[109]	$(BiSe)_{1+\delta}V_{1+x}Se_2$	MLC	0.32
[96]	$[(BiSe)_{1+\delta}]_1(VSe_2)_1$		0.25
[74]	$[(Sn_{1-y}Bi_ySe)_{1+\delta}]_1(V_{1+x}Se_2)_1$	$y=0^g$	0.275^g
		$y=0.06^g$	0.282^g
		$y=0.23^g$	0.145^g
		$y=0.42^g$	0.036^g
		$y=0.57^g$	0^g
[69]	$[(SnSe)_{1+\delta}]_1(VSe_2)_1$		0.34
	$[(SnSe)_{1+\delta}]_1(VSe_2)_2$		0.13
	$[(SnSe)_{1+\delta}]_1(VSe_2)_3$		0.19
	$[(SnSe)_{1+\delta}]_1(VSe_2)_4$		0.16
[67]	$[(SnSe)_{1+\delta}]_1(VSe_2)_1$		0.19
[68]	$[(SnSe)_{1+\delta}]_1(VSe_2)_1$		0.21
	$[(SnSe)_{1+\delta}]_2(VSe_2)_1$		$0.44^{p1}/0.41^{p2}$
	$[(SnSe)_{1+\delta}]_3(VSe_2)_1$		$0.72^{p1}/0.65^{p2}/0.28^{p4}$
[109]	$[(SnSe)_{1+\delta}]_1(V_{1+x}Se_2)_1$	MLC	0.27
	$[(SnSe)_{1+\delta}]_2(V_{1+x}Se_2)_1$	MLC	$0.49^{p1}/0.48^{p2}$
	$[(SnSe)_{1+\delta}]_4(V_{1+x}Se_2)_1$	MLC	$0.61^{p1}/0.71^{p2}/0.70^{p3}/0.64^{p4}$

metallic (3.346 Å for 0.95 Na/unit) or semiconducting (3.566 Å for 1 Na/unit) [36, 66]. When V-V distances are short, the adjacent sulphur atoms are pushed way slightly (~0.2 Å) [43]. Due to the strong modulation amplitude in the *b* direction [35, 49] or at an angle of 120 ° from *a* [76], vanadium atoms form columns along the incommensurate *a* direction in a sinusoidal-like manner [35, 49]. The results of this linear clustering are quasi-1D chains that should behave like quasi-1D metals [76] or tetramer clusters. One noteworthy aspect is that the thermal treatment needs particular consideration at the evaluation of the crystal structure, as some of the V-V distances change dramatically between 300 and 200 K [49].

Last, Atkins *et al.* and Cordova *et al.* observed that, when the stacking sequence increases with *m*, the average distance *d* within the MSe layer is different for interior and exterior layers. The inner layers are, just as for the puckering, less contracted than the outer layers [28, 68]. In addition, the VSe_2 layer is influenced by different stacking sequences. When the stacking sequence *n* is increased, the vanadium position distorts slightly. As a result, the vanadium is asymmetrically sandwiched between the selenium sheets [38, 39, 69]. This effect is particularly pronounced for interstitial vanadium sites in the van der Waals gap [38, 39]. However, the trend of asymmetry is ambiguous, depending on whether the inner or outer layers and the interior or exterior side of the sandwiches are larger, [38, 39, 69].

The van der Waals gaps are located between MX layers, between VX_2 layers, and between MX and VX_2 layers. The interlayer distances in the bulk materials VS_2 and VSe_2 are approximately 2.88 and 2.97 Å [115]. All van der Waals gaps in vanadium-based *fere*crystalline and misfit layer compounds are approximately equal or smaller than the bulk references (refer to Table 9). The gap shrinks significantly for the trivalent cations bismuth and all lanthanides compared to the divalent tin and lead, due to the stronger charge transfer. Also, for heterostructures with increasing *m* values (e.g. MX layers are added), the van der Waals gaps are decreased, due to the increased transfer of electrons to the VSe_2 layer. Heterostructures with increasing *n* values (e.g. VX_2 layers are added) exhibit rather constant interlayer distances. The MX-MX and VX_2-VX_2 gaps are typically smaller than the MX-VX_2 distances.

Table 9: Interlayer distances d of the van der Waals gaps; indices given in the table denote our calculations (*), our approximations from graphs in the literature (g), the gap between the most interior layers of MSe/VSe_2 *(i), and the gap between the most exterior layers of MSe/*VSe_2 *(e).*

Lit.	Compound	Comment	MX-MX [Å]	MX-VX_2 [Å]	VX_2-VX_2 [Å]
[88]*	$(La_{0.95}S)_{1+\delta}VS_2$	MLC		2.421	
[43]*	$(La_{0.95}S)_{1+\delta}VS_2$	MLC		2.722	
[34]*	$(LaS)_{1+\delta}VS_2$	MLC		2.382	
[35]*	$(La_{0.95}Se)_{1+\delta}VSe_2$	MLC		2.820	
[39]*	$[(LaSe)_{1+\delta}]_1V_{n(1+y)+1}Se_{2n+2}$	n=2		2.661	2.780
		n=3		2.432	2.921^e/2.948^i
[71]	$[(LaSe_{1-x})_{1+\delta}]_1(VSe_2)_2$			2.72	2.69
	$[(EuSe)_{1+\delta}]_1(VSe_2)_1$			2.69	
[27]*	$[(PbSe)_{1+\delta}]_1(VSe_2)_1$			3.00	
[28]*	$[(PbSe)_{1+\delta}]_3(VSe_2)_1$		2.865	2.904	
[109]	$(PbSe)_{1+\delta}VSe_2$	MLC		3.220	
[109]	$(BiSe)_{1+\delta}VSe_2$	MLC		2.783	
[96]	$[(BiSe)_{1+\delta}]_1(VSe_2)_1$			2.86	
[74]g	$[(Sn_{1-y}Bi_ySe)_{1+\delta}]_1(V_{1+x}Se_2)_1$	y=0		2.92	
		y=0.06		2.90	
		y=0.23		2.93	
		y=0.42		2.97	
		y=0.57		2.97	
[38]*	$[(SnSe)_{1+\delta}]_1(V_{1+x}Se_2)_2$			2.927	2.915
	$[(SnSe)_{1+\delta}]_1(V_{1+x}Se_2)_3$			2.926	2.903
[67]	$[(SnSe)_{1+\delta}]_1(VSe_2)_1$			3.06	
[69]	$[(SnSe)_{1+\delta}]_1(VSe_2)_1$			2.92	
	$[(SnSe)_{1+\delta}]_1(VSe_2)_2$			3.01	2.88
	$[(SnSe)_{1+\delta}]_1(VSe_2)_3$			2.99	2.89
	$[(SnSe)_{1+\delta}]_1(VSe_2)_4$			3.01	2.89^e/2.9^i
[68]*	$[(SnSe)_{1+\delta}]_1(VSe_2)_1$			2.986	
	$[(SnSe)_{1+\delta}]_2(VSe_2)_1$		2.713	2.849	
	$[(SnSe)_{1+\delta}]_3(VSe_2)_1$		2.610	2.879	
[109]	$[(SnSe)_{1+\delta}]_1(VSe_2)_1$	MLC		2.976	
	$[(SnSe)_{1+\delta}]_2(VSe_2)_1$	MLC	2.771	2.948	
	$[(SnSe)_{1+\delta}]_4(VSe_2)_1$	MLC	2.866^e/2.902^i	3.132	

However, there are some exceptions. In case vanadium is intercalated into the van der Waals gap between two consecutive VSe_2 slabs different effects on the gap distance are reported [38, 39]. On the one hand, the neighbouring selenium atoms are observed to shift closer to the location of the interstitial vanadium and, hence, reduce the gap on average at low vanadium contents (e.g. occ. ~0.25 in [38]). On the other hand, high vanadium contents (e.g. occ. ~0.5 in [39]) are described to expand the lattice. The other exception is observable for mixed “M” positions [74].

When the composition is varied between tin-based [74] and bismuth-based [96] *fere*crystalline endmembers, the van der Waals gap dimensions are altered by the composition in an ambiguous fashion (refer to Table 9). The van der Waals gap contracts between $0 \leq y \leq 0.06$ [38, 74], expands between $0.06 \leq y \leq 0.42$, and plateaus between $0.42 \leq y \leq 0.57$ [74]. Evidently, the van der Waals gap will contract again between $0.57 \leq y \leq 1$ [74, 96]. This is counterintuitive, as the average valency should increase with increasing bismuth contents. Furthermore, the expansion of the van der Waals gap cannot be attributed to bismuth agglomerates or anti-phase boundaries. The authors suggest that changes in the electronic structure (e.g. enhanced Coulomb repulsion of the V 3d-band) weaken the interlayer interactions. However, they observed extensive streaking of *hkl* reflections, which indicates turbostratic disorder [74]. Therefore, another possible explanation might be that the mixed heterostructure interlocks more randomly in relation to the orientation of layers. The less favourable angles between (Bi,Sn)Se and VSe_2 layers, would, in turn, widen the van der Waals gap, increase the total energy of the system, and slightly destabilise the resulting crystalline structure.

The previously mentioned compound $(La_xSe)_{1+\delta}(V_ySe_2)_n$ is the only compound allowing for detailed comparison between *fere*crystalline and misfit layer compound. Interestingly, the $(La_xSe)_{1+\delta}(V_ySe_2)_n$ *fere*crystal is the only known *fere*crystalline compound with a rectangular distortion in both constituent's lattices [71]. This is also reported for the analogous misfit layer compounds [43, 88]. The distortion of 2 % is slightly smaller than that of the misfit layer compound (3 %) and decreases even further with increasing *n* to a value of 1.5 %. This difference, which is observed particularly for the LaSe sublattice and, hence, for the misfit parameter, can be attributed to the lack of lanthanum vacancies in the *fere*crystalline structure [39]. Comparing the substructures' interlayer distances, the values are rather similar. Between the LaSe-layer (d_{MLC}=3.80 Å and 3.86 Å$\geq c_{FC} \geq$3.79 Å), which exhibits puckering of lanthanum and selenium sites (d_{MLC}=0.73 Å and 0.62 Å$\leq c_{FC} \leq$0.81 Å), and the VSe_2-layer (d_{MLC}=2.98 Å and 2.85 Å$\leq c_{FC} \leq$3.38 Å) is a van der Waals gap (d_{MLC}=2.42 Å and 2.66 Å$\geq c_{FC} \geq$2.24 Å) [35, 39]. The van der Waals gap between adjacent VSe_2-layers is partially filled with interstitial vanadium atoms in the *fere*crystal. However, their site location is asymmetrically sandwiched within the gap. The gap closer to the LaSe-layer is larger than the one on the opposing side. This effect is reduced with increasing values for *n* [39].

3.10. Conclusion

In a bibliographic analysis of the available literature on vanadium-based layered compounds, we observed two waves of publications. The literature on misfit layer compounds starts in 1988 and that on *fere*crystals in 2015. The two topics increasingly drifted apart in the last years, despite the close structural relationship. We found that the keywords differ slightly depending on the area of study (e.g. physics, crystallography, phase diagrams, theoretical studies). We suspect that this is due to different styles of writing and publication cultures of the large number of different authors. A major drawback of such differences is that some authors cite similar sources but do not co-cite each other and some authors were not even cited once despite the relatedness of the topic. We propose that a common set of keywords could help making reception easier for future publications;

Synthesis approaches for misfit layer compounds start from pure elements, oxides, and/or binary compounds. They often involve a mineraliser and, depending on the “M” element, annealing temperatures above 800 °C for several days to weeks. For *fere*crystals, only high purity elements are utilised for the synthesis. Both compounds are frequently prepared with a surplus of chalcogen to compensate for eventual losses. After careful calibration, the *fere*crystalline compounds are synthesised by alternating depositions of elements and annealed for short durations (<60min) and at temperatures between 250 °C and 650 °C depending on the “M” element. During that annealing step the amorphous compound crystallises. The nucleation mechanism is a templated growth mechanism, where one slab nucleates first and serves as a template for the second slab. Which of the two slabs functions as the template for the other is still unknown and open for further investigations.

The composition of vanadium-based compounds often remains unclear, as only calculated misfit parameter are stated. Some authors report on slight off-stoichiometric compositions due to vacancies but mention no other defect mechanisms. The exact composition of compounds and slabs should be investigated in more detail. The compositions could also explain the slight deviations in lattice parameters, as it is reported for *fere*crystals. For *fere*crystals the off-stoichiometry due to defects (e.g. oxidic impurities, partial substitution of slabs, interstitials) and the resulting difference in lattice parameters was already investigated in more detail than for misfit layer compounds.

The phase equilibria are still mostly uninvestigated and open for further research in this field of study. It is also unknown, whether all misfit layer compounds are obtainable without a mineraliser and, hence, if they should be included in an equilibrium ternary phase diagram at all.

Regarding the general features of the misfit layer compounds in these systems, the lattice parameters were standardised for their *a* axis to be incommensurate, as suggested by Wiegers [122]. For vanadium-based misfit layer compounds only compositions where $m = n = 1$ can be observed. The Sn-Se-V-system ($m \leq 6$ and $n = 1$) is a remarkable exception to this general trend, which might be attributable to the different synthesis conditions with longer annealing durations. Such altered synthesis conditions may result in different stacking sequences for misfit layer compounds in the other vanadium-based systems as well. Intercalation of lithium into MLCs widens the van der Waals gaps in the lattice and allows a twelvefold symmetry to evolve before the compound amorphises. Upon deintercalation that amorphisation is reversed.

Furthermore, we recalculated all misfit parameters $1+\delta$ and lattice distances d. As different methods for calculation of the misfit parameter and the monoclinic distortion in the unit cells were used in literature, this was necessary to make them comparable to each other and *to fere*crystals.

The *fere*crystals' misfit parameters were recalculated, too, as on the one hand, not all authors stated a calculated parameter but rather a fixed value, and on the other hand, some authors published misfit parameters determined by the M/V-ration in EPMA. Noteworthy for further research in this field, is the fact that there appear to be more and less favourable angles between the slabs, which results in a twelvefold symmetry. Such ordering phenomena should be investigated further for other *fere*crystalline compounds and probably for the intercalated misfit layer compounds, too.

Where available, the thicknesses of layers estimated by linear trends, the actual layer thicknesses, and the puckering of layers are compared for *fere*crystalline and misfit layer compounds. Furthermore, several interlayer and intralayer effects are discussed. In general, it can be stated that there is very little overlap of literature allowing a direct comparison of *fere*crystals and misfit layer compounds, as all publications on the former are for selenium-based and most on the latter for sulphur-based systems. This issue should be tackled in further investigations in this field of study, in order to close the gap between those two deviating branches of research in the area.

3.11. Declarations of interest

The authors declare that there is no conflict of interest.

4. Publication 1: The ternary phase diagram of Sb-Se-V and its subsystems

4.1. Authorship Statement

Chapter 4 describes was published in *The Journal of Alloys and Compounds, Volume 810, Issue 151671* in 2019. It is available by the DOI: 10.1016/j.jallcom.2019.151671. The co-author is Klaus W. Richter, who is my advisor and I am the primary author of the manuscript.

Reisinger: Conceptualisation, Investigation, Writing - Original Draft, Visualisation

Richter: Conceptualisation, Writing - Review & Editing, Supervision, Project administration

4.2. Abstract

The ternary system Sb-Se-V was investigated by means of powder X-ray diffraction (PXRD), differential thermal analysis (DTA) and scanning electron microscopy (SEM) in combination with electron probe microanalysis (EPMA). A special focus was set on the possible existence of misfit layer compounds (MLCs). However, none of these, other materials of low dimensionality, or bulk ternary compounds were observed in the Sb-Se-V system. The results of the evaluations in the ternary system are presented by six isothermal sections at 400 °C, 550 °C, 650 °C, 750 °C, 900 °C and 1000 °C, one solidification scheme and one Scheil's diagram.

Furthermore, new results on the binary systems of Se-V, Sb-Se, and Sb-V are reported. Some alterations of the Se-V system are presented in a revised version. It comprises the elimination of the V_5Se_4 phase and a limitation of the thermal stability of the Se_9V_2 phase.

4.3. Keywords

Ternary alloy system, Phase diagrams, Phase transitions, Misfit layer compounds, Scanning electron microscopy, X-ray diffraction

4.4. Prime novelty statement

In this article, we present the up to now uninvestigated phase diagram Sb-Se-V. Additionally, we present new insights into the Se-V system (e.g. liquid composition and thermal stability of the Se_9V_2 phase) as well as the Sb-V system (e.g. therla stability of the $Sb_{7.46}V_9$ phase)

4.5. Highlights

- Six isothermal sections in the Sb-Se-V system
- Liquidus projection of the Sb-Se-V system
- Solidification scheme of the Sb-Se-V system
- Alterations to the Se-V phase diagram

4.6. Introduction

Low-dimensional materials have gained great interest in the literature since the properties of graphene were discovered. 2D materials, including transition metal dichalcogenides (TMDs), boron nitride, and hybrid perovskites, were not only investigated for their properties for next-generation electronics, but also for anode materials in lithium-ion batteries and for water splitting by hydrogen evolution reaction.

The binary systems of Se-V and Sb-Se gained great interest in the recent literature, as they are hosting inorganic compounds, which can be used as 2D (e.g. Se_2V, Se_9V_2, Sb_2Se_3) [24, 131, 132] and even 1D materials (e.g. Se_9V_2, Sb_2Se_3) [133-138]. Furthermore, the related ternary system might host another type of 2D material, so-called misfit layer compounds (MLCs). These MLCs comprise of a characteristic layered composite structure of two interpenetrating subsystems. The general formula of MLCs is $[(MX)_{1+\delta}]_m(TX_2)_n$ and, hence, based on two different subsystems. On the one hand, its TX_2 subsystem is based on the triple layer of TMDs; sandwiches of a chalcogen with a transition metal in between. On the other hand, the MX subsystem arranges a chalcogenide and Bi, Pb, Sb, Sn or a rare earth in a distorted sodium chloride type crystal structure. Additionally, the general formula reflects the fact, that these incommensurately modulated systems need to be described in (3+1)D superspace symmetry as the two subsystems do not have integer values for their lattice parameters (e.g. a misfit parameter δ is required) [126, 139].

Several MLCs are reported for vanadium- and sulfur-based systems [26, 33, 40, 41, 43, 45, 47, 76, 77, 88, 104, 110-112], whereas reports on those containing vanadium and selenium are limited to that of $(La_{0.95}Se)_{1.21}VSe_2$ [35]. The present publication tries to investigate, whether there are MLCs existing in the ternary system of Sb-Se-V. Therefore, in this paper, we investigate the isothermal sections and solidification scheme in a systematic manner. Furthermore, several open questions in the binary systems are discussed.

4.6.1. Literature review

The binary system of Sb-Se exhibits one binary phase (refer to Figure 5 for a redrawn version). Sb_2Se_3 congruently melts at temperatures between 590 °C [140]

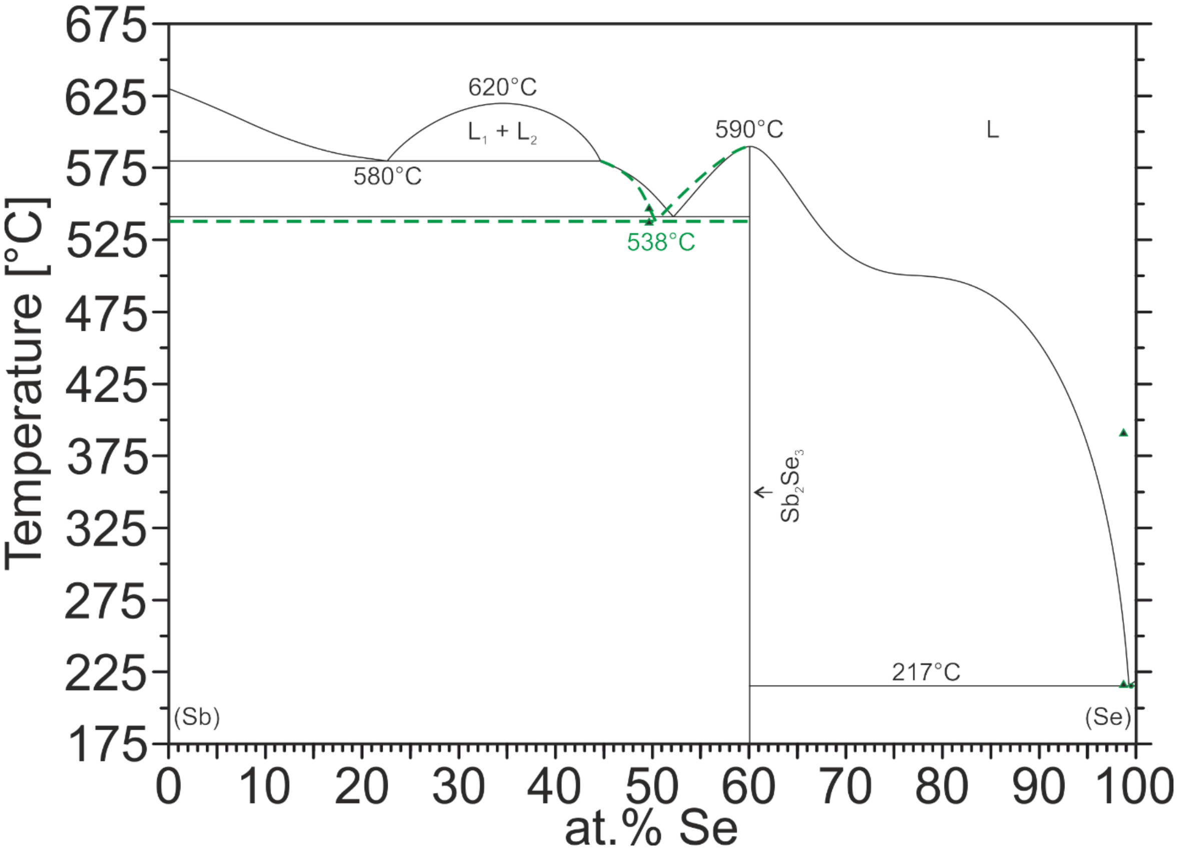

Figure 5: Calculated phase diagram of the Sb-Se system using the ionic solution model of Ghosh [55] redrawn in black; our proposed alterations are shown in green; EPMA measurements of equilibrium samples in the Sb-Se system are indicated by small green circles; the full lines are determined phase boundaries and transitions, whereas dashed lines reflect uncertain phase boundaries and transitions; the invariant reactions observed in DTA measurements are marked by triangles

and 625 °C [141]. The curvature of the liquidus in this region was investigated in detail by Glazov et al [142]. The antimony-rich part is characterised by a liquid miscibility gap. The linked monotectic reaction is flanked by two eutectic reactions. One of those eutectic reactions ($L \rightarrow (Sb) + Sb_2Se_3$) is located around 50 at.% Sb. The exact location is dependent on whether the phase diagram was calculated (e.g. 51 to 54 at. % Sb) or experimentally determined (e.g. 50 to 51 at. % Sb). The other eutectics ($L_1 \rightarrow L_2 + (Sb)$) composition is highly uncertain (e.g. 22 to 28 at. % Sb compared to 17 at. % Sb). The invariant temperatures for the two eutectic reactions are found in a range of 531 °C [142, 143] to 541 °C [140] or between 571 °C [143] and 580 °C [140], respectively. Hence, the liquidus, especially in this region, is discussed controversially.

In the selenium-rich part, there is a metastable liquid immiscibility and a eutectic reaction ($L \rightarrow (Se) + Sb_2Se_3$) at selenium-contents larger than 99 at.% Se and very close to the melting point of pure selenium. Since the comprehensive assessments of Ghosh [144, 145] no new experimental values on the phase equilibria or decomposition temperatures of the phase diagram of Sb-Se were published for the binary system. There is a phase diagram investigation on the related ternary system of I-Sb-Se, which could provide additional insights into the binary system of Sb-Se. However, Aliev et al. [146] appear to have used the experimental values of Wobst for the binary system [140]. Hence, the phase diagram of Ghosh [145] contains the most recent information to the Sb-Se system. The thermodynamic values of the binary system were recently reviewed in detail by Schlesinger [147].

The first phase diagram of the binary system of Sb-V was published recently by Failamani et al [148] (refer to Figure 6 for a redrawn version). It exhibits a congruent melting phase SbV_3. This phase exhibits the highest decomposition temperature and the largest solubility range of all binary phases present in this system. On the vanadium-rich side of the phase, there is a eutectic reaction, whereas, on the vanadium-poor side a peritectic cascade (refer to Figure 7 for detailed information on the reactions occurring in this system) involving the phases SbV_3, SbV_2, $Sb_9V_{7.46}$, and Sb_2V is located, which terminates in another eutectic reaction. The errors for the invariant temperatures given by Failamani et al [148] are between 5 °C and 25 °C. Whilst studying the Sb-V system the highly debated phase of Sb_4V_5 was found to be stabilised by impurities such as carbon in the octahedral 2*b* sites. Hence, Failamani et al [148] eliminated the $C_{1-x}Sb_4V_5$ phase from the equilibrium phase diagram of Sb-V. There are more recent publications on the ternary systems of Sb-V-Zn [149] and Co-Sb-V [150], which could provide additional insights into the binary system of Sb-V. Peng et al [149] did report on significant differences regarding the solubility ranges of the phases, whereas Ronaka et al [150] observed similar ranges as Failamani et al [148]. Hence, the experimental values of Failamani et al [148], which were confirmed by Ronaka et al [150], were utilised in the investigation of the Sb-Se-V phase diagram.

Due to experimental difficulties, the constitution of the binary Se-V phase diagram is not entirely determined (refer to Figure 8 for a redrawn version and Figure 7 for detailed information on the reactions occurring in this system). It shares distinct features with the closely related systems of sulfur or tellurium with vanadium. Hence, hence some data were extrapolated (e.g. the eutectic reaction in the selenium-rich

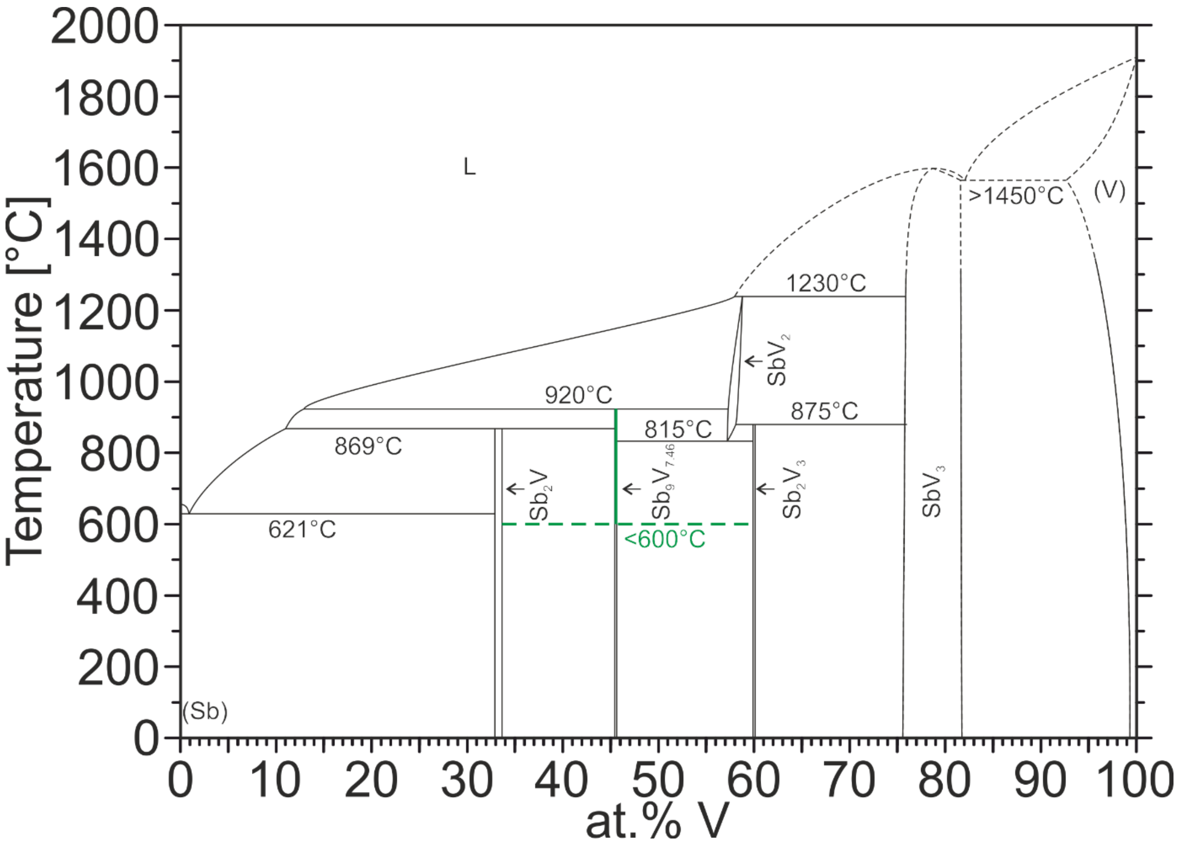

Figure 6: Sb-V system determined by Failamani et al [148] redrawn in black; our proposed alterations are shown in green

part) in the literature [151]. The three intermetallic phases present in that region between 33 and 51 at.% V, are related to the NiAs parental structure. The fact that the hexagonal and monoclinic phase form a pseudo-single phase at elevated

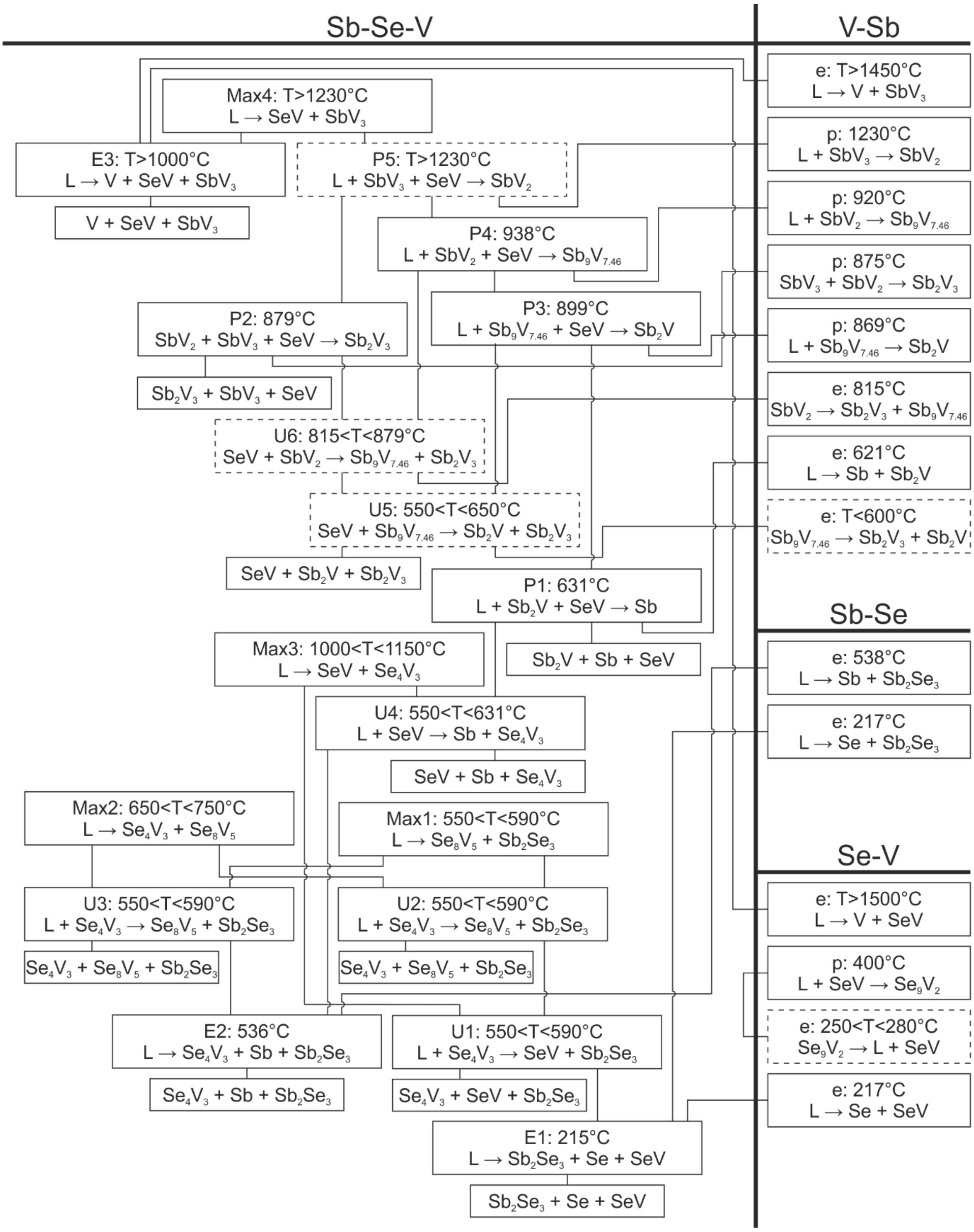

Figure 7: Scheil's diagram of the Sb-Se-V ternary system; reactions with uncertainty are indicated by dashed lines; due to the broad homogeneity range of Se_xV, where $1 \le x \le 2$, the phase was denoted as SeV for readability reasons

temperatures and the fact that superlattices are reported to complicate the determination of the distinct phase boundaries in this system.

Two additional phases are reported apart from those related to NiAs structure type [151]. Se_9V_2, on the one hand, is comprised of a chain-like monoclinic structure with weak bonds between those chains [152]. It is known for the S-V system but lacks an analogous phase in the Te-V system [139]. Se_4V_5, on the other hand, is isostructural to the previously mentioned Sb_4V_5 phase [153] and is also known from the analogous S-V and Te-V systems. Se_4V_5 was observed in the literature several times. Under varying sample preparation techniques, it was observed to be stable up to differing temperatures. It is discussed ambiguously regarding its thermal stability [154, 155]. In the samples prepared in alumina crucibles by Røst et al [154], the Se_4V_5 phase was less stable compared to those prepared in carbonised silica

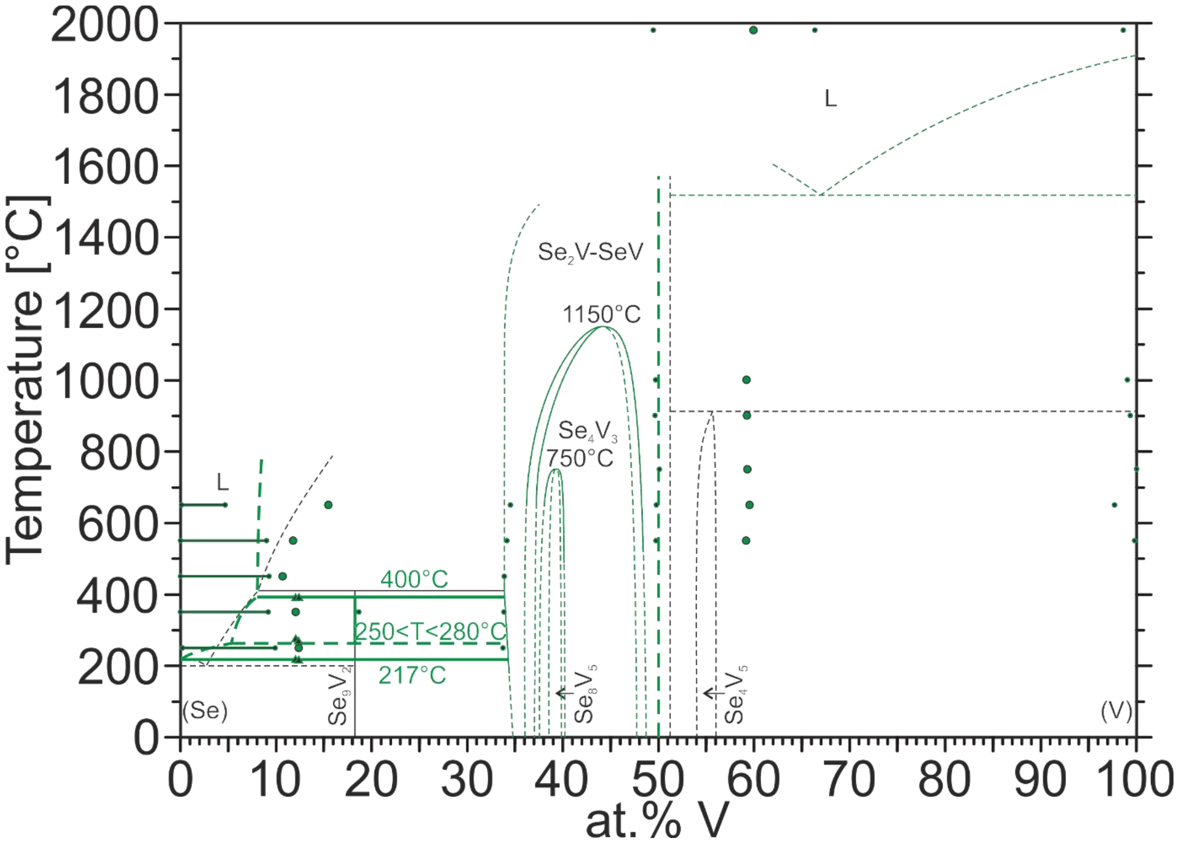

Figure 8: Comparison of the altered phase diagram of the Se-V system with the phase diagram assessed by Smith [151] redrawn in black, and our proposed phase diagram in green; EPMA measurements of equilibrium samples in the Se-V system are indicated by small green circles (point measurements) and bars (area scans with uncertainty); the measured sample compositions are given in large green circles; the full lines are determined phase boundaries and transitions, whereas dashed lines reflect uncertain phase boundaries and transitions; the invariant reactions observed in DTA measurements are marked by triangles

tubes by Carpay [155]. Additionally, its extended homogeneity range is doubted due to the small changes in lattice parameters throughout the phase field [156]. However, Se_9V_2 and Se_4V_5 both were proven to be at least kinetically stable by a modulated elemental reactants synthesis approach [157]. Unfortunately, Overbay et al [157] do not report on the purity of their used source material. Hence, their results on the respective phases are even less comparable.

No literature is available on the ternary system of Sb-Se-V. However, by the cubic phase of $VSb(SeO_3)_4$ at least one systematically related oxide is known [158]. Hence, preventing oxide formation is crucial in the design of synthesis routes in the ternary Sb-Se-V system.

4.7. Experimental procedures

The pure elements in the present ternary system exhibit strongly differing physical (e.g. melting points and vapour pressures) and chemical properties (e.g. oxide formation). This limits the available experimental procedures requires iterative sample preparation schemes in order to reach equilibrated samples.

All binary and ternary samples are originating from powders of vanadium (smart elements – purity 99.9 %), antinomy chunks (Cominco Electronic Materials – purity 99.999 %) and selenium shots (American Smelting and Refining Company – purity 99.999 %). In order to speed up reaction rates, reduce evaporation losses, reduce weighing errors and eventually permit melting in an argon arc, master alloys of Se_2V, SeV, SbV_2, and Sb_2Se_3 were prepared from the powders of the pure elements in large quantities. These were weighed out in an argon-filled glovebox, sealed in silica ampoules under vacuum and subjected to heat. The resulting master alloys were checked for their exact stoichiometric composition and potential impurity phases by EPMA and PXRD investigation methods. Only well homogenised and oxygen-free master alloys were further processed in sample preparation.

All binary and ternary samples were weighed out from powders of the pure elements as well as readily prepared master alloys in an argon-filled glovebox to a total mass of 0.3 g at an accuracy of ±0.5 mg per weighed out compound. The well-mixed powder blends were then cold pressed in a steel die without lubricant in order to obtain dense samples. Additionally, samples located in the vanadium-rich corner were molten under low current with a non-consumable tungsten electrode in an argon atmosphere. The samples subjected to heat treatment were sealed in silica ampoules under vacuum beforehand. Inevitably occurring heat gradients in muffle furnaces were circumvented by placing the sample ampoules in custom-build closed containers. In order to reach the equilibrium conditions in the samples more quickly, especially at low temperatures, not only master alloys were utilised, but most of the samples were subjected to temperature programs too. When choosing the duration and temperature of each step of pre-heat treatment the parameters of the vapour pressures of the pure elements, the reaction of vanadium with the silica ampoules and the presumable proportion of liquid phase present, were considered in order to balance the loss due to evaporation, the impurities of oxygen and silicon at elevated temperatures and the reaction speed. After each step in heat treatment, the samples were quenched in cold water (refer to the supplementary materials section for the specific procedures of each sample).

Similar to the established literature, the transportation agents I_2 or NH_4Cl were added to several samples for a potential MLC-preparation [121, 122]. Additionally, a LiCl/KCl-eutectic salt melt was added to several samples for the same purpose, in order to act as a crystallisation aid. This method was introduced by Clarke and Freedman [159].

All samples prepared were carefully checked under a stereo microscope for crystals, which appear morphologically similar to MLCs. For further sample characterisation powder X-ray diffraction (PXRD) and scanning electron microscopy (SEM) were employed. In order to determine the chemical composition, electron probe microanalysis was performed on a Zeiss Supra 55 VP scanning electron microscope, which was operated at an acceleration voltage of 20 kV and employing energy dispersive X-ray analysis (EDX). Pure cobalt was used for an energy calibration of the EDX signal. The samples were embedded in a carbonised phenolic hot mounting resin for SEM preparation. As the powdered and sintered powders, especially those with low antimony contents, tended to be brittle all samples were soaked in with several layers of epoxy resin for further stabilisation during grinding (SiC abrasive paper grits 500 to 4000). PXRD was done by a Bruker D8

Table 10: The observed phases of selected samples, which represent the reported three-phase equilibria by means of EPMA and PXRD data; The samples description includes the annealing temperatures and the measured composition in at.% V, Se, and Sb; The abbreviations of the phases represents the amount observed of this phase (M – major, T – traces, I - impurity stabilisation) or in cases, in which the liquid was not clearly determinable the variation range of the measurements (Lmax and Lmin)

Sample	Phase (EPMA)	V (at%)	Se (at%)	Sb (at%)	Phase (PXRD)	*a*	*b*	*c*	*α*	*β*	*γ*
so62	Sb2Se3 (M)	0.4(4)	58.1(8)	42(1)	Sb2Se3 (M)	11.784	3.977	11.637	90	90	90
400°C	Se8V5 (M)	37(5)	61.1(1)	1.9(5)	Se8V5 (M)	11.831	6.999	8.312	90	134.15	90
30(1)/57.6(5)/13(1)	Se4V3 (T)	38.6(5)	61.1(9)	0.4(5)	Se4V3 (T)	13.352	3.398	6.126	90	116.11	90
so68	Se4V3 (M)	40.9(5)	58.1(6)	1.1(5)	Se4V3 (M)	13.208	3.438	6.152	90	116.26	90
400°C	Sb2Se3 (M)	0.3(6)	58(1)	42.1(5)	Sb2Se3 (M)	11.785	3.979	11.635	90	90	90
18(5)/50.9(2)/31.1(6)	Sb (M)	0(0)	0.3(1)	99.7(1)	Sb (M)	4.307	4.307	11.278	90	90	90
so71	Se4V3 (M)	40.8(2)	58.1(2)	1.1(4)	Se4V3 (M)	13.209	3.437	6.155	90	116.25	90
550°C	Sb (M)	0(0)	0.8(2)	99.2(2)	Sb (M)	4.307	4.307	11.272	90	90	90
17.5(8)/48(1)/35(2)	L	0(0)	49.6(7)	50.4(7)	N/A	N/A	N/A	N/A	N/A	N/A	N/A
so75	L	1.4(3)	0(0)	98.6(3)	Sb (M)	4.309	4.309	11.272	90	90	90
550°C 45.1(4)/49.1(6)/5.9(7)	Se4V3 (M)	44.6(8)	55.1(6)	0.4(5)	Se4V3 (M)	13.285	3.483	6.212	90	116.32	90
so80	Se4V3 (M)	40.5(5)	59.5(5)	0(0)	Se4V3 (M)	13.202	3.437	6.134	90	116.30	90
550°C	Sb2Se3 (M)	0.2(4)	58.1(3)	41.7(4)	Sb2Se3 (M)	11.784	3.978	11.637	90	90	90
31(2)/55.9(8)/13(2)	L	0(0)	50.1(9)	49.9(9)	N/A	N/A	N/A	N/A	N/A	N/A	N/A
so110	SeV (M)	48.3(7)	50.3(5)	1.5(2)	SeV hP4 (M)	3.659	3.659	5.995	90	90	120
1000°C	SbV2 ht (M)	57.9(5)	0.4(9)	42(1)	SbV2 ht (M)	4.285	4.285	5.451	90	90	120
59.2(4)/17.4(1)/23.4(3)	SbV3 (M)	75.2(3)	0(0)	24.8(3)	SbV3 (M)	4.944	4.944	4.944	90	90	90
so123	SeV (M)	47.1(9)	51.6(8)	1.3(3)	SeV hP4 (M)	3.636	3.636	5.999	90	90	120
750°C	Sb2V0.96 (M)	32.4(6)	0(0)	67.6(6)	Sb2V0.96 (M)	6.555	6.555	5.636	90	90	90
38.6(4)/22(1)/39(1)	Sb9V7.46 (M)	45.3(2)	0(0)	54.7(2)	Sb9V7.46 (M)	9.587	9.587	7.046	90	90	90
so126	Sb2V0.96 (M)	33.2(3)	0(0)	66.8(3)	Sb2V0.96 (M)	6.558	6.558	5.632	90	90	90
550°C	Sb2V3 lt (M)	55.5(1)	0(0)	44.5(1)	Sb2V3 lt (M)	5.542	5.542	20.335	90	90	90
50.3(2)/17.3(5)/32.4(7)	SeV (M)	48(1)	51(1)	1.1(3)	SeV hP4 (M)	3.616	3.616	6.007	90	90	120
so129	SeV (M)	47.7(7)	51.3(6)	1.06(8)	SeV hP4 (M)	3.645	3.645	5.998	90	90	120
900°C	Sb9V7.46 (M)	45.6(1)	0(0)	54.4(1)	Sb9V7.46 (M)	9.582	9.582	7.053	90	90	90
50.2(2)/17.7(3)/32.1(3)	SbV2 ht (M)	56.5(1)	0(0)	43.5(1)	SbV2 ht (M)	4.271	4.271	5.453	90	90	120
so142	Se2V (M)	33.8(4)	66.2(4)	0(0)	Se2V (M)	3.357	3.357	6.104	90	90	90
400°C	Sb2Se3 (M)	0(0)	58.4(1)	41.6(1)	Sb2Se3 (T)	11.782	3.979	11.624	90	90	90

12.1(8)/69.1(2)/18.8(7)	Se (L)	0.1(2)	92.9(5)	7(4)	Se9V2 (T)	10.659	12.391	8.143	90	94.87	90
so143	Se2V (M)	33.9(3)	66.1(3)	0(0)	Se2V (M)	3.356	3.356	6.107	90	90	90
550°C	Sb2Se3 (M)	0(0)	58.6(6)	41.4(6)	Sb2Se3 (M)	11.785	3.978	11.636	90	90	90
18(2)/68.8(8)/13(1)	Se (L)	0(0)	98(8)	2(8)	N/A	N/A	N/A	N/A	N/A	N/A	N/A
so161	SbV3 (M)	80.2(5)	0.3(2)	19.5(3)	SbV3 (M)	4.923	4.923	4.923	90	90	90
1000°C	SeV (M)	49.6(2)	50.4(2)	0(0)	SeV hP4 (M)	3.707	3.707	5.994	90	90	120
58.3(4)/36.3(8)/5.4(4)	V (T)	98.6(7)	0.3(3)	1.1(4)	V (T)	2.990	2.990	2.990	90	90	90
s18	Se2V (M)	34.5(4)	65.5(4)	0(0)	Se2V (M)	3.356	3.356	6.107	90	90	90
650°C	Lmax	5.2(6)	94.8(6)	0(0)	N/A	N/A	N/A	N/A	N/A	N/A	N/A
15.5(5)/84.5(5)/0(0)	Lmin	0(0)	100(0)	0(0)	Se (M)	4.417	4.417	5.016	90	90	90
s20	Se2V (M)	33.8(2)	66.2(2)	0(0)	Se2V (M)	3.356	3.356	6.108	90	90	90
350°C	Se9V2 (M)	18.7(7)	81.3(7)	0(0)	Se9V2 (M)	10.728	12.228	7.975	90	94.65	90
12.1(4)/87.9(4)/0(0)	Lmax	8.8(8)	91.2(8)	0(0)	N/A	N/A	N/A	N/A	N/A	N/A	N/A
	Lmin	0(0)	100(0)	0(0)	Se (M)	4.412	4.412	5.011	90	90	90
s21	Se2V (M)	33.8(2)	66.2(2)	0(0)	Se2V (M)	3.356	3.356	6.108	90	90	90
250°C	Lmax	9.9(5)	90.1(5)	0(0)	N/A	N/A	N/A	N/A	N/A	N/A	N/A
12.4(4)/87.6(4)/0(0)	Lmin	0.2(3)	99.8(3)	0(0)	Se (M)	4.414	4.414	5.007	90	90	90
s25	V (M)	99.8(3)	0.2(3)	0(0)	V (M)	2.987	2.987	2.987	90	90	90
550°C 59.2(4)/40.8(4)/0(0)	SeV (M)	49.7(2)	50.3(2)	0(0)	SeV hP4 (M)	3.703	3.703	5.991	90	90	120
s28	V (M)	99.4(9)	0.6(9)	0(0)	V (M)	2.987	2.987	2.987	90	90	90
900°C	SeV (M)	49.7(3)	50.3(3)	0(0)	SeV hP4 (M)	3.706	3.706	5.993	90	90	120
59.3(1)/40.7(1)/0(0)	N/A	N/A	N/A	N/A	Se4V5 (I)	9.279	9.279	3.419	90	90	90
s30	V (M)	99.998(5)	0.003(5)	0(0)	V (M)	2.982	2.982	2.982	90	90	90
550°C 66.3(2)/33.7(2)/0(0)	SeV (M)	50.4(6)	49.6(6)	0(0)	SeV C2 (I)	6.503	3.708	6.011	90	90.000	90
s33	V (M)	100(0)	0(0)	0(0)	V (T)	2.966	2.966	2.966	90	90	90
900°C 67.4(2)/32.6(2)/0(0)	Se4V5 (I)	56.5(4)	43.5(4)	0(0)	Se4V5 (I)	9.292	9.292	3.420	90	90	90
o4	Sb2Se3 (M)	0(0)	59.2(1)	40.8(1)	Sb2Se3 (M)	11.788	3.978	11.637	90	90	90
250°C 0(0)/98.7(2)/1.3(2)	Se (L)	0(0)	99.26(6)	0.74(6)	Se (M)	4.415	4.415	5.034	90	90	90

diffractometer in Bragg-Brentano pseudo-focussing geometry (Cu-K_α radiation, variable slit, 10°<2θ<120° in steps of 0.01°, silicon strip detector). The analysis of the obtained powder patterns was done by Rietveld refinement technique with the software program Topas4 [160] or Jana2006 [161] (refer to Table 10 for several selected samples; detailed results are given in the supplementary materials section).

Several samples of various admixtures were selected for further differential thermal analysis (DTA). The respective sample parts of a total mass between 75 and 150 mg, were sealed in silica ampoules under vacuum and measured on a DTA 404 PC Netzsch. After careful calibration with Tin, Antimony, and Copper, the samples were measured two times at a heating rate of 5 K/min. Samples in the selenium-rich corner were re-equilibrated in a furnace after one heating cycle due to segregation of Selenium from the rest of the sample (results are given in the supplementary materials section). The invariant and non-invariant reactions, where no phase vanishes, were evaluated by the method of the extrapolated onset [162]. The peak temperature of the last thermal event on heating was selected for the liquidus temperature, which may result in slightly overestimated liquidus temperatures, but yields more reliable values than those of the first onset on cooling in the present study. This method was chosen due to the altered composition by the evaporation of selenium.

4.8. Results and discussion

To construct the isothermal sections at 400 °C, 550 °C, 650 °C, 750 °C, 900 °C, and 1000 °C, as well as a preliminary solidification scheme, all results of PXRD and SEM were combined. Additional DTA experiments were employed, in order to confirm certain assumptions made during the construction of the reaction scheme presented as Scheil-diagram (refer to Table 11). Detailed results of PXRD and EPMA are given in in the supplementary data section.

The binary phase diagrams of Sb-Se [145], Se-V [151] and Sb-V [148], served as a starting point for investigations. However, inconsistencies in the literature, uninvestigated regions, and questionable liquidus behaviour complicated the construction of the ternary phase diagram. The construction of the isothermal sections and solidification scheme was executed in an iterative manner. In cases were the literature of the binary systems exhibited significant scattering of their data points, were the assessment was fruitless in locating errors in the presented literature data and were our data was within the scattering range of the literature values, out data points were favoured over the literature values (e.g. eutectic compositions in the selenium-rich part and the solubility range of the phase of SbV_3),

Table 11: Results of the DTA-experiments grouped by composition regions of the ternary phase diagram; The samples description includes the measured composition in at.% V, Se, and Sb; In cases samples were re-annealed for additional measurments, the sample names were adjusted (e.g. O4_1, O4_2, and O4_3)and the cooling curves neglected; asterisks (*) indicate effects, which are probably caused by the evaporation of selenium; The liquidus was not reached (indicated as "n. r.") in most of the experiments

Sample	T_{Max} [°C]	Run	invariant [°C]			non-invariant [°C]			L [°C]
o4_1 0(0)/98.7(2)/1.3(2)	600	1 up	216.0	-	-	380.8*	-	-	394.1
o4_2 0(0)/98.7(2)/1.3(2)	600	1 up	216.6	-	-	382.6*	-	-	391.3
o4_3 0(0)/98.7(2)/1.3(2)	450	1 up	217.1	-	-	370.9*	-	-	385.8
s20_1 12.1(4)/87.9(4)/0(0)	550	1 up	216.3	268.3	394.0	428.6*	-	-	n. r.
s20_2 12.1(4)/87.9(4)/0(0)	620	1 up	216.6	-	388.2	424.4*	-	-	n. r.
s21_1 12.4(4)/87.6(4)/0(0)	620	1 up	217.4	265.4	399.6	446.1*	-	-	n. r.
s21_2 12.4(4)/87.6(4)/0(0)	620	1 up	217.7	259.2	400.2	440.6*	-	-	n. r.
s21_3 12.4(4)/87.6(4)/0(0)	620	1 up	217.5	290.0	403.9	442.9*	-	-	n. r.
so142	250	1 up	215.5	-	-	-	-	-	n. r.
12.1(8)/69.1(2)/18.8(7)	620	2 up	215.5	-	-	354.3	514.0*	-	n. r.
	250	1 down	-	-	-	-	-	-	n. r.
	620	2 down	-	-	-	-	492.9*	-	n. r.
o5	600	1 up	537.6	-	-	-	-	-	546.9
0/~50/~50	600	2 up	537.5	-	-	-	-	-	549.7
	600	1 down	530.2	-	-	-	-	-	-
	600	2 down	517.5	-	-	-	-	-	-
so70	700	1 up	536.4	572.7	-	612.4	-	-	n. r.
14(2)/41(3)/46(4)	700	2 up	-	573.4	-	618.7	-	-	n. r.
	700	1 down	-	-	-	-	-	-	n. r.
	700	2 down	-	-	-	-	-	-	n. r.
so89	1000	1 up	633.9	899.2	-	698.9	896.9	-	n. r.
25(2)/21(3)/54(4)	1000	2 up	630.9	898.3	938.1	699.4	882.7	-	n. r.
	1000	1 down	618.6	-	869.3	-	-	966.9	n. r.
	1000	2 down	619.3	-	866.4	-	-	966.9	n. r.
so116	1000	1 up	-	-	944.2	473.0	883.7	-	n. r.
48.5(2)/17.9(2)/33.58(9)	1000	2 up	-	-	944.2	475.3	780.3	-	n. r.
	1000	1 down	-	-	881.7	-	-	-	n. r.
	1000	2 down	-	-	879.8	-	-	-	n. r.
so124	1000	1 up	633.8	878.6	942.8	399.8	694.5	-	n. r.
38.5(3)/20(2)/41(2)	1000	2 up	-	881.5	941.8	-	696.9	-	n. r.
	1000	1 down	-	-	873.7	-	-	-	n. r.
	1000	2 down	-	-	866.2	-	-	-	n. r.

whereas in case of contradictions between samples an overall picture of several isothermal sections was gathered for higher reliability in the process of decision-making. In order to reduce uncertainties, several samples in the binary sections were produced.

4.8.1. Binary Se-V

Two regions in the Se-V phase diagram were of higher interest due to several open questions, as they limit the validity of the evaluations in the Sb-Se-V system. On the one hand, the selenium-rich part above 80 at.% Se is of interest for its eutectic composition and temperature, its liquidus behaviour and the temperature of the peritectic decomposition of V_2Se_9, as some of those values are just estimations of Smith [151], which are based on knowledge of the analogous regions in the S-V and Te-V systems. On the other hand, the region of Se_4V_5 is of interest for the questions whether this phase is impurity stabilised, similar to $C_{1-x}Sb_4V_5$, and for its peritectoid decomposition temperature. The revised binary phase diagram according to our new results is given in Figure 8.

The eutectic reaction in the selenium-rich part was found to be at a temperature of ~217.5 °C, which equals a shallower eutectic of approximately similar extent as in the Te-V system [151], comparing the temperature difference between the eutectic temperature in the two systems (217.5 °C and 444 °C) and the melting point of the pure elements selenium and tellurium (221 °C and 449.57 °C). Our EPMA data exhibits no significant vanadium content in the selenium matrix. Hence, we propose a eutectic composition of less the 0.1 at.% V, which is similar to the Te-V system.

Our investigations of the Se_9V_2 phase showed a peritectic decomposition between 394 °C and 404 °C ($L + Se_2V \rightarrow Se_9V_2$, refer to samples S20 and S21 in Table 11), which is similar to thermogravimetric measurements of Oh et al [137], who reported a decomposition at approximately 400 °C. Due to the broadness of the complex peak, which is caused by the evaporation and re-condensation of selenium, the results are varying. Interestingly, Oh et al [137] did not observe a phase formation at 380 °C, which could indicate an even lower decomposition temperature. Additionally, we did observe the phase Se_9V_2 at 350 °C, especially by PXRD analysis, but did not observe the respective phase in samples annealed at or slowly cooled to 250 °C (refer to Figure 9a). This indicates that this phase is involved in another reaction apart from the peritectic formation of this phase at ~400 °C. That reaction is a decomposition upon cooling into the same phases ($Se_9V_2 \rightarrow L + Se_2V$) by a “catatectic” reaction [163] (refer to Figure 8). The respective reaction was probably observed as a tiny peak in a larger temperature range of 259 °C to 268 °C. This is consistent with the literature, as Furuseth et al [152] and Oh et al [137] prepared the Se_9V_2 phase between 280 °C to 400 °C and 320 °C to 340 °C respectively.

We also attempted to measure the composition of the liquid at different temperatures by area scans (e.g. Figure 9a). However, all attempts appear to have failed, as higher temperatures exhibited lower vanadium contents in the liquid and the results were in scattered in a broad range. Nevertheless, the largest vanadium content was no more than 10 at.% V. The respective maximum vanadium contents measured in the liquid are indicated by horizontal bars in Figure 8. DTA measurements were performed till 620 °C in small crucibles in order to reduce the temperature gradient, which causes sample segregation. The segregation phenomenon could not be avoided entirely. However, re-annealing of the same sample resulted in similar values for the reaction temperatures. No complete liquefaction of the samples was observed in the DTA or during annealing experiments (refer to samples S20 and S21 in Table 11). This fact further supports this hypothesis. We conclude that the liquidus has a steeper slope than estimated by Smith [151].

In our first experiment on the stability of the Se_4V_5 phase, which utilised a large sinter sample (refer to S17) only small amounts of the Se_4V_5 phase were observed. After mechanical homogenisation under air and melting in the arc of the very same sample no Se_4V_5 phase was observed even after annealing at different temperatures (refer to samples S25 to S29). Addition of fresh vanadium and treatment in a similar manner yielded exclusively V and the Se_4V_5 phase at annealing temperatures up to 1000 °C (refer to samples S32 to S34 and Figure 9b). This is counterintuitive, as the samples without additional vanadium should have

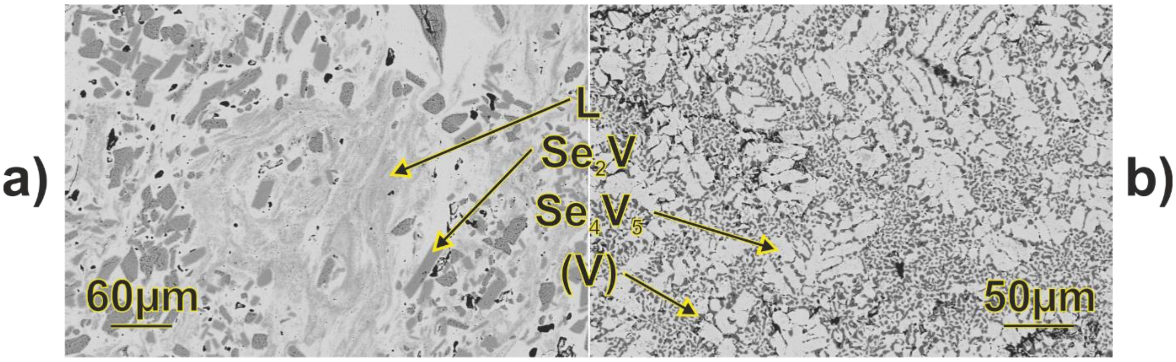

Figure 9: Representative tempered samples in the Se-V system; a and b are typical sections of the samples S21 (250 °C) and S34 (1000 °C), respectively; a) light grey areas of S21 represent the areas measured for the maximum vanadium amount in the liquid, as pure selenium was found in its surrounding; no Se_9V_2 was observed at 250 °C; b) peritectoidic formation of Se_4V_5 resulting in small crystal sizes and twinning

had contained the phases Se_4V_5 and V, too. A reasonable explanation for this issue would be, that impurities in the vanadium powder stabilise the Se_4V_5 phase and that those impurities could be eliminated in the arc melting of the sample without additional vanadium in contrast to that with additional vanadium. If the impurity is carbon, as it is the case for the structurally related $C_{1-x}Sb_4V_5$ phase reported by Failamani et al [148], some residual oxygen in the arc melting process could have gettered all impurity carbon, hence preventing a formation of Se_4V_5, whereas an addition of impure vanadium exceeds the gettering capacity in arc melting process, allowing a formation of the Se_4V_5 phase. This hypothesis is furthermore supported by the fact, that ~3 wt.% C were found in EPMA results of this phase when the all the samples containing the Se_4V_5 phase were re-evaluated under the consideration of carbon. This is significantly more than for other phases in those samples, which exhibited ~1.5 wt.% C (presumably caused by surface impurities). Hence, we propose, that the octahedral sites of the Se_4V_5 phase are filled by impurities (e.g. $C_{1-x}Se_4V_5$) and are by this structurally similar to $C_{1-x}Sb_4V_5$. The prove of this hypothesis is still under investigation and subject to future publications, as no suitable single crystals were found up to now. Furthermore, attempts to arc melt samples containing pure carbon failed due to the significant elevation of the liquidus (refer to S35 and S36). In the respective samples vanadium and carbon depleted from the sample during arc melting by severe vapourisation, yielding samples shifted to the SeV phase composition.

Additionally, some samples (refer to samples S30 and S31 as well as So158) exhibited splitting of all SeV peaks in the measured PXRD pattern (refer to Figure 10 for the pattern of sample So158). This is similar to observations of Carpay [155] and Brunie et al [164]. Attempts to index the respective reflections and solve the structure by charge flipping technique in Jana2006 [161] yielded an at least pseudo-orthorhombic structure (a=6.50, b=3.71, c=6.0, α=90, β=90, γ=90). For this structure, the c-axis is similar to the former c-axis in the NiAs-type structure, whereas the a-axis reflects the former [110] and the b-axis the former [-110] vectors. The observed splitting of reflections is due to slight dislocations in [110] of vanadium positions in the initial c axis of the NiAs type structure as well as strong shifts in [-110] of the selenium positions. Whether this superstructure is present in the Se-V phase diagram or if it is stabilised by impurities could not be determined by PXRD. However, the fact that this phase occurs in the same series of samples as the Se_4V_5 phase as well as that both authors in previous literature utilised carbonised silica ampoules, indicates that the present splitting of reflections in caused by carbon impurities, but present only in samples annealed at low temperature. No suitable single crystals were found due to small crystal sizes and aggregation phenomena. Hence, the solution of this crystal structure is a matter for future publications.

4.8.2. Binary Sb-Se

The eutectic composition on the selenium-rich side of the Sb-Se system determined by our measurements was ~0.6 at% Sb at a temperature of ~217 °C (refer to samples O3 and O4, respectively). Compared to the experimental literature, there is a higher antimony content in the selenium at the eutectic composition we measured, but for the calculated phase diagram, it is in between the values for the ionic and the associated solution model of Ghosh (99.02 at.% Se and 99.93 at.% Se respectively). The temperature is lower than for the experimental values of

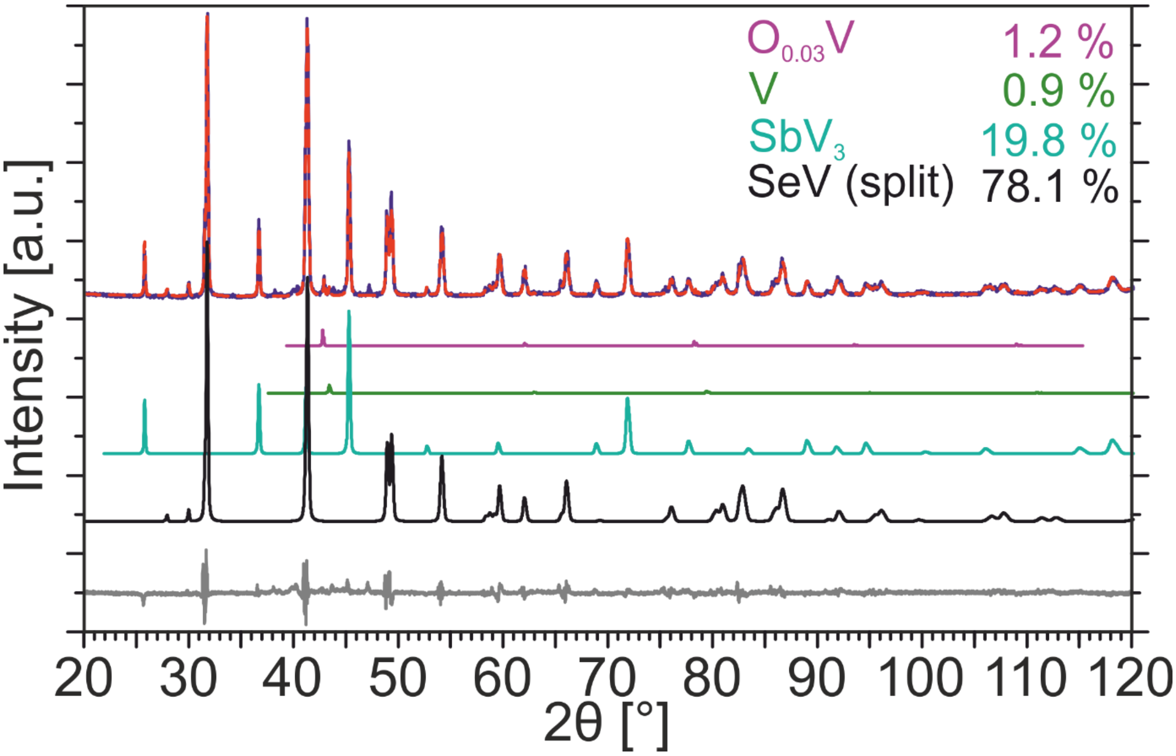

Figure 10: PXRD pattern of sample So158, with the measured curve in blue, the calculated curve in dashed red and the difference curve in gray; the SeV phase (black) exhibits splitting of several peaks, whereas the SbV_3 phase (turquoise) and the V phase (green) are as expected; some oxidic traces (purple) were observed

Wobst [140] as well as the associated solution model of Ghosh [145], but higher than values of the ionic solution model of Ghosh [145]. The experimental values of Berkes and Myers were observed to be similar within the accuracy of measurement [143]. Due to the ambiguity in the literature, our values were chosen in the further evaluation of the ternary phase diagram. The eutectic reaction at 50 at. % Sb was observed at 538 °C, which is very close to the experimental values observed by Wobst [140], but higher than the experimental values of Berkes and Myers [143] or Glazov et al [142].

Despite several different attempts of recalibration of the ZAF corrected EPMA, our measurements for the Sb_2Se_3 phase consistently exhibited a slight surplus of selenium. This surplus of ~1 at.% Se, however, was not supported by an altered occupation in PXRD pattern. Hence, we attribute this shift to matrix phenomena.

4.8.3. Binary Sb-V

No distinct samples were prepared in the binary Sb-V system. Nevertheless, due to the low solubility of selenium in the compounds present in this system, knowledge acquired by studying the ternary V-Se-Sb system (*vide infra*) might be applicable for the binary phase diagram, too. On the one hand, we observed a larger solubility ranges, compared to Failamani et al [148], for some of the binary phases of the Sb-V system. In that cases (e.g. SbV_3 reaching till the stoichiometric composition of 25 at. % V instead of 24.4 at.% V), our own measurement values were favoured over those of Failamani et al [148]. On the other hand, we propose a decomposition of the $Sb_9V_{7.46}$ phase in a eutectoid reaction below 600 °C, as the ternary sample of So126 did not contain any selenium in the equilibrium phases of SbV_2 and Sb_3V_2 and, hence, reflects the binary equilibrium condition to some extent.

4.8.4. Ternary isothermal sections

During the construction of the ternary phase diagram, several assumptions were made. First and foremost, the gas phase was not considered in our experiments, although pure selenium exhibits vapour pressures above 1 bar in several isothermal sections. Thus, the isothermal sections have to be regarded as “under own vapour pressure” rather than “under constant pressure”. Moreover, despite attempts to measure the liquid composition by area scans, no reasonable results could be gathered in most cases. Hence, and because of the primary crystallisation in the as-cast samples, a low vanadium content was assumed for the liquid phase, which reflects a steep curvature of the dominating primary crystallisation field of SeV in the liquidus projection, the liquid composition in the selenium-rich corner of the binary system Se-V is still uncertain (see Figure 8). Nevertheless, we assume a much steeper curvature for the liquidus than proposed by Smith [151]. Hence, and due to the fact, that the solidification scheme is dominated by the SeV phase (*vide infra*), a rather constant vanadium content in the estimated liquid was assigned for all isothermal sections. This value of approximately 8 at.% V was derived from the maximum of vanadium solubility measured in the presumable liquid of the prepared binary samples (refer to S17 to S22). Finally, the Se_4V_5 phase was eliminated for above-mentioned reasons as well as for the fact that it was observed in the ternary in thermodynamically forbidden four phase equilibria (e.g. samples So101 to So105, So159, and So160). These assumptions should be considered when working with the six isothermal sections presented in the Figure 11 to Figure 16.

No additional reflections, neither due to superstructures nor due to new compounds, were noticed during PXRD evaluation of the ternary samples, and no ternary compounds were observed by EPMA in any sample over the whole investigated range. Despite extensive attempts to synthesise an MLC in this system, no such compound was produced. Hence, we conclude, that the phase equilibria in this system are solely determined by phases present in the respective binary subsystems of Sb-Se-V.

The whole system is dominated by the two congruent melting compounds SeV and SbV_3. Those two compounds form a pseudo-binary section. On the vanadium-rich side of the pseudo-binary section, there is only one three-phase equilibrium (V + SeV + SbV_3) present over the investigated temperature range (e.g. Figure 15). On the other side of the SeV-SbV_3 pseudobinary section, there are three-phase fields showing SeV in equilibrium with the vicinal compounds of the binary Sb-V system (e.g. Figure 13). At lower temperatures, the broad SeV solid solution exhibits several phases, which are structurally related to the NiAs type parent phase. Those adjacent phases form ternary equilibria with the liquid (e.g.Figure 13) or, at lower temperatures, the Sb_2Se_3 phase, respectively (e.g.Figure 12). Albeit, no three-phase field of Se_9V_2 was observed (e.g.Figure 11), due to the temperatures of the selected isothermal sections, the only conclusive equilibrium at temperatures slightly lower than 400 °C is L + Se_2V + Se_9V_2. This hypothesis is supported by the traces of the Se_9V_2 phase observed in the PXRD data of sample So142 (refer to Table 10).

All observed solubility ranges into the ternary were below ~2.5 at.% of the additional atom species. SeV exhibited the largest ternary solubility with a maximum of 2.5 at.% Sb The defect mechanisms of the ternary solubilities of all phases present

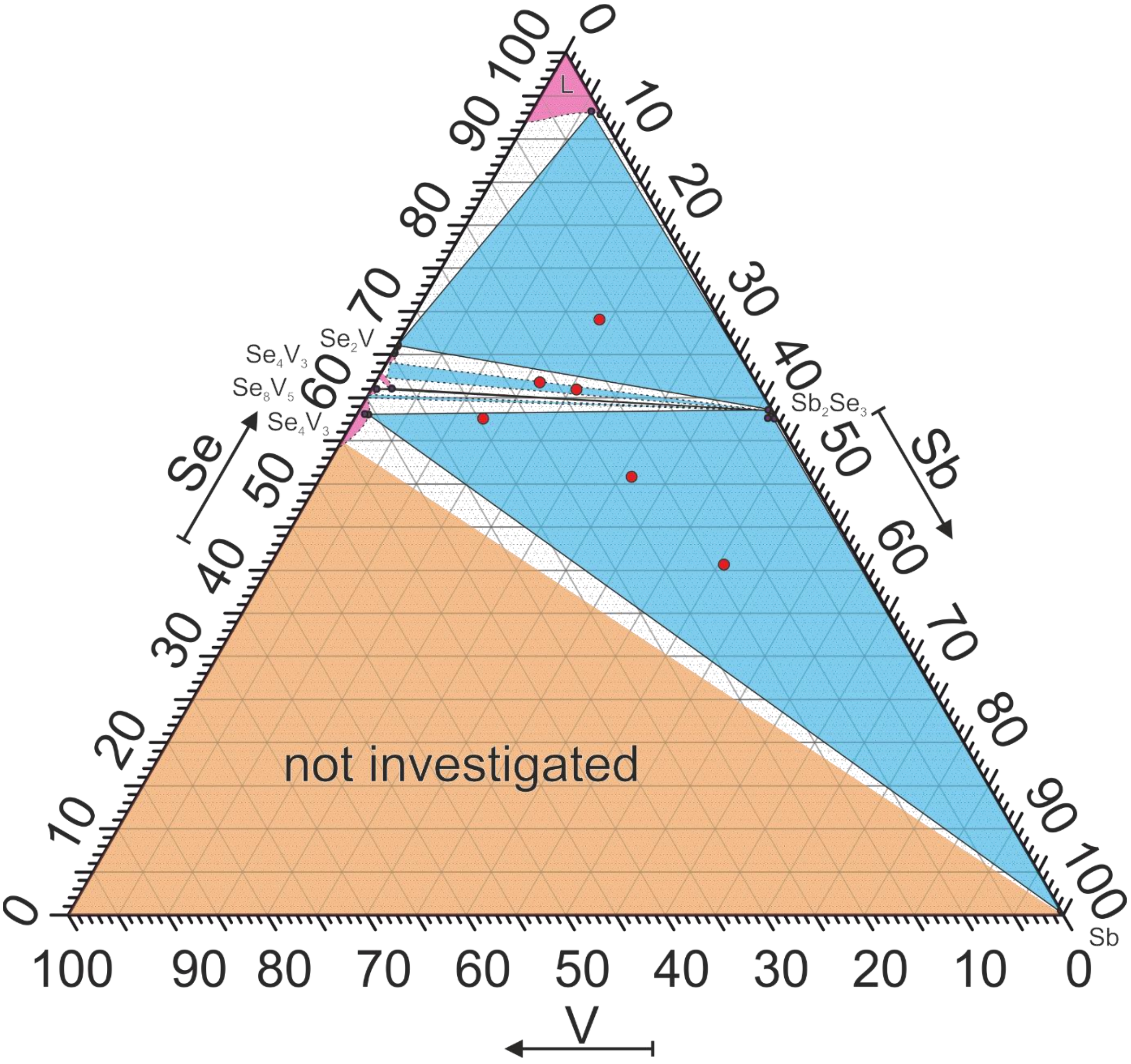

Figure 11: Isothermal section of the V-Se-Sb ternary system at 400 °C; the vanadium-rich region (indicated in orange) was not investigated; the mean sample compositions measured by EPMA area scans are marked by large red dots;small blue dots indicate mean results of point analyses; uncertain phase equilibria are represented by dashed lines, whereas full lines represent determined phase equilibria (used samples for determination: So68 and So142)

in the Sb-Se-V system are difficult to determine. On the one hand, EPMA results only exhibit a clear direction of substitution for the $C_{1-x}Sb_4V_5$ phase (e.g. Sb is exchanged for Se) as the results are at constant vanadium contents (e.g. refer to samples So120 till So130 in the supplementary materials section). On the other hand, there are two effects observed in PXRD measurements, which make the small changes in the electron densities, which need to be detected by Rietveld refinement, almost invisible. The first effect is a strong preferred orientation of the powdered crystals and the second effect is caused the vacancy driven solubility ranges of the

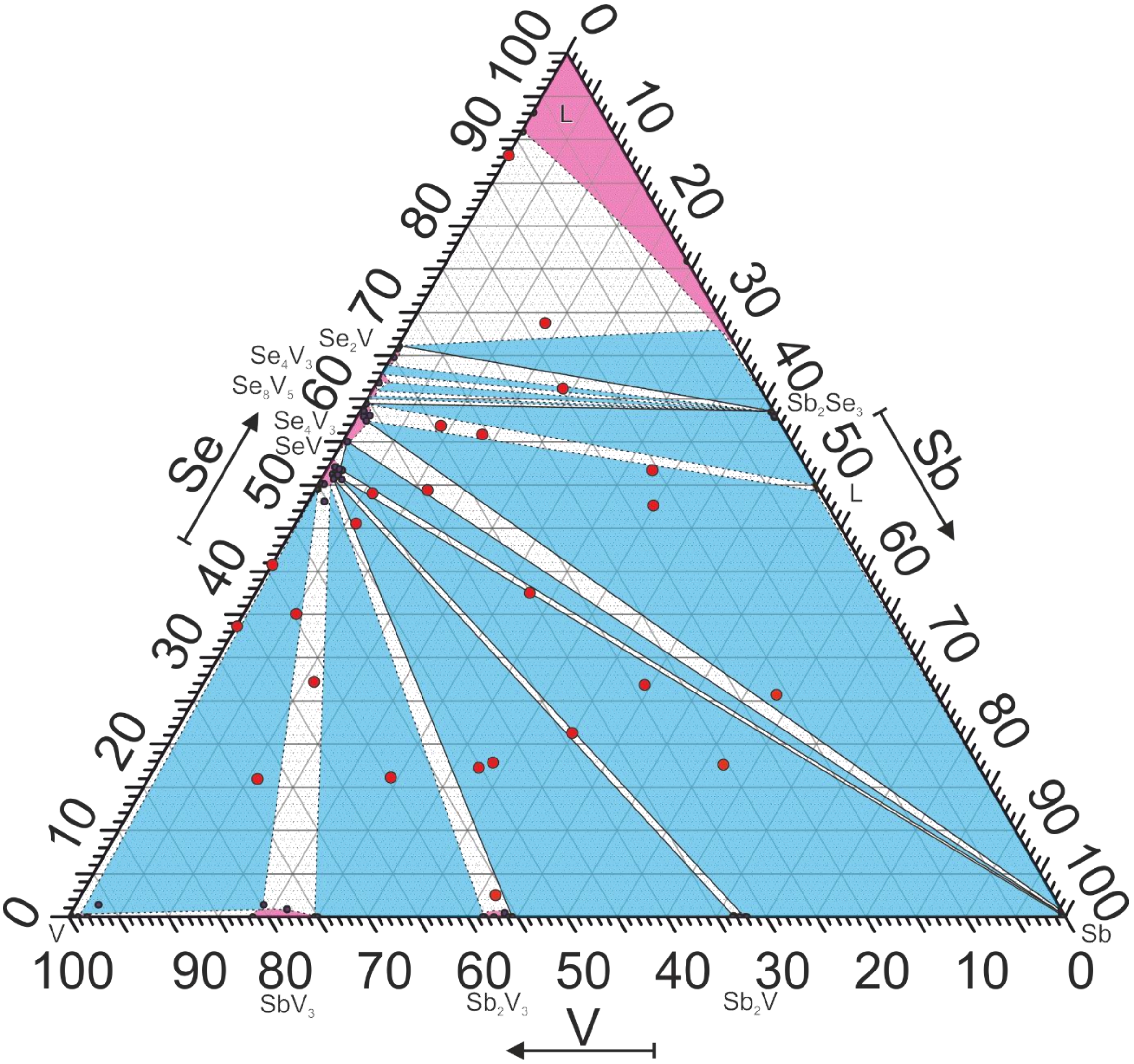

Figure 12: Isothermal section of the V-Se-Sb ternary system at 550 °C; the mean sample compositions measured by EPMA area scans are marked by large red dots; small orange dots indicate the mean area scans of special sample regions (e.g. liquid), whereas small blue dots indicate mean results of point analyses; uncertain phase equilibria are represented by dashed lines, whereas full lines represent determined phase equilibria (used samples for determination: So106, So126, So90, So80, So157, and So143)

binary phases, which lower the electron densities of the respective sites. Both effects are exceptionally strong for the NiAs type phases and their derivatives. Hence, no results can be reported on the defect mechanisms of the crystal structures.

The binary solid solubilities fit our EPMA observations in many cases. However, for the binary V-Sb system, we observed the SbV_3 phase to its stoichiometric composition, compared to Failmani et al [148], who reported on a solid solution

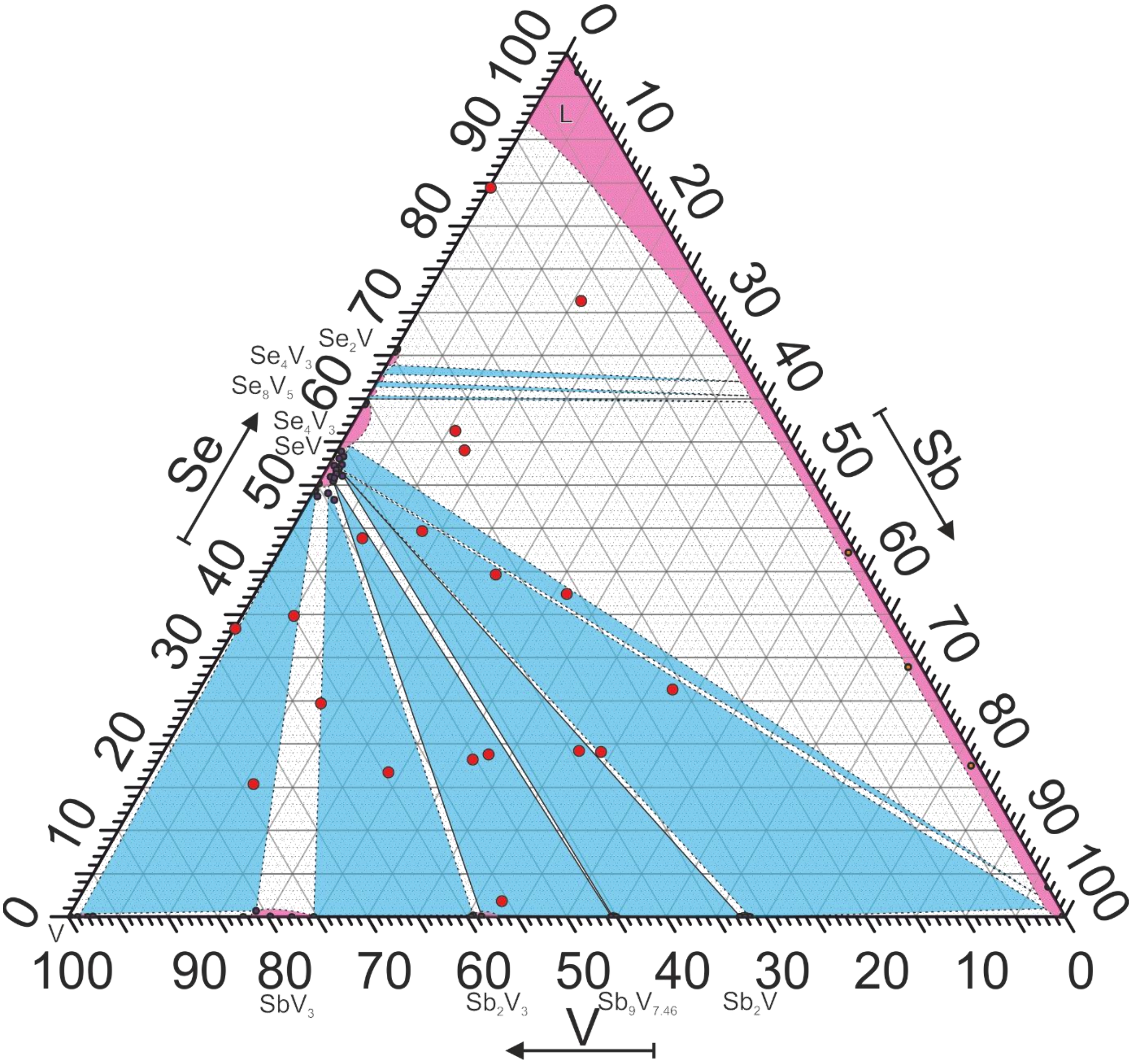

Figure 13: Isothermal section of the V-Se-Sb ternary system at 650 °C; the mean sample compositions measured by EPMA area scans are marked large red dots; small orange dots indicate the mean area scans of special sample regions (e.g. liquid), whereas small blue indicate mean results of point analyses; uncertain phase equilibria are represented by dashed lines, whereas full lines represent determined phase equilibria (used samples determination: So107, So117, So91, So88, and So158)

between 18.4 and 24.4 at.% of Sb. The low-temperature phase Sb_2V_3 and the high-temperature phase SbV_2 show unusual thermal behaviour. Their solid solubility appears to be high at lower temperatures and narrows down to higher vanadium-contents as temperature rises. This effect is probably due to the insufficient equilibration at lower annealing temperatures. The deviations observed for the Sb-Se system were discussed above and as most phase boundaries in the Se-V system are complicated to delineate, a comparison is futile.

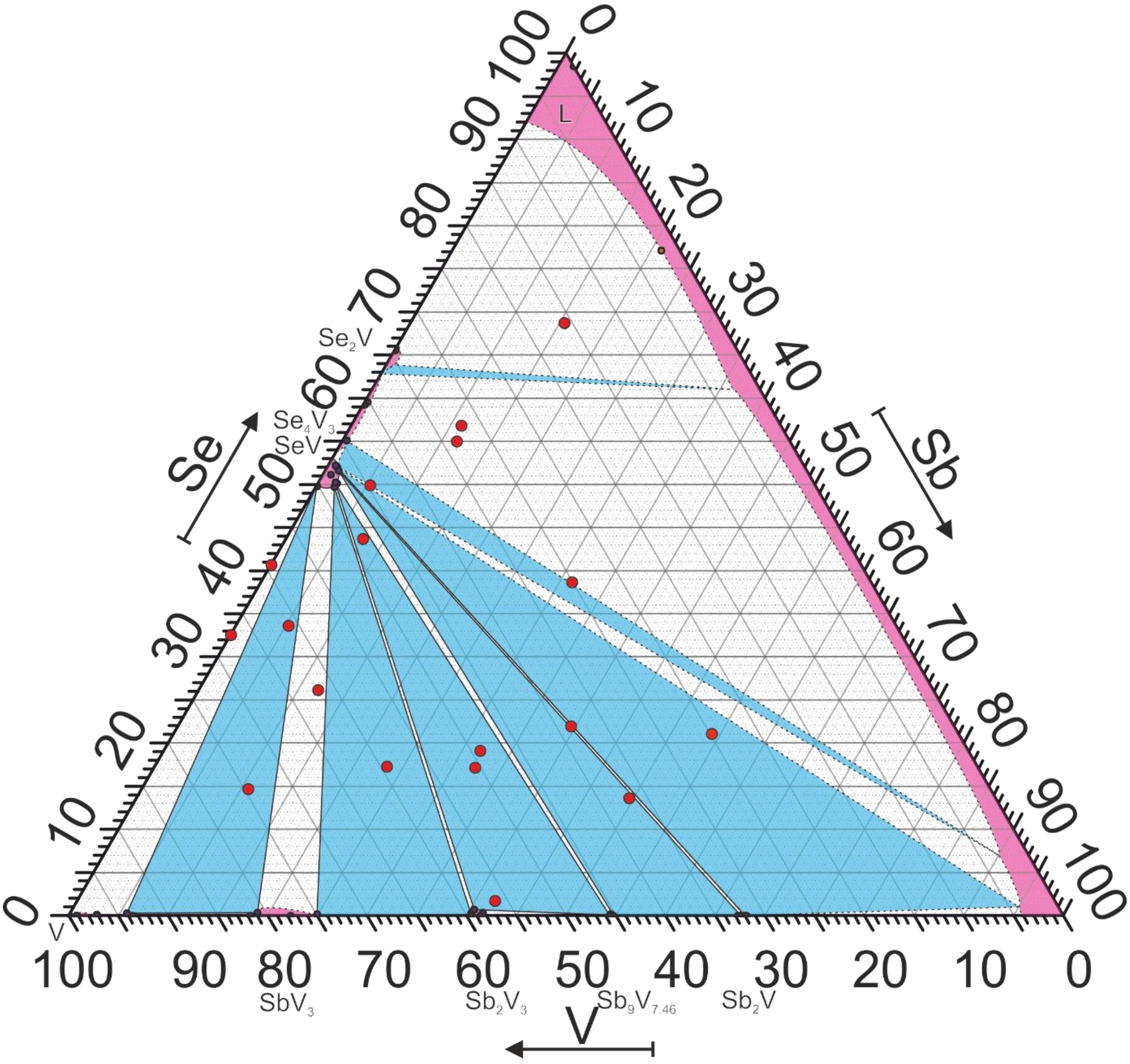

Figure 14: Isothermal section of the V-Se-Sb ternary system at 750 °C; the mean sample compositions measured by EPMA area scans are marked by large red dots; small orange dots indicate the mean area scans of special sample regions (e.g. liquid), whereas small blue dots indicate mean results of point analyses; uncertain phase equilibria are represented by dashed lines, whereas full lines represent determined phase equilibria (used samples for determination: So108, So128, So123, So89, and So159)

Interestingly, the binary phase of $Sb_9V_{7.46}$ was not observed in the isothermal section of 550 °C, albeit the respective samples were pre-annealed at temperatures, where this phase was observed (e.g. 650 °C pre-annealing for one week in sample So110). This rules out the possibility of a kinetically hindered formation of the respective phase at lower temperatures and freezing of liquid traces. Hence, there is a ternary solid-state transition between 650 °C and 550 °C. Either there is a ternary transition reaction $Sb_9V_{7.46}$ + SeV = Sb_3V_2 + SbV_2, or there is a binary

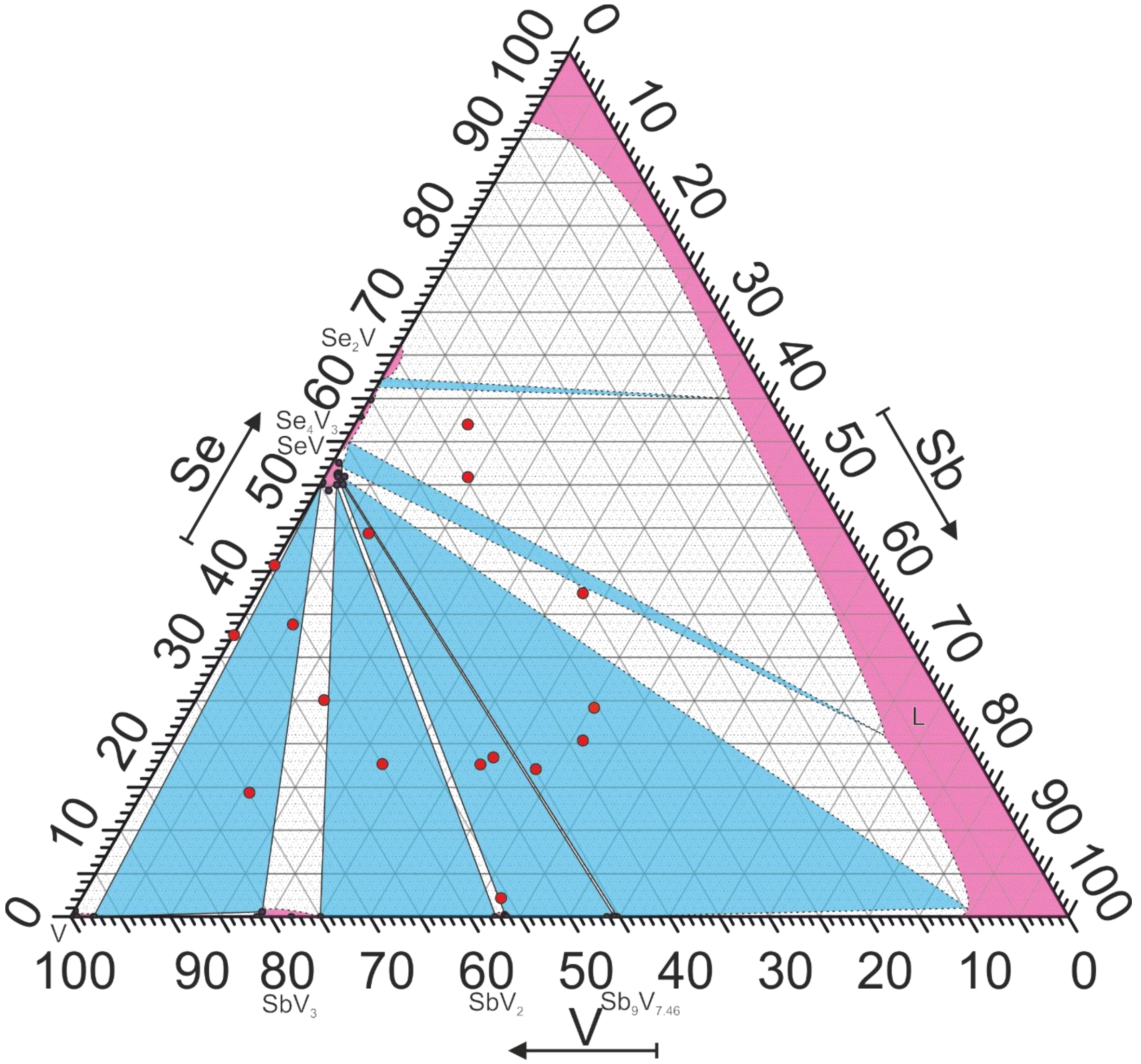

Figure 15: Isothermal section of the V-Se-Sb ternary system at 900 °C; the mean sample compositions measured by EPMA area scans are marked by large red dots; small blue dots indicate mean results of point analyses; uncertain phase equilibria are represented by dashed lines, whereas full lines represent determined phase equilibria (used samples for determination: So160, So150, So129, and So124)

eutectoid reaction below 600 °C, as Failamani at al [148] observed the phase $Sb_9V_{7.46}$ in their samples at 600 °C.

In numerous samples, we observed the phases (presumably carbon stabilised) phase Se_4V_5 and $C_{1-x}Sb_4V_5$ (e.g refer to samples So101 till So105 and So120 till So130 in the supplementary materials section, respectively). Independent of the selected temperature (excepting the as-cast samples), between 3 and 5 at.% Sb or Se solubility into the ternary were measured by EPMA scans. This means in the quaternary phase diagram of C-Sb-Se-V, the capacity of exchange of selenium and

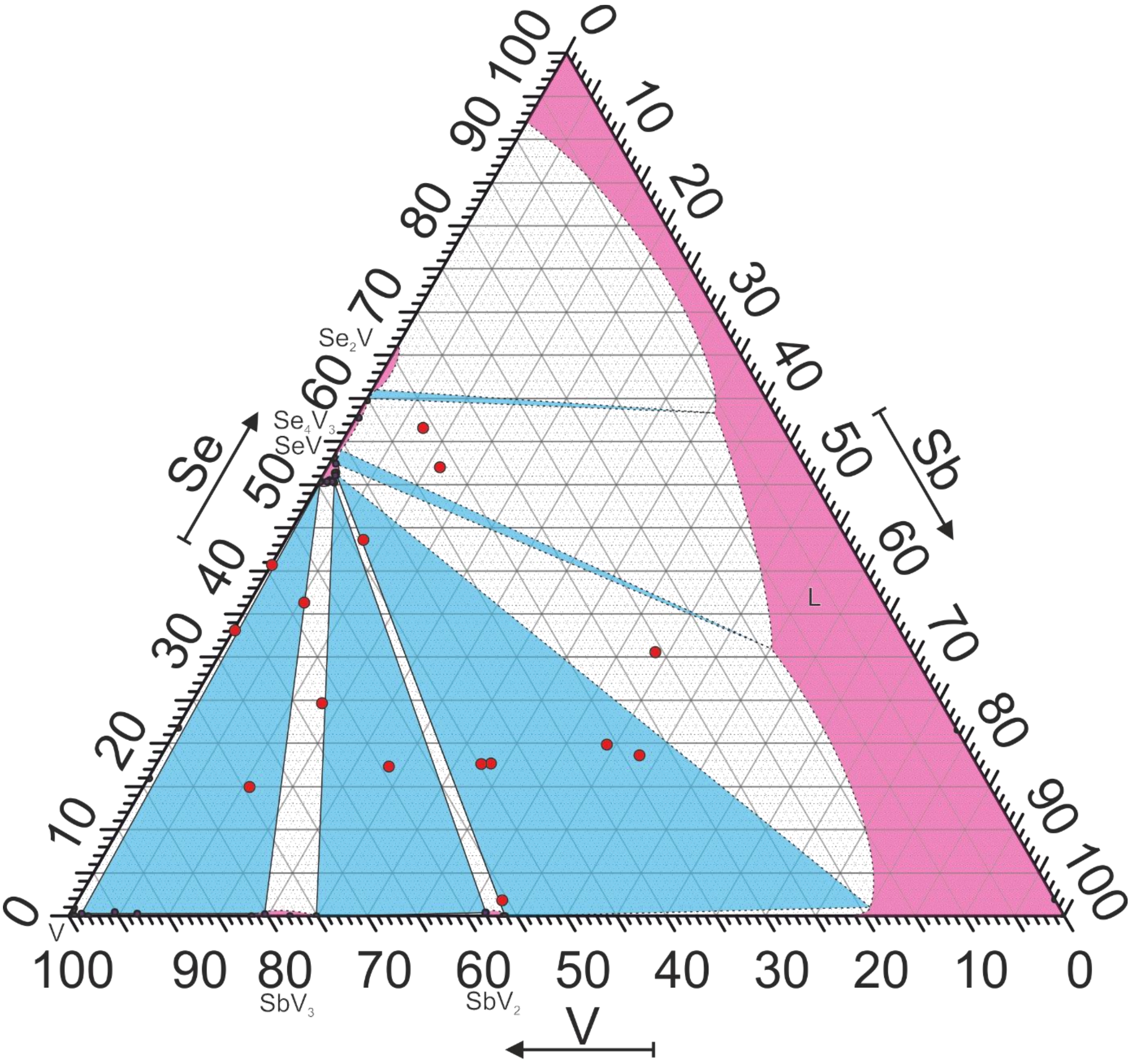

Figure 16: Isothermal section of the V-Se-Sb ternary system at 1000 °C; the mean sample compositions measured by EPMA area scans are marked by large red dots; small blue dots indicate mean results of point analyses; uncertain phase equilibria are represented by dashed lines, whereas full lines represent determined phase equilibria (used samples for determination: So110, So125, and So161)

antimony on their assigned crystallographic positions is between 7 and 11 %. The exchange was detectable in PXRD and fitted the Vegard's law. It is speculative, whether there is a continues solid solution at higher carbon content (e.g. $C(Sb,Se)_4V_5$) or that these values are the maximal exchange the crystal structure can support in the quaternary phase diagram of C-Sb-Se-V (e.g. $C(Sb_xSe_{1-x})_4V_5$ with $x<0.11$ as well as $x>0.89$).

4.8.5. Ternary solidification scheme

The liquidus projection is based on samples, which were molten in an arc furnace. In the vanadium-poor part of the phase diagram, arc melting was impossible due to the high vapour pressures of selenium and antimony. Hence, (partially) molten samples, which were annealed in silica ampoules in a muffle furnace and afterwards quenched in cold water, served as a source of information in this part of the phase diagram. In some cases, it was difficult to distinguish, whether a phase was present during the annealing procedure or formed during quenching. Nevertheless, as this was the case for the primary crystallising phase only, the liquidus projection was not changed.

The whole liquidus projection (Figure 17) is dominated by an extensive field of primary crystallisation of SeV, as well as its derivative phase Se_4V_3. Its high melting point compared to the other phases permits only low vanadium contents of the liquid till temperatures of more than 1000 °C. Hence, all reactions present below this temperature are restricted to the boundary regions of the liquidus projection.

Five phases in the binary phase diagrams decompose in congruent reactions. These result in four maximum reactions in the ternary. Three of them are related to the binary phases Se_4V_3, Se_8V_5, and Sb_2Se_3. The last one is located along the pseudo-binary section of SeV to SbV_3. On the vanadium-rich corner, there is one ternary eutectic reaction. This eutectic composition was found to be around the composition of 70 at.% V, 23 at.% Se, and 7 at.% Sb (refer to samples So146 and So147, as well as the the microstructures represented in Figure 18a and b).

On the vanadium-poor side of the pseudo-binary section, the peritectic cascade observed in the binary phase diagram of V-Sb is stabilised to higher temperatures, resulting in a ternary peritectic cascade at low selenium content (e.g. Figure 18c to e). Close to the Sb-Se system several ternary transition reactions and two ternary eutectic reactions are present on the liquidus-surface. The exact composition of the liquid of all mentioned reactions could not be measured by EPMA area scans (e.g. Figure 18f), and hence, estimated from the DTA results and primary crystallisation of the as-cast samples. The whole system finally solidifies in a ternary eutectic reaction at 215 °C, which is 2 °C lower than the two binary eutectic reactions in the selenium-rich corner. Due to the fact that small deviations in those binary reaction

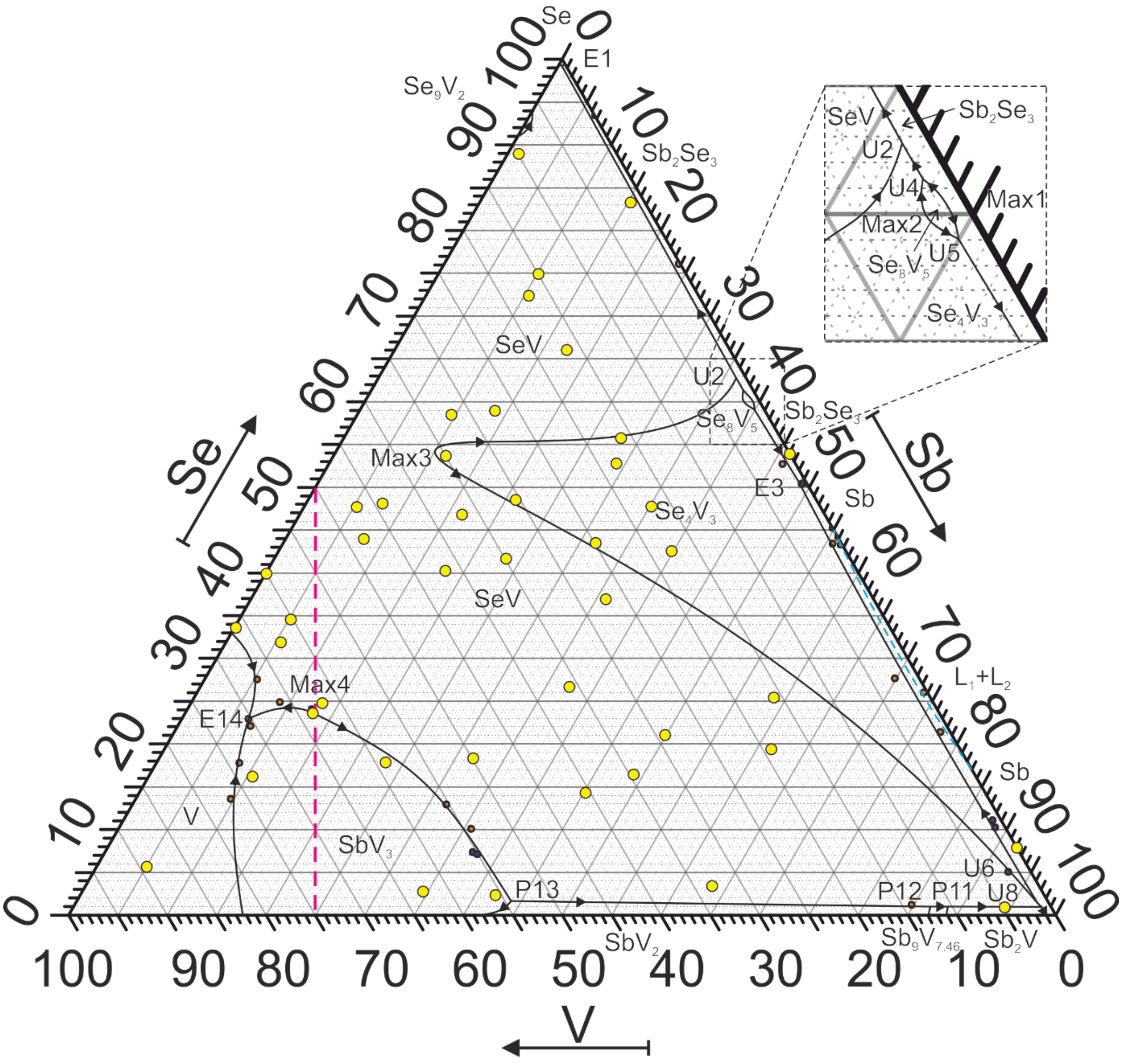

Figure 17: Solidification scheme of the V-Se-Sb ternary system; the mean sample compositions measured by EPMA area scans are marked by large yellow dots; small orange dots indicate the mean area scans of special sample regions (e.g. eutectic or liquid composition), whereas small blue dots indicate mean results of point analyses; the dashed line between the phases SeV and V_3Sb represents a pseudo-binary section; the monotectic reaction present in the binary Sb-Se system is indicated by a blue dashed line

temperatures result in different ternary reaction types, our own measurements were favoured over the literature values.

A Scheil's diagram illustrating the reaction scheme as well as the reaction types and the respective transition temperatures was created and is presented in Figure 7. The evaluation was done by DTA measurements and comparison to the literature values of the respective binary phase diagrams. Three reactions are uncertain regarding their reaction type. The peritectic reaction of P5 could be a transition reaction, too. As our DTA measurements were executed in silica ampoules, the

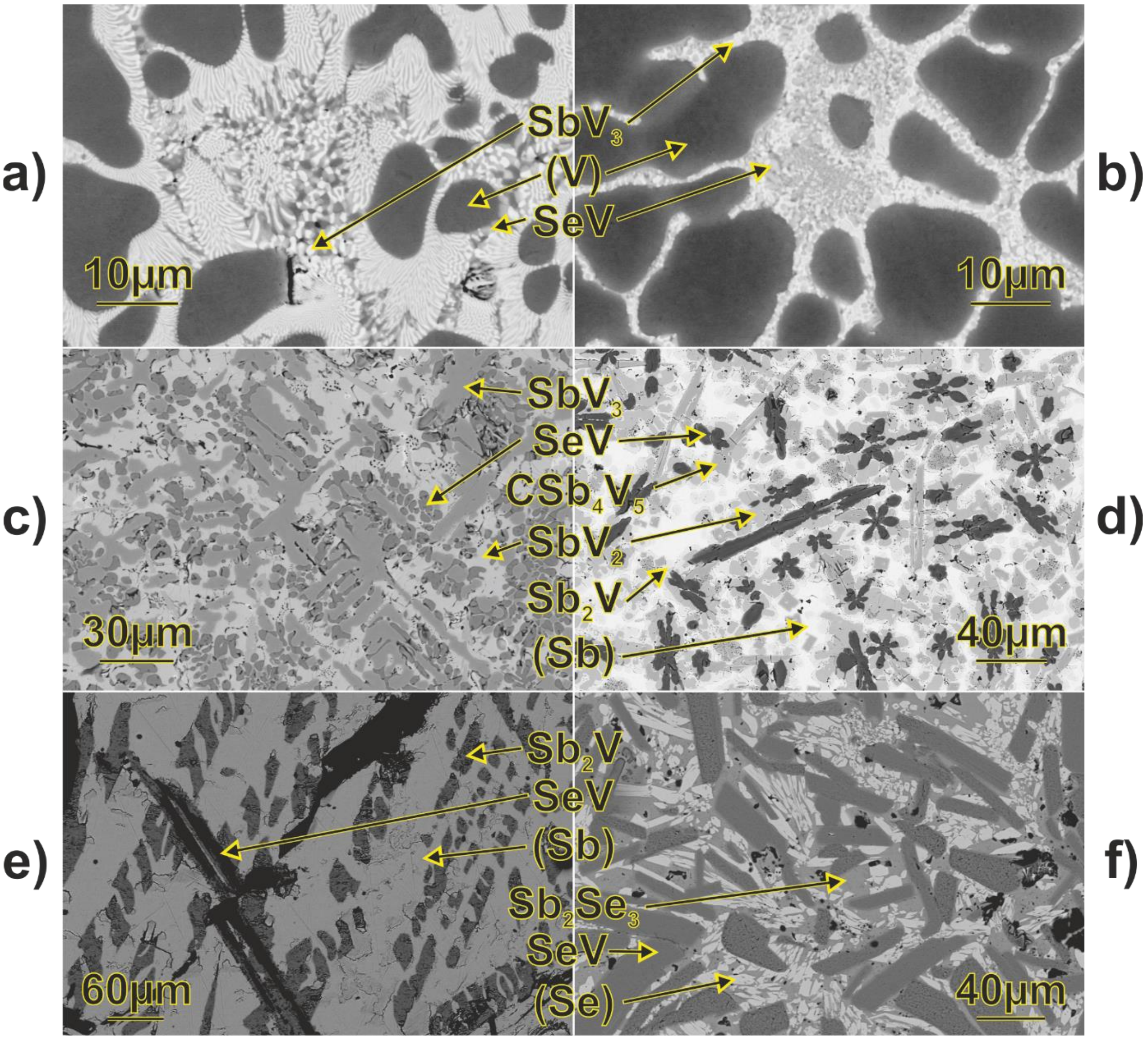

Figure 18: Typical sections of several ternary as-cast samples (a – So147, b – So146, c – So53, d – So57, e – So136, and f – So59); a and b) eutectic reaction in the vanadium-rich part, in the primary crystallisation field of vanadium; c) primary crystallisation field SbV_3; d) $C_{1-x}Sb_4V_5$ was found to be on the liquidus surface (no peritectoid reaction); d, e, and f) primary crystallisation of SeV; due to the broad homogeneity range of Se_xV, where $1 \leq x \leq 2$, the phase was denoted as SeV for readability reasons

maximal measurable temperature was limited to 1100 °C. However, we assumed, that the elevation of all peritectic decomposition temperatures of at least 10 °C is the case for the reaction P5, too. The other two reactions are the solid state transition reactions of U5 and U6. Their respective effects were not detectable beyond doubt in our DTA measurements. Hence, both reactions could be eutectoid reactions, too.

4.9. Conclusion

The current work presents a detailed study of the ternary system Sb-Se-V. No ternary compounds, independent of their dimensionality, were observed in the course of this investigation. Six (partial) isothermal sections, the ternary solidification scheme, and a Scheil's diagram were presented. The isothermal sections exhibit ternary equilibria, which are originating from the SeV phase and its derivatives.

The construction of isopleths for a better illustration of the underlying reactions was not possible due to the significant shifts in sample compositions during the preparation process. Due to this and other difficulties in sample preparation, which are mainly a result of the different physical properties of the elements, the system is prone to errors arising from impurities. Hence, we present a corrected version of the binary Se-V phase diagram, too. This new version speculates on a stabilisation of the Se_4V_5 phase, as it was proven for the isostructural Sb_4V_5 phase. The proof of this hypothesis is the subject of a future publication. Additionally, we propose limited thermal stability for the Se_9V_2 phase. The thermal stability of the binary phase $Sb_9V_{7.46}$, which was not observed in the isothermal section of 550 °C, is limited at least in the ternary.

4.10. Acknowledgements

The authors wish to thank Dr. Stephan Puchegger from the Department of Physics, University of Vienna, for his help with SEM measurements. Special thanks go to Prof. Herta Effenberger from the Department of Mineralogy and Crystallography, University of Vienna, for her patience in attempting to find suitable single crystals of the Se_4V_5 phase.

4.11. Declarations of interest

The authors declare that there is no conflict of interest.

5. Publication 2: Phase equilibria and new misfit layer compound in the ternary system of Pb-Se-V

5.1. Authorship Statement

Chapter 5 describes was published in *The Journal of Alloys and Compounds, Volume 810, Issue 151671* in 2020. It is available by the DOI: 10.1016/j.jallcom.2019.151671. The co-author is Klaus W. Richter, who is my advisor and I am the primary author of the manuscript.

Reisinger: Conceptualisation, Investigation, Writing - Original Draft, Visualisation

Richter: Conceptualisation, Writing - Review & Editing, Supervision, Project administration

5.2. Abstract

The ternary system Pb-Se-V was investigated by means of powder X-ray diffraction (PXRD), scanning electron microscopy (SEM) in combination with electron probe microanalysis (EPMA), and differential thermal analysis (DTA). The results of the evaluations in the ternary system are presented by five full isothermal sections at 550 °C, 700 °C, 800 °C, 1000 °C, and 1100 °C and one partial isothermal section at 375 °C. A special focus was set on finding a misfit layer compound (MLC) in this system. With the phase $(PbSe)_{1+\delta}(VSe_2)$ one MLC can be reported.

5.3. Keywords

Ternary alloy system, Phase diagrams, Phase transitions, Misfit layer compound, Scanning electron microscopy, Scanning transition electron microscopy, X-ray diffraction

5.4. Prime novelty statement

In this article, we present the up to now uninvestigated phase diagram Pb-Se-V. Furthermore, a first draft for the Pb-V binary phase diagram and the new misfit layer compound $(PbSe)_{1+\delta}(VSe_2)$ can be reported.

5.5. Highlights

- Six isothermal sections in the Pb-Se-V system studied

- New misfit layer compound $(PbSe)_{1+\delta}(VSe_2)$ synthesised in the Pb-Se-V system

5.6. Introduction and literature review

Since the discovery of the useful properties of graphene, low-dimensional materials have gained great interest in the literature. Not only graphene, but also other 2D materials, including transition metal dichalcogenides (TMDs), boron nitride, and hybrid perovskites, were investigated extensively. Next-generation electronics, anode materials in lithium-ion batteries, and water splitting by hydrogen evolution reaction are just some of the potential applications.

2D and even 1D materials can be synthesised in the binary Se-V system using the phases Se_2V and Se_9V_2 [24, 131, 132, 135-137] as starting compounds. Additionally, the ternary systems M-Se-V, where M can be bismuth, lead, tin or a rare earth element, might host misfit layer compounds (MLCs), which are another type of 2D materials.

Their crystal structure is comprising of a layered composite (refer to Figure 19). The general formula of MLCs $[(MX)_{1+\delta}]_m(TX_2)_n$ reflects the fact that two interpenetrating, yet structurally different, subsystems are stacked. The TX_2 subsystem is based on the triple layer of TMDs. TMDs are hexagonal structures of a transition metal (e.g. vanadium) in between sandwiches of a chalcogen (e.g. selenium). A distorted sodium chloride type crystal structure is the base MX subsystem. Chalcogens (e.g. selenium) and the above-mentioned elements bismuth, lead, antimony, tin or a rare earth are arranged in an almost cubic lattice. Usually, the two subsystems coincide in one crystallographic direction, but due to their different crystal structures, they do not have rational ratios for their lattice parameters in the other direction of the layer. Hence, MLCs are incommensurately modulated systems, which not only requires the use of a misfit parameter δ, but also a description in (3+1)D super-space symmetry for the solution of the crystal structure. Furthermore, different stacking sequences may be observed. They are described by the parameters m and n in the general formula $[(MX)_{1+\delta}]_m(TX_2)_n$ [126, 139]. However, the thermodynamically most favourable compositions are reported for small values of m and n [101].

Dependent on the synthesis approach the resulting layered composite is not only denoted differently but also exhibits different properties (e.g. crystal structure, stability, conductivity) [126]. MLCs are thermodynamically stable compounds that are synthesised by traditional solid-state chemistry approaches, such as chemical vapour deposition (CVD) with a transporting agent (e.g. NH_4Cl [121, 122]) or crystal growth from salt fluxes (e.g. eutectic melt of LiCl and KCl [159]). *Fere*crystals are obtained by the much more versatile method called modulated elemental reactants synthesis. This is a process of physical vapour deposition (PVD) of the precursors of the layered compound, followed by a low-temperature annealing step. The resulting *fere*cystals permit a much broader variety of the parameters *m* and *n*,

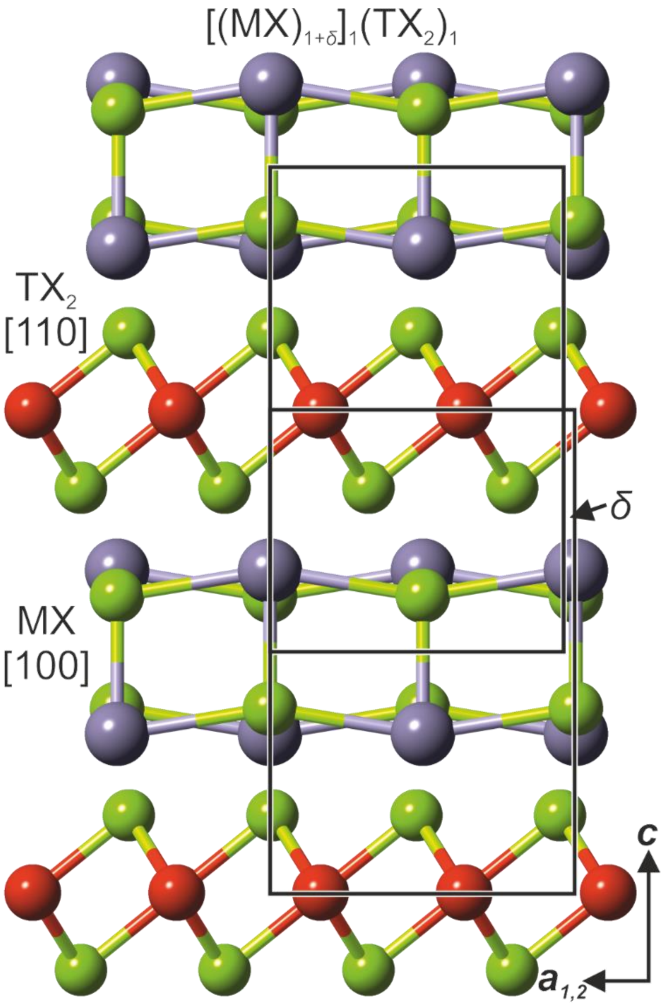

Figure 19: Schematic crystal structure of a misfit layer compound $[(MX)_{1+\delta}]_m(TX_2)_n$ *(m=n=1); T atoms (e.g. vanadium) are red, X atoms (e.g. selenium) are green, and M atoms (e.g. lead) are blue in this picture; the unit cells for the individual sub-lattices of the* TX_2 *and MX are given in order to visualise the misfit parameter* δ*.*

however, at the cost of thermodynamic stability. They are only kinetically stabilised and usually contain more defects than MLCs [126].

The advantage of easier tuneability of *fere*crystals compared to MLCs is reflected in the available literature. For systems based on M-Se-V (M = Bi, Pb, Sb, Sn, or a rare earth element) only one MLC is reported $(La_{0.95}Se)_{1.21}VSe_2$ [35] and in our recent investigations of the Sb-Se-V system, no MLCs were observed [130]. In contrast, however, for *fere*crystals many more are reported for those systems [27, 37, 68, 69, 73, 74, 84, 96, 114, 165].

Neither for the ternary system Pb-Se-V nor for any of the ternary systems of an early transition metal with lead and selenium, a phase diagram is available. This fact might be attributed to difficult sample preparation in these kinds of systems. Nevertheless, four layered compounds $(PbSe)_{1+\delta}(VSe_2)_n$ ($0.08 \leq \delta \leq 0.14$ and n = 1, 2, 3, and 4) were reported for this system [27, 28, 84]. They all were prepared on a SiO_2 substrate by a modulated elemental reactants synthesis approach.

As the reported *fere*crystalline compounds in the Pb-Se-V system are kinetically stabilised, they are not necessarily thermodynamically stable intermetallic phases in this system. Their crystal structure might deviate from closely related and thermodynamically stable MLCs, those are eventually present in ternary system Pb-Se-V. Hence, the main goal of this publication is to investigate the phase equilibria present in this system determine whether Pb-Se-V-based MLCs can be synthesised by a classical solid state chemistry approach.

The system of Pb-Se (refer to Figure 20) was investigated extensively due to the favourable properties, such as thermoelectricity [166], of lead-based chalcogenides. The NaCl-type intermetallic phase of PbSe is the only intermediate phase at atmospheric pressure. Its solubility is reported to be below 0.04 at.% [166-172]. The congruent melting point is reported between 1076 °C [173, 174] and 1088 °C [175] and at a composition of either the stoichiometric composition [166] or 50.012 at.% Se [172].

The lead-rich side is characterised by a eutectic reaction, which is located at 0.013 at.% Se and 0.2 °C below pure lead. The solubility of selenium in lead is below

0.004 at.% Se [176]. According to the experimental data [170, 173-175, 177-181], the liquidus exhibits an inflection point in this part of the phase diagram. This indicates a metastable liquid miscibility gap [172]. Nozato and Igaki described this liquid miscibility gap by a monotectic reaction around 860 °C and 9 wt.% Se [173, 174], which equals approximately 20.5 at.% Se. Their observations were confirmed neither by DTA nor by metallographic experiments of Seidmann et al [179]. Miller and Komarek compared the liquidus curves of the Pb-S, Pb-Se, and Pb-Te systems and did not describe a stable miscibility gap in this region [180]. Hence, recent assessments [172] and CALPHAD models [166, 182] neglect Nozato and Igaki's hypothesis on a monotectic reaction.

The experimental data [170, 173, 174, 179-181] on the liquidus in the selenium-rich part are in fair agreement with the CAPLHAD models [166, 172, 182]. For selenium contents above the monotectic reaction proposed at 75.9 at.% Se, only experimental data of Nozato and Igaki are available [173, 174]. In contrast to all

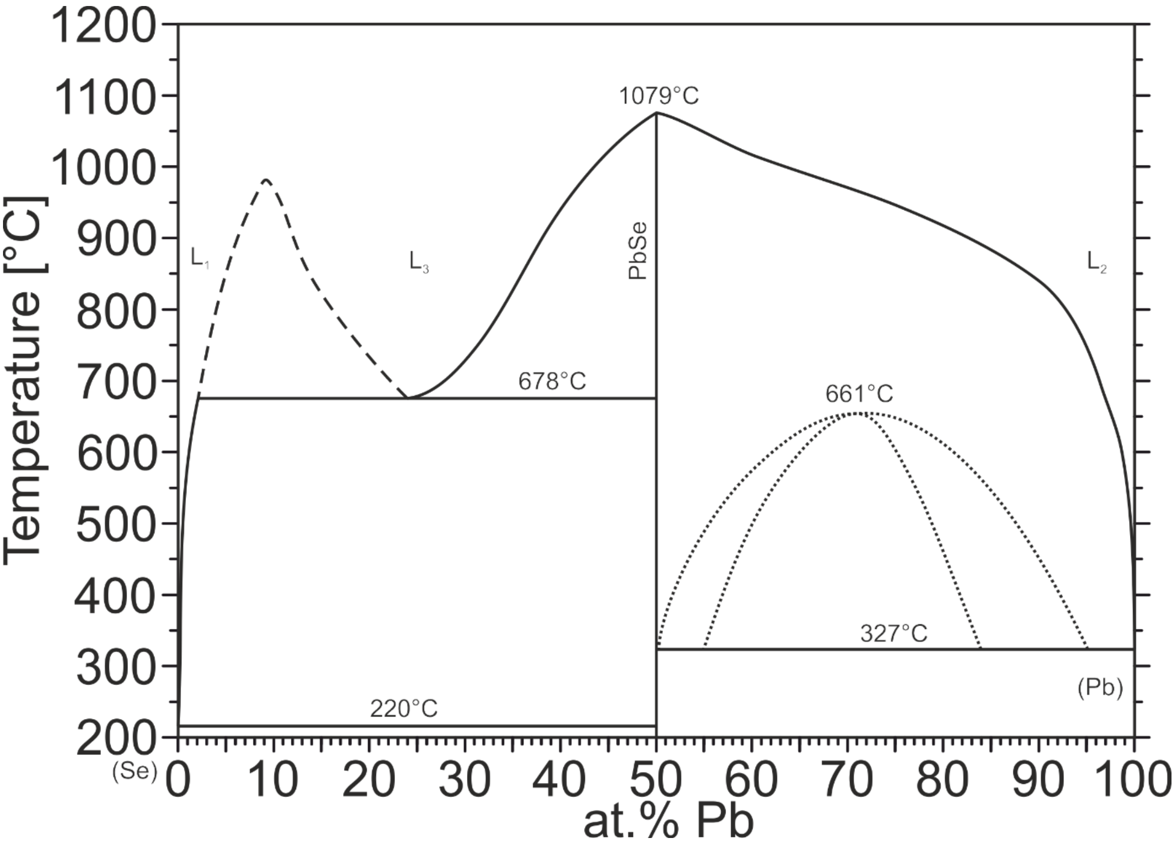

Figure 20: Binary phase diagram Pb-Se redrawn according to Lin et al [172]; dashed lines in the selenium-rich corner were not confirmed experimentally up to now; dotted lines in the lead-rich corner reflect the metastable liquid miscibility gap.

other authors, they also consider the presence of the gas phase in this part, as pure selenium exhibits vapour pressures of more than 1 atm above 684.8 °C, which is close to the invariant temperature of the monotectic reaction. The experimental and CALPHAD modelled values for this monotectic reaction range between 678.3 [181] and 681 °C [173, 174] as well as 674 [182] and 678 °C [172], respectively. For this publication, the assessed phase diagram of Lin et al was used [172].

On the binary system of Pb-V, only a few reports are available. There are debates on a Cr_3Si-type phase close to the stoichiometry of PbV_3. Holleck et al [183] and Savitsykii et al [184] reported poorly matching lattice parameters and incomplete reaction. Ledger and Hall [185] failed in preparing the relevant compound. However, at elevated pressures and temperatures by 25 to 50 kbar and 2000 °C, respectively, they observed a tetragonal phase. Ledger and Hall [185] concluded that the intermetallic phase of PbV_3 is presumably stabilised by impurities as Holleck et al prepared the phase from hot pressing powders in a die made from graphite [183] and Savitsykii et al on a vanadium wire that was diffusion-annealed in lead vapour [184]. This hypothesis is further supported by literature on the entropy of this compound. On the one hand, minor amounts of interstitial contaminants, such as carbon, oxygen, hydrogen, or nitrogen, result in an entropy gain. On the other hand, a shift from the ideal stoichiometry in XV_3 compounds (X is Si, Ge, and Sn) towards higher vanadium contents was observed, which suggests an influence of configurational entropy at higher atomic numbers such as PbV_3 [186]. Hence, PbV_3 is presumably metastable at pressures of 1 atm.

Another phase is proposed to be present in this system. Wang [187] hypothesised on a superconducting compound of the stoichiometry Pb_3V. This Cu_3Au-type phase was predicted by comparing the atomic and metallic radii as well as their relation numbers of existing and hypothetical compounds. The T_c was predicted to be around 13.1 K on the basis of a linear relation of T_c and η of lead-based $L1_2$-type compounds.

No binary phase diagram on the Pb-V system was published up to now [186] and no phase diagram data on any higher-order systems are available. Due to the lack of data an appearance similar to the Bi-V system was chosen as a working hypothesis for this publication. It is characterised by very low vanadium contents in the bismuth-rich liquid and an equilibrium of vanadium with the gas phase of bismuth above its boiling point.

The Se-V phase diagram (refer to Figure 21) comprises four stable phases and one presumably metastable phase [130]. Experimental difficulties, such as the strongly differing melting and boiling behaviours, the sluggish formation of compounds, the closely related structure types and superlattices, the formation of pseudo-single phase fields, and the reaction of vanadium with silica and carbon, complicate the determination of the phase diagram. Hence, this binary system is not entirely determined up to now and contains several extrapolations of distinct features, which are shared with the closely related systems of S-V and Te-V [151].

In the vanadium-rich part, only the Se_4V_5 phase is reported. It is formed in a peritectoid reaction. However, there is evidence that this is not an equilibrium phase [130]. Large deviations in the decomposition temperature depending on the

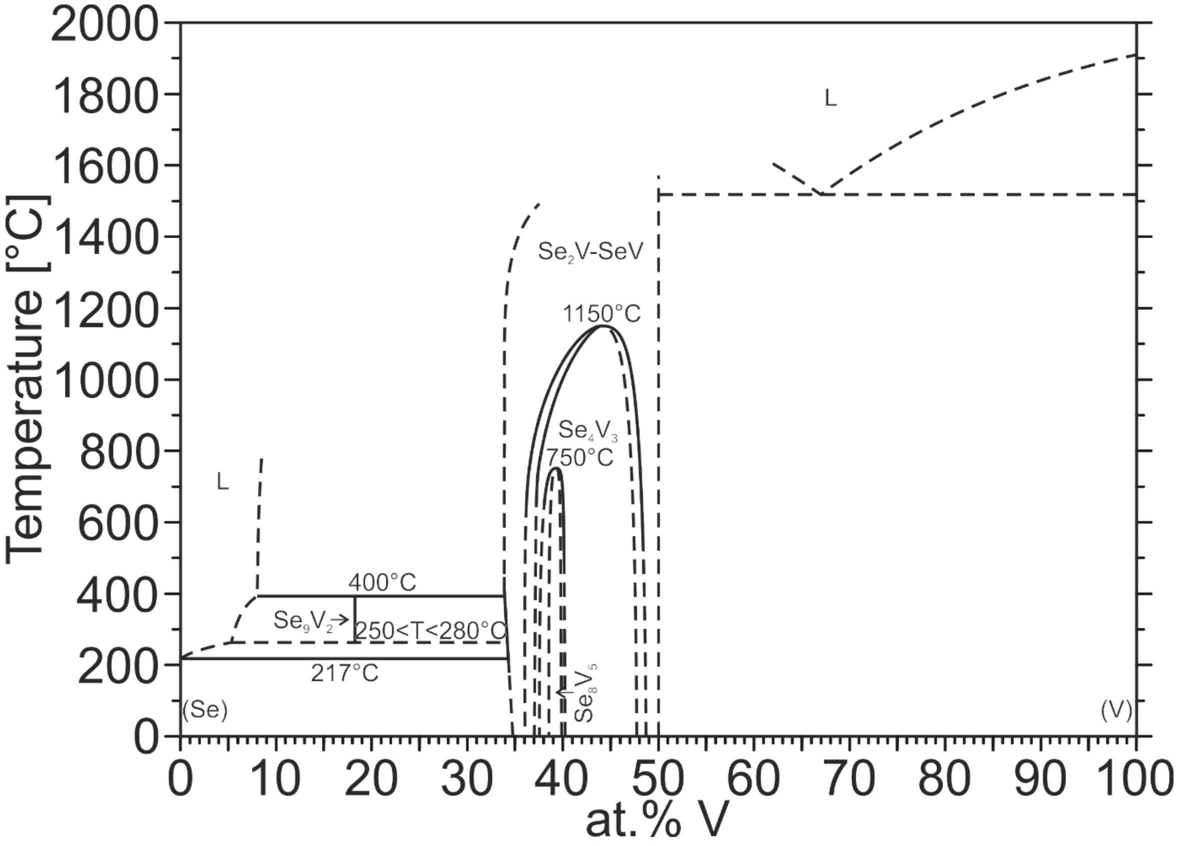

Figure 21: Binary phase diagram Se-V redrawn according to Reisinger and Richter [130]; dashed lines reflect equilibria and reactions with uncertainty.

preparation procedure [154, 155], small lattice parameter changes at large changes in composition [156], and a structure type, which is stabilised by impurities in other vanadium-based systems [148] are reported. Hence, this part of the phase diagram only shows one invariant reaction, which is a eutectic above 1550 °C [130]. Between around 50 and 66.6 at.% Se three phases can be found. All of them are related to a NiAs parental structure. Se_8V_5, which is decomposing in a congruent reaction around 750 °C, exhibits the smallest solubility range and is located within the phase field of Se_4V_3. In the assessed phase diagram of Smith [151] and our recent adaptation [130], the decomposition of Se_8V_5 is a first order phase transition. However, some authors propose a second-order phase transition ($Se_4V_3 \rightarrow Se_8V_5$) to take place. Oka et al [188] and Nakazawa et al [129] described a mechanism for the Se-V and S-V binary systems, respectively. Se_4V_3 itself is located in the phase field of SeV and decomposes congruent too, but at temperatures around 1150 °C. The temperature of the congruent decomposition of SeV is still unknown [151]. At selenium contents higher than 66.6at.% Se only three invariant reactions are observed. Two of them involve the Se_9V_2 phase. This phase is stable in a limited temperature range between a peritectic reaction around 400°C and a catatectic reaction around 250 and 280 °C. The last invariant reaction is a eutectic reaction around 217.5 °C and located at selenium contents higher the 99.9 at.% Se. For this publication, the phase diagram of Reisinger and Richter was used [130].

5.7. Materials and methods

The above mentioned experimental difficulties in the Se-V system (e.g. strongly differing melting and boiling behaviour, reactions with silica and carbon, or sluggish formation of compounds) apply for the ternary Pb-Se-V system, too. Hence, the available procedures of sample preparation are limited and require multiple steps for equilibrating samples quicker and enhancing the reproducibility of results.

Lead rods (purity 99.999 %), Selenium shots (American Smelting and Refining Company – purity 99.999 %), and powders of vanadium (purity 99.99 %; 1250 mesh) were used as source materials. From those the three master alloys PbSe, Se_2V, and SeV were prepared in large quantities by weighing them out in an argon-filled glovebox, sealing them in silica ampoules under vacuum and subjecting them to heat treatment. The master alloys were checked for potential impurity phases by PXRD. Only well homogenised and oxygen-free master alloys were further processed in sample preparation.

The advantages of this additional step are reduced weighing errors and evaporation losses (e.g. lead and selenium) as well as quicker equilibration of final samples. Latter is further improved by using mostly powders and compositions close to the equilibrium. Additionally, the master alloys eventually permit melting in an arc furnace at compositions above 80 at.% V, which is not possible when pure selenium is utilised as a starting material.

All ternary samples were weighed out from powders of the pure elements and/or readily prepared master alloys. The total sample mass (300 mg ± 0.5 mg) was well mixed by shaking and then cold-pressed in a steel die without lubricant in order to obtain dense samples. To prevent any oxygen contamination these steps were executed in an argon-filled glovebox. Samples above 80 at.% V were, additionally, molten in an arc furnace under low current with a non-consumable tungsten electrode in an argon atmosphere. After sealing the samples in evacuated silica ampoules, they were checked for tightness and subjected to heat treatments in muffle furnaces. As small heat gradients were inevitable, which cause sample segregation to emerge, the sample ampoules were placed in custom-build closed containers to even out the temperature gradient. After the heat treatment, the samples were quenched in cold water. Refer to the supplementary materials section for all prepared sample compositions and annealing procedures.

In order to prepare misfit layer compounds, that are eventually present in ternary system Pb-Se-V, dried NH_4Cl [121, 122] was added to several samples. These transporting agents act as a crystallisation aid and facilitate low-temperature or slow crystallization processes. For this purpose anhydrous NH_4Cl prepared by drying NH_4Cl for 4 hours at 160 °C in a dynamic vacuum and then stored in an argon-filled glovebox. The procedure of sample treatment described above was retained unchanged, apart from the addition of less than 1 wt.% (regarding the whole sample mass) of the prepared NH_4Cl.

For the purpose of gaining knowledge about the morphology and in order to not miss out on any phases (e.g. misfit layer compounds tended to nucleate on the silica surface) all samples and sample ampoules were carefully checked under a stereomicroscope. For further sample characterisation powder X-ray diffraction (PXRD) and scanning electron microscopy (SEM) were employed. The chemical composition was determined by electron probe microanalysis performed on a Zeiss Supra 55 VP scanning electron microscope. It was operated at an acceleration voltage of 20 kV. Employing energy dispersive X-ray analysis (EDX), pure cobalt was used for the energy calibration of the EDX signal. The samples were either investigated “as is”, at the disadvantage of uneven surfaces, or embedded in a carbonised phenolic hot mounting resin for SEM preparation. As the sintered powders, as well as the large crystals growing from them in some cases, tended to be brittle, all samples were soaked in with several layers of epoxy resin for further stabilisation during grinding (SiC abrasive paper grits 500 to 4000). PXRD was done by a Bruker D8 diffractometer in Bragg-Brentano pseudo-focussing geometry (Cu-K_α radiation, variable slit, $10° < 2\theta < 120°$ in steps of 0.01°, silicon strip detector). The analysis of the obtained powder patterns was conducted by the Rietveld refinement technique with the software program Topas4 [160] or Jana2006 [161].

In order to determine the phase reactions involving the liquid phase, some selected samples were investigated by DTA measurements. These DTA measurements were performed on a Netzsch DTA 404 S (NETZSCH, Germany) at an applied heating rate of 5 K/min and a constant Argon flow of 20 mL/min. The thermocouples were standardised at the melting points of high purity Tin, Antimony, and Copper. The sample masses were ranging between 80 and 115 mg. After sealing the samples in special evacuated (~10^{-3} mbar) silica crucibles, the samples were re-equilibrated in those containers.

The non-invariant and invariant reactions were evaluated by the method of the extrapolated onset [162]. The peak temperature of the last thermal event on heating was selected for the liquidus temperature, which may result in slightly overestimated liquidus temperatures, but yields more reliable values than those of the first onset on cooling in the present study. As evaporation and re-condensation of the volatile components was observed, the temperature program usually included only one heating/cooling cycle.

5.8. Results and discussion

21 binary samples were prepared in order to determine the vanadium-content in the lead-rich liquid of the Pb-V binary system at different temperatures. A total of 97 ternary Pb-Se-V samples were prepared and investigated for the construction of the six isothermal sections (375 °C, 550 °C, 700 °C, 800 °C, 1000 °C, and 1100 °C). 31 additional samples were prepared at differing temperatures, compositions, and crystallisation agents in order to yield potentially present misfit layered compounds.

5.8.1. Binary Pb-V

In all prepared binary samples only lead and vanadium were observed. No traces of the intermetallic phase of PbV_3 were detected. This indicates that no impurities such as carbon or oxygen, which could stabilise PbV_3 [186], are present in the binary samples. Furthermore, no traces of Pb_3V, which was suggested theoretically by Wang [187], could be observed.

Measuring the composition of the liquid was challenging. Besides small grains of vanadium in a lead-matrix, which is the expected result of such a quenched liquid, large crystals of vanadium were observed to be present in the matrix (refer to Figure 22). Those vanadium pieces have diameters greater than 20 µm and are supposedly the pristine vanadium powder utilised during sample preparation. As this pristine powder is distributed throughout the whole sample and, apart from its crystal size, indistinguishable from the precipitated vanadium in the lead-rich matrix, all

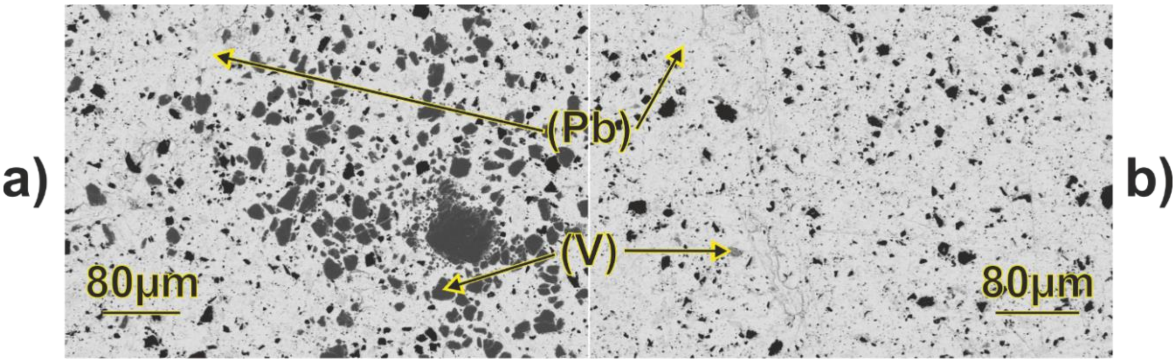

Figure 22: Differences in particle size of vanadium-pieces in lead-matrix (sample: PbV-16); large particle sizes (a) originate from weighed-out powder and small particle sizes presumably precipice from the lead-rich liquid (b).

attempts of measuring the liquid composition are not only aggravated, but the results are more volatile too. In order to overcome these difficulties in future investigations a procedure including high-temperature centrifugation, as it was executed in the Bi-Mn binary system by Marker et al [189], is suggested for more reliable results. The measured results indicate that the vanadium contents in the lead-rich liquid are below 1.3 at.% V at temperatures up to 1100 °C (refer to sample PbV-21). This result is consistent with the initial working hypothesis, that the solubility of the liquid is limited similar to the binary system of Bi-V. This finding is sufficient for extrapolating the liquid solubility in the ternary Pb-Se-V system and assessing the observed measurement values

5.8.2. Ternary isothermal sections

The sample preparation in the ternary system Pb-Se-V is challenging due to the different properties of the three elements. Different approaches (e.g. powders, arc melting) were employed in order to obtain well-equilibrated samples (refer to Figure 23 and Figure 24 for typical sample microstructures).

To construct the isothermal sections at 375 °C, 550 °C, 700 °C, 800 °C, 1000 °C, and 1100 °C, all results of PXRD and SEM were combined (refer to Figure 25 to Figure 30, Table 12 and Table 13). Additional DTA experiments were employed to address problems during the phase diagram construction. Detailed results of PXRD and the mean composition values for the phases determined by EPMA are given in the supplementary data section for all prepared samples.

The binary phase diagrams served as a starting point for investigations. The construction of the isothermal sections and solidification scheme was executed in an iterative manner. In the case of contradictions between samples, an overall picture of several isothermal sections was gathered for higher reliability in the process of sample assessment.

The assessment of the raw data is critical as there are still many open questions in the three binary systems, such as the thermal stability of the phases in the central part of the Se-V phase diagram, the liquidus behaviour in those systems, or the influence of the gas phase, which is certainly involved in the selenium-rich part at higher temperatures. However, we performed our experiments under own vapour pressure; hence, no phase reactions with the gas phase were observed.

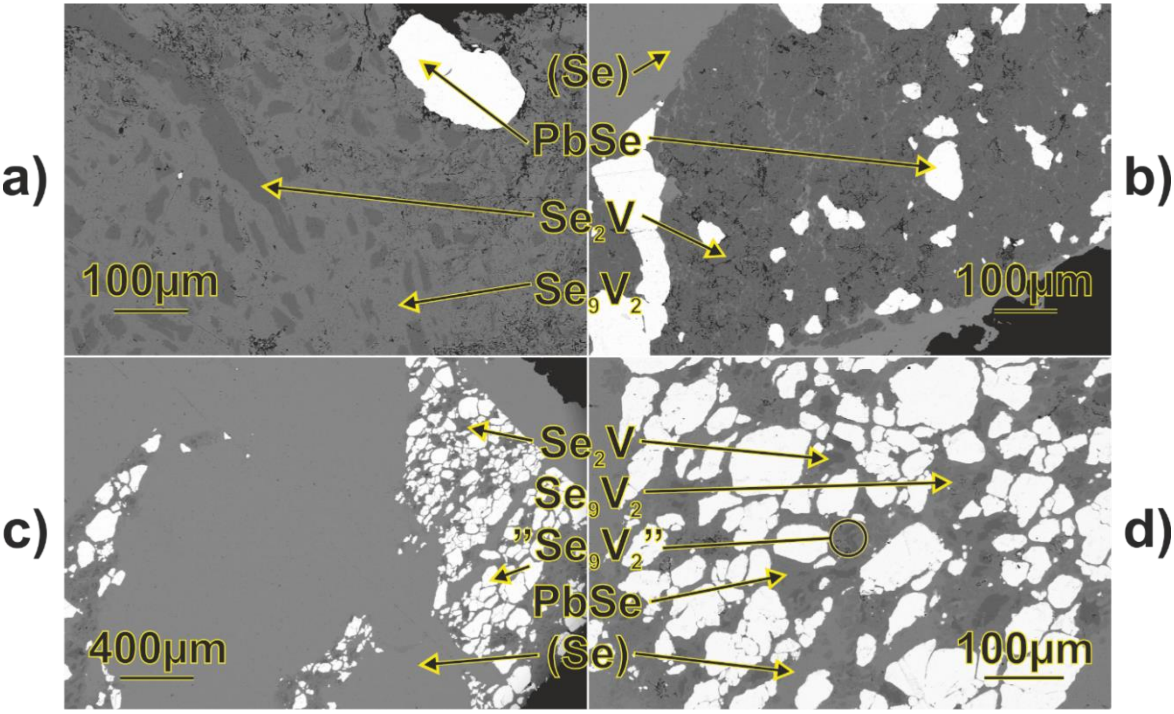

Figure 23: Typical annealed samples in the selenium-rich corner; samples PbSeV-10 (a), PbSeV-15 (b), and PbSeV-12 (c, d) are annealed at 375 °C, 450 °C, and 375 °C, respectively; an equilibrium with the liquid or consequent quenching rates resulted in decomposition of the Se_9V_2 phase into new liquid (binary catatectic reaction) in the former solid grains of Se_9V_2 and Se_2V (c, d).

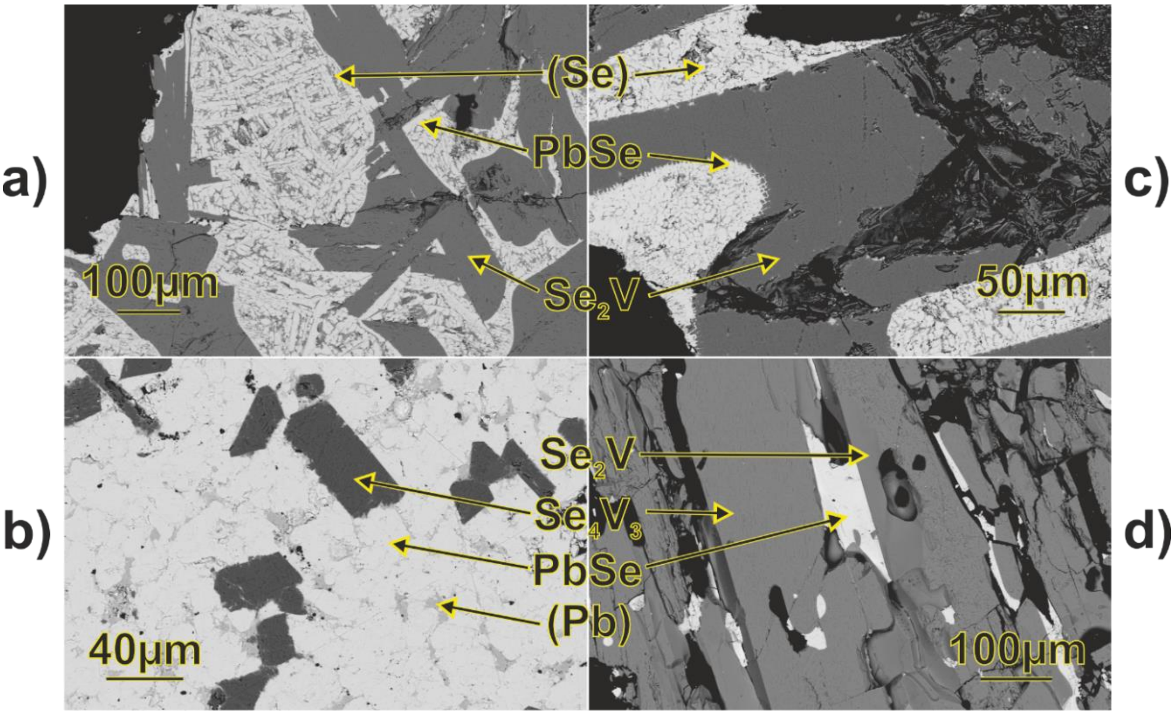

Figure 24: Typical annealed samples; samples PbSeV-81 (a), PbSeV-83 (b), PbSeV-96 (c), and PbSeV-90 (d) are annealed at 1000 °C, 1000 °C, 1100 °C, and 1100 °C, respectively.

Table 12: Assessed measurement data of several selected samples in the text; the samples annealing temperature and nominal composition (in at.% V, Se, and Pb) are visible in the first column; the assessed mean values of EMPA-results for each phase is listed for the equilibrium phases, similar as the corresponding lattice parameters and space groups in PXRD; abbreviated comments describe the phase quantity (main phase (M) or traces (T)), the phase quality (impurity stabilisation (I), liquid(L), not quenchable Se_2V or Se_4V_3 (Q), amorphous selenium (A), and Se_2V sublattice of MLC (MLC)), and the type of detection (area scan (A) or point scan (all others)).

Sample	Phase (EPMA)	Cmt.	V (at%)	Se (at%)	Pb (at%)	Phase (PXRD)	Cmt.	Space group	*a*	*b*	*c*	*β*
PbSeV-1	V	M	99.9(1)	0.03(9)	0.14(9)	V	M	Im-3m	2.991	2.991	2.991	90
80.1/9.9/9.9	SeV	M	51(1)	48.5(9)	0.5(3)	SeV mP19	I	C2	6.470	3.711	6.007	90.38
As Cast	Pb	M	4(2)	0.1(2)	96(3)	Pb	M	Fm-3m	4.949	4.949	4.949	90
PbSeV-8	-	-	-	-	-	Se4V3	M	C12/m1	13.224	3.467	6.198	116.54
30/60/10	Se2V	M	33.7(6)	66.3(6)	0.04(4)	Se2V	M	P-3m1	3.360	3.360	6.103	90
375°C	PbSe	M	0.2(2)	49.4(3)	50.3(2)	PbSe	M	Fm-3m	6.126	6.126	6.126	90
PbSeV-10	Se9V2	M	18.1(4)	81.8(4)	0.04(4)	Se9V2	M	C12/c1	10.588	12.414	8.123	94.94
20/75/5	Se2V	M	34(4)	66(3)	0.02(3)	Se2V	M	P-3m1	3.356	3.356	6.107	90
375°C	PbSe	M	0.2(2)	49.3(3)	50.6(2)	PbSe	M	Fm-3m	6.126	6.126	6.126	90
PbSeV-12	Se9V2	M	18.2(2)	81.7(2)	0.09(4)	Se9V2	M	C12/c1	10.591	12.410	8.121	94.91
5/90.1/5	L1	M/L	0.09(7)	99.9(1)	0.06(5)	Se	M/A	P3121	4.345	4.345	5.483	90
375°C	PbSe	M	0.1(1)	49.8(3)	50(3)	PbSe	M	Fm-3m	6.127	6.127	6.127	90
PbSeV-15	Se2V	M	33.3(7)	66.7(7)	0.01(2)	Se2V	M	P-3m1	3.355	3.355	6.109	90
20/75/5	L1	A/L	15(3)	85(3)	0.04(4)	Se	M/A	P3121	4.438	4.438	5.200	90
450°C	PbSe	M	0.2(1)	49.9(3)	49.9(3)	PbSe	M	Fm-3m	6.127	6.127	6.127	90
PbSeV-22	Se4V3	M	44.365(7)	54.72(5)	0.93(4)	Se4V3	M	C12/m1	13.347	3.503	6.227	116.62
33.3/33.3/33.3	L2	M/L	0.4(2)	0.03(8)	99.6(1)	Pb	M	Fm-3m	4.951	4.951	4.951	90
550°C	-	-	-	-	-	-	-	-	-	-	-	-
PbSeV-23	Se8V5	M	38.8(2)	61.1(3)	0.12(4)	Se8V5	M	C12/m1	11.828	6.997	8.315	134.11
31/59/10	Se2V	M	36.405(7)	63.505(7)	0.085(7)	Se2V	M	P-3m1	3.423	3.423	5.986	90
550°C	PbSe	M	0.2(2)	49.5(5)	50.3(4)	PbSe	M	Fm-3m	6.127	6.127	6.127	90
PbSeV-25	Se8V5	M	39.2(6)	60.6(6)	0.2(2)	Se8V5	M	C12/m1	11.827	6.998	8.317	134.12
30/60/10	Se2V	M	36.1(1)	63.9(1)	0.05(2)	Se2V	M	P-3m1	3.413	3.413	6.003	90
550°C	PbSe	M	0.2(3)	49.4(2)	50.3(1)	PbSe	M	Fm-3m	6.126	6.126	6.126	90
PbSeV-38	Se4V3	M	37(3)	62.9(3)	0.09(7)	Se4V3	M	C12/m1	13.330	3.437	5.953	116.53
30/60/10	PbSe	M	0.4(4)	49.1(2)	50.6(4)	PbSe	M	Fm-3m	6.127	6.127	6.127	90
700°C	Se2V	T	36(0)	64(0)	0(0)	-	-	-	-	-	-	-
PbSeV-50	Se2V	M	33.9(4)	66(4)	0.06(5)	Se2V	M	P-3m1	3.364	3.364	6.093	90
39/51.1/10	PbSe	M	0.3(4)	49.5(2)	50.2(4)	PbSe	M	Fm-3m	6.127	6.127	6.127	90
800°C	L3	A/L	5(1)	69(3)	26(3)	-	-	-	-	-	-	-
PbSeV-58	Se4V3	M	37.9(6)	62(5)	0.09(9)	Se4V3	M	C12/m1	13.247	3.446	6.014	116.47
31/59/10	Se2V	M	37.1(3)	62.8(2)	0.06(4)	-	-	-	-	-	-	-
800°C	PbSe	M	0.2(1)	49.3(2)	50.5(1)	PbSe	M	Fm-3m	6.126	6.126	6.126	90
PbSeV-70	V	M	99.96(3)	0(0)	0.04(3)	V	M	Im-3m	2.989	2.989	2.989	90
80.1/9.9/9.9	Se4V5	I	55.7(6)	44.1(5)	0.3(2)	Se4V5	I	I4/m	9.293	9.293	3.411	90
1000°C	L2	M/L	5(2)	0(0)	95(2)	Pb	M	Fm-3m	4.950	4.950	4.950	90
PbSeV-77	SeV	M	46.5(3)	52.1(8)	1.4(7)	SeV hP4	M	P63/mmc	3.601	3.601	5.989	90
33.3/33.3/33.4	L2	A/L	0.6(5)	11(5)	89(5)	Pb	M	Fm-3m	4.950	4.950	4.950	90
1000°C	-	-	-	-	-	Se4V3	T	C12/m1	13.247	3.463	6.204	116.19
PbSeV-81	Se2V	M	37.9(2)	62(2)	0.1(5)	Se8V5	M/Q	C12/m1	11.868	6.925	8.395	134.69
29/61/10	-	-	-	-	-	Se4V3	M	C12/m1	13.253	3.444	6.014	116.48
1000°C	PbSe in L	M/L	1(1)	49.7(8)	49(2)	PbSe	M	Fm-3m	6.127	6.127	6.127	90
PbSeV-83	Se4V3	M	42.9(5)	56.6(4)	0.5(7)	Se4V3	M	C12/m1	13.245	3.464	6.207	116.16
10.1/40.1/49.8	PbSe	M	0.5(3)	49.4(2)	50.1(3)	PbSe	M	Fm-3m	6.123	6.123	6.123	90
1000°C	L2	A/L	1.4(2)	44.7(5)	53.9(4)	Pb	M	Fm-3m	4.952	4.952	4.952	90
PbSeV-90	Se4V3	M	43(4)	56.9(4)	0.06(1)	Se4V3	M	C12/m1	13.226	3.448	6.184	116.20

35/55/10	Se2V	M	40.9(3)	59(3)	0.09(2)	-	-	-	-	-	-	-
1100°C	L	M/L	3(2)	49.6(3)	47(2)	PbSe	M	Fm-3m	6.125	6.125	6.125	90
PbSeV-92	Se2V	M	39.5(3)	60.4(3)	0.06(4)	Se8V5	M/Q	C12/m1	11.829	6.996	8.378	134.32
31/59/10	-	-	-	-	-	Se4V3	M/Q	C12/m1	13.250	3.445	6.176	117.25
1100°C	L	A/L	5.6(8)	55.4(5)	39(1)	PbSe	M	Fm-3m	6.127	6.127	6.127	90
PbSeV-96	-	-	-	-	-	Se8V5	M/Q	C12/m1	11.825	7.004	8.314	134.07
19.9/60/20.1	Se2V	M	37.8(6)	61.4(5)	0.8(4)	Se2V	T	P-3m1	3.430	3.430	5.984	90
1100°C	L	A/L	7(1)	60(2)	34(2)	PbSe	M	Fm-3m	6.126	6.126	6.126	90
PbV-21	V	M	99(0)	0(0)	1(0)	V	T	Im-3m	2.988	2.988	2.988	90
11/0/89	L	A/L	1(1)	0(0)	99(1)	Pb	M	Fm-3m	4.951	4.951	4.951	90
1100°C	-	-	-	-	-	-	-	-	-	-	-	-
PbSeV-T-6	Se8V5	M	39(7)	60.9(7)	0.1(2)	Se8V5	M	C12/m1	11.828	6.998	8.315	134.10
32/58/10	PbSe	M	0.6(5)	49.2(3)	50.2(3)	Se2V	MLC	P-3m1	3.417	3.417	5.996	90
550°C	MLC	M	20.8(3)	56.6(2)	22.6(2)	PbSe	M	Fm-3m	6.128	6.128	6.128	90
PbSeV-T-31	Se8V5	M	38.8(6)	60.9(6)	0.3(2)	Se8V5	M	C12/m1	11.823	7.003	8.312	134.05
32/58/10	PbSe	M	0.2(2)	49.4(2)	50.3(2)	PbSe	M	Fm-3m	6.124	6.124	6.124	90
550°C	MLC	M	20.6(5)	56.4(4)	23(4)	-	-	-	-	-	-	-

Lead and selenium are liquid in all investigated samples. Pure lead, which was part of the lead-rich liquid, always exhibited similar lattice parameters around 4.95 Å in PXRD (refer to Table 12 and Table 13). Selenium, on the contrary, was observed to be amorphous in PXRD and, hence, is not refinable at all or the resulting refined lattice parameters deviate significantly. As expected, PXRD results indicate that changes of lattice parameters in this system are less influenced by an alteration of temperature (e.g. PbSe) than by a change of phase composition (e.g. Se_4V_3).

Attempts were made to construct an isothermal section at 375 °C. However, multiple samples, especially those at vanadium contents higher than 30 at.%, were not well equilibrated. This can be explained by sluggish reaction rates in samples, which are not in equilibrium with the liquid phase (e.g. the Se_8V_5 phase is missing in the samples PbSeV-8 and PbSeV-23). Only the phase equilibria $L_1 + Se_9V_2 + PbSe$ and $Se_2V + Se_9V_2 + PbSe$ were determined successfully (refer to Figure 25 and Figure 23a). Se_9V_2 is not stabilised to higher temperatures by the introduction of lead in the crystal lattice (refer to Figure 23b), as it is expected for such low solubilities. Interestingly, this phase partially decomposed in one sample (refer to sample PbSeV-12 and Figure 23c/d) during quenching, which can be attributed to the rare catatectic type reaction around 250 and 280 °C in the binary system of Se-V.

The isothermal sections at 550 °C and 700 °C provide a similar picture regarding the solid solubilities of the binary phas es into the ternary and their phase equilibria (refer to Figure 26 and Figure 27). Apart from the liquid, the solubility of the binary

Table 13: Assessed measurement data of samples used in the isothermal sections; the samples annealing temperature and nominal composition (in at.% V, Se, and Pb) are visible in the first column; the assessed mean values of EMPA-results for each phase is listed for the equilibrium phases, similar as the corresponding lattice parameters and space groups in PXRD; abbreviated comments describe the phase quantity (main phase (M) or traces (T)), the phase quality (impurity stabilisation (I), liquid(L), not quenchable Se$_2$V or Se$_4$V$_3$ (Q), amorphous selenium (A), and Se$_2$V sublattice of MLC (MLC)), and the type of detection (area Scan (A) or point scan (all others)).

Sample	Phase (EPMA)	Cmt.	V (at%)	Se (at%)	Pb (at%)	Phase (PXRD)	Cmt.	Space group	*a*	*b*	*c*	*β*
PbSeV-10	Se9V2	M	18.1(4)	81.8(4)	0.04(4)	Se9V2	M	C12/c1	10.588	12.414	8.123	94.94
20/75/5	Se2V	M	34(4)	66(3)	0.02(3)	Se2V	M	P-3m1	3.356	3.356	6.107	90
375°C	PbSe	M	0.2(2)	49.3(3)	50.6(2)	PbSe	M	Fm-3m	6.126	6.126	6.126	90
PbSeV-12	Se9V2	M	18.2(2)	81.7(2)	0.09(4)	Se9V2	M	C12/c1	10.591	12.410	8.121	94.91
5/90.1/5	L1	M/L	0.09(7)	99.9(1)	0.06(5)	Se	M/A	P3121	4.345	4.345	5.483	90
375°C	PbSe	M	0.1(1)	49.8(3)	50(3)	PbSe	M	Fm-3m	6.127	6.127	6.127	90
PbSeV-17	V	M	99.9(1)	0(0)	0.1(1)	V	M	Im-3m	2.992	2.992	2.992	90
48.2/41.8/10	SeV	M	49(9)	50(1)	0.5(4)	SeV hP4	M	P63/mmc	3.688	3.688	5.990	90
550°C	L2	M/L	1.1(3)	0.1(3)	99.3(8)	Pb	M	Fm-3m	4.949	4.949	4.949	90
PbSeV-22	Se4V3	M	44.365(7)	54.72(5)	0.93(4)	Se4V3	M	C12/m1	13.347	3.503	6.227	116.62
33.3/33.3/33.3	L2	M/L	0.4(2)	0.03(8)	99.6(1)	Pb	M	Fm-3m	4.951	4.951	4.951	90
550°C	-	-	-	-	-	-	-	-	-	-	-	-
PbSeV-25	Se8V5	M	39.2(6)	60.6(6)	0.2(2)	Se8V5	M	C12/m1	11.827	6.998	8.317	134.12
30/60/10	Se2V	M	36.1(1)	63.9(1)	0.05(2)	Se2V	M	P-3m1	3.413	3.413	6.003	90
550°C	PbSe	M	0.2(3)	49.4(2)	50.3(1)	PbSe	M	Fm-3m	6.126	6.126	6.126	90
PbSeV-27	Se2V	M	34(2)	66(2)	0.04(2)	Se2V	M	P-3m1	3.356	3.356	6.108	90
20/75/5	L1	M/L	2(1)	98(1)	0.05(5)	Se	M/A	P3121	4.440	4.440	5.183	90
550°C	PbSe	M	0.2(2)	49.8(2)	50(3)	PbSe	M	Fm-3m	6.126	6.126	6.126	90
PbSeV-29	Se4V3	M	40(2)	59(3)	1.3(6)	Se4V3	M	C12/m1	13.229	3.464	6.209	116.19
10/40/50	PbSe	M	0.3(2)	49(4)	50.8(3)	PbSe	M	Fm-3m	6.127	6.127	6.127	90
550°C	L2	M/L	0.5(3)	1(1)	98(2)	Pb	M	Fm-3m	4.951	4.951	4.951	90
PbSeV-31	V	M	99.7(3)	0.02(4)	0.3(3)	V	M	Im-3m	2.989	2.989	2.989	90
47.7/42.3/10	SeV	M	49(1)	49.9(9)	0.8(5)	SeV hP4	M	P63/mmc	3.716	3.716	6.001	90
700°C	L2	M/L	0.8(2)	0(0)	99.2(2)	Pb	M	Fm-3m	4.951	4.951	4.951	90
PbSeV-36	SeV	M	47(1)	51(1)	1.4(6)	SeV hP4	M	P63/mmc	3.608	3.608	5.930	90
33.3/33.3/33.4	Se4V3	T	46.7(2)	52.4(2)	0.89(9)	Se4V3	M	C12/m1	13.456	3.579	6.252	117.12
700°C	L2	M/L	0.4(3)	0(0)	99.6(3)	Pb	M	Fm-3m	4.950	4.950	4.950	90
PbSeV-38	Se4V3	M	37(3)	62.9(3)	0.09(7)	Se4V3	M	C12/m1	13.330	3.437	5.953	116.53
30/60/10	PbSe	M	0.4(4)	49.1(2)	50.6(4)	PbSe	M	Fm-3m	6.127	6.127	6.127	90
700°C	Se2V	T	36(0)	64(0)	0(0)	-	-	-	-	-	-	-
PbSeV-39	Se4V3	M	44(1)	55(1)	0.7(5)	Se4V3	M	C12/m1	13.231	3.463	6.207	116.21
30/40/30.1	PbSe	M	0.2(2)	48.8(4)	51(3)	PbSe	M	Fm-3m	6.126	6.126	6.126	90
700°C	L2	M/L	0.68(7)	0(0)	99.33(7)	Pb	M	Fm-3m	4.951	4.951	4.951	90
PbSeV-41	Se2V	M	34(2)	66(2)	0.03(3)	Se2V	M	P-3m1	3.357	3.357	6.106	90
20/75/5	L1	M/L	0.6(4)	94(1)	5.6(6)	Se	M/A	P3121	4.336	4.336	5.267	90
700°C	L3	A/L	3(1)	75(6)	21(5)	PbSe	M	Fm-3m	6.126	6.126	6.126	90
PbSeV-42	Se2V	M	33.6(4)	66.3(4)	0.05(3)	Se2V	M	P-3m1	3.358	3.358	6.104	90
19.9/60/20.1	PbSe	M	0.7(2)	49.4(2)	49.9(2)	PbSe	M	Fm-3m	6.126	6.126	6.126	90
700°C	-	-	-	-	-	-	-	-	-	-	-	-
PbSeV-49	V	M	99.7(1)	0(0)	0.3(1)	V	T	Im-3m	2.986	2.986	2.986	90
40.5/24.7/34.7	SeV	M	48(2)	50(1)	1.6(9)	SeV hP4	M	P63/mmc	3.710	3.710	5.998	90
800°C	L2	M/L	0.2(2)	0(0)	99.8(2)	Pb	M	Fm-3m	4.949	4.949	4.949	90
PbSeV-56	SeV	M	46.5(4)	52.5(3)	0.9(1)	SeV hP4	M	P63/mmc	3.590	3.590	5.997	90
33.3/33.3/33.3	Se4V3	M	46.2(2)	53.21(3)	0.6(2)	Se4V3	M	C12/m1	13.447	3.574	6.254	117.11
800°C	L2	A/L	1(9)	2(1)	97(2)	Pb	M	Fm-3m	4.951	4.951	4.951	90
PbSeV-58	Se4V3	M	37.9(6)	62(5)	0.09(9)	Se4V3	M	C12/m1	13.247	3.446	6.014	116.47
31/59/10	Se2V	M	37.1(3)	62.8(2)	0.06(4)	-	-	-	-	-	-	-
800°C	PbSe	M	0.2(1)	49.3(2)	50.5(1)	PbSe	M	Fm-3m	6.126	6.126	6.126	90

PbSeV-65	Se4V3	M	44(1)	56(1)	0.5(4)	Se4V3	M	C12/m1	13.247	3.459	6.210	116.20
10.3/30.1/59.7	PbSe	M	0.2(2)	48.7(1)	51.1(2)	PbSe	M	Fm-3m	6.125	6.125	6.125	90
800°C	L2	M/L	0(0)	0(0)	100(0)	Pb	M	Fm-3m	4.947	4.947	4.947	90
PbSeV-66	Se2V	M	34(1)	65.3(4)	0.4(8)	Se2V	M	P-3m1	3.356	3.356	6.108	90
10/65.2/24.8	PbSe in L	M/L	0.3(2)	49.3(4)	50.4(4)	PbSe	M	Fm-3m	6.127	6.127	6.127	90
800°C	L3	A/L	4.2(5)	66(2)	29(2)	-	-	-	-	-	-	-
PbSeV-73	V in L	T/L	99.7(2)	0.05(4)	0.2(2)	V	M	Im-3m	2.986	2.986	2.986	90
40.4/24.7/34.9	SeV	M	48.7(3)	49.9(3)	1.4(3)	SeV hP4	M	P63/mmc	3.683	3.683	5.989	90
1000°C	L2	A/L	4(3)	1(2)	95(5)	Pb	M	Fm-3m	4.950	4.950	4.950	90
PbSeV-77	SeV	M	46.5(3)	52.1(8)	1.4(7)	SeV hP4	M	P63/mmc	3.601	3.601	5.989	90
33.3/33.3/33.4	L2	A/L	0.6(5)	11(5)	89(5)	Pb	M	Fm-3m	4.950	4.950	4.950	90
1000°C	-	-	-	-	-	Se4V3	T	C12/m1	13.247	3.463	6.204	116.19
PbSeV-78	Se2V	M	38.9(3)	61.1(3)	0.07(3)	Se8V5	M/Q	C12/m1	11.824	7.006	8.313	134.06
31/59/9.9	PbSe in L	M/L	0.9(7)	49.4(4)	49.7(6)	PbSe	M	Fm-3m	6.127	6.127	6.127	90
1000°C	L1	A/L	6(2)	57(5)	36(6)	-	-	-	-	-	-	-
PbSeV-80	Se4V3	M	43.9(5)	55.7(5)	0.3(2)	Se4V3	M	C12/m1	13.271	3.476	6.208	116.25
29.9/39.9/30.1	PbSe	M	0.7(2)	48.5(4)	50.8(4)	PbSe	M	Fm-3m	6.126	6.126	6.126	90
1000°C	L2	A/L	1.4(4)	37(6)	61(6)	Pb	M	Fm-3m	4.951	4.951	4.951	90
PbSeV-82	Se4V3	M	39.1(7)	60.04(3)	0.8(7)	Se8V5	M	C12/m1	11.866	6.960	8.329	134.42
20/60/20	Se2V	M	38.2(3)	61.3(5)	0.4(1)	Se2V	M	P-3m1	3.459	3.459	5.927	90
1000°C	PbSe	M/L	0.5(4)	49.2(4)	50.2(2)	PbSe	M	Fm-3m	6.127	6.127	6.127	90
PbSeV-86	Se4V3	M	44.2(4)	54.9(4)	0.9(2)	Se4V3	M	C12/m1	13.315	3.493	6.214	116.40
41/49/9.9	SeV	M	44.9(8)	53.7(3)	1.4(4)	PbSe	M	Fm-3m	6.125	6.125	6.125	90
1100°C	L	M/L	3(1)	2(2)	95(3)	Pb	M	Fm-3m	4.951	4.951	4.951	90
PbSeV-87	V	M	99.7(2)	0.07(7)	0.3(2)	V	M	Im-3m	2.988	2.988	2.988	90
40.1/24.8/35.1	SeV	M	48.8(4)	49.9(7)	1.3(6)	SeV hP4	M	P63/mmc	3.676	3.676	5.988	90
1100°C	L	M/L	0.3(1)	0(0)	99.7(1)	Pb	M	Fm-3m	4.951	4.951	4.951	90
PbSeV-90	Se4V3	M	43(4)	56.9(4)	0.06(1)	Se4V3	M	C12/m1	13.226	3.448	6.184	116.20
35/55/10	Se2V	M	40.9(3)	59(3)	0.09(2)	-	-	-	-	-	-	-
1100°C	L	M/L	3(2)	49.6(3)	47(2)	PbSe	M	Fm-3m	6.125	6.125	6.125	90
PbV-16	V	M	99.7(2)	0(0)	0.3(2)	-	-	-	-	-	-	-
9.8/0/90.2	L2	A/L	0.8(6)	0(0)	99.2(6)	Pb	M	Fm-3m	4.951	4.951	4.951	90
550°C	-	-	-	-	-	-	-	-	-	-	-	-
PbV-17	V	M/I	98.4(8)	0(0)	1.6(8)	V	T	Im-3m	3.043	3.043	3.043	90
10.3/0/89.7	L2	A/L	0.3(4)	0(0)	99.7(4)	Pb	M	Fm-3m	4.951	4.951	4.951	90
700°C	-	-	-	-	-	-	-	-	-	-	-	-
PbV-18	V	M	98(1)	0(0)	2(1)	-	-	-	-	-	-	-
10/0/90	L2	A/L	0.6(4)	0(0)	99.4(4)	Pb	M	Fm-3m	4.951	4.951	4.951	90
800°C	-	-	-	-	-	-	-	-	-	-	-	-
PbV-19	V	M	99.5(3)	0(0)	0.6(3)	V	T	Im-3m	2.989	2.989	2.989	90
10.1/0/89.9	L2	A/L	0.6(5)	0(0)	99.4(5)	Pb	M	Fm-3m	4.951	4.951	4.951	90
900°C	-	-	-	-	-	-	-	-	-	-	-	-
PbV-20	V	M	99.7(3)	0(0)	0.3(3)	V	T	Im-3m	2.988	2.988	2.988	90
9.5/0/90.5	L2	A/L	0.9(3)	0(0)	99.1(3)	Pb	M	Fm-3m	4.951	4.951	4.951	90
1000°C	-	-	-	-	-	-	-	-	-	-	-	-
PbV-21	V	M	99(0)	0(0)	1(0)	V	T	Im-3m	2.988	2.988	2.988	90
11/0/89	L	A/L	1(1)	0(0)	99(1)	Pb	M	Fm-3m	4.951	4.951	4.951	90
1100°C	-	-	-	-	-	-	-	-	-	-	-	-

phases into the ternary were observed to be small. SeV exhibits the largest solubility with 1.4 at.% of Pb (refer to sample PbSeV-22). In the selenium-rich corner, the selenium-rich liquid is in equilibrium with the intermetallic phases of PbSe and Se_2V. The DTA results of sample PbSeV-12 show three invariant reactions in the ternary at 217.2 °C, 417.6 °C, and 697.2 °C, respectively. The first is very close to the binary eutectic temperature (~217 °C [130]) and either a degenerate U-type reaction (L_1 + PbSe → Se + Se_2V) or a degenerate eutectic reaction (Se + Se_2V + PbSe → L_1). The second is a peritectic reaction (L_1 + Se_2V + PbSe → Se_9V_2). The last is a U-type reaction (L_3 + Se_2V → L_1 + PbSe). This temperature is very close to the isothermal section at 700 °C and explains the difficulties in determining the phase-field L_3 + Se_2V + PbSe in this section.

The adjacent phases of Se_2V, Se_8V_5, and Se_4V_3 form three-phase equilibria with each vicinal phase and PbSe. Se_4V_3 again is in equilibrium with the lead-rich liquid and PbSe as well as its vicinal phase SeV and the lead-rich liquid. The intermetallic phase of Se_4V_5 was found in some ternary samples. It is assumed to be impurity stabilised [130]. Therefore, in the vanadium-rich part only the three-phase field of vanadium, SeV and the lead-rich liquid is present in the vanadium-rich part (refer to Figure 32a). This single three-phase equilibrium is further supported by the facts that samples containing the Se_4V_5 phase consistently exhibit forbidden four-phase equilibria (V + SeV + L_2 + Se_4V_5, refer to Figure 32b), that Se_4V_5 is only detectable

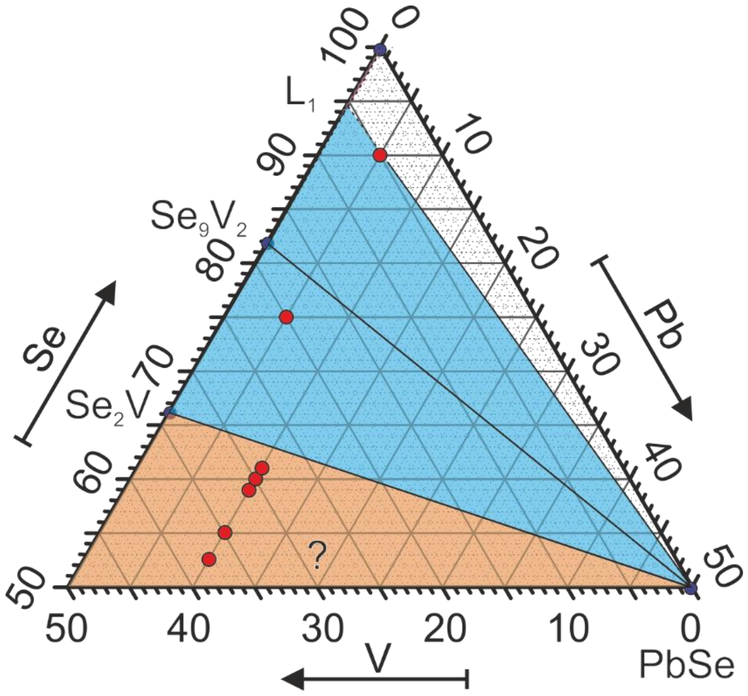

Figure 25: Partial isothermal section at 375 °C; blue triangles reflect the three-phase-fields; samples PbSeV-10, and PbSeV-12 are used for the construction of the three-phase-equilibria; three-phase-equilibria and single-phase fields with uncertainty are indicated by dashed lines; nominal sample locations and selected EPMA results are indicated by red and blue dots, respectively.

in traces in PXRD, and that the lead atom is generally too large to stabilise an impurity stabilised phase by itself (e.g. similar to the Sb-Se-V system [130]).

Several samples above 80 at.% vanadium content were molten in arc-furnace prior to the annealing procedure (refer to Figure 32c). These samples suffered severe mass losses of more than 20 wt.%, inhomogeneity, and some oxidation on the visible surface, despite careful treatment. Those samples exhibited the three-phase equilibrium V + Se_4V_5 + L (refer to Figure 32d) and/or a slight monoclinic distortion

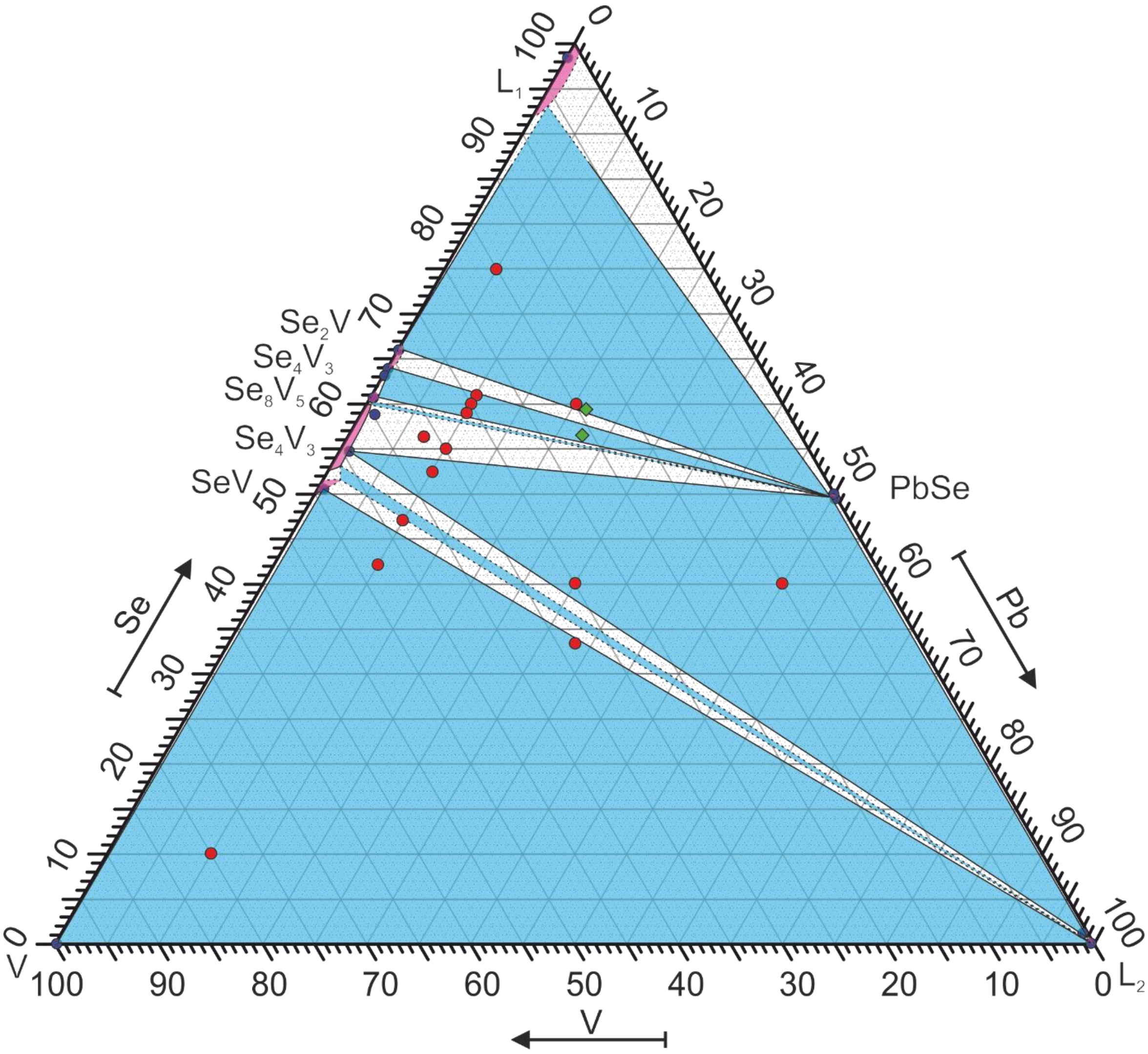

Figure 26: Isothermal section at 550 °C; blue triangles reflect the three-phase-fields; samples PbSeV-17, PbSeV-22, PbSeV-25, PbSeV-27, and PbSeV-29 are used for the construction of the three-phase-equilibria; three-phase-equilibria and single-phase fields with an uncertainty are indicated by dashed lines; nominal sample locations and selected EPMA results are indicated by red and blue dots, respectively; possible locations for the MLC in this system are marked by green squares.

of SeV (refer to PbSeV-1 in Table 12). However, due to the problems in sample preparation, we refrained from including those samples in our final phase diagram.

We observed the Se_8V_5 phase in numerous samples (e.g. PbSeV-81, PbSeV-92) between 550 °C and 1100 °C. This issue contradicts previous experimental investigations and assessments of the binary Se-V system to some extent, which is of relevance for the isothermal sections at 800 °C, 1000 °C, and 1100 °C. The observation of the Se_8V_5 at elevated temperatures requires more detailed discussion, as the contradiction to the assessed phase diagram appears only at first glance.

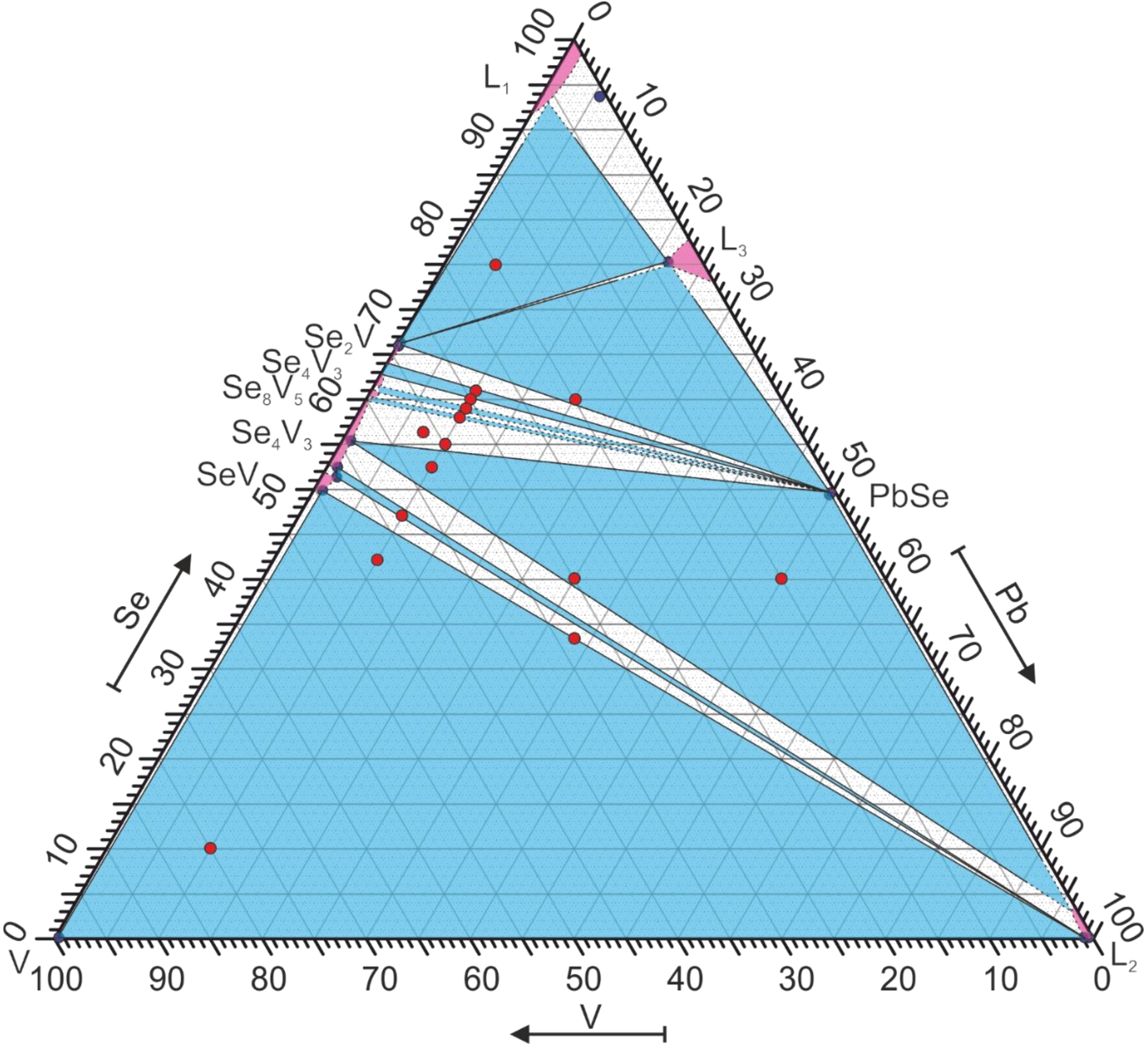

Figure 27: Isothermal section at 700 °C; blue triangles reflect the three-phase-fields; samples PbSeV-31, PbSeV-36, PbSeV-39, PbSeV-41, and PbSeV-42 are used for the construction of the three-phase-equilibria; three-phase-equilibria and single-phase fields with an uncertainty are indicated by dashed lines; nominal sample locations and selected EPMA results are indicated by red and blue dots, respectively.

The phase fields of Se_2V, Se_8V_5, and Se_4V_3 is an experimentally challenging region. All three phases are structurally related to the NiAs-type crystal structure. The relationship Se_2V and Se_4V_3 can be described by intra-layer disordering or by inter-chain disordering within the plane, whereas the relationship between Se_4V_3 and Se_8V_5 can be regarded as intra-chain disordering, which was illustrated by Oka et al [188] and Nakazawa et al [129] for the Se-V and S-V binary systems, respectively. Hayashi and Nakahira [190], Oka et al [188], and Miyauchi et al [191] reported differences between PXRD measurements of quenched samples at room temperature and in-situ measurements with high-temperature PXRD and DTA. The

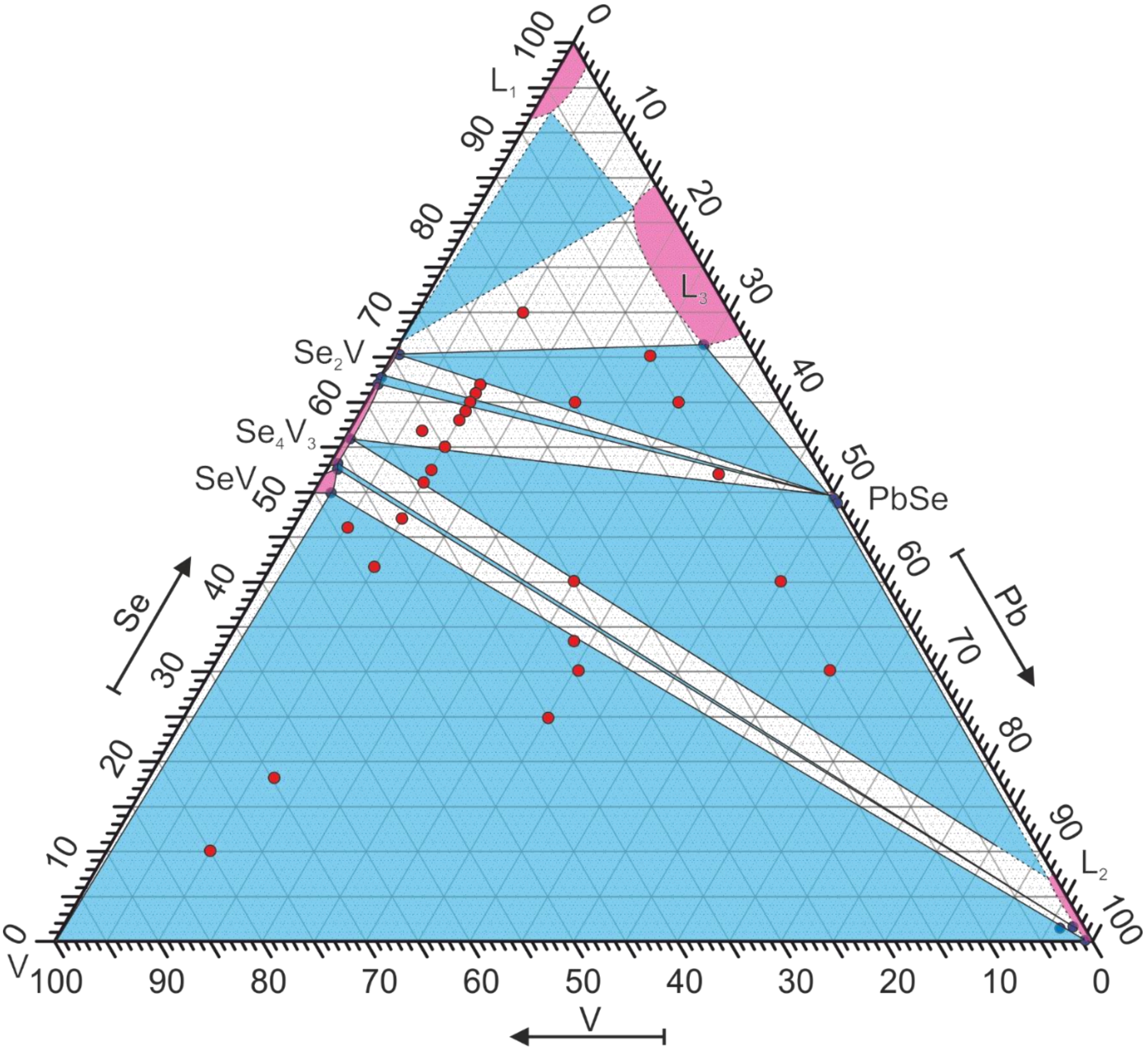

Figure 28: Isothermal section at 800 °C; blue triangles reflect the three-phase-fields; samples PbSeV-49, PbSeV-56, PbSeV-58, PbSeV-65, and PbSeV-66 are used for the construction of the three-phase-equilibria; three-phase-equilibria and single-phase fields with an uncertainty are indicated by dashed lines; nominal sample locations and selected EPMA results are indicated by red and blue dots, respectively.

high-temperature ordered variant of Se_4V_3 appears to be unquenchable at the composition of Se_8V_5. In several samples, Se_4V_3 and Se_8V_5 could not be refined together and were only distinguishable by the weighted R-values (refer to Figure 31 and sample PbSeV-58). Hence, the Se_8V_5 phase, or at least an isostructural variant of Se_4V_3, can be detected in our PXRD results despite annealing temperatures above approximately 750 °C, where the phase transition takes place. Additionally, the stabilisation of the Se_8V_5 phase to higher temperatures can be ruled out by the fact of negligibly small solid solubilities into the ternary.

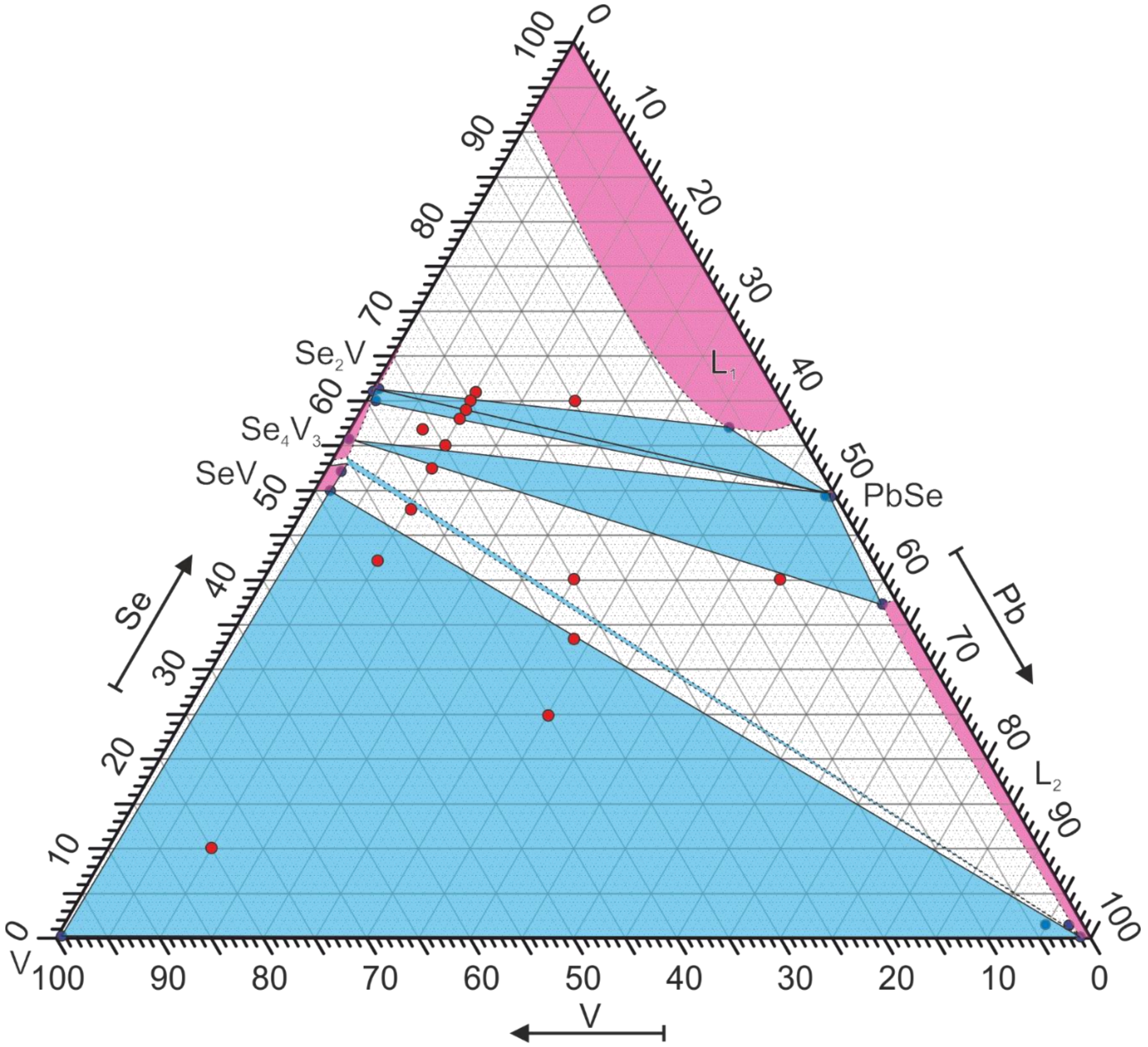

Figure 29: Isothermal section at 1000 °C; blue triangles reflect the three-phase-fields; samples PbSeV-73, PbSeV-77, PbSeV-78, PbSeV-80, and PbSeV-82 are used for the construction of the three-phase-equilibria; three-phase-equilibria and single-phase fields with an uncertainty are indicated by dashed lines; nominal sample locations and selected EPMA results are indicated by red and blue dots, respectively.

Concerning the phase fields of Se_2V, Se_4V_3 (selenium-rich side of Se_8V_5 in the binary phase diagram), and Se_8V_5 with PbSe in the isothermal sections at 550 °C and 700 °C, several samples were especially difficult to evaluate. These difficulties can be attributed to the described structural relationship as well as to the uncertainty, whether there is a first or second-order phase transition ($Se_4V_3 \rightarrow Se_8V_5$). For consistency reasons with the binary Se-V phase diagram, this region is constructed presuming a first-order transition.

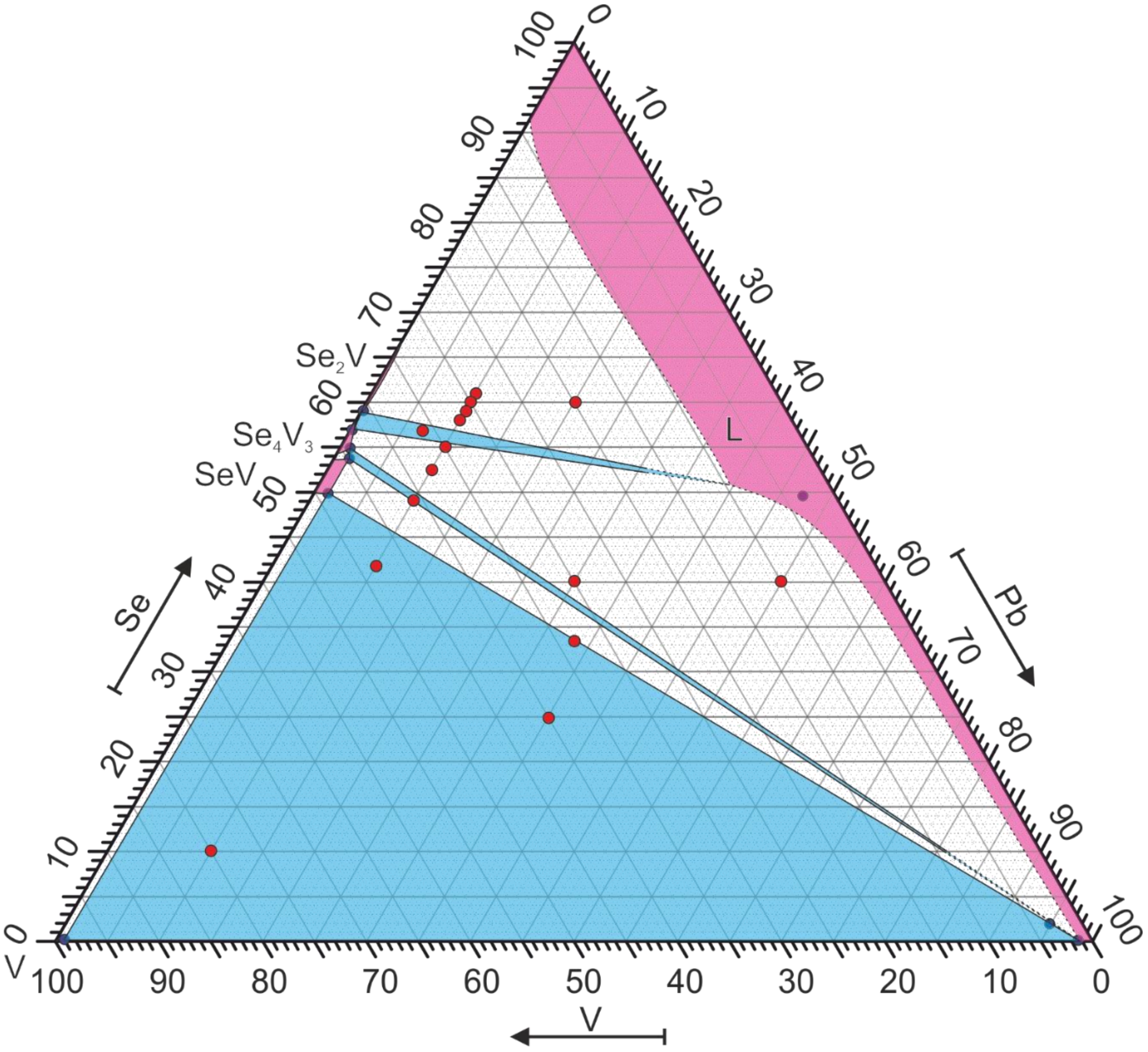

Figure 30: Isothermal section at 1100 °C; blue triangles reflect the three-phase-fields; samples PbSeV-86, PbSeV-87, and PbSeV-90 are used for the construction of the three-phase-equilibria; three-phase-equilibria and single-phase fields with an uncertainty are indicated by dashed lines; nominal sample locations and selected EPMA results are indicated by red and blue dots, respectively.

At 550 °C the ternary equilibrium of Se_2V + Se_8V_5 + PbSe was clearly determined (refer to sample PbSeV-25). Hence, the equilibrium Se_2V + Se_8V_5 + Se_4V_3 is required, which is probably degenerate and only found in a very small composition range close to the binary Se-V system. At 700 °C the ternary equilibrium Se_2V + Se_4V_3 + PbSe was observed (refer to sample PbSeV-38). Hence, a U-type reaction (Se_4V_3 + PbSe → Se_2V + Se_8V_5) between 550 °C and 700 °C is required to reach the consequent phase equilibria Se_2V + Se_4V_3 + PbSe and Se_4V_3 + Se_8V_5 + PbSe. It should be noted that samples at 700 °C neither exhibited the composition of the Se_8V_5 phase in EPMA nor its reflections PXRD. Additionally, the Se_4V_3 phase in the selenium-rich corner was only determined by comparison of the weighted R-values for the structure types of Se_2V, Se_4V_3, and Se_8V_5, which shows the limitations of evaluation in this part of the phase diagram.

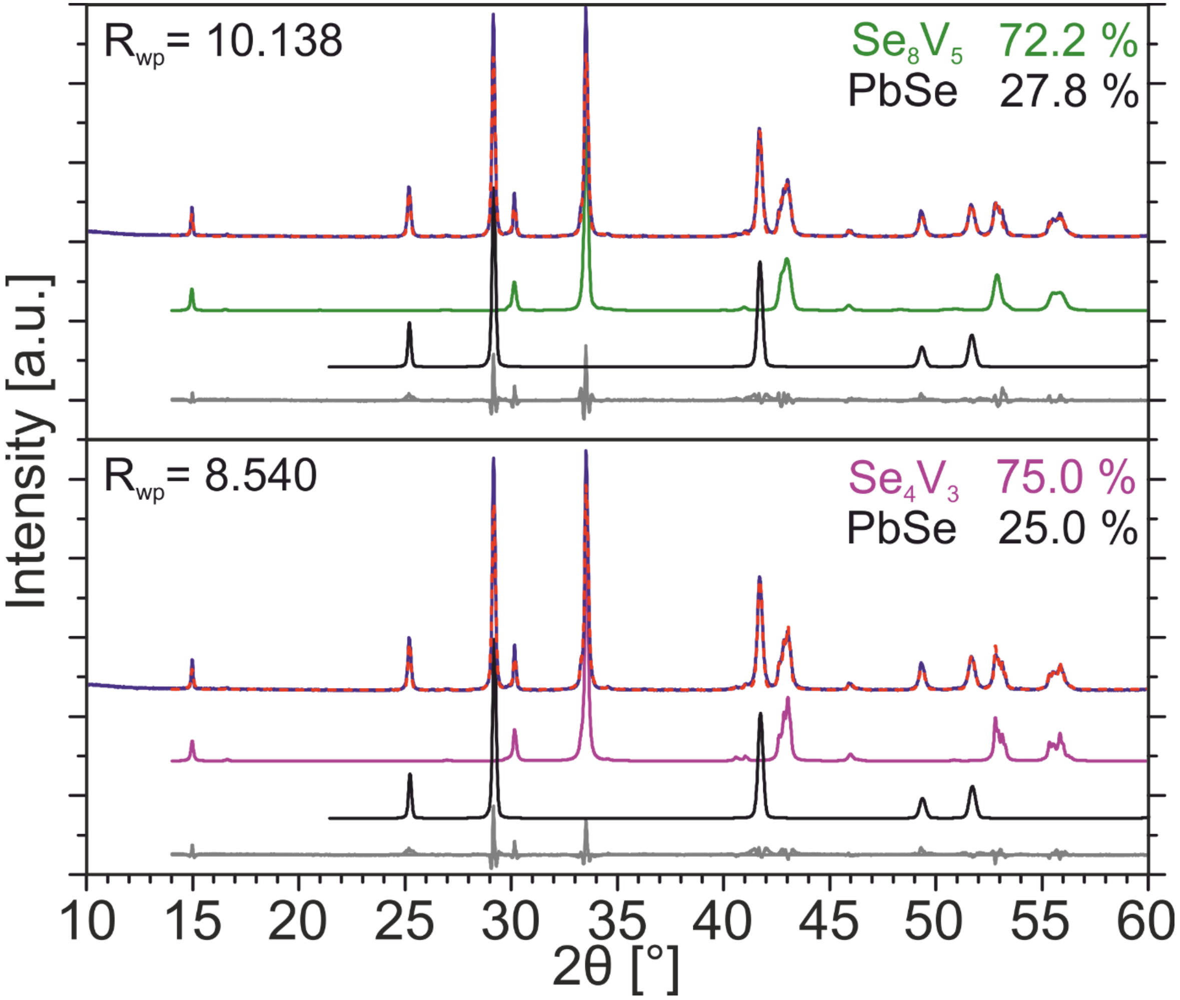

Figure 31: Difficulties in PXRD refinement for all samples containing the Se_4V_3 or Se_8V_5 phase; in some cases (e.g. sample PbSeV-58 at 800 °C) they could be only differentiated by the weighted R-values and not refined together.

The phase equilibria of the isothermal sections at 800 °C and 1000 °C (refer to Figure 28 and Figure 29) are very similar, with except of the solubility ranges reported for the binary phase diagrams (e.g. reduction of solubility for the Se_4V_3 phase with increasing temperature). Like in the isothermal sections at 550 °C and 700 °C, the solubility into the ternary was observed to be small. SeV exhibits the largest solubility with 1.6 at.% of Pb (refer to sample PbSeV-49). The composition of the lead-rich liquid was difficult to determine for several reasons. First, the proportion of the liquid phase is dependent on the lead content. As the sample compositions were around 10 at.% Pb in most of the prepared samples, the liquid content was small compared to the other phases. Area scans of small regions in the sample cause large deviations of results. Second, the PbSe phase is part of the equilibrium phases as well as a crystallization product of the liquid upon cooling (refer to Figure 24a). This might lead to wrong results if the microstructure is not determined exactly. Third, the Pb-Se binary system is reported to have a metastable liquid miscibility gap [172], which was even described by a monotectic reaction in some references [173, 174]. Hence, samples with well-determined microstructures can exhibit EPMA results with misleading liquid compositions (refer to Figure 24b).

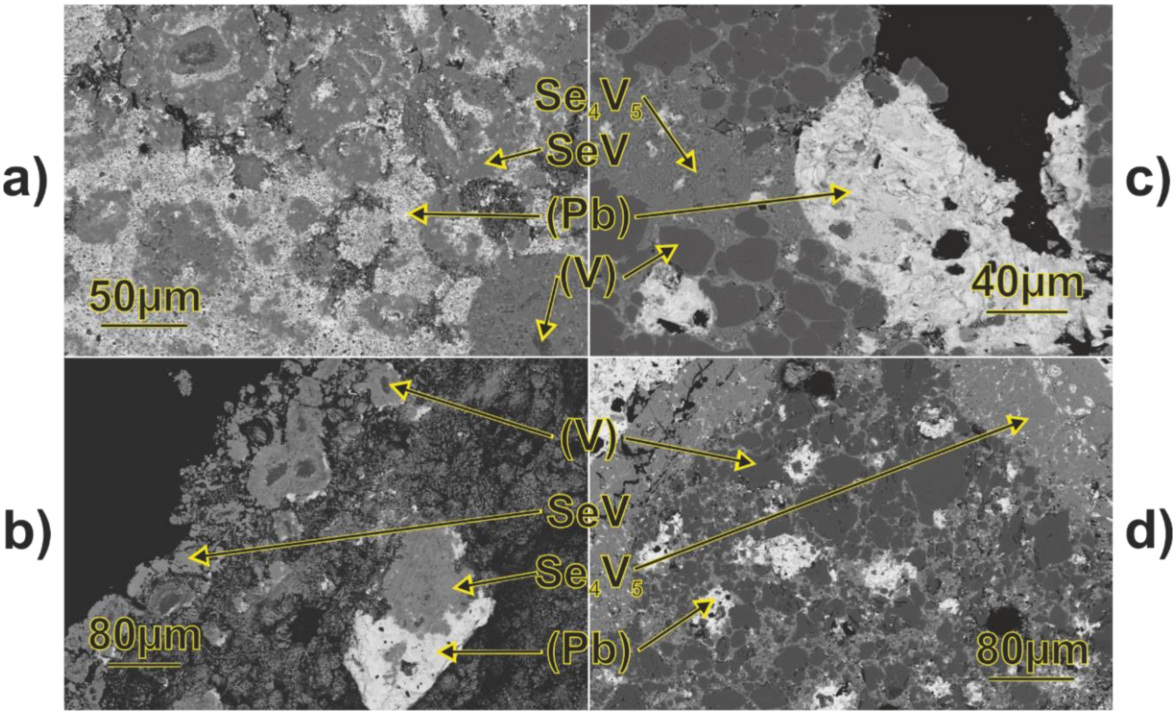

Figure 32: Difficulties in investigations caused by the supposedly impurity stabilised phase of Se_4V_5; samples PbSeV-77 (a), PbSeV-49 (b), PbSeV-1 (c), and PbSeV-70 (d) are annealed at 1000 °C, 800 °C, as-cast, and 1000 °C respectively.

Last but not least, quenching rates might always be insufficient at such temperatures. For the selenium-rich liquid similar problems, as just described, occur. Additionally, for the miscibility gap in the selenium-rich corner of the binary Pb-Se system, only experimental data of Nozato and Igaki [173, 174] or CALPHAD modelling [166, 172, 182] are available. Therefore, all shown boundaries of the liquid phase might not reflect the exact shape of the liquid but indicate its approximate location.

At 1100 °C (refer to Figure 30) the entire Pb-Se phase diagram is liquefied. Hence, all remaining vicinal phases of the Se-V binary system are in equilibrium with the liquid (refer to Figure 24c/d). The curvature of this liquid reflects the liquid composition of the isothermal sections below. The vanadium content in the selenium-rich part is significantly higher than in the lead-rich part. Our results indicate, that the melting point of PbSe is not elevated by the addition of vanadium. Nevertheless, PbSe was observed in the liquid without additional (Se) or (Pb) that might be found upon quenching of the liquid phase (refer to Figure 24d), which is presumably due to the close proximity of this section to the melting point of PbSe. We propose a cascade of ternary reactions occurring around the congruent decomposition of PbSe (between 1076 °C [173, 174] and 1088 °C [175]). Due to the uncertainties in the binary phase diagram regarding the exact melting point and contradicting data from our DTA experiments, which are a result of a changing sample composition during the DTA experiments due to the evaporation and condensation of volatile components in the sample, no proposal on the reaction scheme can be provided.

5.8.3. Misfit layer compound $(PbSe)_{1+\delta}(VSe_2)$

No ternary phase was observed in the isothermal sections (375 °C, 550 °C, 700 °C, 800 °C, 1000 °C, and 1100 °C) shown above. For this reason, new samples in two additional isothermal sections were created at 550 °C and 650 °C. Those samples contained small amounts of additional NH_4Cl which is known to function as crystallisation aid in misfit layer compound synthesis.

Apart from rather similar phase equilibria and solubilities, as well as some small recondensed NH_4Cl crystals on the walls of the sample ampoules, an additional phase was observed at a composition of 22.6(2), 56.6(2), and 20.8(3) at.% Pb, Se, and V, respectively (e.g. refer to samples PbSeV-T-6 and PbSeV-T-31 in Figure 33). The composition, the morphology (refer to Figure 33), and the additional reflections in XRD caused by the superstructure (refer to Figure 34 for the MLC and the publication of Hite et al [27] on the respective *fere*crystaline compound) indicate the presence of an MLC. This MLC grows on the surface of the sintered pills with crystal sizes of approximately 200 x 200 x 10 µm. Steps on the surface indicate a synthesis route including gas-phase species, as expected when using NH_4Cl al crystallization aid. The delicate layered structure is sensitive to any manipulation, aggravating attempts of a crystallographic investigation.

The observed composition is at higher vanadium content than expected for an MLC. This might be attributed either to a systematic error in EPMA measurements or to an actual surplus of vanadium in the compound. The composition would be the $(PbSe)_{1+\delta}(VSe_2)$ in the former and $(PbSe)_{1+\delta}(V_{1+x}Se_2)$ in the latter case, respectively (refer to Figure 26, where the two potential locations are indicated by green

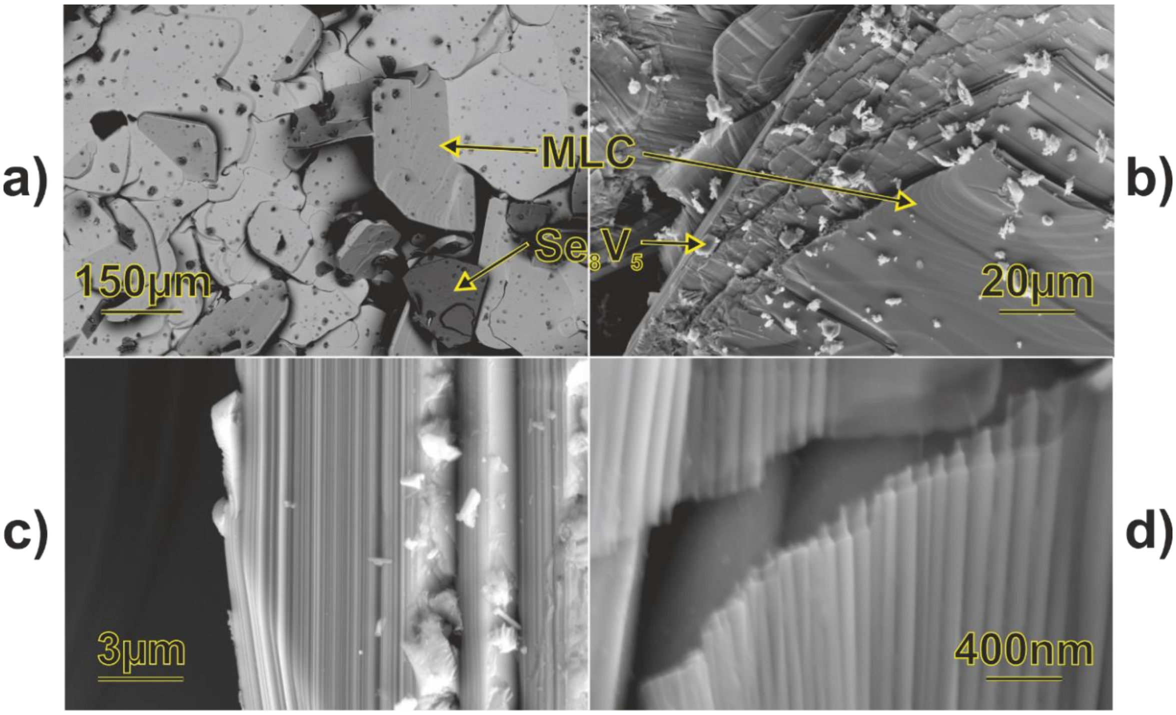

Figure 33: Misfit layer compound in the Pb-Se-V system growing from the sintered powder pill (sample: PbSeV-T-31 for a and PbSeV-T-6 for b to d); crystallite sizes of approximately 200 x 200 x 10 µm were obtained (a); MLCs exhibit step-wise crystal growth (b); even SEM investigations the layered structure was visible along the crystallographic c-axis (c); any manipulation yielded in rippled surfaces aggravating crystallographic experiments (d).

squares). This issue can be only determined by analysis of the crystal structure, which is still under investigation. A comprehensive study of the structural properties, the thermal stability and the synthesis of this new misfit layer compound, as well as a comparison to the *ferecrystalline* compounds of this system, are subject to a forthcoming publication.

Due to the open question of the actual MLC composition and the insufficient data on the phase equilibria, the MLC was not included in the isothermal sections shown above. Two scenarios for ternary phase equilibria can be derived hypothetically. In the case of a systematic deviation of composition measurement results and a composition close to $(PbSe)_{1+\delta}(VSe_2)$, only two three-phase equilibria of the type VSe_2 + PbSe + MLC should be present. In the case of a composition that is actually shifted to higher vanadium contents, $(PbSe)_{1+\delta}(V_{1+x}Se_2)$ is surrounded by three three-phase equilibria (VSe_2 + V_8Se_5 + MLC, VSe_2 + PbSe + MLC, and V_8Se_5 + PbSe + MLC). To our knowledge previous investigation on phase diagrams with

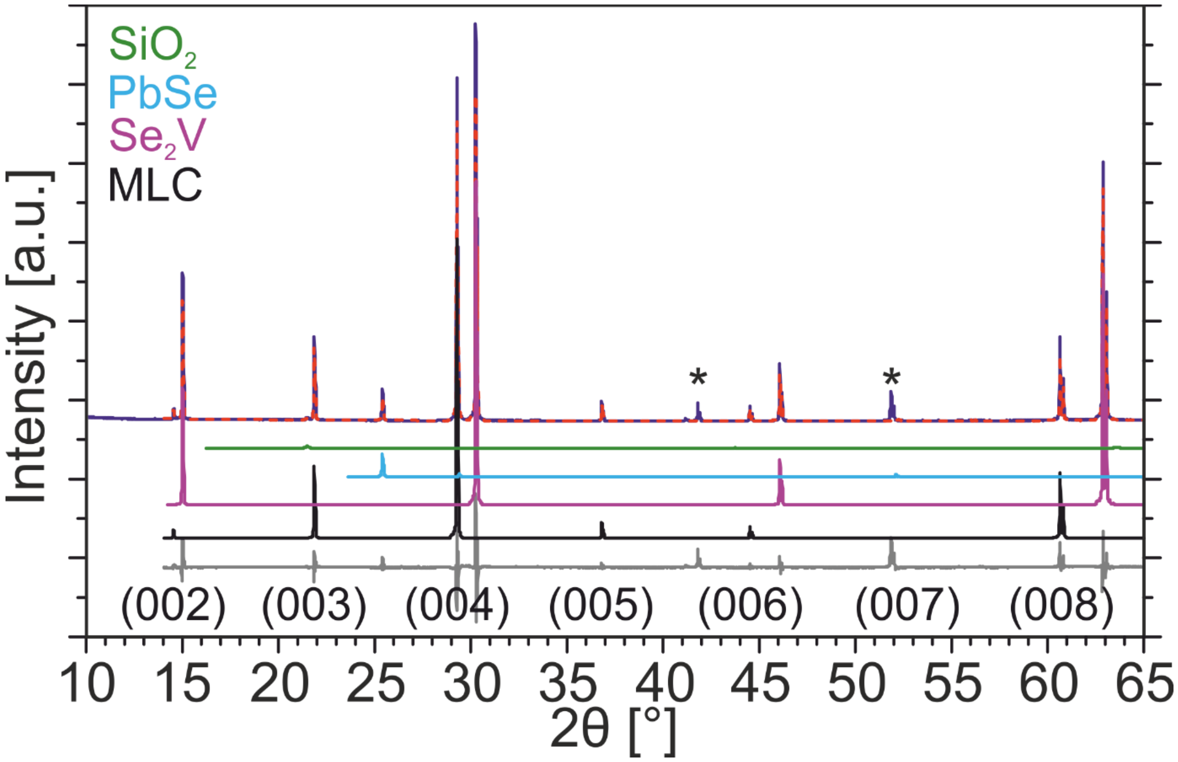

Figure 34: Out-of-plane XRD pattern of the unpowdered sample PbSeV-T-31; the experimental, calculated, and difference pattern from the Rietveld refinement are shown in blue, dashed red, and grey, respectively; the typical 00l reflections for a MLC with n=m=1 are appropriately indexed; some additional reflections (marked with an asterisk), next to Se_2V, PbSe, and SiO_2, are presumably higher-order reflections of the MLC due to nonplanarity or stacking defects.

MLCs, only included MLCs in the pseudo-binary vertical sections between TX_2 and MX (e.g. Bi-Cr-Se [159]), but not in isothermal sections. Hence, neither hypothetical scenario can be favoured by comparison with the established literature.

5.9. Conclusion

One partial and five full isothermal sections were constructed in the ternary system of Pb-Se-V for 375 °C, 550 °C, 700 °C, 800 °C, 1000 °C, and 1100 °C. Two impurity stabilised phases might be present. In contrast to PbV_3, Se_4V_5 was observed but neglected in the construction of the isothermal section. Apart from the selenium-rich liquid, the binary compounds in these sections exhibit only small solid solubilities into the ternary. In order to investigate the solubility of the ternary lead-rich liquid, further experiments in the binary Pb-V system were conducted. We conclude on low vanadium-contents in the liquid till 1100 °C (e.g. max. 1.3 at.% V) and similar low lead-contents in vanadium that is in equilibrium with the respective liquid (e.g. max. 2 at.% Pb).

A new misfit layer compound was observed in this ternary system at a composition of 22.6(2), 56.6(2), and 20.8(3) at.% Pb, Se, and V, respectively. It was obtainable only by the addition of NH_4Cl to the powder pills. Due to several difficulties this phase was not included in the equilibrium phase diagram. Nevertheless, two possible scenarios for ternary phase equilibria are stated and, similar as the crystal structure, under further investigation.

5.10. Acknowledgements

Special thanks go to Prof. Herta Effenberger from the Department of Mineralogy and Crystallography, University of Vienna, for her patience in attempting to find suitable single crystals for XRD of the phases Se_4V_5 and $(PbSe)_{1+\delta}(VSe_2)$. The authors wish to thank Dr. Stephan Puchegger from the Department of Physics, University of Vienna, for his help with SEM measurements and express gratitude to Dr. Patricia Jenner for proof-reading and her linguistic advice.

5.11. Declarations of interest

The authors declare that there is no conflict of interest.

6. Manuscript 2: The 550 °C and 700 °C isothermal sections and new misfit layer compounds in the Se-Sn-V system

6.1. Authorship Statement

Chapter 6 describes material that will be submitted to *The Journal of Alloys and Compounds* in 2020. The co-author is Klaus W. Richter, who is my advisor and I am the primary author of the manuscript.

Reisinger: Conceptualisation, Investigation, Writing - Original Draft, Visualisation

Richter: Conceptualisation, Writing - Review & Editing, Supervision, Project administration

6.2. Abstract

The phase relations of the ternary system Se-Sn-V was investigated over the whole composition range utilising powder X-ray diffraction (PXRD) and scanning electron microscopy (SEM) coupled with electron probe microanalysis (EPMA). The results of the evaluations in the ternary system are presented by two isothermal sections at 550 °C and 700 °C. A special focus was set on finding a misfit layer compound (MLC) in this system. Six MLCs are present at the compositions $[(\mathrm{SeSn})_{1+\delta}]_m(\mathrm{VSe}_2)$ (m = 1, 2, 3, 4, 5, and 6).

6.3. Keywords

Ternary alloy system, Phase diagrams, Phase transitions, Misfit layer compound, Scanning electron microscopy, X-ray diffraction

6.4. Prime novelty statement

In this article we present the up to now uninvestigated phase diagram Se-Sn-V. The compositions of six new MLCs $[(\mathrm{SeSn})_{1+\delta}]_m(\mathrm{VSe}_2)$ (m = 1, 2, 3, 4, 5, and 6) are reported.

6.5. Highlights

- Two isothermal sections in the Se-Sn-V system
- New misfit layer compounds $[(\mathrm{SeSn})_{1+\delta}]_m(\mathrm{VSe}_2)$ in the Se-Sn-V system

6.6. Introduction and literature review

Low dimensional materials exhibit different properties than their bulk counterparts, which makes them candidates for replacing expensive or inefficient materials in established applications (e.g. anode materials in lithium-ion batteries, next-generation electronics, and water splitting by hydrogen evolution reaction) or, due to some exotic properties, unknown future applications. Hence, 2D materials such as graphene, boron nitride, transition metal dichalcogenides (TMDs), and hybrid perovskites are investigated extensively.

The binary system of Se-V hosts one 1D and one 2D phase. For the 1D phase Se_9V_2 only a few reports are available [131, 135-137]. The 2D phase Se_2V is of greater interest in literature, not only due to its properties [24, 132] but also as it is constituent of another type of 2D material in some ternary systems. These, so-called misfit layer compounds (MLCs) can be present in ternary systems M-Se-V, where M can be bismuth, lead, tin, or a rare earth element [122, 139].

MLCs are hybrid solids comprising two structurally different crystal structures that are stacked in an alternating manner (refer to Figure 35). The general formula $[(MX)_{1+\delta}]_m(TX_2)_n$ reflects the structural properties of the layered composite. The former subsystem (MX) exhibits a bilayer of a (distorted) sodium chloride type crystal structure and comprises a chalcogen, such as selenium, and at least one of the elements bismuth, lead, antimony, and tin or a rare earth element. The latter subsystem (TX_2) is a triple layer of a TMD, where a hexagonal layer of an early transition metal, such as vanadium, is sandwiched between two layers of a chalcogen. In the resulting MLC, the two subsystems lattice parameters coincide in one crystallographic orientation in the plane of the interface. In the other direction, the subsystems are incommensurate. The difference in their lattice parameters and the resulting misfit is described in the misfit parameter δ. Furthermore, the lattice misfit causes modulations in the subsystems (e.g. out-of-plane shift of atomic positions). These modulations in the MLCs require a description in (3+1)D superspace symmetry for the solution of the crystal structure. The intensity of these modulations is also dependent on the stacking sequence, which is described by the parameters m and n [122, 126, 139]. Compositions with small values for the stacking parameters *m* and *n* are found to be thermodynamically the most favourable ones (e.g. *m* = 2 and *n* = 1 is more stable than *m* = 4 and *n* = 2) [101].

The properties of these crystals, such as the thermodynamic stability, the crystal structure, the number of defects, or the electrical conductivity, are dependent on the route of synthesis [126]. Alternating physical vapour deposition (PVD) of the precursors of the layered compound, which is followed by a low-temperature annealing step, permits the synthesis of compounds with a broad variation range for the parameters *m* and *n*. The resulting compounds of the so-called modulated elemental reactants synthesis are only kinetically stabilised and referred to as *fere*cystals [126]. By traditional solid-state chemistry approaches, such as chemical

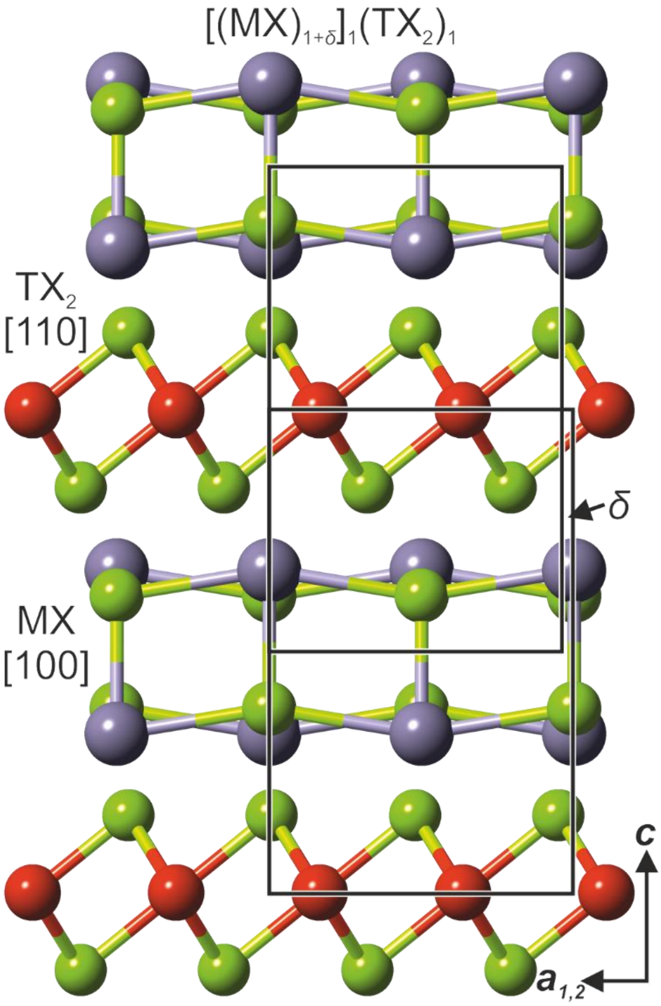

Figure 35: Schematic representation of a misfit layer compound with the composition $[(MX)_{1+\delta}]_m(TX_2)_n$ *(m=n=1); T atoms (e.g. vanadium) are red, X atoms (e.g. selenium) are green, and M atoms (e.g. lead) are blue in this picture; the unit cells for the individual sub-lattices of the* TX_2 *and MX are given to visualise the misfit parameter δ.*

vapour deposition (CVD) with a transporting agent (e.g. NH_4Cl [121, 122]) or crystal growth from salt fluxes (e.g. eutectic melt of LiCl and KCl [159]), only thermodynamically stable compounds (e.g. parameters *m* and *n* are close or equal 1) can be synthesised, which are denoted as MLCs [126].

Due to the versatility of the modulated elemental reactants synthesis, the research interest on *fere*crystals is higher in recent literature compared to that of the MLCs. Likewise, for the systems based on M-Se-V (M = Bi, Pb, Sb, Sn, or a rare earth element), the *fere*crystals in these systems are well investigated [27, 37, 68, 69, 73, 74, 84, 96, 114, 165] compared to the MLCs. In the antimony-based systems no MLC was observed [130] and for the lanthanum- and lead-based systems the two MLCs $(La_{0.95}Se)_{1.21}VSe_2$ [35] and $(PbSe)_{1+\delta}(VSe_2)$ [107] are reported. Furthermore, there are some investigations on bismuth- [59, 106] and tin-based systems [61, 95], which do not comment on the composition or report a final crystal structure.

Neither the ternary system Se-Sn-V nor any of the ternary systems of an early transition metal with tin and selenium were investigated heretofore by an isothermal section, which we might have been utilising as a starting point for our investigation. Besides, in the same ternary systems only one isopleth is available. This isopleth between Cr_2Se_3 and Se_2Sn, exhibits a large single-phase field of an unspecified ternary compound [192] with a similar composition as MLCs have (*nota bene* later investigation observed layered compounds at a rather similar composition [193, 194]).

Multiple *fere*crystalline compounds are reported in the Se-Sn-V system. These compounds exhibit the stoichiometry $[(SeSn)_{1+\delta}]_m(VSe_2)_n$ ($\delta = 0.15$, $m = 1$ to 4, and $n = 1$ to 6). The investigations on them include, among other properties, the crystal structures, the electrical properties, the defects, and the influence of doping [37, 38, 67-69, 73, 114]. As the modulated elemental reactants synthesis approach was utilised, these *fere*crystalline compounds all were prepared on a SiO_2 substrate and only kinetically stabilised. Not only the crystal structure might deviate from closely related and thermodynamically stable MLCs probably present in this system, but the phase equilibria in the ternary system Se-Sn-V are unknown as well. Hence, this publication aims to determine the phase equilibria present in the ternary system Se-

Sn-V as well as gain knowledge on MLCs that might be observed in the course of the investigation of the phase equilibria.

The Se-Sn phase diagram (refer to Figure 36) has last been investigated and assessed by Feutelais et al [195]. Three binary phases are reported in this system. Se_2Sn, which melts congruent at 657 °C, crystallises in CdI_2 structure type. The stoichiometric compound SeSn possesses a low-temperature and a high-temperature form with the prototypes GeS and TlI, respectively [196] (*nota bene* these structure types are distinct from the distorted NaCl type observed in MLCs). Whether this phase transition is first- or second- order is still under debate. Likewise, it is still unclear if this transition involves one peritectoid and one eutectoid or one metatectoid and two eutectoid invariant reactions. The invariant reaction temperatures are at 520 °C and 526 °C on the selenium-rich and tin-rich side, respectively. At 880 °C the high-temperature modification of SeSn decomposes in a congruent reaction.

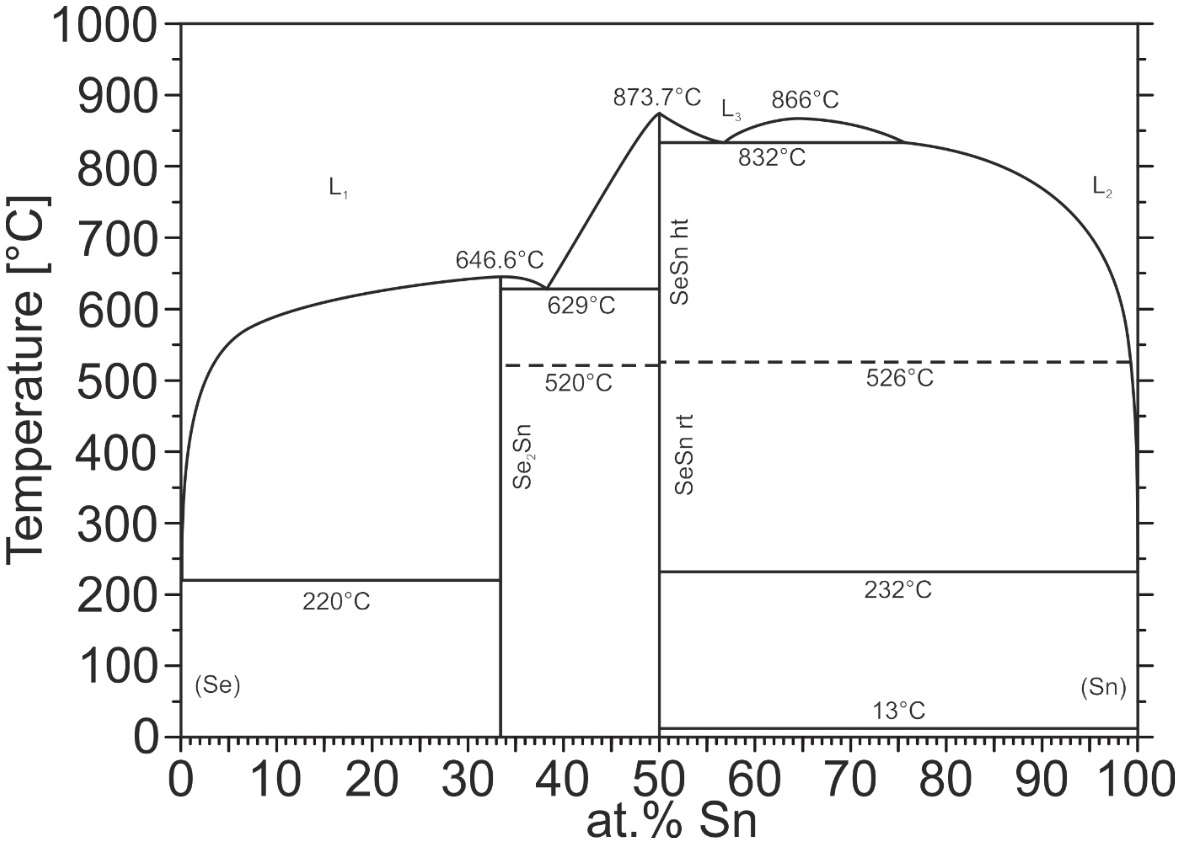

Figure 36 Binary phase diagram Se-Sn redrawn according to Feutelais et al [195]; uncertain reaction temperatures of the transition reaction between the low and high-temperature modification of SeSn are indicated by dashed lines; the liquids are denoted in accordance to the ternary phase diagram for clarification.

Three eutectic reactions are observed at the liquidus. Two of them are degenerated reactions and occur less than 1 °C below the melting point of the pure elements. The third eutectic reaction is observed between SeSn and Se_2Sn at 628 °C. In the tin-rich part of the binary phase diagram, a monotectic reaction with undefined liquidus shape is reported at 822 °C.

The solid solubilities are reported to be small. The largest composition rage was determined to be in SeSn. Close to the phase transition temperature, the solubility varied within 2 to 3 at.% around the ideal stoichiometric composition. Apart from the solubilities, the calculated phase diagram of Feutelais et al [195] is in good agreement with the experimental data. In contrast to older assessments it also includes the phase transition of SeSn. This phase diagram was used in our publication.

The Sn-V binary system comprises two intermetallic phases (refer to Figure 37). Interestingly, in many investigations, both phases exhibit a different composition than their stoichiometry suggests [197-201]. “SnV_3“ and “Sn_2V” are observed close to the compositions SnV_4 and Sn_3V_2, respectively. These unusual denotations derive from their crystal structures (Cr_3Si and $CuMg_2$) [202] and probably some configurational disorder [203]. The solubilities of the two intermetallic phases are either negligibly small [204] or in the range of up to 2 at.% [203]. For the liquid, the solubility of vanadium is negligibly small below 600 °C and at 1000 °C still below 1 at.% V. The high solubility of 8 at.% Sn in body centred cubic V is unlikely at room temperature and might be considered as an artefact from insufficient equilibration procedures [204].

Four invariant reactions are observed in this system. A degenerated eutectic reaction is located very close to the composition and melting temperature of pure Sn. The two intermetallic phases, “Sn_2V” and “SnV_3“, both decompose peritectically around 759 °C and 1598 °C, respectively. Finally, a monotectic reaction is reported for the tin-rich part of the Sn-V phase diagram at approximately 1500 °C [204].

Different parts of the Sn-V system were investigated experimentally by several authors [201, 204, 205]. Yet, the phase diagram was never examined in its entirety, except for CALPHAD modellings and assessments [204, 206]. As a result, inconsistencies in experimental data are observed [204]. Additionally, misinterpretations, such as the improbable liquid miscibility gap at 90 at.% Sn [207], were just corrected by the most recent calculations of Studnitzky et al [204] and Yue et al [206]. For those reasons, the ternary results in this publication require particular care in the assessment of data. The calculated phase diagram of Studnitzky et al [204], who also conducted some experiments, was used as a starting point in this study. However, we found disagreements with the proposed non-stoichiometric compositions of “Sn_2V” and “SnV_3“. Our results rather indicate the stoichiometric compositions for these compounds, which is discussed in detail below.

The Se-V phase diagram (refer to Figure 38) is experimentally challenging as the physical properties of the elements and compounds are unfavourable (e.g. strongly differing melting and boiling behaviours, closely related structure types and superlattices, the formation of pseudo-single phase fields and sluggish reaction

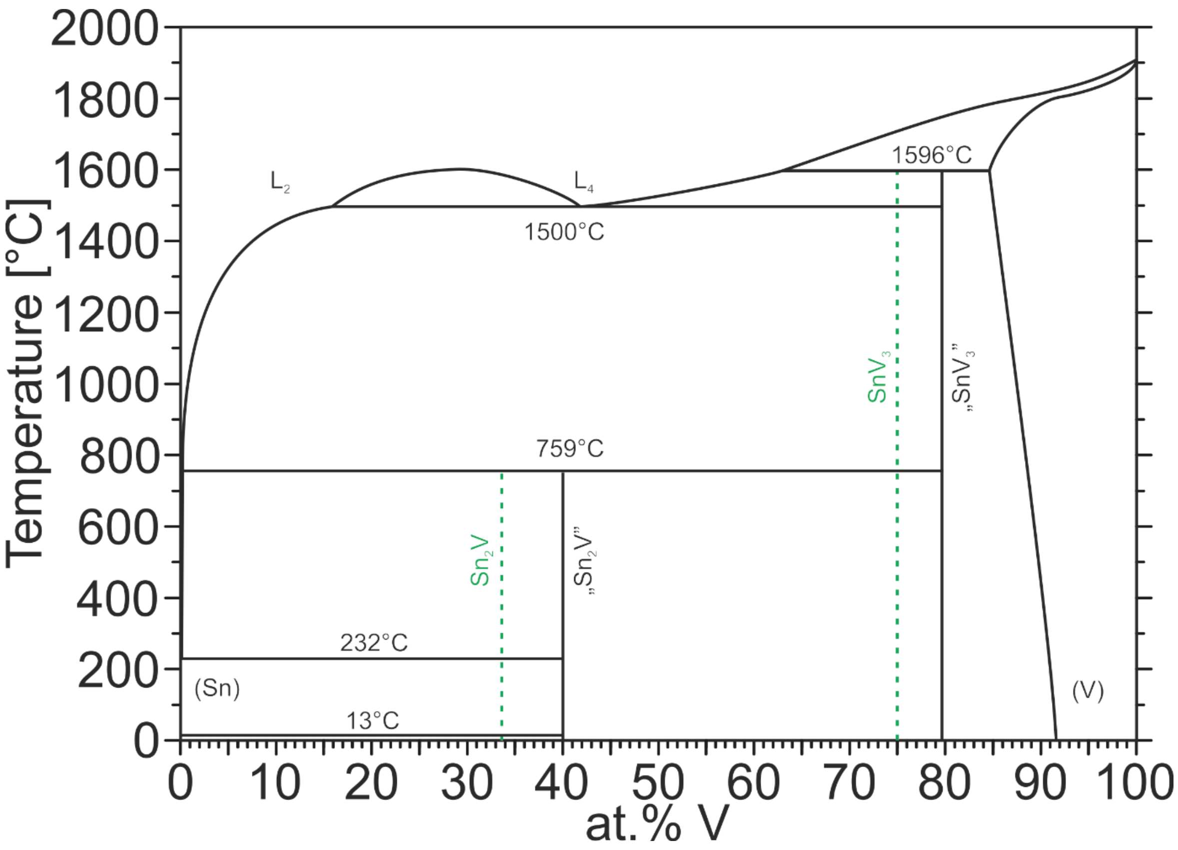

Figure 37: Binary phase diagram Sn-V redrawn according to Studnitzky et al [204]; the transformation reaction between the α-Sn and β-Sn and the phase compositions we observed (dashed green) were added by the authors; the liquids are denoted in accordance to the ternary phase diagram for clarification.

rates). Hence, several features were not determined experimentally, but are extrapolations of the binary systems of S-V and Te-V [151].

Comprising just four stable phases and one presumably metastable phase, the number of intermetallic phases that require discussion is limited. The non-equilibrium phase Se_4V_5 is presumably stabilised by impurities [130]. Similar behaviour was reported for other vanadium-based systems of this composition. That assumption is further supported by the facts that the structure type of Se_4V_5, a filled Te_4Ti_5 structure, exhibits right enough space in the octahedral 2*b* sites, for carbon to occupy it [148] and that it never occurred to be a major component in pure samples with the respective stoichiometric composition. Of the four stable phases, only one is not structurally related to the remaining three [130]. The Se_9V_2 phase comprises of 1D chains that are only weakly assembled via van der Waals forces. Hence, the electrons are confined in these chains [137]. With NiAs as their parental structure the compounds, Se_8V_5, Se_4V_3, and Se_2V-SeV, are loosely bonded by van der Waals forces, too.

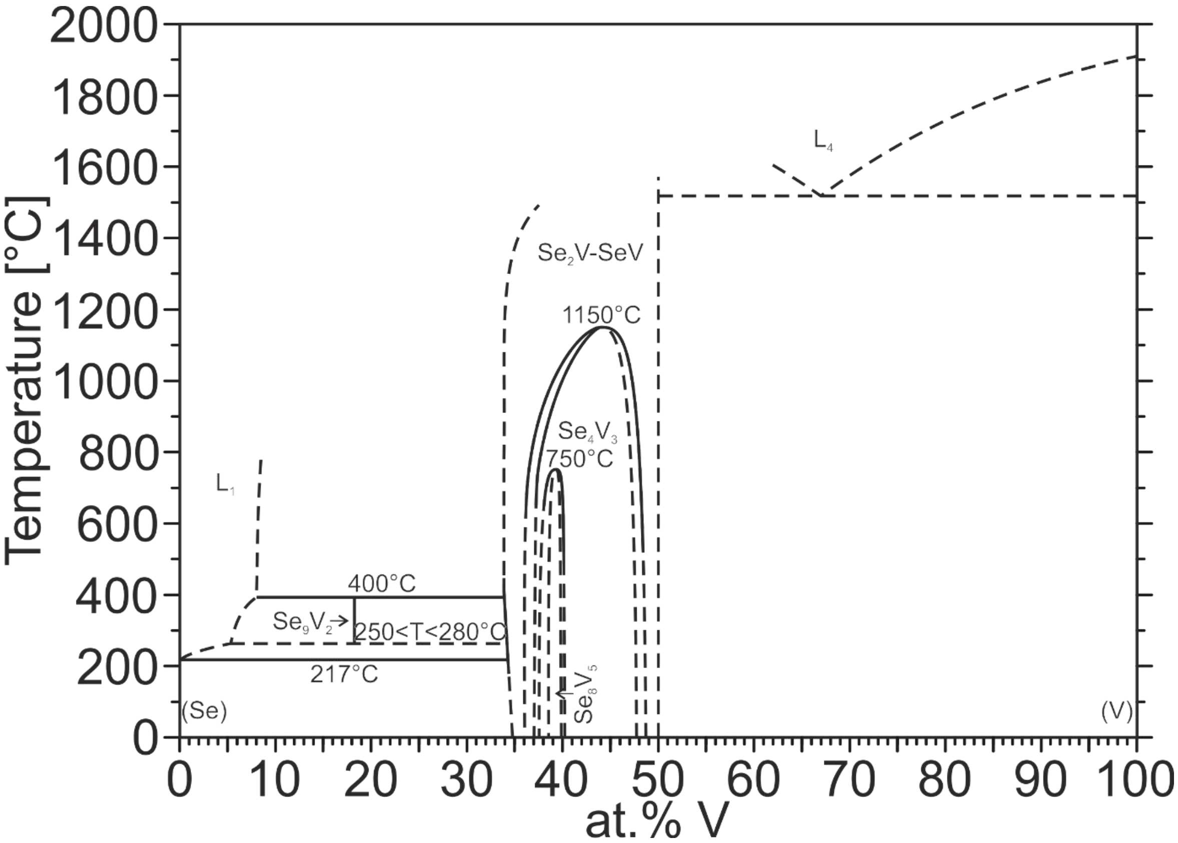

Figure 38: Binary phase diagram Sn-V redrawn according to Reisinger and Richter [130]; the liquids are denoted in accordance with the ternary phase diagram for clarification.

Reactions involving the liquid are difficult to determine experimentally due to the high vapour pressure of selenium. Hence, the melting point of SeV and the eutectic reaction in the vanadium-rich part are only known to be above 1550 °C. Within the phase field of Se_2V-SeV, Se_4V_3 and Se_8V_5 are nested in one another. Whereas Se_4V_3 decomposes in a congruent reaction around 1150 °C, the transition of Se_8V_5 around 750 °C is discussed ambiguously in literature [130]. It might be either a first-order congruent transition or a second-order transition [129, 188, 190, 191]. The investigations in this part are difficult due to pseudo-single phase fields that, and in some cases, can only be distinguished by R-values in PXRD [107]. For this publication, the phase diagram of Reisinger and Richter was used [130], which is based on the assessment of Smith and proposes a congruent decomposition of Se_8V_5 [151].

6.7. Materials and methods

Tin shots (Alfa Aesar – purity 99.999 %), selenium shots (American Smelting and Refining Company – purity 99.999 %), and powders of vanadium (purity 99.99 %; 1250 mesh) were used as source materials. As experimental difficulties of the binary Se-V system worsen in the ternary, due to the larger number of compounds with different physical properties, master alloys were prepared. The utilisation of master alloys yields a phase composition in the sample, which is close to the equilibrium phase composition. Hence, master alloys permit quicker equilibration of samples. Moreover, the reproducibility of results is enhanced, because potential weighing errors and evaporation losses are reduced significantly. The four compounds Se_2Sn, SeSn, Se_2V, and SeV were prepared in large quantities. For this purpose, the pure elements were weighed out in an argon-filled glovebox, sealed in silica ampoules under vacuum and annealed in the muffle furnace. The master alloys were checked for potential impurity phases by powder X-ray diffraction (PXRD). Only well homogenised and oxide-free master alloys were further processed in sample preparation.

All ternary samples were prepared in the glovebox from powders of the readily prepared master alloys and the pure elements in a similar manner. The weighed out sample mass was 300 mg ± 0.5 mg. After intimately mixing the powders by shaking,

Table 14: Samples in the Se-Sn-V system; the nominal compositions, the temperature programs in hours (h) and weeks(w), and the corresponding isothermal sections are stated for all samples.

Sample	Se (at.%)	Sn (at.%)	V (at.%)	Temperature program	Section
sd49	80.0	10.0	10.0	700°C 1h → quenched → 550°C 8w	550°C
sd50	80.0	10.0	10.0	700°C 8w	700°C
sd51	65.0	24.9	10.1	700°C 1h → quenched → 550°C 8w	550°C
sd52	65.0	25.0	10.0	700°C 8w	700°C
sd53	60.0	20.0	20.0	900°C 1h → quenched → 550°C 8w	550°C
sd54	60.0	20.1	19.9	900°C 1h → quenched → 700°C 8w	700°C
sd55	55.0	35.0	10.0	900°C 1h → quenched → 550°C 8w	550°C
sd56	55.0	35.1	9.9	900°C 1h → quenched → 700°C 8w	700°C
sd57	63.4	10.0	26.6	900°C 1h → quenched → 550°C 8w	550°C
sd58	63.4	10.0	26.6	900°C 1h → quenched → 700°C 8w	700°C
sd59	61.0	10.0	29.0	900°C 1h → quenched → 550°C 8w	550°C
sd60	61.0	9.9	29.1	900°C 1h → quenched → 700°C 8w	700°C
sd61	60.0	10.1	29.9	900°C 1h → quenched → 550°C 8w	550°C
sd62	59.9	10.1	30.0	900°C 1h → quenched → 700°C 8w	700°C
sd63	59.0	10.1	30.9	900°C 1h → quenched → 550°C 8w	550°C
sd64	59.0	10.0	31.0	900°C 1h → quenched → 700°C 8w	700°C
sd65	58.0	10.0	32.0	900°C 1h → quenched → 550°C 8w	550°C
sd66	58.0	10.0	32.0	900°C 1h → quenched → 700°C 8w	700°C
sd67	55.0	10.0	35.0	900°C 1h → quenched → 550°C 8w	550°C
sd68	55.0	10.1	34.9	900°C 1h → quenched → 700°C 8w	700°C
sd69	52.5	10.0	37.5	900°C 1h → quenched → 550°C 8w	550°C
sd70	52.5	10.1	37.4	900°C 1h → quenched → 700°C 8w	700°C
sd71	40.1	49.7	10.2	900°C 1h → quenched → 550°C 8w	550°C
sd72	40.0	50.1	9.9	900°C 1h → quenched → 700°C 8w	700°C
sd73	33.4	33.3	33.4	900°C 1h → quenched → 550°C 8w	550°C
sd74	33.3	33.4	33.3	900°C 1h → quenched → 700°C 8w	700°C
sd75	46.9	10.2	42.9	900°C 1h → quenched → 550°C 8w	550°C
sd76	47.0	9.9	43.1	900°C 1h → quenched → 700°C 8w	700°C
sd77	42.2	10.1	47.7	900°C 1h → quenched → 550°C 8w	550°C
sd78	41.8	10.1	48.1	900°C 1h → quenched → 700°C 8w	700°C
sd79	20.1	10.1	69.8	900°C 1h → quenched → 550°C 8w	550°C
sd80	19.8	10.1	70.1	900°C 1h → quenched → 700°C 8w	700°C
sd81	10.1	60.3	29.6	900°C 1h → quenched → 550°C 8w	550°C
sd82	10.1	60.4	29.5	900°C 1h → quenched → 700°C 8w	700°C
sd83	10.1	35.3	54.6	900°C 1h → quenched → 550°C 8w	550°C
sd84	10.0	34.9	55.1	900°C 1h → quenched → 700°C 8w	700°C

the samples were cold-pressed in a steel die without lubricant. The obtained dense samples were thereafter sealed in evacuated silica ampoules, checked for tightness, and subjected to their respective heat treatments in a muffle furnace. To minimise temperature gradients in the furnace that might alter the sample composition, the samples were placed in custom build closed containers. After this annealing procedure, the samples were quenched in cold water. Refer to Table 14 for all prepared sample compositions and annealing conditions.

Despite attempts to minimise the temperature gradients with the aid of closed sample containers, MLCs tend to nucleate on the silica surface. Hence, and in order to detect all phases present in the silica ampoules, all samples and sample ampoules were carefully checked for additional crystals under a stereomicroscope. For the determination of phases present in the samples PXRD and scanning electron microscopy (SEM) were utilised. The former, was performed on a Bruker D8 diffractometer in Bragg-Brentano pseudo-focussing geometry (Cu-K_α radiation, variable slit, $10° < 2\theta < 120°$ in steps of 0.01°, silicon strip detector). Rietveld refinement technique with the software programs Topas4 [160] or Jana2006 [161] was used to analyse the obtained diffraction patterns. The latter, was performed on a Zeiss Supra 55 VP scanning electron microscope that was operated at an acceleration voltage of 20 kV. It served not only to gather knowledge on the morphology and microstructures but on the chemical composition, too. To determine the chemical composition pure cobalt was used for the energy calibration of the energy dispersive X-ray analysis (EDX) signal. The samples were embedded in a carbonised phenolic hot mounting resin for SEM preparation. As the remaining holes would destabilise the matrix of the sintered powder pills, prior to grinding (SiC abrasive paper grits 500 to 4000) the sintered powder pills were soaked with several layers of epoxy resin for further stabilisation. To investigate the morphology several selected samples were investigated without metallographic preparation, too. This is at the disadvantage of uneven surfaces and, hence, reduced reliability of EDX measurement results.

6.8. Results and discussion

A total of 36 ternary Pb-Se-V samples were prepared and investigated for the construction of the two isothermal sections at 550 °C and 700 °C (refer to Figure 39 and Figure 40, respectively). The sample preparation in the ternary system Se-Sn-V is challenging due to the different properties of the three elements. However, the obtained samples appeared well-equilibrated (refer to Figure 41 and Figure 42 for typical samples). In some cases, the microstructures were not conclusive on the first glance, especially, for phases which are in equilibrium with the liquid (refer to Figure 41a and Figure 42a) and for those with different compositions of MLCs (refer to Figure 41b). But also the bad contrast between vicinal binary phases (refer to Figure 41c) or the breaking loose of parts of the embedded pills (refer to Figure 41d) are hurdles in the investigation of the microstructures in this system. As some samples were more difficult to evaluate, we present the equilibrium phases of each sample in Table 15 and Table 16 not in the commonly used split of the two distinct annealing temperatures. We chose to split the samples in those located in the easier boundary region of the ternary phase diagram (refer to Table 15) and those in the complex central part of the phase diagram (refer to Table 16).

As expected by comparison to the previously investigated ternary systems of Sb-Se-V [130] and Pb-Se-V [107], the solid solubilities and the solubilities of the liquids are small in the two isothermal sections. The binary phases with the highest solubilities into the ternary are SeSn with vanadium-contents of 1.2 at.%, SeV with tin-contents of 1.3 at.%, and SnV_3 with selenium-contents of 0.6 at.%.

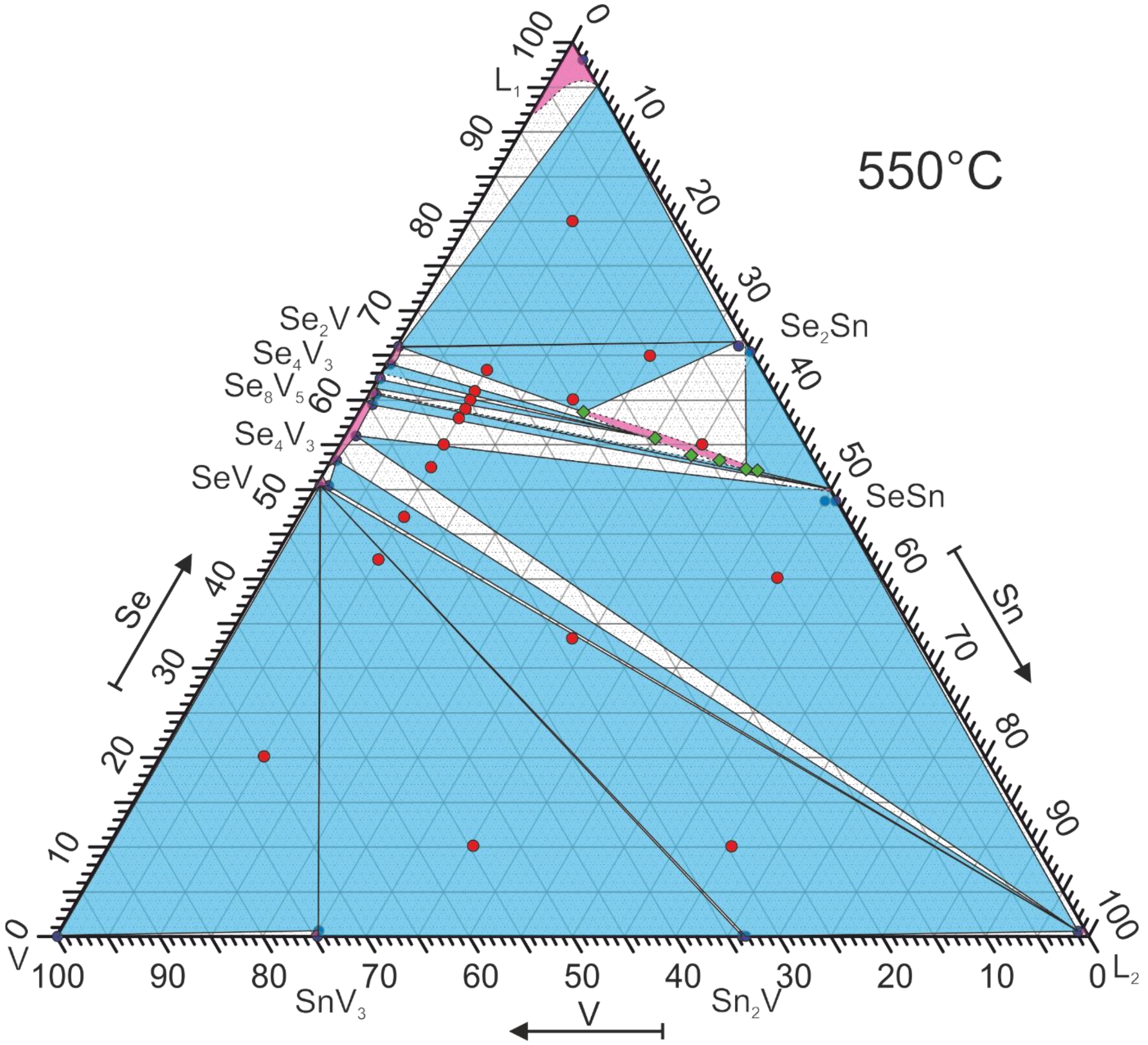

Figure 39: Isothermal section at 550 °C; blue triangles reflect the three-phase-fields; samples Sd49, Sd51, Sd57, Sd61, Sd63, Sd67, Sd73, Sd77, Sd79, Sd81, and Sd83 are used for the construction of the three-phase-equilibria; three-phase-equilibria and single-phase fields with uncertainty are indicated by dashed lines; nominal sample locations and selected EPMA results are indicated by red and blue dots, respectively; possible locations for the MLC in this system are marked by green squares.

Below a selenium content of 50 at.% no ternary phase was observed in neither of the two isothermal sections. Regarding the solubilities of the binary compounds into the ternary, only slight deviations can be observed at the two temperatures and also the two phase equilibria are alike. Hence, the appearance of the two isothermal sections resemble each other as well as the previously investigated ternary systems of Sb-Se-V [130] and Pb-Se-V [107]. In all of the systems of the type M-Se-V (M = Pb, Sb, and Sn), the three-phase equilibria in this part connect the phases of the binary M-V phase diagram with the SeV phase in a radial manner (e.g. SeV + V + SnV_3, SeV + SnV_3 + Sn_2V, and SeV + Sn_2V + L_2 – refer to Figure 42c/d).

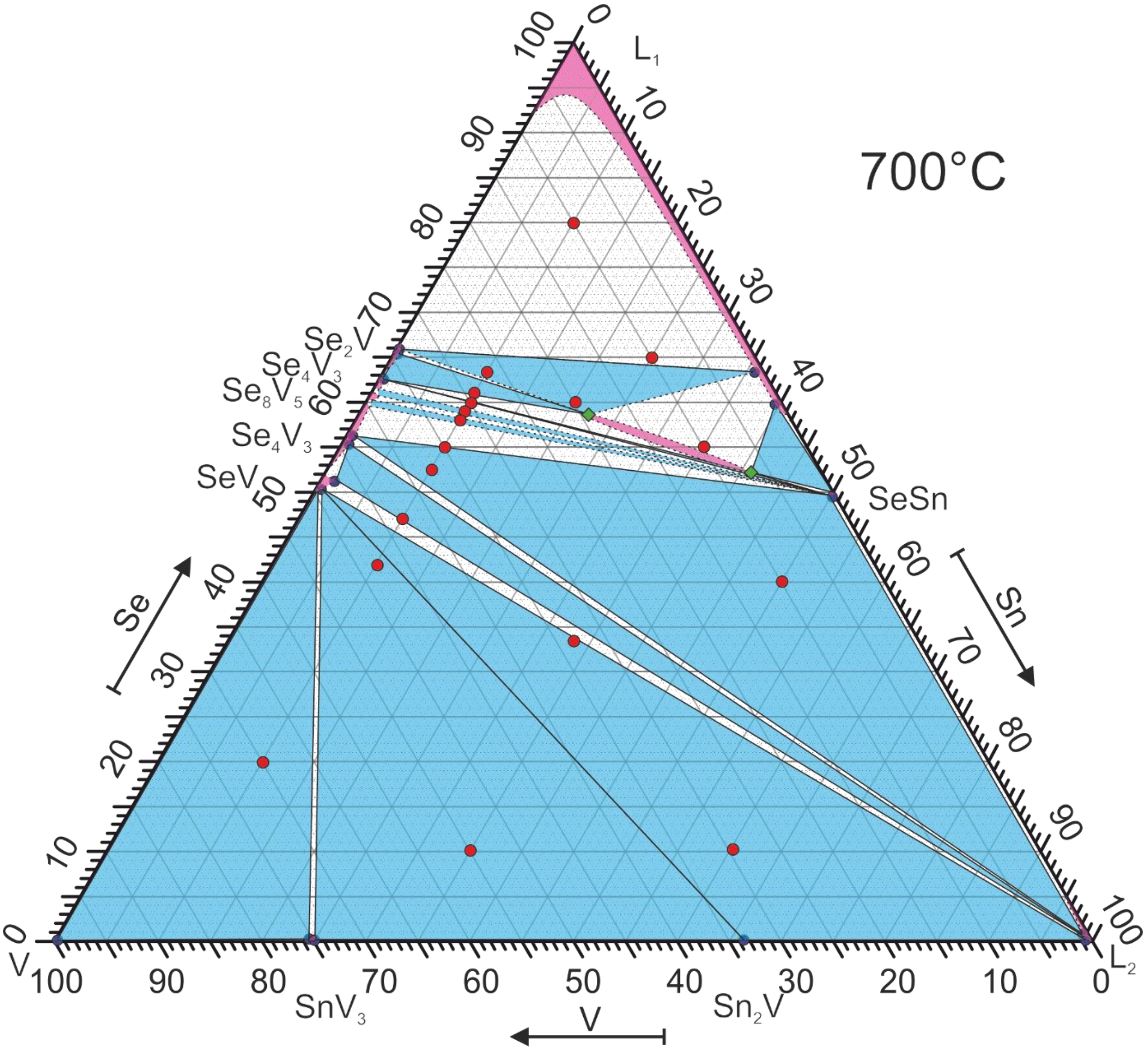

Figure 40: Isothermal section at 700 °C; blue triangles reflect the three-phase-fields; Sd52, Sd54, Sd56, Sd64, Sd72, Sd76, Sd80, Sd82, and Sd84 are used for the construction of the three-phase-equilibria; three-phase-equilibria and single-phase fields with uncertainty are indicated by dashed lines; nominal sample locations and selected EPMA results are indicated by red and blue dots, respectively; possible locations for the MLC in this system are marked by green squares.

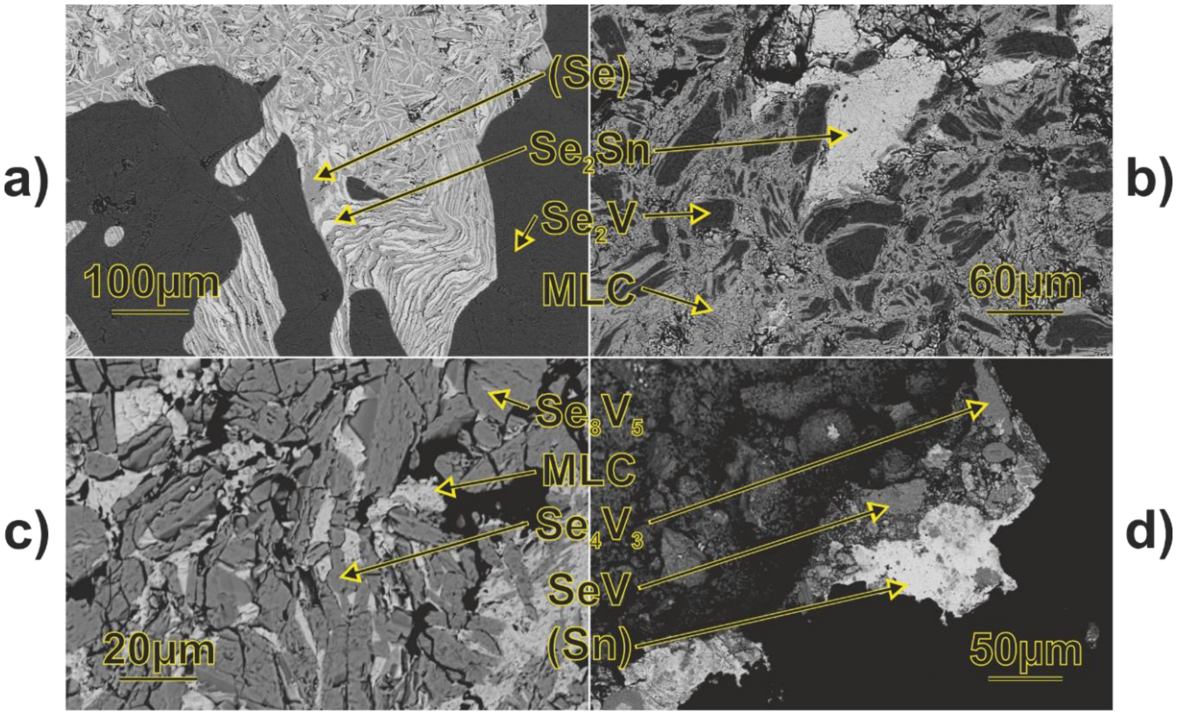

Figure 41: Typical microstructures of samples annealed at 550 °C (Sd49 (a), Sd51 (b), Sd63 (c), and Sd77 (d)); (Se) and (Sn) are liquified at the annealing conditions and represent compositions o L_1 and L_2, respectively.

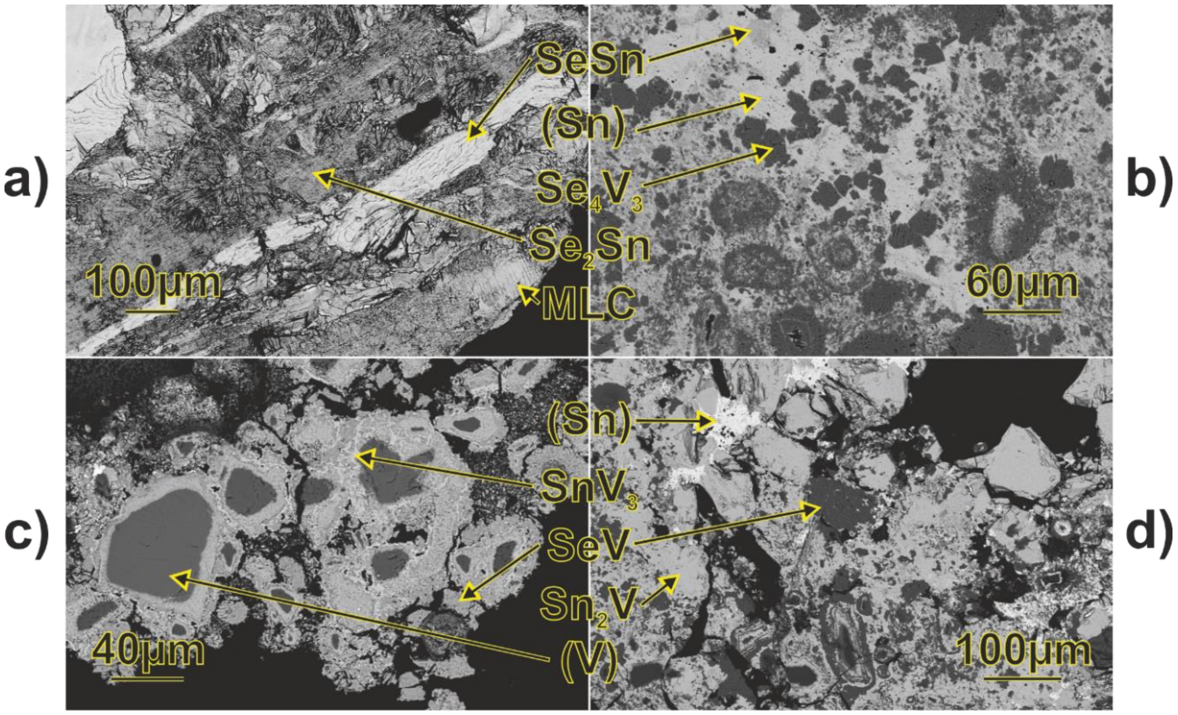

Figure 42: Typical microstructures of samples annealed at 700 °C (Sd54 (a), Sd72 (b), Sd80 (c), and Sd82 (d)); Se_2Sn and (Sn) are liquified at the annealing conditions and represent compositions of L_1 and L_2, respectively.

Surprisingly, the phase compositions of “SnV_3” and “Sn_2V” were observed at their stoichiometric composition and not the deviating compositions of SnV_4 and Sn_3V_2, respectively [203, 204]. In contrast to this, Komathy reported a homogeneity for “SnV_3” ranging between a tin content of 22 and 26 at.% [198] Furthermore, a metastable, yet stoichiometric, variant in the Ni_3Sn prototype is reported [200]. Phase diagrams and crystallographic data are in contradiction for the “Sn_2V” compound. Whereas the phase diagrams report the compound at 60 at.% Sn [203, 204] or 60 to 62 at.% Sn [199, 200], which are based on the comparison of theoretical and actual densities, the most recent single-crystal XRD refinements of this phase showed nearly full occupancy of all sites [206, 208]. Smith concluded in his assessment that for the phases “SnV_3” and “Sn_2V” some configurational disorder is contributing to their stabilisation [203]. This is relevant as substitution by foreign atom species can have a similar stabilising effect. As as matter of fact, several investigations on ternary systems including tin and vanadium (Fe-Sn-V [209], Mn-Sn-V [210], and Ni-Sn-V [211]) reported the “SnV_3” and “Sn_2V” phases right at their stoichiometric composition or with some homogeneity range around it. This is consistent with the present investigation. However, there are also reports for ternary systems where “SnV_3” and “Sn_2V” are near SnV_4 and Sn_3V_2 – but in combination with a larger solubility into the ternary (Mn-Sn-V [212] and Sn-Ti-V [197, 213]). Hence, either most of the binary Sn-V phase diargams published are incorrect regarding the composition of “SnV_3” and “Sn_2V”, as it was already noted for “Sn_2V” by Yue et al [206], or there might be an error in the three ternary systems Fe-Sn-V [209], Mn-Sn-V [210], and Ni-Sn-V [211] as well as our present work for these compounds. Additional studies in the binary Sn-V system are required to resolve this question.

As expected by comparison with the closely related Pb-Se-V system, the phase equilibria SeV + L_2 + Se_4V_3 and L_2 + Se_4V_3 + SnSe (refer to Figure 42b) were observed in both sections. In our first measurements, the liquid showed an unexpected composition (approximately 42 at.% Se, 43 at.% Sn, and 15 at.% V in sample Sd67 – for detailed compositions of all measurements refer to the supplementary materials sections). This is due to the sample treatment, where all samples were heated to 900 °C for 1h, in order to homogenise them well, and afterwards annealed at 550 and 700 °C, respectively. It indicates a ternary reaction ($L_3 = L_2 + Se_4V_3 + SnSe$) between 700 and 832 °C and with L_3 being around that composition (refer to Figure 36).

The by far most challenging region of the Se-Sn-V phase diagram is located between the phases Se_2Sn, SeSn, Se_4V_3, and Se_2V. Besides the readily described pseudo-single phase fields of Se_4V_3 and Se_8V_5, which were reported to be challenging in the determination of phase equilibria in the Pb-Se-V system [107], a slight shift of SeSn und Se_2Sn otablef approximately 1.5 at.% towards tin-rich compositions was observed. Additionally, no traces of a high-temperature variant of SeSn could be found in PXRD (refer to Table 15 and Table 16). In contrast to the previous investigations conducted by Hernan et al [61, 95] on MLCs in this system, not only one but a total of six MLCs were observed in our experiments. It was not necessary to add NH_4Cl to obtain those six new intermetallic phases. NH_4Cl is frequently utilised in MLCs' synthesis, where it functions as crystallisation aid and facilitate the formation of those compounds [35, 107, 121, 122].

The six new misfit layer compounds' average compositions are visible in Table 17. These MLCs grow on the surface of the sintered pills up to crystal sizes of approximately 4.000 x 4.000 x 20 µm and in the sintered pills up to crystal sizes of approximately 30 x 30 x 8 µm. The morphology (refer to Figure 43), especially the steps on the surface, indicate a synthesis route including gas-phase species. The delicate layered structure is sensitive to any manipulation, complicating our attempts of a crystallographic investigation.

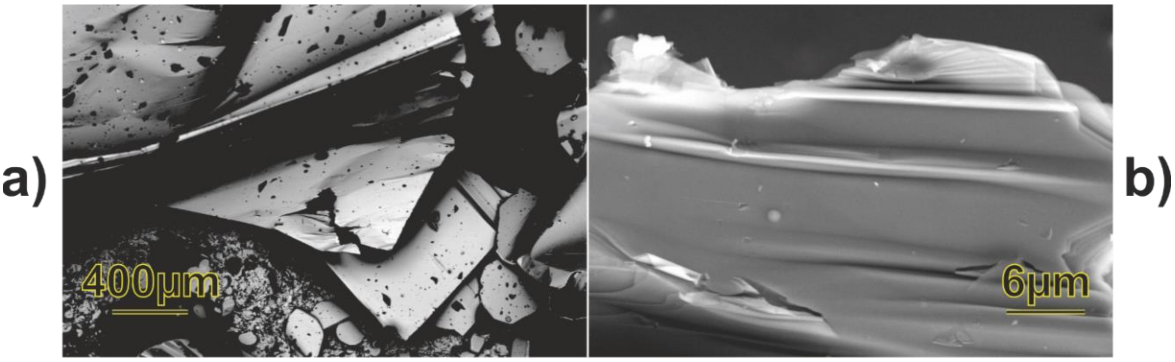

Figure 43: Misfit layer compound in the Se-Sn-V system; (a) large MLCs' crystals growing from the sintered powder pill of sample Sd58; (b) delamination of MLCs' due to mechanical stress yields thin and rippled layers.

Table 15: Assessed measurement data and ternary phase equilibria of all samples located in the boundary region of the Se-Sn-V system; the samples annealing temperature and nominal composition (in at.% Se, Sn, and V) are visible in the first column; the assessed mean values of EMPA-results for each phase is listed for the equilibrium phases, similar as the corresponding lattice parameters and space groups in PXRD.

Sample	Phase (EPMA)	Se (at%)	Sn (at%)	V (at%)	Phase (PXRD)	Space group	a	b	c	α	β	γ
sd49	Se2V	66.2(3)	0.07(6)	33.8(3)	Se2V	P-3m1	3.353	3.353	6.10	90	90	90
80/10/10	Se2Sn	66(7)	33(6)	1(3)	Se2Sn	P-3m1	3.807	3.807	6.13	90	90	90
550°C	Se (L1)	98(2)	2(2)	0.1(5)	Se amophous	-	-	-	-	-	-	-
sd50	Se2V	66.1(3)	0.03(2)	33.9(3)	Se2V	P-3m1	3.357	3.357	6.11	90	90	90
80/9.9/10	Se2Sn (L1)	65.5(3)	34.4(3)	0.07(6)	Se2Sn	P-3m1	3.810	3.810	6.13	90	90	90
700°C	Se (L1)	99.3(3)	0.5(4)	0.1(1)	Se amophous	-	-	-	-	-	-	-
sd66	SeSn	48.7(4)	51.2(4)	0.1(1)	SeSn lt	Pnma	11.501	4.152	4.44	90	90	90
58/10/32	Se4V3	62.4(5)	0.09(7)	37.5(5)	Se4V3	C12/m1	13.276	3.440	5.99	90	116.45	90
700°C	-	-	-	-	-	-	-	-	-	-	-	-
sd67	SeSn	48.6(6)	50.4(7)	1(2)	-	-	-	-	-	-	-	-
55/10/35	Se8V5	60.6(3)	0.6(8)	38.8(8)	Se8V5	C12/m1	11.830	7.017	8.32	90	134.07	90
550°C	Se4V3	59.5(3)	0.8(7)	39.6(6)	Se4V3	C12/m1	13.201	3.440	6.12	90	116.36	90
sd68	SeSn	48.7(6)	51.1(6)	0.22(2)	SeSn lt	Pnma	11.502	4.153	4.44	90	90	90
55/10.1/35	Se4V3	59.6(3)	0.11(5)	40.3(3)	Se4V3	C12/m1	13.202	3.437	6.13	90	116.31	90
700°C	-	-	-	-	-	-	-	-	-	-	-	-
sd69	SeSn	48.7(4)	50.1(6)	1.2(5)	SeSn lt	Pnma	11.506	4.156	4.44	90	90	90
52.5/10/37.5	Se4V3	57.5(9)	0.5(3)	42(9)	Se4V3	C12/m1	13.220	3.445	6.17	90	116.21	90
550°C	-	-	-	-	-	-	-	-	-	-	-	-
sd70	SeSn	48.6(5)	51.2(7)	0.1(2)	SeSn lt	Pnma	11.500	4.153	4.45	90	90	90
52.5/10.1/37.4	Se4V3	56.7(5)	0.3(1)	43.1(5)	Se4V3	C12/m1	13.226	3.452	6.19	90	116.19	90
700°C	-	-	-	-	-	-	-	-	-	-	-	-
sd71	Sn (L2)	0.2(2)	99.3(7)	0.5(5)	Sn beta	I41/amdZ	5.832	5.832	3.18	90	90	90
40.1/49.8/10.2	SeSn	48.3(3)	51.605(7)	0.2(2)	SeSn lt	Pnma	11.499	4.153	4.44	90	90	90
550°C	Se4V3	56.8(3)	0.36(9)	42.9(2)	Se4V3	C12/m1	13.234	3.461	6.20	90	116.18	90
sd72	Sn	0.8(3)	98.5(4)	0.6(1)	Sn beta	I41/amdZ	5.835	5.835	3.18	90	90	90
40/50.1/9.9	SeSn	48.5(4)	51.3(3)	0.2(1)	SeSn lt	Pnma	11.501	4.155	4.45	90	90	90
700°C	Se4V3	56.3(5)	0.4(1)	43.3(4)	-	-	-	-	-	-	-	-
sd73	Sn (L2)	1(6)	98.4(8)	0.6(2)	Sn beta	I41/amdZ	5.831	5.831	3.18	90	90	90
33.4/33.3/33.4	SeSn	48.7(4)	51.1(3)	0.2(2)	SeSn lt	Pnma	11.499	4.157	4.43	90	90	90
550°C	Se4V3	55.9(7)	1(1)	43.1(8)	Se4V3	C12/m1	13.231	3.461	6.21	90	116.20	90
sd74	Sn	2(1)	96(2)	2(7)	Sn beta	I41/amdZ	5.832	5.832	3.18	90	90	90
33.3/33.4/33.3	Se4V3	54(1)	1(1)	44(1)	Se4V3	C12/m1	13.235	3.464	6.21	90	116.21	90
700°C	-	-	-	-	-	-	-	-	-	-	-	-
sd75	Fine micro-structure (L3)	48(2)	26(8)	27(7)	Sn beta	I41/amdZ	5.831	5.831	3.18	90	90	90
46.9/10.2/42.9	-	-	-	-	SeSn lt	Pnma	11.515	4.158	4.43	90	90	90
550°C	Se4V3	56(1)	0.5(2)	44(1)	Se4V3	C12/m1	13.233	3.461	6.21	90	116.18	90
sd76	Sn (L2)	1(2)	84(3)	15(2)	Sn beta	I41/amdZ	5.832	5.832	3.18	90	90	90
47/9.9/43.1	SeV	52.3(3)	0.3(2)	47.3(1)	SeV hP4	P63/mmc	3.658	3.658	6.04	90	90	120
700°C	Se4V3	55(1)	0.6(7)	44(1)	Se4V3	C12/m1	13.233	3.462	6.21	90	116.19	90
sd77	Sn (L2)	1(1)	97(3)	2(2)	Sn beta	I41/amdZ	5.833	5.833	3.15	90	90	90
42.2/10.1/47.7	SeV	50(1)	1(1)	48(2)	SeV hP4	P63/mmc	3.603	3.603	6.00	90	90	120
550°C	Se4V3	53.2(7)	0.5(7)	46.3(7)	Se4V3	C12/m1	13.310	3.494	6.22	90	116.44	90
sd78	Sn	0.7(5)	98.8(7)	0.5(2)	Sn beta	I41/amdZ	5.833	5.833	3.18	90	90	90
41.8/10.2/48.1	SeV	51.2(7)	1.3(8)	48(1)	SeV hP4	P63/mmc	3.636	3.636	5.99	90	90	120
700°C	-	-	-	-	-	-	-	-	-	-	-	-
sd79	V	0.003(8)	0.12(8)	99.87(8)	V	Im-3m	3.043	3.043	3.04	90	90	90
20.1/10.1/69.8	SnV3	0.6(9)	25(1)	74.3(9)	SnV3	Pm-3n	4.976	4.976	4.98	90	90	90
550°C	SeV	49.9(8)	0.4(4)	49.7(8)	SeV hP4	P63/mmc	3.723	3.723	6.01	90	90	120
sd80	V	0(0)	0.12(1)	99.89(1)	V	Im-3m	3.033	3.033	3.03	90	90	90
19.8/10.1/70.1	SnV3	0.1(2)	24.4(4)	75.5(5)	SnV3	Pm-3n	4.984	4.984	4.98	90	90	90
700°C	SeV	51(1)	0.2(2)	49(1)	SeV hP4	P63/mmc	3.708	3.708	6.00	90	90	120
sd81	Sn2V	0(0)	66.7(2)	33.3(2)	Sn2V	FdddS	9.494	5.487	18.68	90	90	90
10.1/60.3/29.6	Sn (L2)	0.6(4)	98.6(8)	0.8(5)	Sn beta	I41/amdZ	5.831	5.831	3.18	90	90	90
550°C	SeV	51(8)	0.4(3)	48.6(6)	SeV hP4	P63/mmc	3.682	3.682	5.99	90	90	120

Considering the different stacking possibilities and the thermodynamic stability of layered compounds [101, 126], those compositions for $[(SeSn)_{1+\delta}]_m(VSe_2)_n$ most probably reflect stacking scenarios with *m* being 1, 2, 3, 4, 5, and 6 and *n* being 1. The smallest integer ratio for *m* and *n* (e.g. $m = 2$ and $n = 1$) is reported to be more stable than a multiple of these values (e.g. $m = 4$ and $n = 2$) [101, 126]. As a matter of fact, our out-of-plane XRD and PXRD measurements did not exhibit the additional satellite reflections in (00*l*) that would be expected in the case of higher integer ratios ($m = n = 2$) as proposed by Hernan et al [61, 95] in their investigation on tin-based

Table 16: Assessed measurement data and ternary phase equilibria of all samples located in the central part of the Se-Sn-V system; the samples annealing temperature and nominal composition (in at.% Se, Sn, and V) are visible in the first column; the assessed mean values of EMPA-results for each phase is listed for the equilibrium phases, similar as the corresponding lattice parameters and space groups in PXRD; abbreviated comments describe the type of detection (area scan (A) or point scan (all others)), the MLCs' m and n stacking sequence (MLCm-n), and when several MLC modifications were observed the presumable equilibrium composition (*) is stated.

Sample	Phase (EPMA)	Cmt.	Se (at%)	Sn (at%)	V (at%)	Phase (PXRD)	Space group	a	b	c	α	β	γ
sd51	Se2V		65.9(4)	0.12(9)	33.9(5)	Se2V	P-3m1	3.355	3.355	6.14	90	90	90
65/24.9/10.1	Se2Sn		65.3(3)	34(3)	0.7(4)	Se2Sn	P-3m1	3.812	3.812	6.14	90	90	90
550°C	MLC1-1		58.6(7)	21.9(5)	19.5(4)	MLC	-	-	-	-	-	-	-
sd52	Se2V		65.9(3)	0.1(1)	33.9(3)	Se2V	P-3m1	3.356	3.356	6.10	90	90	90
65/25.1/10	(L1)	A	63(1)	36(1)	0.9(2)	Se2Sn	P-3m1	3.810	3.810	6.13	90	90	90
700°C	-	-	-	-	-	-	-	-	-	-	-	-	-
sd53	Se2V		66(3)	0.2(1)	33.9(3)	Se2V	P-3m1	3.358	3.358	6.12	90	90	90
60/20/20	MLC1-1		58.3(4)	22.2(2)	19.5(4)	MLC	-	-	-	-	-	-	-
550°C	-	-	-	-	-	-	-	-	-	-	-	-	-
sd54	SeSn		49.1(7)	50.6(7)	0.2(1)	SeSn lt	Pnma	11.518	4.158	4.42	90	90	90
60/20.2/19.9	MLC1-1		52.2(7)	41(7)	6.8(2)	Se2Sn	P-3m1	3.808	3.808	6.14	90	90	90
700°C	(L1)	A	60(1)	40(1)	0.6(2)	MLC	-	-	-	-	-	-	-
sd55	Se2V		66(2)	0.08(5)	33.9(2)	Se2V	P-3m1	3.357	3.357	6.10	90	90	90
55/35/10	MLC1-1		58.3(3)	22.1(5)	19.6(3)	MLC	-	-	~	12.07	90	90	90
550°C	-	-	-	-	-	-	-	-	-	-	-	-	-
sd56	SeSn		48.7(3)	51.1(3)	0.2(1)	SeSn lt	Pnma	11.508	4.148	4.44	90	90	90
55/35.1/9.9	Se2V		65.2(5)	0.2(4)	34.6(6)	Se2V	P-3m1	3.377	3.377	6.07	90	90	90
700°C	MLC1-1	*	58.4(5)	22.3(2)	19.3(3)	MLC	-	-	-	-	-	-	-
sd57	SeSn		49(2)	50.9(2)	0.13(8)	SeSn lt	Pnma	11.519	4.156	4.41	90	90	90
63.4/10/26.6	Se2Sn		65.4(2)	34.5(2)	0.11(2)	Se2Sn	P-3m1	3.808	3.808	6.18	90	90	90
550°C	MLC 5-1	*	52.3(6)	40.6(9)	7.1(3)	MLC	-	-	-	-	-	-	-
sd58	Se2V		65.4(3)	0.07(4)	34.5(3)	Se2V	P-3m1	3.369	3.369	6.08	90	90	90
63.4/10/26.7	MLC 1-1		59(1)	22.1(5)	19.3(6)	MLC	-	-	-	-	-	-	-
700°C	(L1)	A	59(1)	40.5(8)	0.7(2)	-	-	-	-	-	-	-	-
sd59	Se2V		64.3(4)	0.2(1)	35.5(4)	Se2V	P-3m1	3.404	3.404	6.02	90	90	90
61/10/29	MLC 1-1	*	58.6(4)	21.7(5)	19.6(4)	MLC	P-1	-	-	-	-	-	-
550°C	-	-	-	-	-	-	-	-	-	-	-	-	-
sd60	SeSn		49.5(5)	50.3(8)	0.3(3)	SeSn lt	Pnma	11.503	4.152	4.44	90	90	90
61/9.9/29.1	Se2V		64.7(2)	0.04(3)	35.2(2)	Se2V	P-3m1	3.390	3.390	6.04	90	90	90
700°C	-	-	-	-	-	-	-	-	-	-	-	-	-
sd61	Se4V3		63.5(1)	0.2(1)	36.3(2)	Se4V3	C12/m1	13.270	3.460	6.29	90	117.24	90
60/10.1/29.9	Se2V		63.9(2)	0.3(3)	35.7(3)	Se2V	P-3m1	3.413	3.413	6.00	90	90	90
550°C	MLC 2-1		55.5(5)	30.4(6)	14.1(3)	MLC	-	-	-	-	-	-	-
sd62	SeSn		48.5(4)	51.3(4)	0.2(2)	SeSn lt	Pnma	11.502	4.153	4.44	90	90	90
59.9/10.1/30	Se2V		64(3)	0.06(6)	36(3)	Se2V	P-3m1	3.410	3.410	6.01	90	90	90
700°C	-	-	-	-	-	-	-	-	-	-	-	-	-
sd63	Se8V5		61.3(2)	0.22(4)	38.5(2)	Se8V5	C12/m1	11.831	7.000	8.31	90	134.12	90
59/10.1/30.9	Se4V3		62.4(6)	0.15(4)	37.5(6)	Se4V3	C12/m1	13.470	3.416	5.96	90	116.78	90
550°C	MLC 2-1	*	55.7(4)	29.9(4)	14.45(7)	MLC	-	-	-	-	-	-	-
sd64	SeSn		48.8(3)	51.1(2)	0.1(1)	SeSn lt	Pnma	11.501	4.154	4.44	90	90	90
59/10/31	Se4V3		62.9(5)	0.06(5)	37(5)	Se4V3	C12/m1	13.420	3.399	6.10	90	117.03	90
700°C	MLC 6-1		52.2(9)	42(1)	6.3(3)	MLC	-	-	-	-	-	-	-
sd65	Se8V5		61.3(4)	0.3(2)	38.4(5)	Se8V5	C12/m1	11.829	6.996	8.32	90	134.11	90
58/10/32	MLC 3-1	*	55(2)	34(2)	10.6(2)	-	-	-	-	-	-	-	-
550°C	MLC 4-1	*	54(2)	36(1)	9.4(5)	MLC	-	-	-	-	-	-	-

Table 17: Misfit layer compounds present in the Se-Sn-V system; the theoretical values for the corresponding MLCs at different m and n are calculated with a misfit parameter δ=0.

Sample	Experimental			Theory				
	Se (at%)	Sn (at%)	V (at%)	m	n	Se (at%)	Sn (at%)	V (at%)
sd51	58.6(7)	21.9(5)	19.5(4)	1	1	60.0	20.0	20.0
sd63	55.7(4)	29.9(4)	14.45(7)	2	1	57.1	28.6	14.3
sd65	55(2)	34(2)	10.6(2)	3	1	55.6	33.3	11.1
sd65	54(2)	36(1)	9.4(5)	4	1	54.5	36.4	9.1
sd57	52.3(6)	40.6(9)	7.1(3)	5	1	53.8	38.5	7.7
sd64	52.2(9)	42(1)	6.3(3)	6	1	53.3	40.0	6.7

MLCs (refer to Figure 44). However, the crystal structures of the present MLCs are still under investigation and will be published elsewhere. This lack of final crystal structure models complicates the PXRD refinements and, hence, no lattice parameters of the MLCs are presented in Table 16.

Some samples contained not only three phases but a multitude of MLCs (e.g. Sd57). Multiphase samples, which were observed several times (refer to Table 16), are presumably caused by the gas phase, regardless of the description model. The gas phase, which is certainly involved in the MLCs' synthesis, certainly changes gradually in a temperature gradient just like MLCs' composition does. Such unavoidable temperature gradients may explain the multitude of observed MLCs. Yet, it is unknown whether at lower temperatures higher multiples of values for stacking sequence parameters *m* and *n* can be obtained, when there is a kinetic hindrance for equilibration to the smallest integer ratio for *m* and *n* but still high enough vapour pressures or diffusivities for the MLCs' formation.

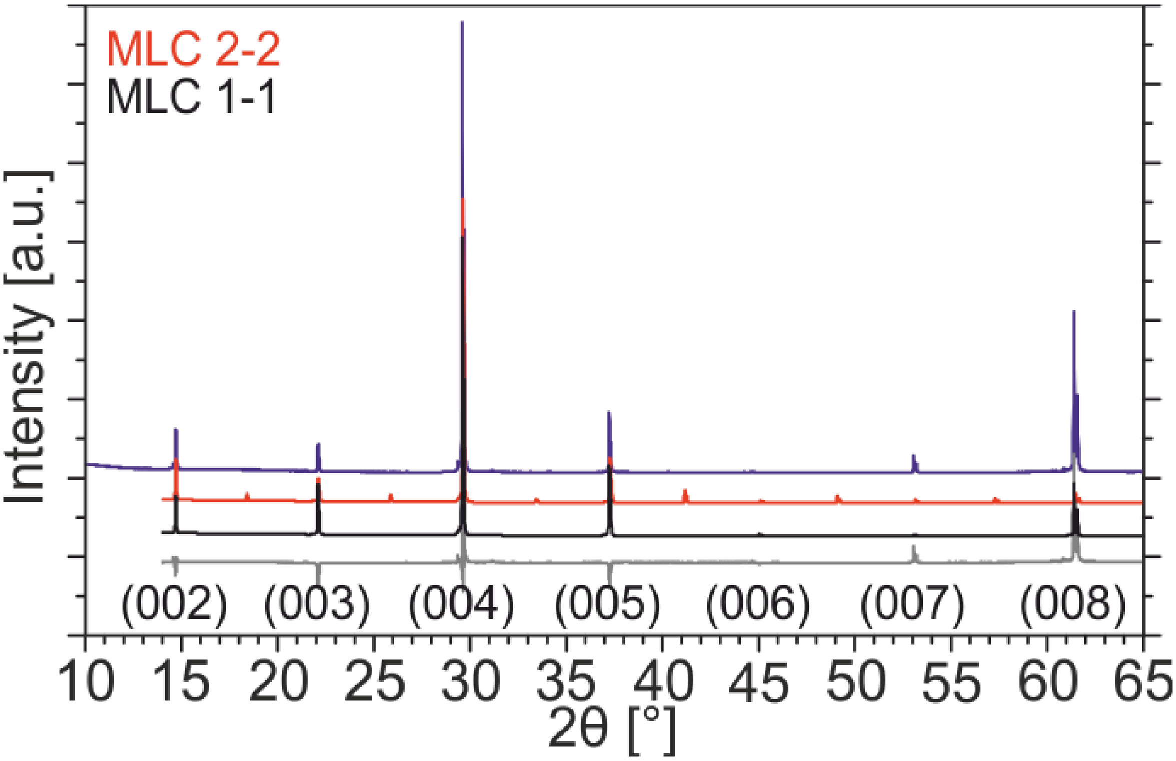

Figure 44: Out-of-plane XRD pattern of the unpowdered sample Sd58; the experimental and difference pattern from the Rietveld refinement are shown in blue and grey, respectively; the calculated patterns for MLCs with m=n=1 (black) and m=n=2 (red), show that only former is present; the typical 00l reflections for an MLC with n=m=1 appropriately indexed.

The phase equilibria involving these MLCs, which are located on the pseudo-binary section between Se_2V_{1+x} and SeSn, allow two different descriptions (refer to Figure 45 and Figure 46 for the exemplary description at 550 °C). On the one hand, each MLC can be treated as an individual phase with different *c* parameters. On the other hand, the MLCs can be treated like a homogeneous single-phase field with rather similar lattice parameters for *a* and *b*, but with modulation in *c*. Comparable situations are known in the literature for phase diagrams such as the extensively investigated Bi-Se binary system, where Okamoto [214] utilises the former and Antipov et al and Lind et al the latter description model [215-217]. However, both models have certain advantages and limitations in the case of the Se-Sn-V system.

Treating all MLCs, that were observed in the two isothermal sections, as individual phases necessitate a larger number of three-phase equilibria (refer to Figure 45). From a thermodynamic view, this description is certainly more accurate, as only MLCs with $n = 1$ were observed in our experiments. Hence, a continuous description would (erroneously) suggest that any stacking sequence for the parameters *m* and *n* could be obtained by standard solid-state chemistry synthesis methods, as it is possible for the binary Bi-Se system employing a description of different building blocks. This, however, is only experimentally possible by the utilisation of the modulated element approach for the metastable *fere*crystaline compounds. The argument supporting the model of individual phases is the fact that only rational ratios with $1 \leq m \leq 6$ and $n = 1$ were observed. Unfortunately, a description by individual misfit layer compound phases requires a large number of very narrow three-phase fields. For instance, the phase fields of Se_8V_5 + $[(SeSn)_{1+\delta}]_4(VSe_2)_1$ + $[(SeSn)_{1+\delta}]_5(VSe_2)_1$ and SeSn + $[(SeSn)_{1+\delta}]_5(VSe_2)_1$ + $[(SeSn)_{1+\delta}]_6(VSe_2)_1$ are merely visible in Figure 45. This large number of narrow three-phase fields not only complicates their determination (e.g. small inhomogeneities in the samples might cause failure) but yields rather incomprehensible visualisations in the form of full isothermal sections.

When one single-phase field for all observed MLCs is employed in the isothermals sections the clarity and comprehensibility are ultimately improved (refer to Figure 46). In this description, only six three-phase fields involving MLCs are necessary (compared to 16 in the other case), which could all be determined successfully by direct and/or indirect means. In our isothermal sections, no values for the stacking sequence parameter other than $n = 1$ were observed, which does not permit such a single-phase field as described. However, a large single-phase field would fit our

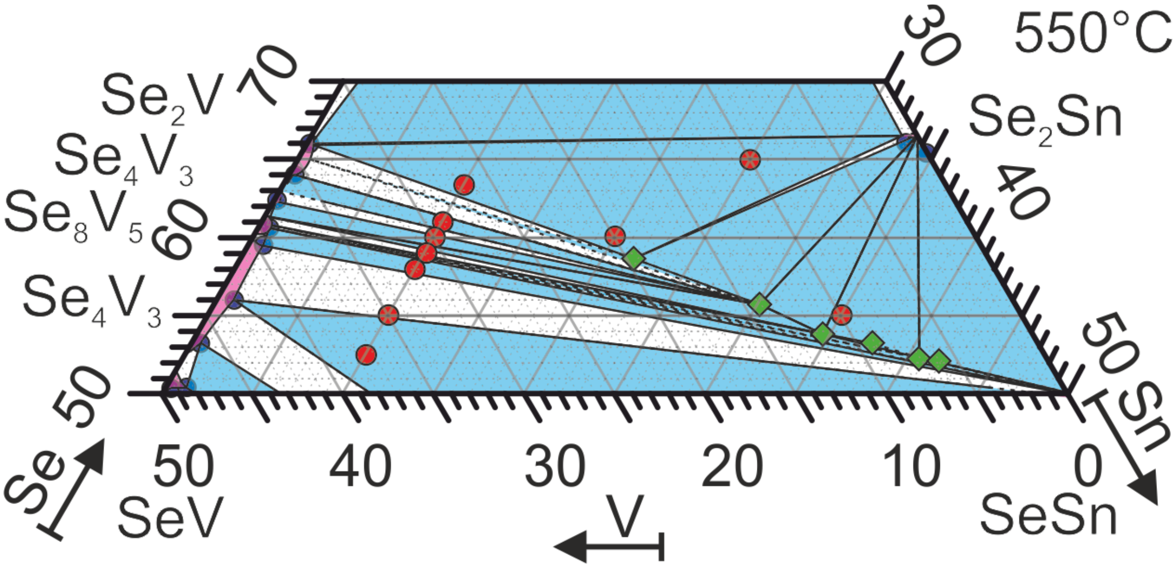

Figure 45: Partial isothermal section at 550 °C utilising the model of individual MLC-phases; blue triangles reflect the three-phase-fields; samples Sd49, Sd51, Sd57, Sd61, Sd63, Sd65, Sd67, Sd73, and Sd77 are used for the construction of the three-phase-equilibria; three-phase-equilibria and single-phase fields with uncertainty are indicated by dashed lines; nominal sample locations and selected EPMA results are indicated by red and blue dots, respectively; possible locations for the MLC in this system are marked by green squares.

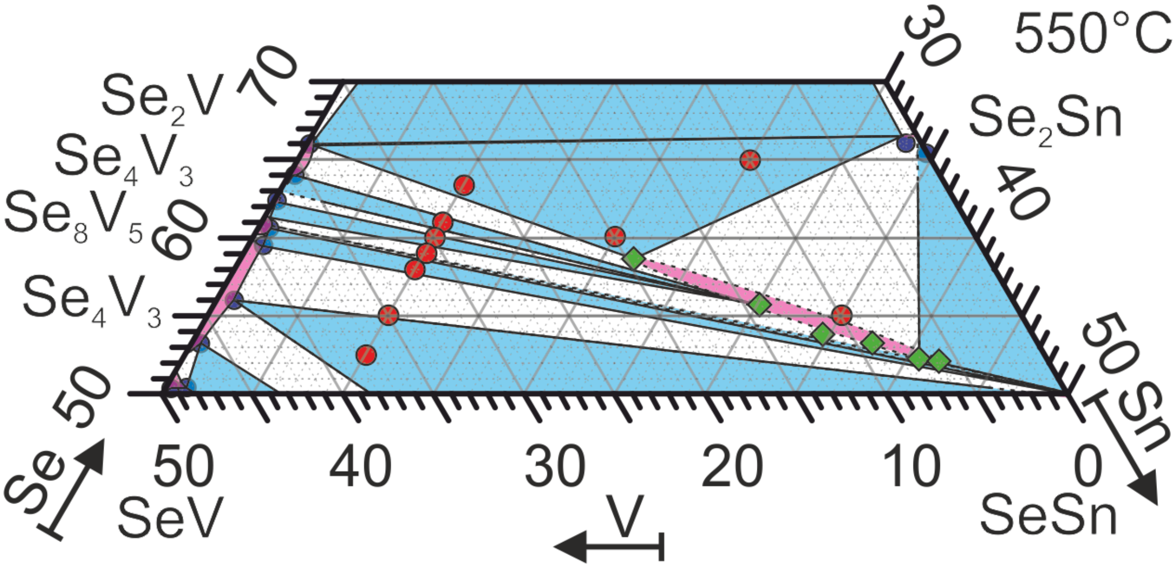

Figure 46: Partial isothermal section at 550 °C utilising the model of a single homogeneity range for all MLC-phases; blue triangles reflect the three-phase-fields; samples Sd49, Sd51, Sd57, Sd61, Sd63, Sd67, Sd73, and Sd77 are used for the construction of the three-phase-equilibria; three-phase-equilibria and single-phase fields with uncertainty are indicated by dashed lines; nominal sample locations and selected EPMA results are indicated by red and blue dots, respectively; possible locations for the MLC in this system are marked by green squares.

difficulties to obtain suitable single crystals for single crystal XRD measurements, as even small amounts of stacking faults hamper such an investigation.

After careful data assessment, both models can be used for the description. Of the two possible models, we favour the latter model of one single-phase field for all observed MLCs for both isothermal sections at 550 °C and 700 °C, respectively. It permits the reader of phase diagrams an overview in a clear and concise manner. However, crystallographic investigations in future might favour the former model of individual phases as it might be easier to describe individual phases rather than a modulated and incommensurate structure.

6.9. Conclusion

Two isothermal sections were constructed for the ternary system of Se-Sn-V for 550 °C and 700 °C. The shift in composition for the compounds “Sn_2V” and “SnV_3”, which was reported for the binary Sn-V system [202-204, 206], was not observed but the stoichiometric compositions can be reported. Additional research, which specifically focuses on these phases, is suggested for future investigations in the binary Sn-V system.

The phase equilibria exhibit similar behaviour as in the previously investigated Pb-Se-V and Sb-Se-V systems [107, 130]. Also, the solid solubilities and the solubilities of the liquids are small in the two isothermal sections as in those two systems. As maximal values we report vanadium-contents of 1.2 at.% in SeSn, tin-contents of 1.3 at.% in SeV, and selenium-contents of 0.6 at.% in SnV_3.

Six MLCs are observed in the two isothermal sections without addition of NH_4Cl. Their respective compositions correspond to stacking values of m = 1, 2, 3, 4, 5, and 6 in the general formula $[(SeSn)_{1+\delta}]_m(VSe_2)$. Two possible models may explain the difficult situation for determining the ternary phase equilibria in this part. We suggest a large single-phase field of different compositions of MLCs, as this not only enhances readability. Nevertheless, the crystal structures present in this system are still under investigation. A detailed description of the present MLCs is in preparation and will be published elsewhere.

6.10. Acknowledgements

Special thanks go to Herta Effenberger from the Department of Mineralogy and Crystallography, University of Vienna, and Alexander Roller from the Department of Chemistry, University of Vienna, for their patience in attempting to find suitable single crystals for XRD of the MLC phases $[(SeSn)_{1+\delta}]_m(VSe_2)$. The authors wish to thank Stephan Puchegger from the Department of Physics, University of Vienna, for his help with SEM measurements and express gratitude to Patricia Jenner for proof-reading and her linguistic advice.

6.11. Declarations of interest

The authors declare that there is no conflict of interest.

7. Manuscript 3: Vanadium-selenium-based misfit layer compounds – insights into synthesis, morphology, and structure

7.1. Authorship Statement

Chapter 7 describes material that will be submitted to *The Journal of Alloys and Compounds* in 2020. The co-author is Klaus W. Richter, who is my advisor and I am the primary author of the manuscript.

Reisinger: Conceptualisation, Investigation, Writing - Original Draft, Visualisation

Richter: Conceptualisation, Writing - Review & Editing, Supervision, Project administration

7.2. Abstract

Different approaches and conditions of synthesis for misfit layer compounds (MLCs) are compared for the ternary systems V-Se-Bi, V-Se-Pb, and V-Se-Sn. Best results were obtained with NH_4Cl as crystallisation aid, moderate annealing temperatures, and long annealing durations. The compositions, the morphology, and the structure are discussed. Depending on the stacking sequence of the compound, only plate-like or tube-like MLC crystals could be obtained. The structural properties, but not all the structural defects, of the MLC $(PbSe)_{1+\delta}VSe_2$ are comparable to the respective ferecrystals in the literature.

7.3. Keywords

Ternary alloy system, misfit layer compounds, Synthesis, Scanning electron microscopy, Transmission electron microscopy, X-ray diffraction

7.4. Prime novelty statement

In this letter, we compare synthesis approaches for vanadium-based MLCs. Some insights into the morphology and crystal structure of these crystals are given.

7.5. Highlights

- Comparison of synthesis approaches

- Microwave-assisted synthesis method is not successful for synthesising vanadium-based MLCs
- Tubular shaped MLCs in the V-Se-Sn system
- Structural insights into MLC in the V-Se-Pb system

7.6. Introduction

Since the isolation of graphene and the discovery of strikingly different properties of these 2D-materials, many investigations concerned the preparation of other low dimensional materials. Especially, quasi-2D-materials, such as boron nitride, hybrid perovskites, and transition metal dichalcogenides (TMDs), as well as their heterostructures, raised interest for a wide range of electrical properties in the bulk. Nanosheets of those compounds and heterostructures derived from them might be candidates for replacing expensive or inefficient materials in established applications (e.g. anode materials in lithium-ion batteries, next-generation electronics, and water splitting by hydrogen evolution reaction) or, due to some exotic properties, in unknown future applications.

Misfit layer compounds (MLCs) are hybrid structures with two substructures that are stacked in an alternating sequence (refer to Figure 47). The general formula $[(MX)_{1+\delta}]_m(TX_2)_n$ (T = early transition metal, X = chalcogen and M = Bi, Pb, Sb, Sn, or a rare earth element) reflects the alternating sequence of the distorted sodium chloride type bilayer (MX) and the TMD triple layer (TX_2). The stacking sequence is delivered by the parameters m and n [122]. Such MLC structures might stabilise properties of 2D-materials (e.g. superconductivity, charge density wave transitions, and magnetism) to ambient conditions and even alter them, by the precise control of sheet thicknesses or the manipulation of their orientation.

Up to now only little is known about vanadium-selenium-based MLCs [35, 59-61, 95, 107, 108, 130] and nothing is known about tellurium-based MLCs. For this reason, this work aimed to evaluate the different synthesis routes available and to apply them to the V-M-X (X = Se or Te and M = Bi, Pb, Sb, or Sn) ternary systems. Additionally, we attempted to gather knowledge on the morphological and structural properties of the resulting MLCs and compare them to the literature on MLCs and *fere*crystals [27, 28, 32, 37, 38, 67-70, 74, 80, 84, 85, 87, 96, 114, 120], which are obtained via a synthesis route that involves physical vapour deposition.

7.7. Materials and Methods

We attempted to synthesise vanadium-based MLCs of the formula $[(MX)_{1+\delta}]_m(VX_2)_n$ in systems where "M" denotes bismuth, lead, antimony, or tin and "X" denotes the chalcogens selenium or tellurium. Only high purity elements (>99.5 %), that were mostly stored in a glovebox, were utilised as source materials. Detailed information on the steps of weighing-out, pre-alloying, pressing of pills, and encapsulating in silica ampoules is reported elsewhere [107, 108, 130]. The synthesis conditions and procedures in the V-Se-Bi system were implemented in analogy to those reported steps. Various annealing procedures were attempted for the solid-state approach,

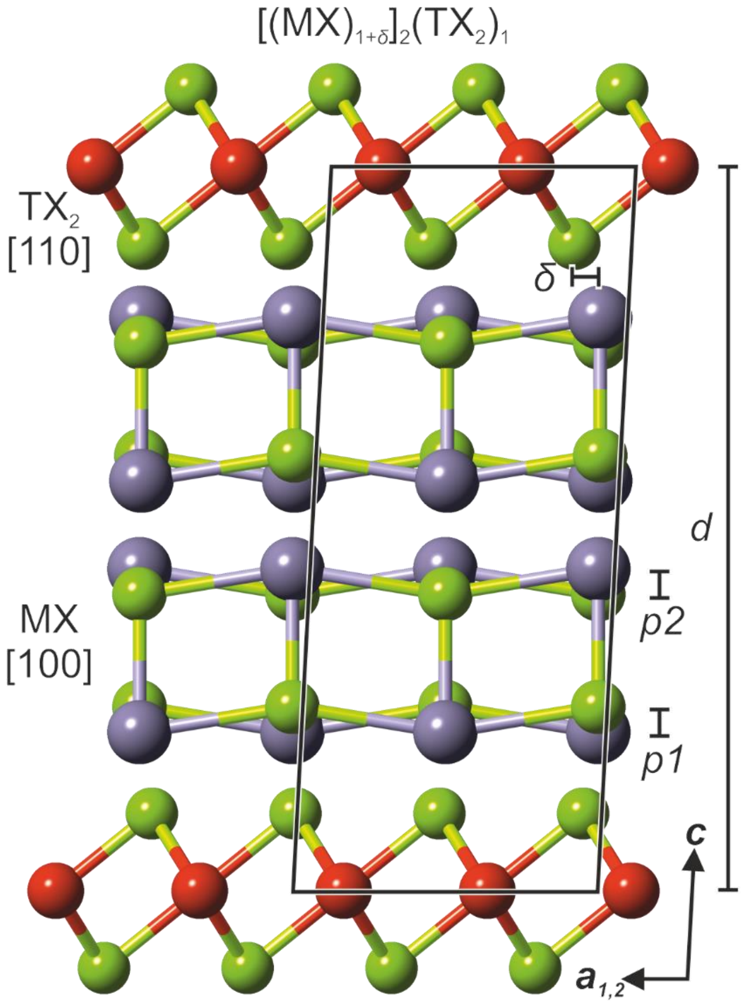

Figure 47: Schematic structure of a $[(MX)_{1+\delta}]_2(TX_2)_1$ *type MLC; the structure shows a monoclinic distortion in β; the misfit parameter (δ), the puckering of MX layers (p1 and p2), and the interlayer distance (d) are indicated.*

with durations and temperatures up to 18 months and up to 1000 °C. Different crystallisation aids (e.g. I_2, NH_4Cl [121, 122], and LiCl/KCl-eutectic [159]) were added to samples to investigate their influence and to compare it to synthesis without any mineraliser added.

Additionally, a second route of synthesis was attempted. Chaturvedi et al [218] successfully synthesised sulphides and selenides of early transition metals via a microwave-induced-plasma-assisted method. Based on their process setup, we constructed a similar device (refer to Figure 48). The major difference being that the silica ampoules contained the three elements required to synthesise a MLC as starting material and not just two as required for a transition metal dichalcogenide. Just like Du et al [219] reported, the pressure in the sample ampoules and in the

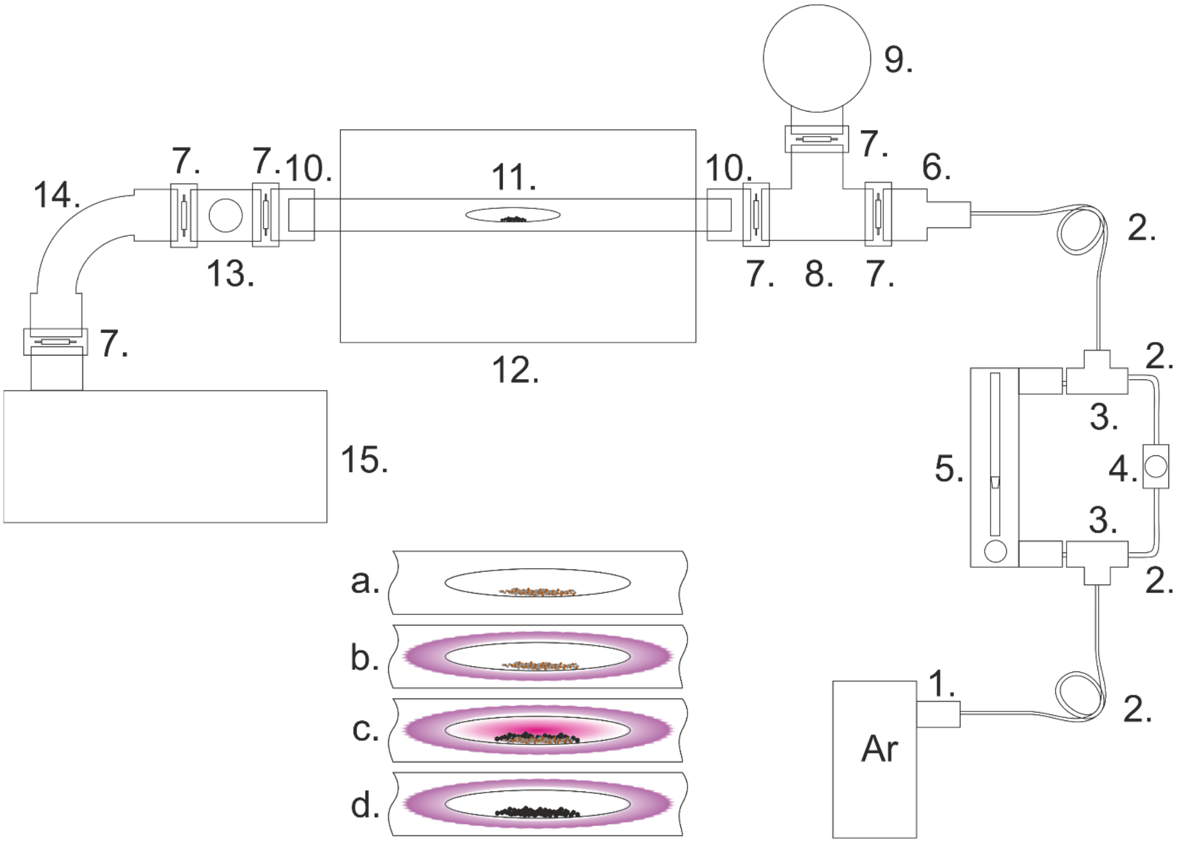

Figure 48: Schematic blueprint of the device and mechanism of the microwave-induced-plasma-assisted method; abbreviations denote: 1. hose fitting, 2. Teflon hose, 3. T-piece, 4. ball valve, 5. flow meter, 6. adapter, 7. clamping ring and centring ring, 8. T-piece, 9. digital pressure gauge (Thermovac), 10. flange with compression fitting, 11. Glass tube with sample ampoule, 12. 1000 W microwave oven, 13. Valve, 14. Corrugated metal hose, 15. Vacuum pump; stages: (a) without plasma heating, (b) heating of the powder by the outer tube argon plasma, (c) ignition of the inner tube selenium plasma, (d) collapse of the inner tube plasma and crystal growth.

outer silica tube was most favourable between 5 to 15 mbar. In our 1000 W microwave oven, the synthesis duration was shorter than 60 minutes.

The investigation methods we used for powder X-ray diffraction (PXRD), optical microscopy, and scanning electron microscopy (SEM) are reported elsewhere [107, 108, 130]. Additionally, we utilised transmission electron microscopy (TEM) and selected area electron diffraction (SAED) to further characterise the MLCs. The MLCs were exfoliated onto SiO_2 covered silicon wafers by the scotch tape method. After selecting the desired crystals by optical microscopy, they were transferred onto carbon-supported TEM grids. Scanning transition electron microscopy (STEM) images were obtained using a Nion Ultra STEM 100 electron microscope. It was operated at a 60 kV accelerating voltage in near ultra-high vacuum (2×10^{-7} Pa). High angle annular dark-field (HAADF) and medium-angle annular-dark-field (MAADF) images were collected. Selected area diffraction (SEAD) images were taken for the very same sample on another device (JEOL JEM-2100F at 200 kV).

7.8. Results and discussion

7.8.1. Synthesis

Vanadium-based misfit layer compounds with the formula $[(MX)_{1+\delta}]_m(VX_2)_n$ could be synthesised in the systems of V-Se-Bi [59, 60, 106], V-Se-Pb [107], and V-Se-Sn [95, 108] but not the V-Se-Sb system [130]. In the two ternary systems V-Se-Bi and V-Se-Pb, only the compositions with the stacking parameters $m = n = 1$ and in the V-Se-Sn ternary system all compositions with $m \leq 6$ and $n = 1$ were observed. Best results were obtained when NH_4Cl was utilised as mineralising agent. Apart from the V-Se-Sn system, no MLCs were observed, when no mineraliser was added, when I_2 was added, or when an eutectic salt melt of LiCl/KCl was utilisied. Hence, we conclude, that some chloride gas species favours the synthesis of vanadium-based MLCs. Noteworthy, the utilisation of the salt melt in V-Se-Sn had the advantage that the resulting MLCs were not intergrown but had the disadvantage of more difficult extraction and quicker corrosion/oxidation of the crystals. Albeit, the ideal source materials composition as well as the annealing temperature and duration varied slightly depending on the "M" element, some similarities were observable.

When the weighed out composition was close to the stoichiometric composition of the MLC, none or only small quantities of MLC crystals were obtained. We observed that with an off-stoichiometric sample composition (in the region between the three compositions of VSe_2, V_5Se_8, and MLC) larger qualities of MLC crystals could be obtained. A composition with larger vanadium content and close to V_5Se_8 was most favourable. Hence, we conclude that higher vanadium activities in vanadium-rich phases facilitate the MLCs' crystal growth via the gas phase and that this vanadium-based gas species determines the yield and the reaction speed of the MLCs' synthesis.

An annealing duration of one to three months (excluding pre-alloying time) at approximately 550 °C was found to be most successful for synthesising large crystals. This differs significantly literature where the utilised conditions for annealing were chosen to be between 2 days at 700 °C [60] and 15 days at 900 °C [95]. The largest obtainable crystal sizes varied for each composition and “M” element. The largest crystals were approximately 1.200 x 1.200 x 20 µm, 4.000 x 4.000 x 20 µm [108], and 200 x 200 x 10 µm [107] in size for the bismuth-, tin-, and lead-based system, respectively. In tellurium-based systems and antimony-based systems synthesis of MLCs was not feasible, regardless of the synthesis approach or annealing conditions.

A synthesis route via a microwave-induced-plasma could be expected to reduce the duration of synthesis from several weeks to several hours, as it was reported for sulphides and selenides. As described in literature, an argon plasma in the outer tube (refer to Figure 48a to d) heats the sample ampoule until the vapour pressure of selenium is sufficiently high to be ignited. In the second phase of synthesis, the selenium plasma in the inner tube reacts with the metal powders until the source is depleted and the selenium plasma collapses. Thereafter, the outer tube argon plasma heats the sample ampoule, anneals the crystals, and favours crystal growth [218, 219]. Albeit, we observed the ignition of a selenium plasma in the sample ampoules, that inner tube plasma collapsed very quickly. The results were metal powders in a selenium-rich liquid matrix. We suspect that this liquid phase, which forms in all the “M”-Se phase diagrams, significantly lowers the vapour pressure of selenium and that the annealing conditions caused by the outer tube argon plasma are rather mild. Hence, no MLCs could be synthesised in this setup via the microwave-induced-plasma-assisted method – contrary to our expectations.

7.8.2. Morphology

The appearance of the observed MLCs is usually that of crystals with metallic lustre and a plate-like morphology (refer to red arrows in Figure 49a and b), independent of the “M” element, yet, at varying sizes. These individual crystals are frequently bent and, less frequently, intergrown. Interestingly, the composition of $m = 3$ and $n = 1$ in the V-Se-Sn system was observed to be the only vanadium-based MLC, which is frequently bent at an angle, which eventually causes tubular structures of diameters between approximately 8 and 35 µm to emerge (refer to yellow arrows in Figure 49a and b). Nonetheless, the appearance is that of a layered compound (refer to Figure 49c and d), with layer thicknesses below approximately 25 nm (refer to arrow in Figure 49d). Guemas et al [94] and Moëlo et al [127] also report on hollowed tubes in other MLC containing systems. The reason, whether plate-like or tubular crystals are formed, are intrinsically related to the layered nature of the compound [94, 220]. In analogy to the minerals Chrysotile and Antigorite, the plates

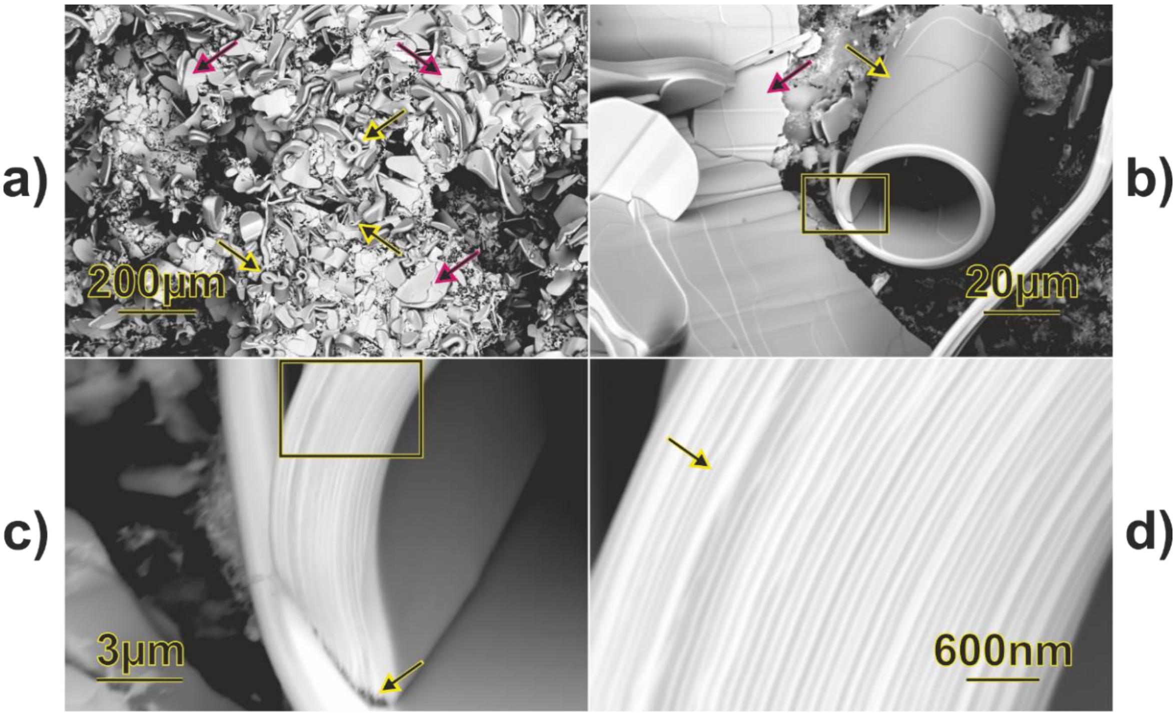

Figure 49: SEM images of MLCs in the V-Se-Sn system; plate-like and tube-like crystals are indicated by red and yellow arrows, respectively (a and b); the layered structure of the tube in image b is visible by the fringed edge (c) and the different contrast of layers on the rim (d).

are macro-twinned arrangements of alternate curved arcs, whereas the tubes are unidirectionally curved.

Another interesting feature of the prepared compounds is the rim region of the crystals. The rim of the plate-like and tubular crystals is frequently protected by a layer of crystal nuclei (refer to Figure 50a). This layer varies in thickness and appearance. In some cases, only small islands of nuclei and, in other cases, a thick layer with liquid appearance is observed (refer to Figure 50b). That layer makes an investigation on the morphology difficult as the bending of crystals might be a result of intrinsic (e.g. van der Waals bonds between layers) or extrinsic effects (e.g. deformation during manipulation). The former, would show intact layers along the crystallographic *c* axis (refer to Figure 49d), whereas, the latter, would show delamination or breaking of layers (refer to Figure 50c and d).

7.8.3. XRD

Despite the strong preferred orientation of the prepared powders, our PXRD results prove that the observed compositions are layered compounds with two different crystal substructures. Due to this preferred orientation and the two different crystal

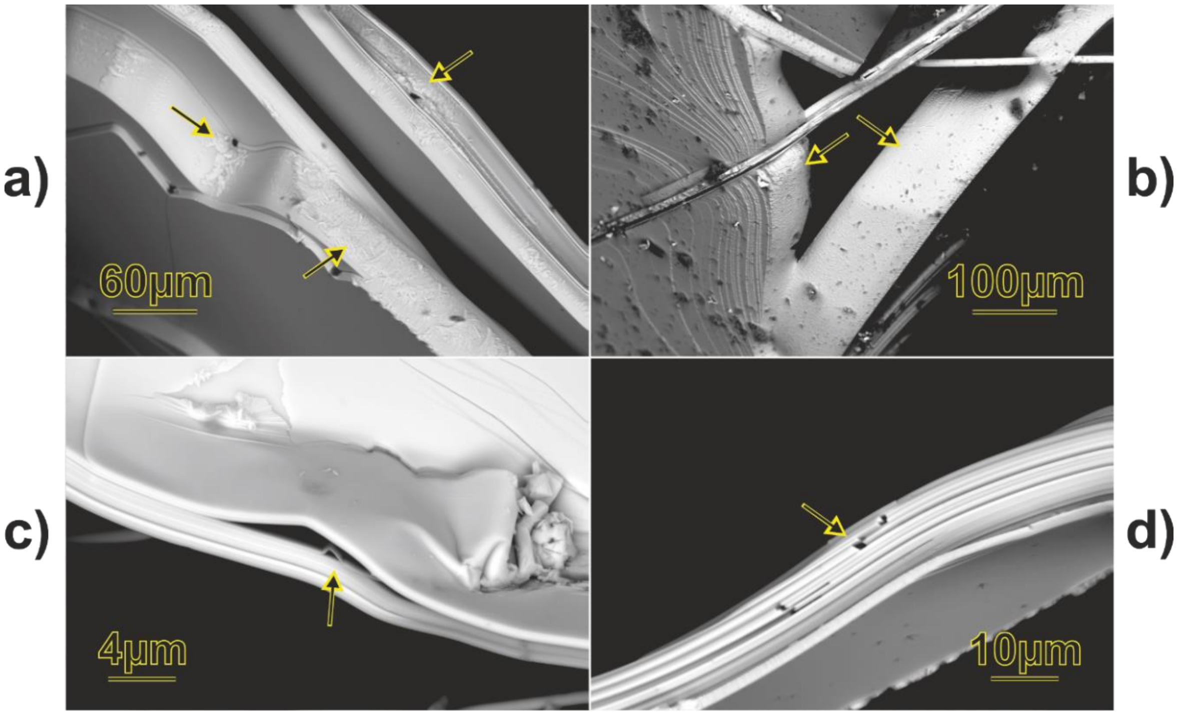

Figure 50: SEM images of the rim of vanadium-based MLCs; small (a) and large amounts (b) of crystal nuclei were observable; mechanical deformation leads to delamination along the c axis (c) and fractures in the layered structure (d).

Table 18: Comparison of lattice distances d of vanadium-based ferecrystalline and MLCs; the index (*) denotes estimations from linear interpolation of d values vs. the stacking sequence m or n; the index (^{x}) denotes experimental values.

Compound	*Comment*	*d [Å]*	*1+δ*	*Lit.*
$(BiSe)_{1+\delta}VSe_2$	MLC	11.920	N/A	[59]
$(BiSe)_{1+\delta}VSe_2$	MLC	11.920	N/A	[60]
$(BiSe)_{1+\delta}VSe_2$	MLC	11.885	0.88^x	this work
$(BiSe)_{1+\delta}VSe_2$	Ferecrystal	11.80	N/A	[96]
$(BiSe)_{1+\delta}VSe_2$	Ferecrystal	11.86	N/A	[96]
$(Bi_xSe)_{1+\delta}VSe_2$	Ferecrystal	11.78	N/A	[96]
$(PbSe)_{1+\delta}VSe_2$	MLC	12.208	$1.10/1.15^x$	this work
$(PbSe)_{1+\delta}VSe_2$	Ferecrystal	12.31	1.11	[84]
$(PbSe)_{1+\delta}VSe_2$	Ferecrystal	12.25	1.11	[27]
$(PbSe)_{1+\delta}VSe_2$	Ferecrystal	12.730	1.12	[28]
$(SnSe)_{1+\delta}VSe_2$	MLC	24.2	N/A	[95]
$(SnSe)_{1+\delta}VSe_2$	MLC	24.2	N/A	[61]
$[(SnSe)_{1+\delta}]_1(VSe_2)_1$	MLC	12.066	1.17^x	this work
$[(SnSe)_{1+\delta}]_2(VSe_2)_1$	MLC	17.866	1.17^x	this work
$[(SnSe)_{1+\delta}]_3(VSe_2)_1$	MLC	23.71*	1.15^x	this work
$[(SnSe)_{1+\delta}]_4(VSe_2)_1$	MLC	29.549	1.15^x	this work
$[(SnSe)_{1+\delta}]_5(VSe_2)_1$	MLC	35.35*	1.15^x	this work
$[(SnSe)_{1+\delta}]_6(VSe_2)_1$	MLC	41.16*	1.16^x	this work
$[(SnSe)_{1+\delta}]_1(VSe_2)_1$	Ferecrystal	12.034	$1.15/1.16^x$	[68]
$[(SnSe)_{1+\delta}]_2(VSe_2)_1$	Ferecrystal	17.828	$1.15/1.16^x$	[68]
$[(SnSe)_{1+\delta}]_3(VSe_2)_1$	Ferecrystal	23.640	$1.15/1.16^x$	[68]
$[(SnSe)_{1+\delta}]_4(VSe_2)_1$	Ferecrystal	29.300	N/A	[68]
$[(SnSe)_{1+\delta}]_1(VSe_2)_1$	Ferecrystal	12.01	$1.06/1.15^x$	[69]
$[(SnSe)_{1+\delta}]_1(VSe_2)_1$	Ferecrystal	12.01	1.15	[87]
$[(SnSe)_{1+\delta}]_1(VSe_2)_1$	Ferecrystal	12.02	1.09	[32]
$[(SnSe)_{1+\delta}]_1(VSe_2)_1$	Ferecrystal	12.03	1.15	[67]
$[(SnSe)_{1+\delta}]_1(VSe_2)_1$	Ferecrystal	12.01	$1.11/1.12^x$	[70]
$[(SnSe)_{1+\delta}]_1(V_{1+x}Se_2)_1$	Ferecrystal	12.030	1.15	[38]

structures, an indexation of reflections and a subsequent estimation of the crystal structure by charge flipping technique was not feasible. However, additional reflections were observed in several samples around the strongest reflection between 2θ values of 29 ° and 30 °. These are hints for a monoclinic (90 ° $\leq \beta \leq$ 99.0 °) or even a triclinic distortion of the lattice, just as for other vanadium-based MLCs [122]. For all these reasons, a lattice model was chosen that only considers the interlayer distances and lattice distance d perpendicular to the layers. The starting lattice models were selected to be structurally analogous to those available in literature on *fere*crystals [27, 28, 37, 38, 67, 84, 96]. The refined values are in agreement with the results from previous works on ferecrystalline and misfit layer compounds (refer to Table 18). As expected from literature [122], the lattice distance d is smaller for the compound with a trivalent “M” element (e.g. bismuth), than for that with a bivalent “M” element (e.g. tin and lead). The puckering in the MSe layer

Table 19: Puckering of the MSe layers and van der Waals gaps of vanadium-based ferecrystalline and MLCs; indices given in the table denote van der Waals gaps between exterior (e) and interior (i) MSe layers; the indices denoting the puckering of MSe layers are (p1) for the most exterior layer and (pn) for the most interior layer (compare Figure 47).

Compound	*Comment*	*Puckering [Å]*	*MSe-VSe₂ [Å]*	*MSe-MSe [Å]*	*Lit.*
$(BiSe)_{1+\delta}VSe_2$	MLC	0.316	2.784		this work
$(BiSe)_{1+\delta}VSe_2$	Ferecrystal	0.25	2.86		[96]
$(PbSe)_{1+\delta}VSe_2$	MLC	0.406	3.220		this work
$(PbSe)_{1+\delta}VSe_2$	Ferecrystal	0.367	3.00		[27]
$[(SnSe)_{1+\delta}]_1(VSe_2)_1$	MLC	0.269	2.976		this work
$[(SnSe)_{1+\delta}]_2(VSe_2)_1$	MLC	0.488^{p1}/ 0.475^{p2}	2.948	2.771	this work
$[(SnSe)_{1+\delta}]_4(VSe_2)_1$	MLC	0.611^{p1}/ 0.712^{p2}/ 0.697^{p3}/ 0.641^{p4}	3.132	2.866^{e}/ 2.902^{i}	this work
$[(SnSe)_{1+\delta}]_1(VSe_2)_1$	Ferecrystal	0.21	2.986		[68]
$[(SnSe)_{1+\delta}]_2(VSe_2)_1$	Ferecrystal	0.44^{p1}/ 0.41^{p2}	2.849	2.713	[68]
$[(SnSe)_{1+\delta}]_3(VSe_2)_1$	Ferecrystal	0.72^{p1}/ 0.65^{p2}/ 0.28^{p3}	2.879	2.610	[68]
$[(SnSe)_{1+\delta}]_1(VSe_2)_1$	Ferecrystal	0.19	3.06		[67]
$[(SnSe)_{1+\delta}]_1(VSe_2)_1$	Ferecrystal	0.34	2.92		[69]

and the van der Waals gap between the layers is influenced by that valency, too. The puckering effect and the van der Waals gap is larger for compounds containing a divalent “M” element, which is in agreement with the literature on ferecrystals (refer to Table 19). Atkins et al showed for the ferecrystalline compounds $[(SnSe)_{1+\delta}]_m(VSe_2)_1$, that layer thicknesses can be easily extrapolated by plotting the linear relationship of the stacking sequence *m* and the lattice distance *d* [68]. Their results for the slope (VSe_2 layer: 6.298 Å [68] and 6.255 Å) and the intercept (SnSe layer: 5.761 Å [68] and 5.818 Å) are in agreement with our results. We conclude that the minor differences are a result of slightly different compositions, as it was shown for ferecrystals with stoichiometric composition [69], and/or compositions with a surplus of vanadium [38]. However, it could also be attributed to the compound’s different commensurability. In ferecrystals, turbostratic disorder and, hence, the lack of a long-range order is observed, whereas, for MLCs the lattice is commensurate in the *b* direction. Despite the slight differences, our experiments prove that using a linear fit to estimate the lattice distance *d* is a valuable tool not only for ferecrystalline, but for misfit layer compounds, too.

7.8.4. TEM

The lattice parameters *a* and *b* could not be determined by XRD. This is similar previous works on VSe_2-based MLCs, where no *a* and *b* parameters are reported for partially undisclosed reasons. For PXRD, the preferred orientation was very strong, and for single-crystal XRD the deformation of the MLC crystals in the course of sample preparation as well as the anisotropic crystal dimensions made an investigation not only difficult but impossible as individual reflections, if any, could not be successfully indexed. Therefore, we exfoliated multiple crystals of different MLCs via the scotch tape method onto carbon-supported TEM grids. Apart from one, all crystals deteriorated in the electron beam and/or were severely oxidised. Fortunately, the $(PbSe)_{1+\delta}VSe_2$ crystal was not only stable in the electron beam but bend by 90° at the boundary region. For this reason, the crystal could be investigated for the lattice parameters *a* and *b* via SAED (refer to Figure 51) as well as for the stacking sequence and the stacking faults in STEM (refer to Figure 52).

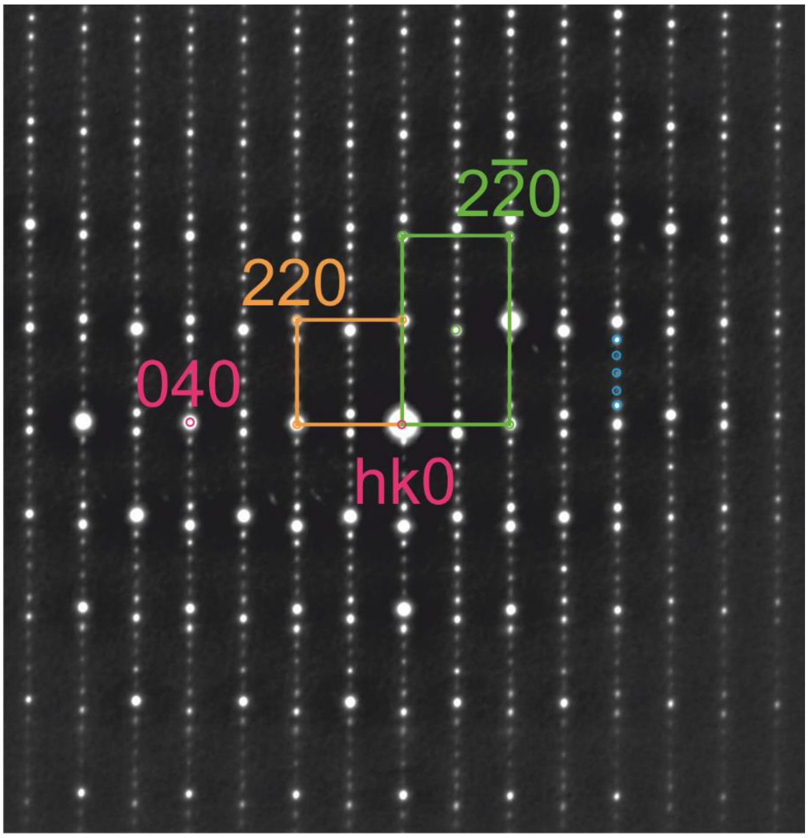

Figure 51: TEM SAED image of the MLC $(PbSe)_{1+\delta}VSe_2$ along the c axis; the green rectangle, circle, and hkl-indices represent the diffraction spots that belong to the VSe_2 sublayers (green), the PbSe sublayers (orange), the superlattice of the MLC (pink), and the multiplicity (blue).

Assuming an orthorhombic unit cell for both sublattices in SAED (refer to Figure 51), the commensurate lattice parameter *b* is observed to be around 5.69 Å. 5.93 Å and 3.26 Å are the approximate incommensurate lattice parameters in the *a* direction for

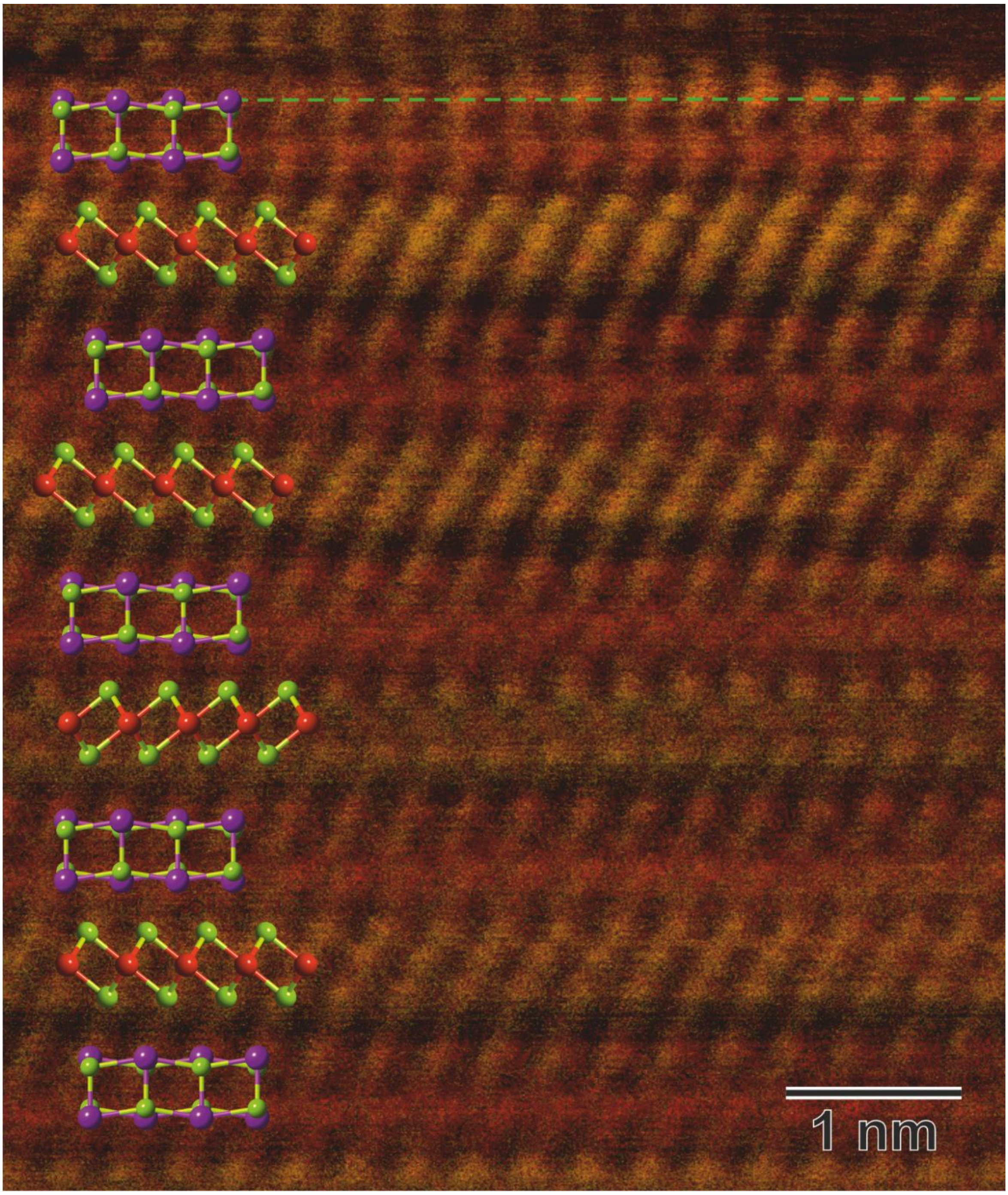

Figure 52: STEM image in pseudo colours of the MLC (PbSe)$_{1+\delta}$VSe$_2$ with schematic inserts that indicate the individual orientation of each layer; pseudo colours in the image arise from a combination a HAADIF (yellow) and a MAADIF (red) greyscale image; the sublayers orientation in the schematic inserts (Pb – purple, Se – green, V – red) correspond to [100] in the bulk setting of PbSe and [110] or [-110] in the bulk setting of VSe$_2$; a dashed line (green) is added for the readers convenience to see the lattice undulations.

the PbSe and the VSe_2 lattice, respectively. These values are less than 5 % smaller than that of the respective ferecrystalline [27, 28, 84], but 10 % smaller than the bulk compounds' *a* axes [221, 222] and correspond to a calculated misfit parameter of $1+\delta = 1.10$ (according to Wiegers formula [122]). In our diffraction pattern, a six-fold multiplicity along *h*00 was observable, which is typical for MLCs. This suggests that there might be an ordered supercell setting for the MLC $(PbSe)_{1+\delta}VSe_2$.

Slight interlayer and intralayer undulations are visible in Figure 52 (green line). It remains unclear whether these undulations are caused by structural and/or electronic effects [66], such as the macro-twinned arrangements of alternate curved arcs, or are just artefacts of the sample preparation by exfoliation. Apart from the undulations, structural defects can be observed in the MLC $(PbSe)_{1+\delta}VSe_2$.

Generally, the structural defects observed in *fere*crystalline and misfit layer compounds manifest in various ways. As described in literature, they may have different sources of origin.

For vanadium-based *fere*crystals mainly differently oriented layers (i.e. turbostratic disorder) [70-73], partially replaced single layers (e.g. MSe by VSe_2) [28, 37, 84], interstitial layers of vanadium between consecutive VSe_2 layers (for $n > 1$) [38], and substitutions of the metal atom in the VSe_2 layer (e.g. V by Ta) [114, 120] are reported. Turbostratic disorder affects the stability, as energetically more favourable and less favourable angles between layers can form [73]. Replaced layers and interstitial layers are a result of non-stoichiometry during the synthesis [37, 38]. Substitution defects only occurs when a quaternary system is chosen.

For MLCs less structural defects are reported. At the ideal stoichiometric composition, an interchange of “M” and “T” elements, was proposed by Kalläne et al [223]. This stabilisation mechanism denoted as “cross metal substitution”, alters the charge balance between the layers and, hence, increases the stability of the compound [223]. Other possible defects manifest in a non-stoichiometric composition. Figure 53 illustrates the variations in composition for different sources of non-stoichiometry.

Bidirectional variation of the actual composition between the endmenbers (refer to Figure 53a) may be caused by misfit parameter, stacking defects [127], or partial replacement of constituent layers. The actual composition can be altered unidirectional via the substitution of “M” by “T” sites via a “cationic coupling” mechanism, where $M_{MSe}^{2+} + T_{TSe_2}^{4+}$ are replaced by $T_{MSe}^{3+} + T_{TSe_2}^{3+}$ (Figure 53b) [127, 128], via interstitial “T” between constituent layers (Figure 53c) [127], or via selenium-vacancies (Figure 53d).

For all our MLCs we observed non-stoichiometric compositions when only EDX measurement values close to 100 wt.% are considered. However, for the compound $(PbSe)_{1+\delta}VSe_2$, only a few rotational stacking faults in STEM (refer to Figure 52, where one VSe_2 layer is inversely oriented) but no partial substitution of whole layers, were found. Apart from partial replacement of layers, all other (stoichometric and non-stoichometric) mechanisms found in MLCs and described above would manifest in PXRD measurements as altered site occupation factors, which were not observed for any of the compounds in the three ternary systems V-Se-Bi, V-Se-Pb, and V-Se-Sn we report on here. Hence, we conclude that the variation of

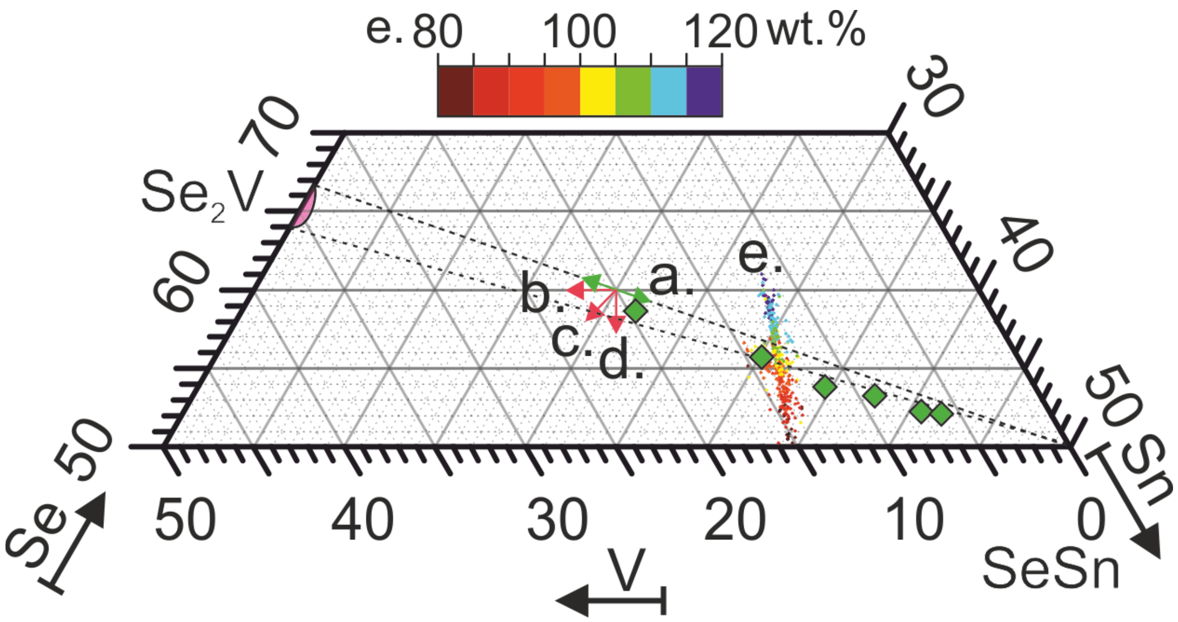

Figure 53: Different causes for a measurement with a non-stoichiometric composition exemplary in the V-Se-Sn system; misfit parameter (a), stacking defects (a), partial replacement of constituent layers (a), substitution of “M” by “T” sites via a “cationic coupling” mechanism (b), any interstitial “T” between constituent layers (c), selenium-vacancies (d), and matrix effects of the material (e – compositions measured by EDX in wt.% with colour code according to scale); mean measured compositions of the V-Se-Sn system are visible as green squares.

composition, we observed for the MLCs, is caused by a different mechanism. When matrix effects of the EDX measurement are considered and the single spot measurements, which are not close to 100 wt.% in total mass, are plotted (refer to Figure 53e), a systematic trend is visible where the ideal composition is around 105 wt.% total mass in EDX. Noteworthy, the proposed compositions (refer to green squares in Figure 53), are sometimes within the phase-field between $V_{1+x}Se_2$ + SnSe (indicated by dashed lines) and are sometimes outside, but always deviating around 1.5 at.% from the ideal composition. This is of importance, as the number of structural defects would be altered for different stacking sequences in most cases, as the constituent layers are not equally affected (e.g. a substitution of 10 % of all Pb sites by V would be weaker for $m = 1$ than for $m = 6$). These systematic variations occur despite careful calibration and selection of measurement points, probably due to different angles to the surface and strong anisotropy of the material. When a stoichiometric composition is proposed and the trends are extrapolated, the misfit parameters are 0.88 for the bismuth-based, 1.15 for the lead-based, and between 1.15 and 1.17 for the tin-based system. These values are comparable to the literature on *fere*crystalline and misfit layer compounds regarding their magnitude (refer to Table 18) as well as to the misfit parameter calculated from the lattice parameters $(PbSe)_{1+\delta}VSe_2$, which is $1+\delta = 1.10$.

7.9. Conclusion

The MLCs we synthesised in the three ternary systems V-Se-Bi, V-Se-Pb, and V-Se-Sn via different approaches are comparable to previous investigations of misfit layer compounds and *fere*crystalline compounds with respect to the cell dimensions. Apart from one compound (which is tubular) all are plate-like crystals, presumably as a result of macroscopical twinning phenomena. In some instances, and especially when the crystal is mechanically damaged, the rim-region is clearly visible and exhibits a layer structure in SEM images. However, in most crystals of the MLCs we investigated the rim is protected by at least a small amount of crystal nuclei.

In analogy to *fere*crystals in literature [67-69], the different stacking sequences of MLCs in the V-Se-Sn system permitted to extrapolate the thickness gain of an individual VSe_2 and SnSe layer. These are comparable in their magnitude, yet, slightly deviating regarding exact values of the extrapolated thicknesses, which is most likely a result of the different compositions of the crystals.

Apart from rotational disorder, no structural defects were observable in STEM images for the MLCs in the V-Se-Pb system. The variations in compositions we measured in EDX are suspected to be artefacts that arise from matrix effects. When they are corrected by regression lines, the results are comparable to literature.

7.10. Acknowledgements

Special thanks go to Kenan Elibol and Jani Kotakoski from the Department Physics of Nanostructured Materials, University of Vienna, for their help with TEM measurements. The authors wish to thank Herta Effenberger from the Department of Mineralogy and Crystallography, University of Vienna, and Alexander Roller from the Department of Chemistry, University of Vienna, for their patience in attempting to find suitable single crystals for XRD of the MLC phases $(BiSe)_{1+\delta}VSe_2$, $(PbSe)_{1+\delta}VSe_2$, and $[(SnSe)_{1+\delta}]_m(VSe_2)$. The authors express gratitude to Patricia Jenner for proof-reading and her linguistic advice and thank Stephan Puchegger from the Department of Physics, University of Vienna, for his help with SEM measurements.

7.11. Declarations of interest

The authors declare that there is no conflict of interest.

8. Unpublished data

Apart from the readily described methods of characterisation, such as powder XRD, optical microscopy, SEM, and TEM, several further methods were employed. These investigations aimed to gain insights into the structural, thermal, and physical properties. Unfortunately, different difficulties that could not be resolved hampered a comprehensive acquisition of knowledge about the investigated vanadium-based misfit layer compounds. Utilised methods, difficulties, and obtained results will be presented in this chapter.

8.1. Raman and Cryro-Raman

We performed Raman and Cryro-Raman spectroscopic experiments. Raman spectroscopy was employed to determine the Raman shifts that are characteristic of the prepared MLC materials. In subsequent Cryo-Raman experiments, we attempted to detect phase transitions by peak shifts and/or the appearance of additional peaks, as it is described in literature for materials such as the transition metal dichalcogenides VSe_2 [224] and $TiSe_2$ [225-227].

The experiments were performed on a WITec alpha 300A. This device is a confocal Raman system that is equipped with lasers of the wavelengths 488 nm, 532 nm, 633 nm, and 785 nm. Laser energies of up to 20 mW were used. The samples were placed on an XYZ linear translation stage either at ambient conditions or in a cryo-chamber cooled with liquid nitrogen and flushed with nitrogen gas. The collected signal was dispersed by a spectrograph and detected by a CCD detector.

Up to now only, Raman spectroscopic measurements are reported for VS_2-based MLCs [49, 78, 110, 111] but not for VSe_2-based *fere*crystals or MLCs. Hence, other MLCs' Raman shifts (e.g. [49, 78, 110, 111, 122, 228]), that of vanadium oxide [229-232], and that of the binary constituents, when available, served as starting points for our investigations. The Raman spectra of the binary compounds VSe_2 [224, 233-237], SnSe [238-242], and PbSe [243-246] are reported. Noteworthy, the crystal structure of SnSe is differing in the bulk (e.g. GeS and TlI type [196]) and in the slabs of MLCs (e.g. NaCl type). Different crystal structures will result in different Raman shifts. For this reason, the literature shifts of SnSe cannot be compared to our results. No Raman spectra on the binary BiSe compound are available in literature, apart from calculated modes [247, 248], as the investigations in this system focus on the Bi_2Se_3 compound (e.g. [249, 250]). Bi_2Se_3 is structurally related, yet, lacks a bilayer of Bi compared to BiSe [216, 217, 247].

Several difficulties occurred during our Raman spectroscopic measurements of the three MLCs $(MSe)_{1+\delta}VSe_2$ (M = Bi, Pb, and Sn). Only some of those could be resolved satisfactorily.

First and foremost, the plate-like crystals exhibit metallic lustre, which manifests in a high reflectivity of the investigated compounds and very low signal-to-noise ratios. Hence, the laser fluencies required for excitation are elevated, compared to a similar (hypothetical) compound with low reflectivity. However, the excitation energies may not be elevated without adverse consequences. For the compounds we investigated, elevated fluencies manifest in the oxidation of the surface and/or holes, which indicate a decomposition of the compound due to evaporation (refer to Figure 54). Faced with such a dilemma, to compromise between absorption and emission of scattered light, a possible solution is to retain high fluencies but to reduce the thermal damage by rotation/spinning of the sample [251-254] or, as we did, by fast scanning speeds. Despite some thermal degradation was inevitable over long measurement durations (refer to Figure 55), the signs could be reduced significantly. Noteworthy, slight oxidation on MLC surfaces was removable via an exfoliation by the scotch tape technique, which is facilitated by the loosely bonded crystal

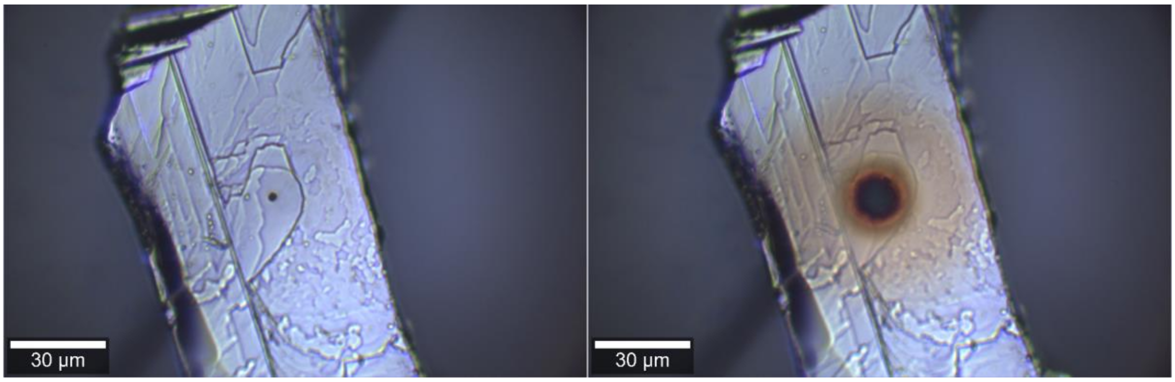

Figure 54: Thermal degradation of MLCs due to high fluencies; the crystal on the left shows slight degradation (small black dot in the centre), whereas the same crystal on the right is heavily degraded (black dot) and oxidised (brown corona).

structure. That technique also has the advantage of yielding fresh surfaces without any dust or residual metallic powders.

Second, the signal-to-noise ratios were low, despite the higher fluencies permitted by the fast scanning speeds. This issue was circumvented by long accumulation durations and averaging of several hundred spectra. The individual spectra were carefully selected to be such without cosmic ray spikes and/or by removal of cosmic spikes. In doing so the signal-to-noise ratios could be significantly increased.

Last, Cryo-Raman experiments were negatively affected by the cryo-chamber design. On the one hand, the cover glass of the chamber reduced the laser fluencies significantly. Hence, the results derived from our measurements at ambient conditions are not transferable without modification. At low temperatures much higher fluencies were required. On the other hand, ice crystals could be observed in the inner part of the cryo-chamber at lower temperatures, especially below temperatures of approximately -100 °C and -130 °C. We suspect that either residual humidity in the chamber or small qualities of water in the liquid nitrogen do crystallise in this cryo-chamber. Freezing of the measurement area could only be circumvented by continuous area measurements and high fluencies (refer to Figure 56).

Rather consistent results could be obtained for the MLCs $(BiSe)_{1+\delta}VSe_2$ and $(SnSe)_{1+\delta}VSe_2$. For $(PbSe)_{1+\delta}VSe_2$, however, the results for the different excitation wavelength are ambiguous. For an excitation wavelength of 488 nm no signal that

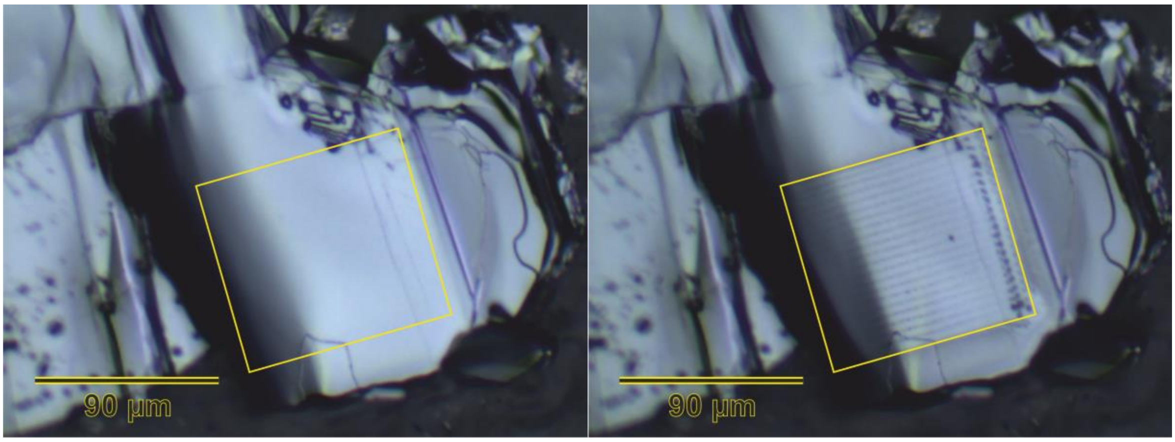

Figure 55: Thermal degradation of MLCs over long measurement durations; the measurement area is indicated in yellow; the crystal on the left shows no degradation at the beginning of the measurements, whereas the same crystal on the right is partially degraded (black dots and lines) after several measurements, especially the starting point of each row.

is distinguishable from the background noise could be obtained for the lead-based compound. This is of importance, as Raman shifts should be practically equivalent for altered excitation wavelengths, apart from slight shifts of bands or their shape (e.g. due to differing excitation energies, differing wavenumber calibrations of the spectrometer, or dispersion). Hence, the spectra observed for $(PbSe)_{1+\delta}VSe_2$ at other wavelengths might be interpreted as “noise”, too. The fact that the signal-to-noise ratios of $(BiSe)_{1+\delta}VSe_2$ and $(SnSe)_{1+\delta}VSe_2$ are also worse for 488 nm compared to the other excitation wavelengths oppose this interpretation. More likely the signal for $(PbSe)_{1+\delta}VSe_2$ at 488 nm is below the detection limit of the device and the other wavelengths exhibit some additional fluorescence phenomena.

Best signal-to-noise ratios could be obtained in the infrared region with 785 nm excitation wavelengths. Measuring Raman shifts with a longer wavelength of the laser source has three advantages in our measurements. First, the spatial resolution is ultimately improved in our setup employing a grating type spectrometer. Second, generally less or no fluorescence is observed when a NIR laser is utilised as

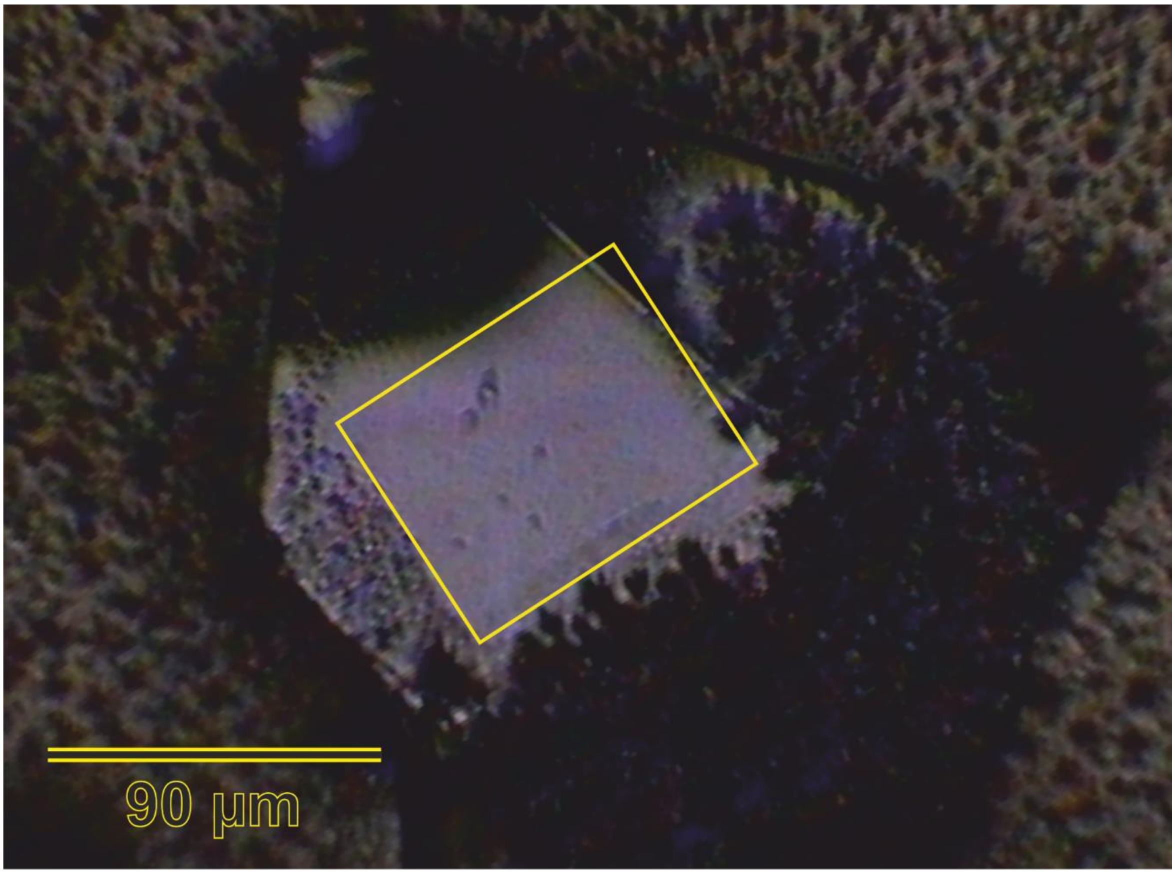

Figure 56: Freezing phenomenon of the crystals in the Raman cryo-chamber with the measurement area indicated in yellow; ice crystals (black) are visible on the MLCs’ surface (gray).

Table 20: Observed Raman shifts in experiments with VSe_2 for different laser wavelengths and excitation energies; Modes related to VSe_2 are shaded green; the indices (r) and (o) indicate residues of the Rayleigh peak and the formation of oxides, respectively.

Laser	E [mW]	Raman shift [cm^{-1}]				
488nm	3.0	86.3^{r}				
	4.0	85.3^{r}				
	5.0	85.3^{r}				
	7.5	85.4^{r}			201.3	
	10.0	85.8^{r}			199.3	
	12.5	84.9^{r}			201.2	
532nm	3.0			105.0	208.3	
	5.0			103.7	202.9	
	7.0			103.4	201.9	
	8.0			98.7	201.6	
	9.0			100.9	201.6	
	10.0			97.6	201.6	
	12.5				200.2	
	13.0^{o}				199.3	238.7^{o}
633nm	7.0					
	7.5^{o}		72.8^{o}	110.3	204.7	232.3^{o}
	9.0^{o}		76.5^{o}	114.3	200.2	246.9^{o}
785nm	5.0	41.4^{r}				
	7.5	40.9^{r}				
	10.0	40.9^{r}				
	12.5	40.4^{r}	73.4		203.0	
	15.0	40.3^{r}	63.4		203.9	

fluorescence is a two-photon process and Raman scattering is a one-photon process [255-260]. As pointed out above, we suspect that all of our Raman spectra excited with a UV/Vis-Laser contain fluorescence phenomena, especially for crystals of the constituent structure VSe_2 at 532 nm. Such fluorescence is not observed for the spectra that were excited with wavelengths of 785 nm. Finally, the notch filter in our setup allows collecting the weak inelastically scattered light closer to the elastically scattered radiation when the wavelengths are longer. Hence, the results at 785 nm can be trusted most regarding the positions of the observed bands. Generally, longer wavelengths are accompanied by disadvantages. First, the usable excitation energies are decreased before the sample is oxidised (refer to Table 20 – oxidation stating at 13 mW and 7.5 mW for 532 nm and 633 nm, respectively). Second, the Raman scattering efficiencies, which are proportional to

λ^{-4}, are lower. Finally, the absorption coefficient and the reflectivity need to be considered. Latter show a sweet spot around 610 cm^{-1} [257].

Several Raman shifts can be observed for the MLCs and VSe_2 crystals we prepared. The Raman patterns of MLCs are more difficult to interpret than those of VSe_2 due to the availability of comparable literature.

Our Raman patterns of 1T-VSe_2 exhibit the Raman active A_{1g} mode around between 199 cm^{-1} and 208 cm^{-1}. Those values and the fact that no E_g mode is observable at ambient conditions are comparable to the literature [224, 233, 234, 236, 261]. Our experiments with a 532 nm laser show that this mode is shifted to lower wavenumbers when the fluency is increased. Modes around 232 cm^{-1} and 247 cm^{-1} indicate the formation of oxides [232, 262] on the crystal surface (refer to Table 20).

As Shirai et al point out in their publication, the out-of-plane modes of the host layers are commonly unaltered in MLCs compared to bulk materials. On the contrary, the in-plane modes are increased regarding their frequency [263]. Where comparable, this can be observed also for the $(BiSe)_{1+\delta}VSe_2$ MLC (refer to Figure 57 and Table 21). For $(BiSe)_{1+\delta}VSe_2$ at least five independent modes were detected. Frequencies between 194 cm^{-1} to 209 cm^{-1} may be attributed to the A_{1g} mode of the VSe_2 slabs. Noteworthy, Raman studies of chemically exfoliated VSe_2 do report on this frequency in a VSe_2 bilayer but not the monolayer [237]. The remaining Raman modes below 200 cm^{-1} can arise from several different sources. First, the modes can stem from phonons of the MSe part in the MLC. Second, the modes can be second-order modes and/or two-photon processes. Third, the modes can be disorder-induced [264]. Last, the modes may originate from impurities and/or oxides on the surface [228]. Unfortunately, the bulk crystal structure of BiSe is not the distorted NaCl type one observed in MLCs, so the reported Raman active modes [248] of the bulk BiSe are not comparable. Also, no phonon calculations of a NaCl type BiSe is available. Furthermore, to our knowledge, no bismuth-based MLCs were investigated up to now regarding their Raman spectra. Hence, our interpretation is restricted to compare the $(BiSe)_{1+\delta}VSe_2$ MLC to other MLCs in literature as well as the various vanadium-based oxides. The hypothesis that the observed modes arise from oxides can be easily ruled out by comparing the spectra.

Table 21: Observed Raman shifts in experiments with $(BiSe)_{1+\delta}VSe_2$ for different laser wavelengths and excitation energies; Modes presumably related to $(BiSe)_{1+\delta}VSe_2$ are shaded green; the indices (r) and (o) indicate residues of the Rayleigh peak and the formation of oxides, respectively.

Laser	E [mW]	Raman shift [cm^{-1}]								
488nm	3.0				86.4^{r}		116.1			
	4.0				85.8^{r}		132.7			
	5.0				86.2^{r}		131.3			
532nm	2.0				87.9		129.4		201.8	
	3.0				87.4		131.4		200.5	
	4.0				88.4		131.5		194.2	
	5.0				87.3		130.1		201.9	
	6.0				87.0		131.0		194.7	
	7.0				86.5		131.5		204.3	
	8.0				86.5		132.1		209.3	
	12.5^{o}				87.1		131.9			225.8^{o}
633nm	2.0				80.3	101.7	133.9	144.0		
	3.0			75.8		99.3	137.5	145.0	198.1	
	4.0			77.7		99.0	134.3	145.1	197.9	
	5.0			78.0		98.5	133.5	145.4	196.2	
	6.0			77.1		98.0	133.1	145.1	199.4	
	7.0			76.7		97.7	134.6	145.8		
	8.0			75.0		95.1	133.8	145.7		
	12.5			72.8		90.9	133.4	145.1		
785nm	3.0	40.6^{r}	58.3	72.5		100.2	138.5	145.5	197.5	
	4.0	40.8^{r}	58.4	72.9		99.9	136.6	145.5	197.8	
	5.0	40.8^{r}	58.3	72.8		99.6	135.9	144.9	196.2	

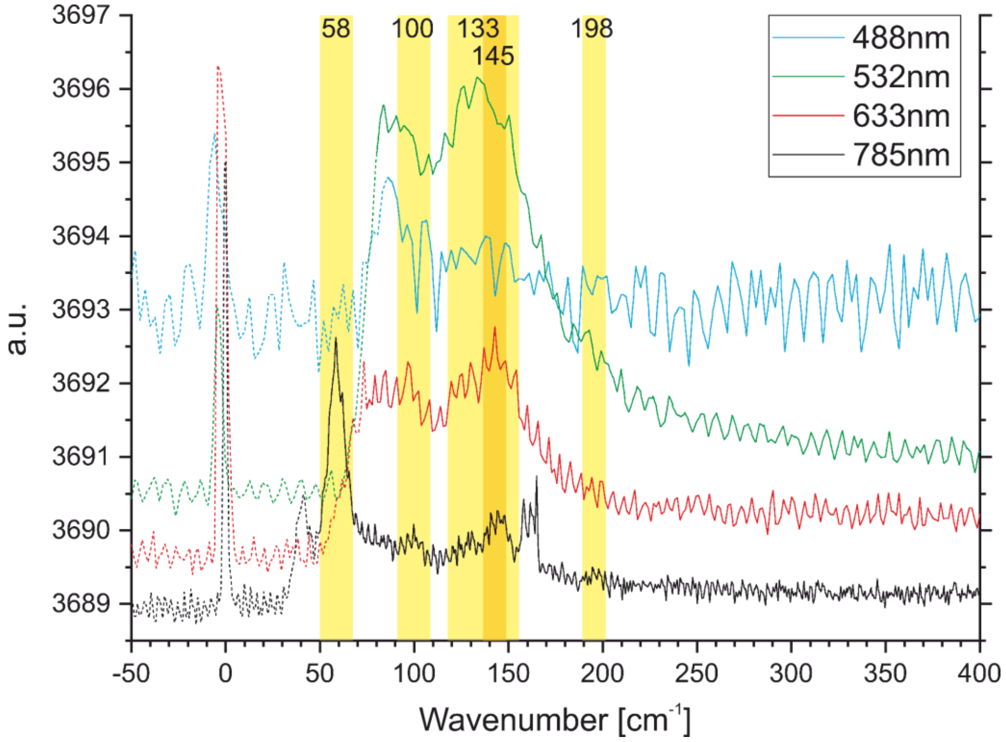

Figure 57: Observed Raman spectra of $(BiSe)_{1+\delta}VSe_2$ for different laser wavelengths.

Oxides, which possess Raman peaks around 150 cm^{-1}, also exhibit significant peaks around higher wavenumbers (e.g. vanadium oxide nanotubes at ~250 cm^{-1} and ~900 cm^{-1}). Such peaks are not observed in our Raman spectra. Also, the crystal surfaces do not appear to be severely oxidised. More likely the detected modes originate from the BiSe layers and/or are interlayer modes. Assuming a simplified and undistorted NaCl type structure for the MSe layer, the four phonon modes $2A_{1g} + 2E_g$ are expected to be Raman active [265, 266]. These appear to be below approximately 200 cm^{-1} in experiments with PbS-based [110-112, 228, 266-270], SnS-based [110, 266-270], and rare-earth-based MLCs [265, 268, 271-273]. However, the individual Raman peaks cannot be assigned to certain Raman modes for the $(BiSe)_{1+\delta}VSe_2$ MLC.

The $(PbSe)_{1+\delta}VSe_2$ (refer to Figure 58 and Table 22) and $(SnSe)_{1+\delta}VSe_2$ MLCs (refer to Figure 59 and Table 23) also cannot be interpreted by comparing the Raman spectra to those of PbS-based, SnS-based, and rare-earth-based MLCs. Interestingly, no peaks between 190 cm^{-1} to 210 cm^{-1}, which may be assigned to the A_{1g} mode of the VSe_2 layers, are observed. Similar to the $(BiSe)_{1+\delta}VSe_2$ MLC, we interpret the peaks at wavenumbers below approximately 200 cm^{-1} to originate from modes of the MSe layers and/or the interlayer modes. The modes in the $(SnSe)_{1+\delta}VSe_2$ MLC cannot be assigned by comparing them to the literature on the bulk material due to the different crystal structures.

For the $(PbSe)_{1+\delta}VSe_2$ MLC the crystal structure is comparable to literature, as it is (approximately) equivalent to the bulk structures PbSe and VSe_2. However, there are inconsistencies between publications regarding the assignment of modes, which requires discussion. On the one hand, Manciu et al assign the strongest Raman peak of their prepared PbSe nanoparticles at 140 cm^{-1} to the LO(Γ) phonon mode [245], similar to publications on PbSe bulk materials such as that of Vodopyanov et al [274] or Ovsyannikov et al [243]. On the other hand, Kuzivanov et al used different laser fluencies for their experiments on PbSe films. They observed Raman peaks at the same transition frequencies, but only at higher fluencies (>0.4 mW/µm^2) and accompanied by photo-and thermo-induced sample modifications. At low fluencies (0.06 mW/µm^2) the signal-to-noise ratio is comparable to our results. They assign

Table 22: Observed Raman shifts in experiments with $(PbSe)_{1+\delta}VSe_2$ for different laser wavelengths and excitation energies; Modes presumably related to $(PbSe)_{1+\delta}VSe_2$ are shaded green; the indices (r) and (o) indicate residues of the Rayleigh peak and the formation of oxides, respectively.

Laser	E [mW]	Raman shift [cm^{-1}]					
488nm	2.5						
	4.0						
532nm	2.0			84.1	112.7	159.9	
	2.5^{o}			83.9	115.5		171.5^{o}
	4.0^{o}			84.2	116.4		175.1^{o}
633nm	2.5			76.2	122.6		
	4.0			85.2	122.9	149.3	
	5.0			82.6	119.3	156.4	
	6.0^{o}			80.1	119.6		177.8^{o}
785nm	4.0	41.0^{r}			110.3		
	5.0		52.6		116.4		
	6.0	41.3^{r}			105.9		
	7.0		61.7		116.4		

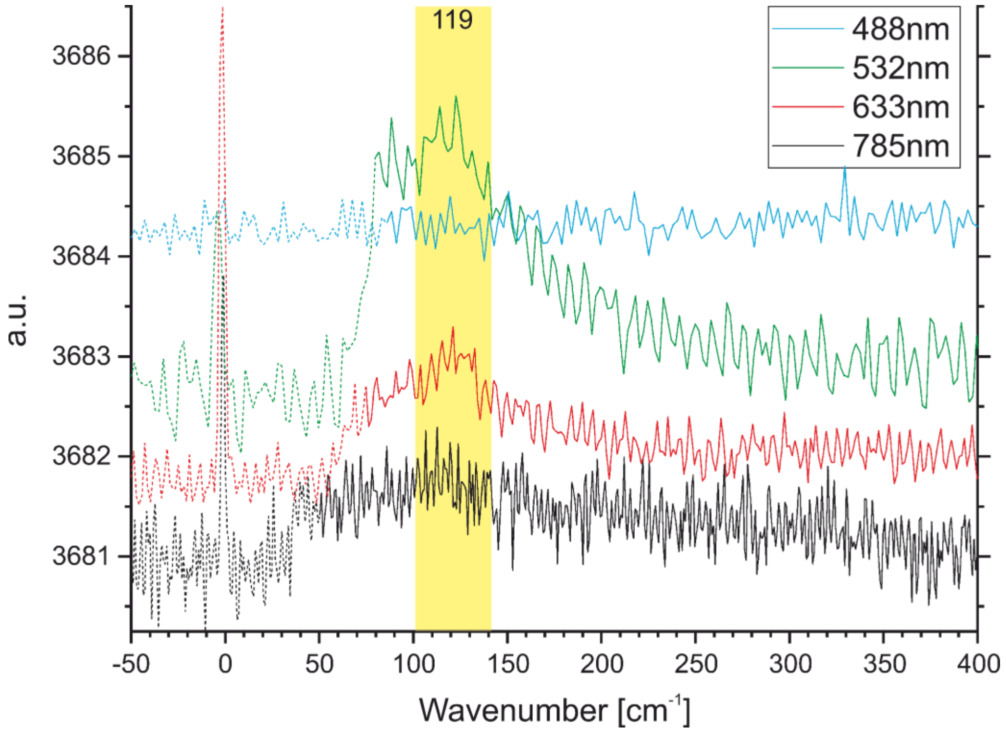

Figure 58: Observed Raman spectra of $(PbSe)_{1+\delta}VSe_2$ for different laser wavelengths.

the multitude of transitions below approximately 200 cm^{-1} in their Raman spectra to different overtones and combinational tones [246] in contrast to the previous authors, yet, consistent with phonon calculations [275]. Due to the similar thermal degradation effects as for our MLCs we assume the results of Kuzivanov et al to be more comparable and reliable. Presuming that the shift of modes is similar as

Table 23: Observed Raman shifts in experiments with (SnSe)$_{1+\delta}$VSe$_2$ for different laser wavelengths and excitation energies; Modes presumably related to (SnSe)$_{1+\delta}$VSe$_2$ are shaded green; the indices (r) and (o) indicate residues of the Rayleigh peak and the formation of oxides, respectively.

Laser	E [mW]	Raman shift [cm^{-1}]							
488nm	4.0				103.3	154.4			
532nm	1.0			82.1	98.4	167.1			
	2.0			77.2	99.3	163.5			
	3.0			83.3	104.7	157.3			
	4.0			84.6	106.0	162.5			
	5.0			82.8	103.1	161.1			
	5.5^{o}			82.2	101.6	141.4	218.8^{o}	250.4^{o}	354.5^{o}
	6.0^{o}			82.4	102.4	142.2	215.2^{o}	250.3^{o}	357.1^{o}
	7.0^{o}			82.8	102.1	140.9	214.0^{o}	256.4^{o}	347.8^{o}
633nm	2.0		67.3	86.9		151.4		249.4^{o}	
	3.0		65.7	78.8	106.7	162.0		253.9^{o}	
	4.0		66.2	80.4	106.4	156.5		250.3^{o}	
	5.0		66.9	81.6	104.5	155.2		245.3^{o}	
	6.0		67.0	77.6	100.4	152.2	221.4^{o}	248.4^{o}	
	8.0		67.6	78.3	99.8	152.2		246.6^{o}	
785nm	4.0	53.2	65.3	90.2	111.7	159.3	216.1^{o}		
	6.0	51.0	65.2	81.9	103.3	158.4	212.9^{o}		
	8.0	51.0	65.1	82.0	104.8	158.7	215.1^{o}		

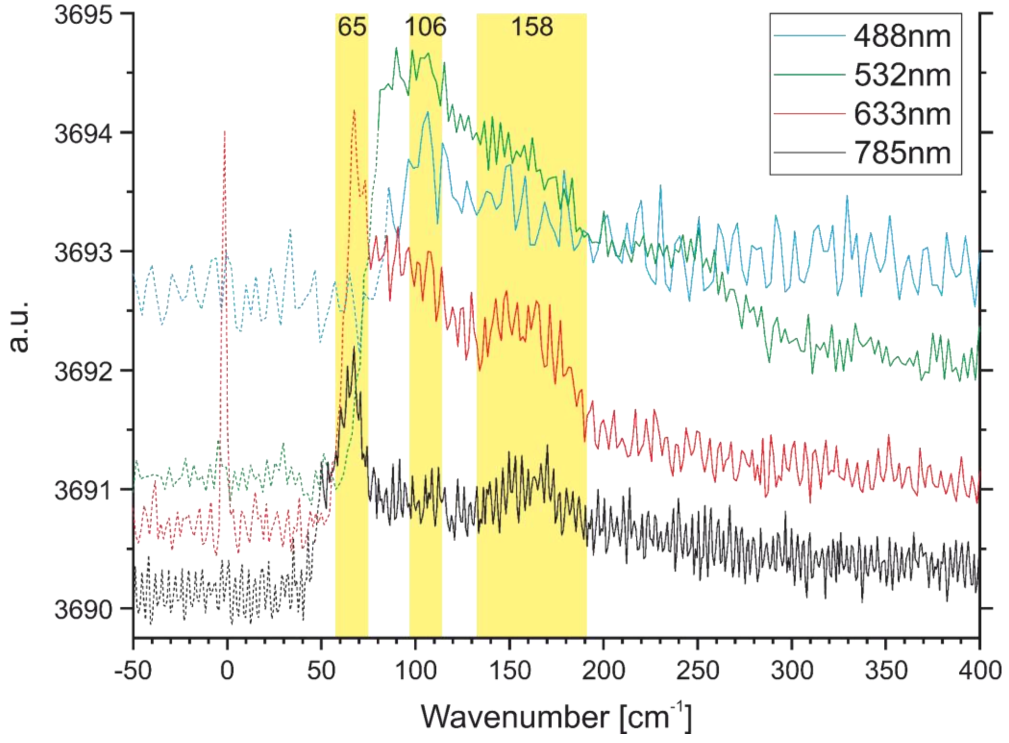

Figure 59: Observed Raman spectra of (SnSe)$_{1+\delta}$VSe$_2$ for different laser wavelengths.

proposed by Shirai et al (e.g. unaltered frequency for out-of-plane modes and increased frequency for in-plane modes) [263] the most likely assignments for our peak at 119 cm^{-1} is either the 2TO(Δ) overtone mode (124 cm^{-1} [275]) or the combinational tones of LA(Δ)+TA(Δ) (102 cm^{-1} [275]). The combinational modes of TO(X)+LA(X) (122 cm^{-1} [275]) and LA(X)+TA(X) (124 cm^{-1} [275]) are less likely, as their longitudinal component may shift to even higher frequencies.

Independent of the difficulties described for assigning the individual Raman peaks, the temperature behaviour of the frequencies observed can be investigated. Due to the bad signal-to-noise ratio and the low number of interpretable Raman peaks for the MLCs $(PbSe)_{1+\delta}VSe_2$ and $(SnSe)_{1+\delta}VSe_2$, only the $(BiSe)_{1+\delta}VSe_2$ was studied successfully. At least two different indicators for phase transitions are described in literature. Emerging of new peaks in the Raman spectra indicates a phase transition. This is characteristic for one with some structural changes and breaking of symmetries (e.g. CDW transition of VSe_2 at ~110 K [224, 233, 234, 236]). Also, when peak frequencies, FWHM of peaks, and/or integral of peaks exhibit points of discontinuity in trend with temperature that can suggest a first-order or a second-order phase transition.

However, the peak frequencies, the FWHM of peaks, and the peak areas are influenced by laser fluencies, too. As described above, ice crystals condensed on the surface of the MLCs our cryo-chamber. This reduces the actual excitation energies on the sample surface compared to an unfrozen sample. The peak positions vary significantly in our experiments below temperatures of approximately -100 °C and -130 °C due to this freezing effect (refer to Figure 60). This complicates the determination eventual phase transitions of the $(BiSe)_{1+\delta}VSe_2$ MLC, not to mention to compare it to the VSe_2 constituents' CDW transition in bulk, as the effects of reduced fluencies by freezing and the subtle changes of phase transitions cannot be distinguished.

8.2. Resistivity

We attempted to perform resistivity measurements for all misfit layer compound compositions we synthesized. Apart from obtaining the required crystal sizes, contacting the delicate plate-like shaped crystals via the van der Pauw contacting method with 40 µm diameter Au-wires and Ag conductive paste was most challenging. Either the contacts were placed within the perimeter of the sample surface, which may lead to tearing apart of thin crystals, or the crystals were contacted at the rim, which may lead to breaking loose of contacts. Of all attempts, only one misfit layer compound crystal, $(PbSe)_{1+\delta}(VSe_2)$ from sample Sg30, was successfully contacted and measured. These successful experiments were performed on plate-like shaped crystals (200 µm x 200 µm x 10 µm and 500 µm x 100 µm x 10 µm) with a standard four-probe method, using an AC resistance bridge (LakeShore 370) and measurement temperatures between 4 K and 293 K. By this setup, with either all four contacts on the rim or two contacts on each crystal surface, the in-plane and out-of-plane resistivities of the $(PbSe)_{1+\delta}(VSe_2)$ misfit layer compound could be measured.

As expected for such a layered compound the physical properties are strongly anisotropic (e.g. thermal resistivity is lower in *fere*crystalline and misfit layer

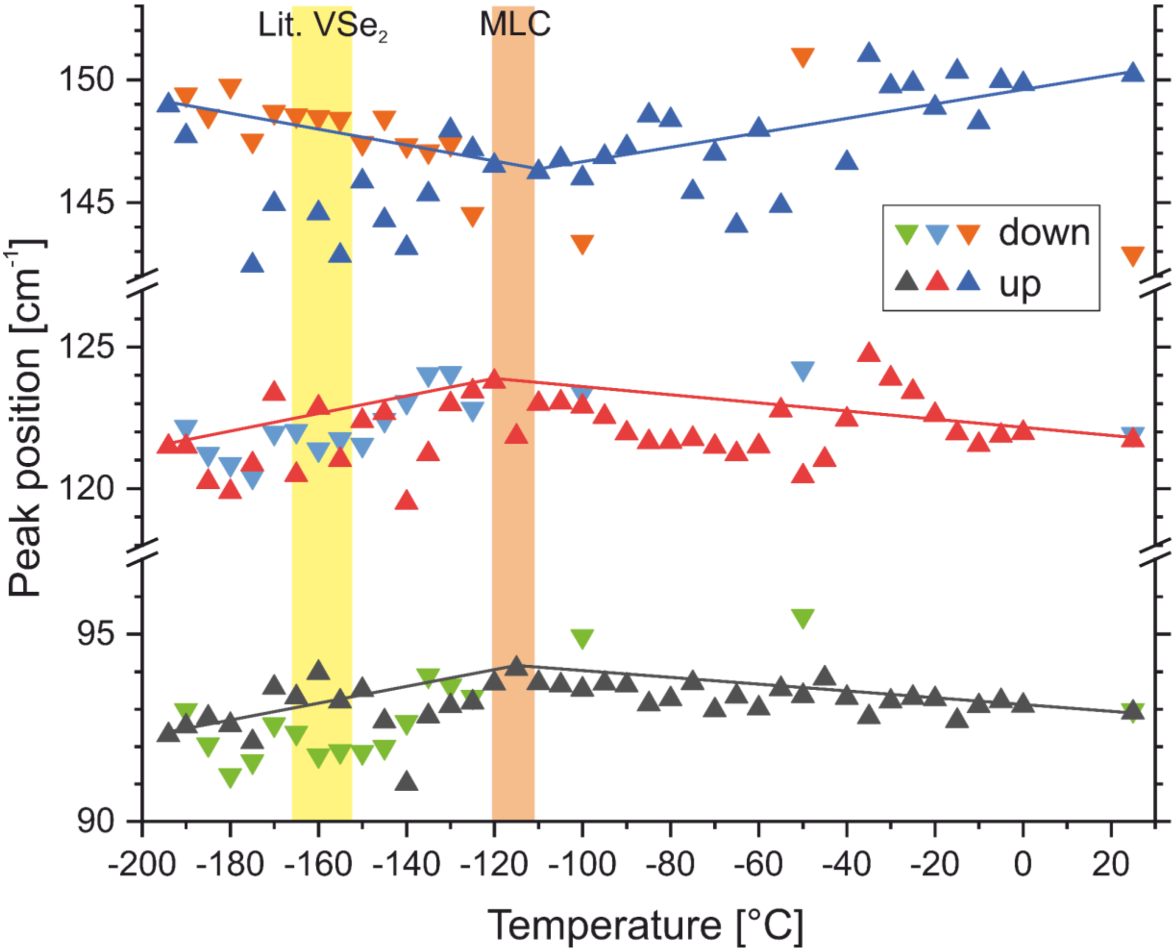

Figure 60: Shift of Raman peak positions of $(BiSe)_{1+\delta}VSe_2$ in Cryo-Raman experiments;"down" and "up" refer to the cooling and the heating cycle, respectively.

compounds than for some amorphous materials [23]). This also applies to the measured resistivities. The temperature dependence of the electrical resistivity reveals normal conducting metallic behaviour for the out-of-plane direction, whereas the in-plane temperature dependence resembles that of a semiconductor (refer to Figure 61). This is consistent with the literature on the misfit layer compound (PbS)$_{1+\delta}$(VS$_2$) [25, 26] and the (PbSe)$_{1+\delta}$(VSe$_2$) *fere*crystals [27, 28]. It is suggested that the semiconducting behaviour originates in the VS$_2$ slab [25], more precisely the CDW-like modulation of V clusters in this layer [26]. Whether it is that of a typical intrinsic or extrinsic semiconductor, cannot be derived from the curvature, as our measurements were performed only down to till 4 K. However, for the structurally related *fere*crystals (PbSe)$_{1+\delta}$(VSe$_2$)$_n$ p-type and n-type semiconductivity is reported for n = 1 and $n \geq 2$, respectively [27], which suggests that our misfit layer compound might be an extrinsic semiconductor regarding the in-plane temperature dependence of the resistivity.

At least three anomalies can be observed in our measurements. They are indicated by arrows in Figure 61.

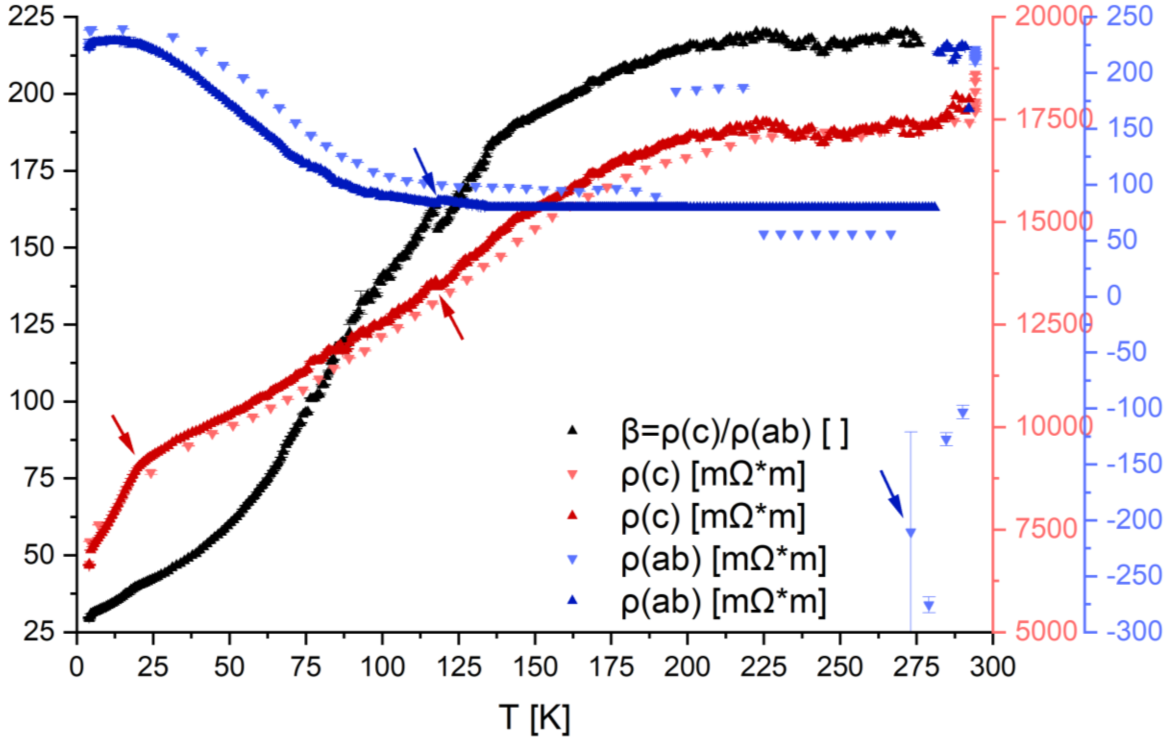

Figure 61: Out-of-plane (ρ_c) and in-plane resistivities (ρ_{ab}) of the MLC (PbSe)$_{1+\delta}$(VSe$_2$); error bars are given for all measurement values; downward and upward pointing triangles are measurement values of the cooling and the heating cycle, respectively; arrows indicate anomalies in the measurements.

First, a jump discontinuity between 117.5 K and 118 K is visible in both, the out-of-plane and in-plane direction, and might be attributed to some CDW phase transition in the VSe_2 layer. In the bulk, the respective transition is observed around 105 K [276] to 110 K [277]. When the number of layers is reduced by mechanical exfoliation to thicknesses of 11.6 nm to 66 nm, the transition temperature is decreased till 81.8 K [276]. However, there are reports that the transition temperature is increased for ultrathin nanosheets up to 135 K [278, 279]. For the $(PbSe)_{1+\delta}(VSe_2)$ *fere*crystals the CDW transition temperature is at approximately 90 K [28] to 110 K [27].

Second, the sharp kink at 20 K in the out-of-plane measurement might indicate some phase transition, such as a magnetic transition or some additional ordering phenomena in the lattice. However, no similar effect is reported for the bulk or the comparable layered compounds.

Third, apparently a negative resistivity is observed in our in-plane resistivity measurements. Such a phenomenon might occur for several reasons. First, the contacting of the four-probe method might be insufficient. Second, when the test currents (in this measurement 10 mA) are too small, they are prone to other errors, such as thermoelectric electromagnetic fields and offsets generated by the voltmeter input circuit or the rectification of some radio frequency interference. Third, some effects as observed in “negative resistance” diodes, such as quantum mechanical tunnelling effects (e.g. tunnel diode) or the Gunn effect (e.g. Gunn diode), might be considered. The negative resistivity is irreversibly observed upon cooling and the measured values are vitiated by a manifest error. These facts indicate that a measurement error generated by external influences is the most probable explanation for this effect.

9. Conclusive discussion

Misfit layer compounds of the composition $[(MX)_{1+\delta}]_m(TX_2)_n$ can be usually observed in ternary systems where “M” is antimony, bismuth, lead, tin, or a rare earth element, “X” is sulphur or selenium, and “T” is titanium, zirconium, vanadium, niobium, tantalum, chromium, molybdenum, or tungsten. A literature search for phase diagrams of those ternary systems reveals only very few investigations. For the systems Mo-S-Sn [280, 281], S-Sn-W [281], and Bi-Mo-S [282-284] full isothermal sections without any MLCs are reported. Partial isothermal sections in the systems Mo-Pb-S [285-289] and Mo-Pb-Se [290, 291] do not include MLCs, too. Only the vertical sections of the Bi-Cr-S [292], Bi-Cr-Se [159, 293], Cr-S-Sb [294], and Cr-Sb-Se [295, 296] systems as well as the isothermal section of the Cr-Sb-Se system [296] contain one or more MLC phases. Hence, one aim of this thesis was to investigate phase diagrams of vanadium-based MLCs and determine whether the observed MLC phases can be added into an equilibrium phase diagram.

In this study, we report on the phase diagrams of the three ternary systems Pb-Se-V, Sb-Se-V, and Se-Sn-V (refer to chapters 4, 5, and 6). In the tin-based system, a total of six MLCs were observed. Additional experiments that employ mineralisers for successful MLCs’ synthesis could show that, on the one hand, the MLCs’ crystal sizes in the tin-based system can be increased by adding NH_4Cl, and that, on the other hand, MLCs are only obtainable for the Pb-Se-V and the Bi-Se-V systems when NH_4Cl is added. This indicates that a chloride gas species can facilitate the crystal growth of vanadium-based MLCs, yet, not in all cases as the lack of MLCs in the Sb-Se-V system demonstrates, but is not required in all systems (refer to chapter 7). Hence, the observed six MLCs in the Se-Sn-V can be undoubtedly included in the phase diagram. For the Bi-Se-V and the Pb-Se-V system, it is not entirely understood whether the MLCs are equilibrium phases that are kinetically hindered in their formation or if the MLCs are just stabilised by small impurities (e.g. chlorides, oxides). The former would require them to be included in the phase diagrams regardless of the utilised mineraliser. The latter would require them to be eliminated from phase diagrams. Clarke et al, for instance, included their MLCs into their isothermal section despite the fact that they prepared the investigated crystals in a eutectic melt of LiCl/KCl [159]. However, this is contrasted with the larger number of isothermal sections that do not include MLCs (described above). The fact that these publications are mostly older than the discovery of MLCs is a noteworthy aspect.

As described in chapter 3, the properties of the misfit layer compounds based on vanadium and selenium are little investigated in literature. Suspecting that ambiguous synthesis conditions of different authors may have resulted in crystals that are more difficult to investigate (e.g. impurities, oxides, small crystal sizes) and that more recent measurement equipment may tackle such problems more easily, the second aim of this thesis was to investigate the properties of those MLCs more in detail.

For this purpose, the different synthesis approaches were collected and compared (refer to chapters 3 and 7). The synthesis of vanadium-selenium-based MLCs was optimised in a second step. Optimal parameters are observed to be rather moderate annealing conditions and with additional NH_4Cl that acts as mineraliser. With the knowledge gathered in those experiments additional (unsuccessful) attempts to synthesise also vanadium-tellurium-based MLCs were made. Microwave-induced plasma synthesis, which is successfully used in literature for synthesising transition metal dichalcogenides, was (unsuccessful) tried for synthesising MLCs.

The crystal sizes of the synthesised MLCs are (partially) promising for exploring the properties further. However, intrinsic properties of the investigated compounds, such as the bending/breaking of crystals upon manipulation, the anisotropic plate-like crystal dimensions, the oxidation of the crystal surfaces, or the high reflectivity of the crystals, render an investigation rather difficult (refer to chapters 3 and 7). Such difficulties are not reported in the literature for vanadium-based MLCs. Also, the little available and comparable literature complicate the interpretation of results. Hence, only small progress can be reported on the structural, the thermal, and the physical properties of vanadium-selenium-based MLCs (refer to chapters 3, 7, and 8).

This study provides insights into the structural properties the up to now unknown MLC $(PbSe)_{1+\delta}VSe_2$. The crystal structure is comparable to the *fere*crystalline compound regarding the lattice dimensions but not for all the defects reported in literature. On the basis of the MLCs $[(SeSn)_{1+\delta}]_mVSe_2$, this study presents evidence that the sublayer thicknesses can be estimated by plotting the stacking parameters m or n against the lattice distance d in analogy to *fere*crystals. To our knowledge, this method is new for MLCs, which is most probably a result of available stacking sequences in MLCs that are commonly observed to be only $m = n = 1$. However, the lattice parameters a and b of the $(PbSe)_{1+\delta}VSe_2$ and the $[(SeSn)_{1+\delta}]_mVSe_2$ MLCs need to be determined in follow-up research in order to calculate the misfit parameters of these compounds and compare them to the structurally related *fere*crystals.

Vanadium-selenium-based MLCs tend to oxidise, especially when they are treated thermally or strongly irradiated. Hence, Raman spectroscopy is not the method of choice when phase transitions of MLCs are to be investigated. Standard measurement procedures can lead to strongly oxidised surfaces. These measurements exhibit good signal-to-noise ratios, yet, that of undesired oxides rather than that of an investigated MLC. In order to attribute the observed Raman frequencies to the respective modes, additional *ab initio* calculations are required.

Temperature-dependent resistivity measurements of the $(PbSe)_{1+\delta}VSe_2$ MLC showed that the CDW transition is elevated by more than 8 K compared to the VSe_2 bulk. For the out-of-plane direction, the temperature dependence of the electrical resistivity is metallic and semiconducting in the in-plane direction. This behaviour is similar to other MLCs and most likely originates in the VSe_2 slabs but requires further verification. Also, the phase transition around 20 K requires additional studies to be entirely understood.

10. Summary

This thesis not only aimed to investigate several phase diagrams of systems that potentially host vanadium-based misfit layer compounds but also to explore these MLCs further. Special emphasis was set on the synthesis, the composition, and the crystal structures of the prepared MLCs.

The current study provides a comprehensive review of the literature available on the synthesis and the structural properties of vanadium-based layered compounds. For the first time, the literature of vanadium-based *fere*crystalline and misfit layer compounds is standardised in a common framework and compared in detail. We present several open questions, which might be of interest for researchers of future investigations in this field of study.

Isothermal sections in the three-phase diagrams of Pb-Se-V, Sb-Se-V, and Se-Sn-V are presented. The samples were synthesised by standard solid-state preparation techniques (excluding arc melting) and by utilising mostly powders of oxide-free binary compounds. Most of the samples could be investigated only via PXRD, optical microscopy, SEM, and EDX but not DTA or DSC, which is due to the high vapour pressures of antimony, lead, selenium, and tin that often resulted in a transport of constituent phases in temperature gradients during measurements. Nevertheless, the reaction scheme of the Sb-Se-V phase diagram is presented, which was determined by careful evaluation of the reaction sequences in partially liquid samples annealed at different temperatures. We also present alterations to the current versions of the Pb-V, Sb-Se, Sb-V, Se-V, and Sn-V binary phase diagrams.

A total of six MLCs can be reported to be stable in the Se-Sn-V ternary system. The MLCs in the Bi-Se-V and the Pb-Se-V system can only be prepared by when NH_4Cl is added during synthesis, which acts as a mineraliser. MLCs in the ternary systems of Sb-Se-V, Bi-Te-V, Pb-Te-V, Sb-Te-V, and Sn-Te-V cannot be prepared regardless of the addition of a mineraliser. Also, the synthesis approach via microwave-induced plasmas is not yielding any MLCs.

Intrinsic properties, such as the bending of crystals upon manipulation or the strongly anisotropic properties and crystal dimensions, hamper attempts to characterise vanadium-based MLCs. Hence, we exclusively report on the structure of the MLC $(PbSe)_{1+\delta}VSe_2$. The lattice parameters and the defects of this compound are compared to the literature values of the structurally closely related ferecrystals $(PbSe)_{1.11}VSe_2$. For the other prepared MLC, only the stacking sequences and the interlayer distances can be stated. Hence, the crystal structures require additional determination in follow-up research.

The anisotropic dimensions of the MLC crystals also influence EDX signals. The current study provides evidence that the measured non-stoichiometric compositions are based on matrix effects rather than on defects, which would influence the actual crystal composition. Some unpublished values on the Raman spectra and resistivity values, which may aid to gain insights into the anisotropic properties and phase transitions in these MLCs in future works in this field, are provided in this study.

11. Zusammenfassung

Eines der primären Ziele dieser Arbeit bestand darin, Phasendiagramme von Systemen zu untersuchen, welche möglicherweise Vanadium-basierende Misfit-Layer-Compounds enthalten. Ein weiteres Ziel war es, die synthetisierten MLCs genauer zu charakterisieren, wobei ein besonderes Augenmerk auf die Kristallstrukturen und die exakte Zusammensetzung dieser Verbindungen gelegt wurde.

Im Konkreten wurden drei Phasendiagramme in den ternären Systemen Pb-Se-V, Sb-Se-V und Se-Sn-V untersucht und mittels isothermer Schnitte dargestellt. Dabei wurden etablierte Techniken der Festkörpersynthese zur Probenpräparation herangezogen, wobei vorwiegend mit Pulvern von oxidfreien binären Verbindungen gearbeitet wurde. Die meisten Proben konnten nur mittels PXRD, optische Mikroskopie, SEM und EDS, jedoch nicht mittels DTA oder DSC untersucht werden. Dies ist auf die hohen Dampfdrücke von Antimon, Blei, Selen und Zinn zurückzuführen, wodurch es zur Bildung von Inhomogenitäten im Temperaturgradienten während der Messung kommen kann. Zudem wird auch ein Reaktionsschema des Sb-Se-V-Phasendiagramms vorgestellt, welches durch sorgfältige Auswertung der Reaktionssequenzen von teilflüssig getemperten Proben bestimmt wurde. Außerdem werden in der vorliegenden Arbeit Änderungen an den aktuellen Versionen der binären Phasendiagramme Pb-V, Sb-Se, Sb-V, Se-V und Sn-V vorgeschlagen.

In den ternären Systemen Bi-Se-V und Pb-Se-V, wurde lediglich jeweils eine MLC-Verbindung gefunden, wohingegen im System Se-Sn-V insgesamt sechs MLCs synthetisiert werden konnten. In den Fällen von Bi-Se-V und Pb-Se-V musste während der Synthese, das als Mineralisator wirkende NH_4Cl, zugesetzt werden. Für die ternären Systeme Sb-Se-V, Bi-Te-V, Pb-Te-V, Sb-Te-V und Sn-Te-V konnten, ebenso bei der Zugabe eines Mineralisators, keine MLCs synthetisiert werden. Auch ein Syntheseansatz unter der Verwendung von mikrowelleninduzierten Plasmen lieferte keine MLCs.

Sämtliche Charakterisierungsversuche, wurden durch die intrinsischen Eigenschaften von MLCs auf Vanadiumbasis erschwert. Zu diesen gehören die leichte Verformbarkeit von Kristallen bei Manipulation oder auch die stark anisotropen Eigenschaften sowie Kristalldimensionen. Aufgrund dessen berichtet diese Arbeit ausschließlich über die Struktur des MLCs $(PbSe)_{1+\delta}VSe_2$. Dessen Gitterparameter und Defekte sind mit den Literaturwerten des strukturell eng verwandten *Fere*crystals, mit der Zusammensetzung $(PbSe)_{1.11}VSe_2$, vergleichbar. Für die anderen synthetisierten MLCs konnten nur die Stapelsequenzen und die Schichtabstände berichtet werden. Die Kristallstrukturen bedürfen daher einer zusätzlichen Charakterisierung im Zuge weiterer Forschungsarbeiten.

Wie gezeigt wurde, beeinflussen die stark anisotropen Dimensionen der MLC-Kristalle auch die EDX-Signale. Dabei liefert die aktuelle Studie Hinweise darauf, dass die gemessenen nicht-stöchiometrischen Zusammensetzungen auf Matrixeffekten und nicht auf Defekten beruhen, welche tatsächlich die Kristallzusammensetzungen beeinflussen würden. In der vorliegenden Arbeit werden auch einige unveröffentlichte Daten zu den Raman-Spektren und den elektrischen Widerständen der synthetisierten MLCs angegeben. Diese könnten bei zukünftigen Arbeiten auf diesem Gebiet dazu beitragen, Einblicke in die anisotropen Eigenschaften und Phasenübergänge dieser MLCs zu ermöglichen.

Abschließend fasst die aktuelle Arbeit die verfügbare Literatur zur Synthese und den strukturellen Eigenschaften von Schichtverbindungen auf Vanadiumbasis zusammen, wobei erstmalig die Literatur zu *Fere*crystals und Misfit-Layer-Compounds auf Vanadiumbasis in einem gemeinsamen Schema standardisiert und detailliert verglichen wurde. Dabei werden einige offene Fragen vorgestellt, welche für die ForscherInnen bei zukünftigen Untersuchungen in diesem Forschungsgebiet von Interesse sein könnten.

Literature

[1] S. Stern, M. Daub, J. Klier, A. Wiesinger, A. Domeyer, Public Services Government 4.0 – the public sector in the digital age, in: M. Company (Ed.), Visual Media Europe, 2018.

[2] D. Wee, M. Breunig, R. Kelly, R. Mathis, Industry 4.0 after the initial hype - Where manufacturers are finding value and how they can best capture it, in: M. Company (Ed.), Visual Media Europe, 2016.

[3] J. Burgess, P. Mitchell, T. Highfield, Automating the digital everyday: an introduction, Media Int Aust, 166 (2018) 6-10.

[4] K. Santos, E. Loures, F. Piechnicki, O. Canciglieri, Opportunities Assessment of Product Development Process in Industry 4.0, Procedia Manuf, 11 (2017) 1358-1365.

[5] B. Slusarczyk, Industry 4.0 - Are We Ready?, Pol J Manag Stud, 17 (2018) 232-248.

[6] K.J. Kim, D.H. Shin, An acceptance model for smart watches Implications for the adoption of future wearable technology, Internet Res, 25 (2015) 527-541.

[7] Y. Al Mtawa, A. Haque, B. Bitar, Does Internet of Things Disrupt Residential Bandwidth Consumption?, IEEE VTS VEH Technol, (2018).

[8] C.A. Mack, Fifty Years of Moore's Law, Ieee T Semiconduct M, 24 (2011) 202-207.

[9] M. Golio, Fifty Years of Moore's Law, P Ieee, 103 (2015) 1932-1937.

[10] J. Wang, M. Lundstrom, Does source-to-drain tunneling limit the ultimate scaling of MOSFETs?, International Electron Devices 2002 Meeting, Technical Digest, (2002) 707-710.

[11] G. Yeric, Moore's Law at 50: Are we planning for retirement?, 2015 Ieee International Electron Devices Meeting (Iedm), (2015).

[12] P. Avouris, Z.H. Chen, V. Perebeinos, Carbon-based electronics, Nat Nanotechnol, 2 (2007) 605-615.

[13] Y. Liu, X.D. Duan, Y. Huang, X.F. Duan, Two-dimensional transistors beyond graphene and TMDCs, Chem Soc Rev, 47 (2018) 6388-6409.

[14] D. Schaming, H. Remita, Nanotechnology: from the ancient time to nowadays, Found Chem, 17 (2015) 187-205.

[15] J. Jeevanandam, A. Barhoum, Y.S. Chan, A. Dufresne, M.K. Danquah, Review on nanoparticles and nanostructured materials: history, sources, toxicity and regulations, Beilstein J Nanotech, 9 (2018) 1050-1074.

[16] M. Miernicki, T. Hofmann, I. Eisenberger, F. von der Kammer, A. Praetorius, Legal and practical challenges in classifying nanomaterials according to regulatory definitions, Nat Nanotechnol, 14 (2019) 208-216.

[17] J. Potočnik, Commission Recommendation of 18 October 2011 on the definition of nanomaterial Text with EEA relevance (2011/696/EU), in: E. Commission (Ed.), Official Journal of the European Union, Brussels, 2011.

[18] R.W. Siegel, Nanostructured Materials - Mind over Matter, Nanostruct Mater, 3 (1993) 1-18.

[19] C. Suryanarayana, Non-equilibrium processing of materials, in: R.W. Cahn (Ed.) Pergamon materials series, Pergamon, Amsterdam ; New York, 1999, pp. xx, 438 p.

[20] J.N. Tiwari, R.N. Tiwari, K.S. Kim, Zero-dimensional, one-dimensional, two-dimensional and three-dimensional nanostructured materials for advanced electrochemical energy devices, Prog Mater Sci, 57 (2012) 724-803.

[21] B.S. Murty, P. Shankar, B. Raj, B.B. Rath, J. Murday, Textbook of Nanoscience and Nanotechnology, Springer, Bangalore, 2013.

[22] V.V. Pokropivny, V.V. Skorokhod, Classification of nanostructures by dimensionality and concept of surface forms engineering in nanomaterial science, Mat Sci Eng C-Bio S, 27 (2007) 990-993.

[23] M. Beekman, C.L. Heideman, D.C. Johnson, Ferecrystals: non-epitaxial layered intergrowths, Semicond. Sci. Technol., 29 (2014).

[24] M. Bonilla, S. Kolekar, Y.J. Ma, H.C. Diaz, V. Kalappattil, R. Das, T. Eggers, H.R. Gutierrez, M.H. Phan, M. Batzill, Strong room-temperature ferromagnetism in VSe_2 monolayers on van der Waals substrates, Nat Nanotechnol, 13 (2018) 289-293.

[25] Y. Gotoh, M. Goto, K. Kawaguchi, Y. Oosawa, Preparation and Characterization of a New Composite-Layered Sulfide, $(PbS)_{1.12}VS_2$, $PbVS_3$, Mater Res Bull, 25 (1990) 307-314.

[26] Y. Ohno, Modulation structure in the STM images of the non-metallic misfit-layer compound $(PbS)_{1.12}VS_2$, Surf. Sci., 600 (2006) 4829-4837.

[27] O.K. Hite, M. Falmbigl, M.B. Alemayehu, M. Esters, S.R. Wood, D.C. Johnson, Charge Density Wave Transition in $(PbSe)_{1+\delta}(VSe_2)_n$ Compounds with n=1, 2, and 3, Chem Mater, 29 (2017) 5646-5653.

[28] D.L.M. Cordova, S.S. Fender, T.M. Kam, J. Seyd, M. Albrecht, P. Lu, R. Fischer, D.C. Johnson, Designed Synthesis and Structure-Property Relationships of Kinetically Stable $[(PbSe)_{1+\delta}]_m(VSe_2)_1$ (m=1, 2, 3, 4) Heterostructures, Chem Mater, 31 (2019) 8473-8483.

[29] A.K. Geim, I.V. Grigorieva, Van der Waals heterostructures, Nature, 499 (2013) 419-425.

[30] M.J. Grant, A. Booth, A typology of reviews: an analysis of 14 review types and associated methodologies, Health Info Libr J, 26 (2009) 91-108.

[31] P.C. Donohue, Preparation and Properties of $LnMX_3$, Where Ln = Rare-Earths, Bi - M = Ta, Nb, Ti, V, and X = S, Se, J Solid State Chem, 12 (1975) 80-83.

[32] R. Atkins, B.D. Anderson, I.M. Anderson, P. Zschack, D.C. Johnson, Synthesis of new ferecrystals $(SnSe)_y(TSe_2)$ where T = V and Ta, 2011 11th IEEE International Conference on Nanotechnology, (2011) 1230-1234.

[33] L. Cario, J. Rouxel, A. Meerschaut, Y. Moelo, B. Corraze, O. Chauvet, Band structure and electronic properties of the incommensurate misfit compound $(LaS)_{1.18}VS_2$, J Phys-Condens Mat, 11 (1999) 2887-2900.

[34] K. Kato, M. Onoda, A. Sato, N.W. Cho, S. Kikkawa, F. Kanamaru, K. Ohsumi, T. Takase, M. Uchida, O. Jarchow, K. Friese, Structure of the 1-Dimensionally Disordered Composite Crystal $(LaS)_{1,18}VS_2$, Z Kristallogr, 210 (1995) 432-437.

[35] Y. Ren, J. Baas, A. Meetsma, J.L. deBoer, G.A. Wiegers, Vacancies and electron localization in the incommensurate intergrowth compound $(La_{0.95}Se)_{1.21}VSe_2$, Acta Crystallogr B, 52 (1996) 398-405.

[36] J. Rouxel, A. Meerschaut, Misfit layer compounds $(MX)_{1+x}(TX_2)_m$ M=Pb, Bi, Sn; T=Ti, V, Cr, Ta, Nb; X=S, Se; 0.08<x<0.28; m=1, 2, 3, in: C. Schlenker,

J. Dumas, M. Greenblatt, S. vanSmaalen (Eds.) Physics and Chemistry of Low-Dimensional Inorganic Conductors, Plenum Press Div Plenum Publishing Corp, New York, 1996, pp. 59-70.

[37] M. Falmbigl, D. Putzky, J. Ditto, M. Esters, S.R. Bauers, F. Ronning, D.C. Johnson, Influence of Defects on the Charge Density Wave of $([SnSe]_{1+\delta})_1(VSe_2)_1$ Ferecrystals, Acs Nano, 9 (2015) 8440-8448.

[38] M. Falmbigl, D. Putzky, J. Ditto, D.C. Johnson, Influence of interstitial V on structure and properties of ferecrystalline $([SnSe]_{1.15})_1(V_{1+x}Se_2)_n$ for n=1, 2, 3, 4, 5, and 6, J Solid State Chem, 231 (2015) 101-107.

[39] N.S. Gunning, T. Dankwort, M. Falmbigl, U. Ross, G. Mitchson, D.M. Hamann, A. Lotnyk, L. Kienle, D.C. Johnson, Expanding the Concept of van der Waals Heterostructures to Interwoven 3D Structures, Chem Mater, 29 (2017) 8292-8298.

[40] Y. Yasui, T. Nishikawa, Y. Kobayashi, M. Sato, T. Nishioka, M. Kontani, Effects of Carrier Doping into the Misfit-Layer Compounds $(La_{1-y}R_yS)_{1+\alpha}VS_2$ (R=Sr and Pb): Transport and Magnetic Studies, J Phys Soc Jpn, 64 (1995) 3890-3896.

[41] S. Kikkawa, A. Nakatuka, N. Cho, F. Kanamaru, Sulfur Deficiency in misfit layered $(LaS)_{1.18}VS_2$, Eur. J. Solid State Inorg. Chem., 32 (1995) 771-778.

[42] T. Nishikawa, Y. Yasui, Y. Kobayashi, M. Sato, Thermal properties of two dimensional Mott system $La_{1.17-x}Sr_xVS_{3.17}$, J Phys Soc Jpn, 65 (1996) 2543-2547.

[43] L. Cario, A. Meerschaut, B. Corraze, O. Chauvet, Determination of the modulated structure of the misfit layer compound $(LaS)_{1.196}VS_2$, Mater Res Bull, 40 (2005) 125-133.

[44] T.B. Williams, B.G. Hyde, Electron diffraction observations from some so-called '$LnMS_3$' layer compounds isostructural with '$\sim LaCrS_3$' and from cannizzarite, $\sim Pb_{46}Bi_{54}S_{127}$, Acta Crystallogr B, 44 (1988) 467-474.

[45] M. Onoda, K. Kato, Y. Gotoh, Y. Oosawa, Structure of the Incommensurate Composite Crystal $(PbS)_{1.12}VS_2$, Acta Crystallogr B, 46 (1990) 487-492.

[46] Y. Gotoh, J. Akimoto, Y. Oosawa, H. Yamawaki, M. Sakashita, K. Aoki, Mutual incommensurability and interlayer interaction in $(MX)_xTX_2$-type ternary chalcogenides with layered composite crystal structure, Physica B, 237 (1997) 177-178.

[47] T. Kondo, K. Suzuki, T. Enoki, Transport and magnetic properties of incommensurate layer compounds $(RES)_xVS_2$ (RE = RARE EARTHS), Solid State Commun, 84 (1992) 999-1003.

[48] J. Rouxel, A. Meerschaut, Misfit Layer Compounds $(MX)_n(TX_2)_m$ [M=Sn, Pb, Bi, Rare Earth; T=Transition Metal; X=S, Se; 1.08<n<1.25; m=1, 2], Mol. Cryst. Liq. Cryst. Sci. Technol. Sect. A-Mol. Cryst. Liq. Cryst., 244 (1994) 343-354.

[49] V.T. Phuoc, V. Brouet, B. Corraze, E. Janod, M. Zaghrioui, L. Cario, Relation between Thermally Induced Structural Distortions and Electronic Properties of the Layered Misfit Chalcogenide $(LaS)_{1.196}VS_2$, J Phys Chem C, 118 (2014) 19273-19279.

[50] V. Brouet, J. Mauchain, E. Papalazarou, J. Faure, M. Marsi, P.H. Lin, A. Taleb-Ibrahimi, P. Le Fevre, F. Bertran, L. Cario, E. Janod, B. Corraze, V.T.

Phuoc, L. Perfetti, Ultrafast filling of an electronic pseudogap in an incommensurate crystal, Phys Rev B, 87 (2013).

[51] K. Suzuki, T. Kondo, T. Enoki, S. Bandow, Conduction Mechanism and Two-Dimensional Magnetism in Incommensurate Layered Compounds $(ReS)_xMS_2$ (Re=Rare Earth Metal,M=Ta,V), Synth. Met., 56 (1993) 1741-1746.

[52] K. Suzuki, T. Kondo, M. Iwasaki, T. Enoki, Variety of Magnetism in Incommensurate Misfit Layer Compounds $(RES)_xTS_2$ (RE= Rare Earths, T= Ta, V, Ti, Cr), Japanese Journal of Applied Physics Part 1-Regular Papers Short Notes & Review Papers, 32 (1993) 341-343.

[53] T. Kondo, K. Suzuki, T. Enoki, S. Bandow, Magnetism in Incommensurate Layer Compounds $(RES)_xVS_2$ (Re=Rare-Earths), Mol. Cryst. Liq. Cryst. Sci. Technol. Sect. A-Mol. Cryst. Liq. Cryst., 244 (1994) A117-A122.

[54] T. Nishikawa, Y. Yasui, M. Sato, Transport Anomalies of Misfit-Layer Compounds $La_{1.17-x}Sr_xVS_{3.17}$ with Mott Metal-Insulator Transition, J Phys Soc Jpn, 63 (1994) 3218-3221.

[55] T. Kondo, K. Suzuki, T. Enoki, H. Tajima, T. Ohta, Conduction and localization in incommensurate misfit layer compounds, J Phys Chem Solids, 57 (1996) 1105-1108.

[56] T. Nishikawa, Y. Yasui, Y. Kobayashi, M. Sato, Studies of the metal-insulator transition of misfit-layer compounds $La_{1.17-x}Sr_xVS_{3.17}$, Physica C, 263 (1996) 554-557.

[57] A. Ino, S. Fujimori, T. Okane, A. Fujimori, T. Mizokawa, Y. Yasui, T. Nishikawa, M. Sato, Photoemission study of the filling-control metal-insulator transition in the two-dimensional system $La_{1.17-x}Pb_xVS_{3.17}$, J Magn Magn Mater, 226 (2001) 263-265.

[58] A. Ino, T. Okane, S.I. Fujimori, A. Fujimori, T. Mizokawa, Y. Yasui, T. Nishikawa, M. Sato, Evolution of the electronic structure from electron-doped to hole-doped states in the two-dimensional Mott-Hubbard system $La_{1.17-x}Pb_xVS_{3.17}$, Phys Rev B, 69 (2004).

[59] Y. Gotoh, M. Onoda, K. Uchida, Y. Tanaka, T. Iida, H. Hayakawa, Y. Oosawa, Preparation and Characterization of $BiMX_3$ (M = Ti, V, Nb, Ta, X = S, Se), New Composite-Layered Chalcogenides, Chem Lett, (1989) 1559-1562.

[60] Y. Oosawa, Y. Gotoh, J. Akimoto, M. Onoda, Preparation and Characterization of Bi-Containing Ternary Chalcogenides with Layered Composite Crystal-Structure, J Alloy Compd, 176 (1991) 319-327.

[61] L. Hernán, J. Morales, J. Pattanayak, J.L. Tirado, Lithium Intercalation into $PbNb_2S_5$, $PbNbS_3$, $SnNb_2Se_5$, $BiVS_3$, $SnVSe_3$, and $PbNb_2Se_5$ Misfit Layer Chalcogenides, J Solid State Chem, 100 (1992) 262-271.

[62] L. Hernán, P. Lavela, J. Morales, J. Pattanayak, J.L. Tirado, Structural aspects of lithium intercalated $PbVS_3$, $PbTiS_3$, $PbTi_2S_5$ and $SnNbS_3$ misfit layer compounds, Mater Res Bull, 26 (1991) 1211-1218.

[63] C. Barriga, P. Lavela, J. Morales, J. Pattanayak, J.L. Tirado, Electrochemical Lithium Intercalation into Misfit Layer Sulfides, Chem Mater, 4 (1992) 1021-1026.

[64] R. Guzmán, L. Hernán, J. Morales, J. Pattanayak, J.L. Tirado, Lithium/N-Alkylamine Intercalation into Lead, Vanadium Misfit Layer Sulfide, Mater Res Bull, 28 (1993) 469-476.

[65] C. Auriel, A. Meerschaut, P. Deniard, J. Rouxel, Lithium Intercalation into Misfit Layer Compounds of MT_2X_5-Type (M = Rare-Earth, Sn, Pb, Bi, T = Ti, V, Cr, Nb, Ta, X = S, Se), Example of $PbNb_2S_5$, Comptes Rendus De L Academie Des Sciences Serie Ii, 313 (1991) 1255-1259.

[66] J. Rouxel, A. Meerschaut, About chemical bonds in misfit layer chalcogenides, in: P.K. Davies, A.J. Jacobson, C.C. Torardi, T.A. Vanderah (Eds.) Solid-State Chemistry of Inorganic Materials, Materials Research Society, Warrendale, 1997, pp. 3-13.

[67] R. Atkins, S. Disch, Z. Jones, I. Haeusler, C. Grosse, S.F. Fischer, W. Neumann, P. Zschack, D.C. Johnson, Synthesis, structure and electrical properties of a new tin vanadium selenide, J Solid State Chem, 202 (2013) 128-133.

[68] R. Atkins, M. Dolgos, A. Fiedler, C. Grosse, S.F. Fischer, S.P. Rudin, D.C. Johnson, Synthesis and Systematic Trends in Structure and Electrical Properties of $[(SnSe)_{1.15}]_m(VSe_2)_1$, m=1, 2, 3, and 4, Chem Mater, 26 (2014) 2862-2872.

[69] M. Falmbigl, A. Fiedler, R.E. Atkins, S.F. Fischer, D.C. Johnson, Suppressing a Charge Density Wave by Changing Dimensionality in the Ferecrystalline Compounds $([SnSe]_{1.15})_1(VSe_2)_n$ with n=1, 2, 3, 4, Nano Lett, 15 (2015) 943-948.

[70] I. Häusler, R. Atkins, M. Falmbigl, S.P. Rudin, W. Neumann, D.C. Johnson, Insights from STEM and NBED studies into the local structure and growth mechanism of misfit layered compounds prepared using modulated reactants, Z Kristallogr, 230 (2015) 45-54.

[71] N.S. Gunning, Synthesis, characterization and properties of $[(SnSe)_{1+\delta}]_m(MoSe_2)_n$ and new rare earth $(LaSe_{1-x})_{1.17}(VSe_{2-y})_n$ (n=2-4) and $[(EuSe)_{1+\delta}]_1(VSe_2)_n$ (n=1-3) Ferecrystal Systems, in, University of Oregon, Oregon, 2015, pp. 146.

[72] R. Atkins, D.B. Moore, D.C. Johnson, Insights into the Self-Assembly of Ferecrystalline Compounds from Designed Amorphous Precursors, Chem Mater, 25 (2013) 1744-1750.

[73] S.P. Rudin, D.C. Johnson, Density functional theory calculations of the turbostratically disordered compound $[(SnSe)_{1+y}]_m(VSe_2)_n$, Phys Rev B, 91 (2015).

[74] M. Falmbigl, Z. Hay, J. Ditto, G. Mitchson, D.C. Johnson, Modifying a charge density wave transition by modulation doping: ferecrystalline compounds $([Sn_{1-x}Bi_xSe]_{1.15})_1(VSe_2)_1$ with 0 <= x <= 0.66, J Mater Chem C, 3 (2015) 12308-12315.

[75] J. Rouxel, Y. Moelo, A. Lafond, F.J. Disalvo, A. Meerschaut, R. Roesky, Role of Vacancies in Misfit Layered Compounds: Case of the Gadolinium Chromium Sulfide Compound, Inorg Chem, 33 (1994) 3358-3363.

[76] L. Cario, B. Corraze, A. Meerschaut, Y. Moelo, O. Chauvet, Electronic properties of the $(LaS)_{1.18}VS_2$ incommensurate misfit compound, Synth. Met., 103 (1999) 2640-2643.

[77] L. Cario, B. Corraze, A. Meerschaut, O. Chauvet, Dielectric breakdown and current switching effect in the incommensurate layered compound $(LaS)_{1.196}VS_2$, Phys Rev B, 73 (2006) 4.

[78] S.P. Abramov, Motif of misfit layer compounds $(SnS)_xTS_2$ (T = Ti, V, Nb, Ta) in the matrix of SnS_2, Solid State Commun, 112 (1999) 265-267.
[79] M.B. Alemayehu, K. Ta, M. Falmbigl, D.C. Johnson, Charge transfer vs. dimensionality: what affects the transport properties of ferecrystals?, Nanoscale, 7 (2015) 7378-7385.
[80] M. Beekman, G. Rodriguez, R. Atkins, J. Kunert, D.B. Moore, D.C. Johnson, Detection of nanoscale embedded layers using laboratory specular X-ray diffraction, Journal of Applied Physics, 117 (2015).
[81] L. Cario, H. Kabbour, A. Meerschaut, Designing new inorganic compounds from 2D building blocks, Chem Mater, 17 (2005) 234-236.
[82] L. Cario, A. Meerschaut, Y. Moelo, Redox competition and stability: rare earth misfit layer compounds as an example, Comptes Rendus Acad. Sci. Ser. II C, 2 (1999) 617-624.
[83] N. Cho, S. Kikkawa, F. Kanamaru, Y. Takeda, O. Yamamoto, H. Kido, T. Hoshikawa, Crystal structural, electric and magnetic studies on the misfit layer compounds “$LnMS_3$” (Ln=rare-earth metal; M=Ti,V,Cr), Solid State Ion., 63-5 (1993) 696-701.
[84] D.L.M. Cordova, T.M. Kam, S.S. Fender, Y.H. Tsai, D.C. Johnson, Strong Non-Epitaxial Interactions: Crystallographically Aligned PbSe on VSe_2, physica status solidi (a), 216 (2019) 1800896.
[85] M. Esters, M. Falmbigl, D. Johnson, Mechanistic studies in kinetically controlled solid state synthesis: The case of $[(SnSe)_{1.15}][VSe_2]$, Abstr. Pap. Am. Chem. Soc., 249 (2015).
[86] M. Falmbigl, M.B. Alemayehu, D.R. Merrill, M. Beekman, D.C. Johnson, In-plane structure of ferecrystalline compounds, Cryst Res Technol, 50 (2015) 464-472.
[87] M. Falmbigl, M. Esters, D.C. Johnson, Formation of a Selenide-Based Heterostructure From a Designed Precursor, Cryst Res Technol, 52 (2017).
[88] K. Friese, O. Jarchow, K. Kato, The structure of the disordered composite crystal $(LaS)_{1.18}VS_2$: The domain structure, Z Kristallogr, 212 (1997) 648-655.
[89] A. Fujimori, A. Ino, T. Mizokawa, T. Tsujioka, T. Yoshida, M. Satake, K. Okazaki, H. Eisaki, S. Uchida, K. Kishio, Y. Taguchi, T. Katsufuji, Y. Tokura, Y. Yasui, T. Nishikawa, M. Sato, Chemical potential shifts in correlated electron systems studied by photoemission spectroscopy, J. Electron Spectrosc. Relat. Phenom., 92 (1998) 59-63.
[90] Y. Gotoh, J. Akimoto, Y. Oosawa, M. Onoda, Synthesis and characterization of mutually incommensurate $(BiS)_{1.16}VS_2$ with layered composite crystal structure, Jpn. J. Appl. Phys. Part 2 - Lett. Express Lett., 34 (1995) L1662-L1665.
[91] Y. Gotoh, H. Fujihisa, S. Takeya, I. Yamaguchi, The structural representation and properties of mutually incommensurate composite crystal $(BiS)_xTS_2$ (T = Ti, V, Nb and Ta), Phys. Status Solidi A-Appl. Mat., 203 (2006) 2852-2855.
[92] Y. Gotoh, M. Onoda, M. Goto, Y. Oosawa, Preparation and Characterization of $PbVS_3$ a New Composite Layered Compound, Chem Lett, (1989) 1281-1282.
[93] Y. Gotoh, I. Yamaguchi, Y. Takahashi, J. Akimoto, M. Goto, K. Kawaguchi, N. Yamamoto, M. Onoda, Preparation, characterization and property of

$(BiS)_xTS_2$-type ternary chalcogenides (T=V, Nb and Ta) with layered composite crystal structure, Solid State Ion., 172 (2004) 519-522.

[94] L. Guemas, P. Rabu, A. Meerschaut, J. Rouxel, Characterization of New $SnNbS_3$, $PbNbS_3$, $PbNb_2S_5$, $SnTiS_3$ and $SnTi_2S_5$ Compounds, Mater Res Bull, 23 (1988) 1061-1069.

[95] L. Hernán, J. Morales, J. Pattanayak, J.L. Tirado, Preparation and Characterization of New Misfit Layer Selenides $SnVSe_3$ and $SnNb_2Se_5$, Chem Lett, (1991) 1981-1984.

[96] O.K. Hite, M. Nellist, J. Ditto, M. Falmbigl, D.C. Johnson, Transport properties of VSe_2 monolayers separated by bilayers of BiSe, Journal of Materials Research, 31 (2016) 886-892.

[97] M. Imada, A. Fujimori, Y. Tokura, Metal-insulator transitions, Rev Mod Phys, 70 (1998) 1039-1263.

[98] Y. Kawasaki, Y. Kishimoto, T. Tanaka, T. Ohno, S. Niitaka, N. Katayama, H. Takagi, NMR study of magnetic excitation in $LiVX_2$ (X = O, S), International Conference on Frustration in Condensed Matter (Icfcm), 320 (2011).

[99] Y. Kobayashi, M. Kasai, Y. Yasui, T. Nishikawa, M. Sato, ^{51}V-NMR study of the misfit layer compounds $La_{1.17-x}Sr_xVS_{3.17}$, J Phys Soc Jpn, 66 (1997) 4027-4030.

[100] M. Lejman, G. Galle, J. Faure, L. Cario, D. Boschetto, Coherent phonon dynamics in misfit-layered chalcogenide $LaVS_3$ crystal, Proc Spie, 10530 (2018).

[101] A.C. Lygo, D.M. Hamann, D.B. Moore, D.R. Merrill, J. Ditto, M. Esters, J. Orlowicz, S.R. Wood, D.C. Johnson, Kinetically Controlled Formation and Decomposition of Metastable $[(BiSe)_{1+\delta}]_m[TiSe2]_m$ Compounds, Journal of the American Chemical Society, 140 (2018) 3385-3393.

[102] A. Meerschaut, Y. Moelo, L. Cario, A. Lafond, C. Deudon, Charge transfer in misfit layer chalcogenides, $[(MX)_n]_{1+x}(TX_2)_m$: a key for understanding their stability and properties, Mol. Cryst. Liquid Cryst., 341 (2000) 805-812.

[103] A. Meetsma, G.A. Wiegers, R.J. Haange, J.L. Deboer, The Incommensurate Misfit Layer Structure of $(SnS)_{1.17}NbS_2$, $SnNbS_3$ .1. A Study by Means of X-Ray-Diffraction, Acta Crystallogr A, 45 (1989) 285-291.

[104] S. Morishita, N. Yamamoto, Y. Gotoh, Y. Oosawa, Incommensurate modulated structure and staking disorder of misfit layer compounds PbS-VS_2 and BiS-TaS_2, Editions Physique, Les Ulis, 1994.

[105] T. Murugesan, S. Ramesh, J. Gopalakrishnan, C.N.R. Rao, Rare earth transition metal sulfides, $LnMS_3$, J Solid State Chem, 38 (1981) 165-172.

[106] Y. Oosawa, Y. Gotoh, M. Onoda, Composite-Layered Chalcogenides: A New Candidate for Superconductor, in: T. Ishiguro, K. Kajimura (Eds.) Advances in Superconductivity II: Proceedings of the 2nd International Symposium on Superconductivity (ISS '89), Springer, Tokyoc, 1990, pp. 193-196.

[107] G.R. Reisinger, K.W. Richter, Phase equilibria and new misfit layer compound in the ternary system of Pb–Se–V, J Alloy Compd, 831 (2020).

[108] G.R. Reisinger, K.W. Richter, Manuscript 2: The 550 °C and 700 °C isothermal sections and new misfit layer compounds in the Se-Sn-V system, submitted to the Journal of Alloys and Compounds, (2020).

[109] G.R. Reisinger, K.W. Richter, Manuscript 3: Vanadium-selenium-based misfit layer compounds – insights into synthesis, morphology, and structure, to be submitted to the Journal of Alloys and Compounds, (2020).

[110] C. Sourisseau, R. Cavagnat, M. Fouassier, J.L. Tirado, J. Morales, Raman, resonance Raman and lattice dynamics studies of misfit layered compounds: $(SnS)_{1.17}NbS_2$, $(PbS)_{1.18}TiS_2P$, $(PbS)_{1.12}VS_2$, John Wiley & Sons Ltd, Chichester, 1994.

[111] C. Sourisseau, R. Cavagnat, M. Fouassier, J.L. Tirado, J. Morales, Raman-Study and Lattice-Dynamics Calculation of the Misfit Layer Compound $(PbS)_{1.12}VS_2$, J Raman Spectrosc, 26 (1995) 675-681.

[112] C. Sourisseau, R. Cavagnat, M. Fouassier, J.L. Tirado, J. Morales, Raman-Study and Lattice-Dynamics Calculations of Misfit Layered Compounds - $(PbS)_{1.18}TiS_2$ and $(PbS)_{1.12}VS_2$, J Mol Struct, 348 (1995) 107-110.

[113] C. Wan, Y. Wang, W. Norimatsu, M. Kusunoki, K. Koumoto, Nanoscale stacking faults induced low thermal conductivity in thermoelectric layered metal sulfides, Appl Phys Lett, 100 (2012).

[114] R.D. Westover, G. Mitchson, O.K. Hite, K. Hill, D.C. Johnson, Suppression of a Charge Density Wave in $([SnSe]_{1.15})_1(VSe_2)_1$ Ferecrystals Via Isoelectronic Doping with Ta, J Electron Mater, 45 (2016) 4898-4902.

[115] G.A. Wiegers, Physical-Properties of First-Row Transition-Metal Dichalcogenides and Their Intercalates, Physica B & C, 99 (1980) 151-165.

[116] G.A. Wiegers, Charge transfer between layers in misfit layer compounds, J Alloy Compd, 219 (1995) 152-156.

[117] G.A. Wiegers, A. Meerschaut, Structures of misfit layer compounds $(MS)_nTS_2$ (M = Sn, Pb, Bi, rare earth metals; T = Nb, Ta, Ti, V, Cr; $1.08<n<1.23$), J Alloy Compd, 178 (1992) 351-368.

[118] G.A. Wiegers, A. Meetsma, S. Vansmaalen, R.J. Haange, J.L. Deboer, Structural relationship between the orthorhombic, monoclinic and triclinic misfit layer compounds $(MS)_nTS_2$ (M = Sn, Pb, rare earth metals, T = Ti, V, Cr, Nb, Ta; $1.13 < n < 1.21$), Solid State Commun, 75 (1990) 689-692.

[119] L.J. Zhang, D.J. Singh, Electronic structure and thermoelectric properties of layered PbSe-WSe_2 materials, Phys Rev B, 80 (2009).

[120] R. Westover, R.A. Atkins, M. Falmbigl, J.J. Ditto, D.C. Johnson, Self-assembly of designed precursors: A route to crystallographically aligned new materials with controlled nanoarchitecture, J Solid State Chem, 236 (2016) 173-185.

[121] J. Rouxel, A. Meerschaut, G.A. Wiegers, Chalcogenide Misfit Layer Compounds, J Alloy Compd, 229 (1995) 144-157.

[122] G.A. Wiegers, Misfit layer compounds: Structures and physical properties, Prog Solid State Ch, 24 (1996) 1-139.

[123] N.J. van Eck, L. Waltman, Software survey: VOSviewer, a computer program for bibliometric mapping, Scientometrics, 84 (2010) 523-538.

[124] K. Kato, I. Kawada, T. Takahashi, Die Kristallstruktur von $LaCrS_3$, Acta Crystallogr B, 33 (1977) 3437-3443.

[125] G.A. Wiegers, A. Meetsma, S. Vansmaalen, R.J. Haange, J. Wulff, T. Zeinstra, J.L. Deboer, S. Kuypers, G. Vantendeloo, J. Vanlanduyt, S. Amelinckx, A. Meerschaut, P. Rabu, J. Rouxel, Misfit Layer Compounds $(MS)_nTS_2$ (M = Sn, Pb, Bi, Rare-Earth Elements - T = Nb, Ta - n = 1.08 -

1.19), a new class of layer compounds, Solid State Commun, 70 (1989) 409-413.

[126] D.R. Merrill, D.B. Moore, S.R. Bauers, M. Falmbigl, D.C. Johnson, Misfit Layer Compounds and Ferecrystals: Model Systems for Thermoelectric Nanocomposites, Materials, 8 (2015) 2000-2029.

[127] Y. Moëlo, A. Meerschaut, J. Rouxel, C. Auriel, Precise Analytical Characterization of Incommensurate Sandwiched Layered Compounds $((Pb,Sn)S)_{1+x}((Nb,Ti)S_2)_m$ ($0.08 \leq x \leq 0.28$, $m = 1$-3). Role of Cationic Coupling on the Properties and the Structural Modulation, Chem Mater, 7 (1995) 1759-1771.

[128] E. Kabliman, P. Blaha, K. Schwarz, *Ab initio* study of stabilization of the misfit layer compound $(PbS)_{1.14}TaS_2$, Phys Rev B, 82 (2010) 8.

[129] H. Nakazawa, M. Saeki, M. Nakahira, Order-Disorder Phenomena of Cationic Vacancies in a Vanadium Sulfide, V_5S_8, Journal of the Less-Common Metals, 40 (1975) 57-63.

[130] G.R. Reisinger, K.W. Richter, The ternary phase diagram of Sb-Se-V and its subsystems, J Alloy Compd, 810 (2019).

[131] H.T. Xu, Z.Q. Jiang, H.J. Zhang, L. Liu, L. Fang, X. Gu, Y. Wang, New Efficient Electrocatalyst for the Hydrogen Evolution Reaction: Erecting a V_2Se_9@Poly(3,4-ethylenedioxythiophene) Nanosheet Array with a Specific Active Facet Exposed, Acs Energy Lett, 2 (2017) 1099-1104.

[132] M.Y. Yan, X.L. Pan, P.Y. Wang, F. Chen, L. He, G.P. Jiang, J.H. Wang, J.Z. Liu, X. Xu, X.B. Liao, J.H. Yang, L.Q. Mai, Field-Effect Tuned Adsorption Dynamics of VSe_2 Nanosheets for Enhanced Hydrogen Evolution Reaction, Nano Lett, 17 (2017) 4109-4115.

[133] H.B. Song, T.Y. Li, J. Zhang, Y. Zhou, J.J. Luo, C. Chen, B. Yang, C. Ge, Y.Q. Wu, J. Tang, Highly Anisotropic Sb_2Se_3 Nanosheets: Gentle Exfoliation from the Bulk Precursors Possessing 1D Crystal Structure, Adv Mater, 29 (2017).

[134] S.S. Yao, J. Cui, Z.H. Lu, Z.L. Xu, L. Qin, J.Q. Huang, Z. Sadighi, F. Ciucci, J.K. Kim, Unveiling the Unique Phase Transformation Behavior and Sodiation Kinetics of 1D van der Waals Sb_2S_3 Anodes for Sodium Ion Batteries, Advanced Energy Materials, 7 (2017).

[135] S. Chae, A.J. Siddiqa, B.J. Kim, S. Oh, K.H. Choi, K.H. Lee, H.Y. Kim, H.K. Yu, J.Y. Choi, Isolation of inorganic molecular chains from rod-like bulk V_2Se_9 crystal by liquid exfoliation, Rsc Adv, 8 (2018) 35348-35352.

[136] B.J. Kim, B.J. Jeong, S. Oh, S. Chae, K.H. Choi, T. Nasir, S.H. Lee, K.W. Kim, H.K. Lim, I.J. Choi, J.Y. Moon, H.K. Yu, J.H. Lee, J.Y. Choi, Exfoliation and Characterization of V_2Se_9 Atomic Crystals, Nanomaterials-Basel, 8 (2018).

[137] S. Oh, S. Chae, B.J. Kim, K.H. Choi, W.S. Jang, J.M. Jang, Y. Hussain, D.K. Lee, Y.M. Kim, H.K. Yu, J.Y. Choi, Synthesis of a one-dimensional atomic crystal of vanadium selenide (V_2Se_9), Rsc Adv, 8 (2018) 33980-33984.

[138] W. Yang, J. Ahn, Y. Oh, J. Tan, H. Lee, J. Park, H.C. Kwon, J. Kim, W. Jo, J. Kim, J. Moon, Adjusting the Anisotropy of 1D Sb_2Se_3 Nanostructures for Highly Efficient Photoelectrochemical Water Splitting, Advanced Energy Materials, 8 (2018).

[139] G.A. Wiegers, Misfit Layer Compounds Based on Double Layers MX and Sandwiches TX_2 (M=Sn, Pb, Sb, Bi, Ln; T=Ti, V, Cr, Nb, Ta; X=S, Se), Japanese Journal of Applied Physics Part 1-Regular Papers Short Notes & Review Papers, 32 (1993) 705-710.

[140] M. Wobst, Course of Miscibility Gaps of Binary Systems Silver-Tellurium, Indiumtellurium, Thallium-Tellurium and Antimony-Selenium, Scripta Metall Mater, 5 (1971) 583-585.

[141] R. Blachnik, Schneide.A, Enthalpies of Melting III/V, IV/V and V/VI Compounds, Z Anorg Allg Chem, 372 (1970) 314-&.

[142] V.M. Glazov, L.M. Pavlova, D.S. Gaev, Study of Thermal-Stability of Selenides of Periodic System Group-Iv and Group-V Elements Based on Data of Liquidus Curvature at the Melting-Point, Zhurnal Neorganicheskoi Khimii, 29 (1984) 1079-1085.

[143] J.S. Berkes, M.B. Myers, Phase Relations and Liquid Structure in System As-Sb_2Se_3-Se, J. Electrochem. Soc., 118 (1971) 1485-1491.

[144] G. Ghosh, H.L. Lukas, L. Delaey, A Thermodynamic Assessment of the Sb-Se System, Zeitschrift Fur Metallkunde, 80 (1989) 663-668.

[145] G. Ghosh, The Sb-Se (antimony-selenium) system, J Phase Equilib, 14 (1993) 753-763.

[146] Z.S. Aliev, S.S. Musaeva, D.M. Babanly, A.V. Shevelkov, M.B. Babanly, Phase diagram of the Sb-Se-I system and thermodynamic properties of SbSeI, J Alloy Compd, 505 (2010) 450-455.

[147] M.E. Schlesinger, Thermodynamic Properties of Solid Binary Antimonides, Chem. Rev., 113 (2013) 8066-8092.

[148] F. Failamani, P. Broz, D. Maccio, S. Puchegger, H. Muller, L. Salamakha, H. Michor, A. Grytsiv, A. Saccone, E. Bauer, G. Giester, P. Rogl, Constitution of the systems {V,Nb,Ta}-Sb and physical properties of di-antimonides $\{V,Nb,Ta\}Sb_2$, Intermetallics, 65 (2015) 94-110.

[149] S.Y. Peng, Z.X. Zhu, W.B. Ma, Q.L. Xu, M.L. Chen, F.C. Yin, The 600°C and 800°C isothermal sections of the Zn-V-Sb system, Int J Mater Res, 107 (2016) 21-27.

[150] L. Romaka, V.V. Romaka, N. Melnychenko, Y. Stadnyk, L. Bohun, A. Horyn, Experimental and DFT study of the V-Co-Sb ternary system, J Alloy Compd, 739 (2018) 771-779.

[151] J.F. Smith, Phase diagrams of binary vanadium alloys, ASM International, Metals Park, Ohio, 1989.

[152] S. Furuseth, B. Klewe, Crystal-Structure and Properties of V_2Se_9, Acta Chem Scand A, 38 (1984) 467-471.

[153] M. He, A. Simon, V. Duppel, Ti_5Se_4: The first step of cluster condensation with titanium selenides, Z Anorg Allg Chem, 630 (2004) 535-540.

[154] E. Røst, L. Gjertsen, On the Vanadium Selenides, Z Anorg Allg Chem, 328 (1964) 299-308.

[155] F.M.A. Carpay, System Vanadium-Selenium near Composition VSe, J Inorg Nucl Chem, 28 (1966) 2827-&.

[156] R.J. Meyer, J. Pietsch, T.G. Maple, Vanadium, in: Teil B — Lieferung 1. Verbindungen bis Vanadium und Wismut, Springer-Verlag, Berlin Heidelberg, 1967, pp. XXIV, 368.

[157] M. Overbay, T. Novet, D.C. Johnson, The low temperature synthesis of vanadium selenides using superlattice reactants, J Solid State Chem, 123 (1996) 337-343.
[158] Y. Shin, D.W. Lee, K.Y. Choi, H.J. Koo, K.M. Ok, $VSb(SeO_3)_4$, First Selenite Containing V^{3+} Cation: Synthesis, Structure, Characterization, Magnetic Properties, and Calculations, Inorg Chem, 52 (2013) 14224-14230.
[159] S.M. Clarke, D.E. Freedman, $(BiSe)_{1.23}CrSe_2$ and $(BiSe)_{1.22}(Cr_{1.2}Se_2)_2$: Magnetic Anisotropy in the First Structurally Characterized Bi-Se-Cr Ternary Compounds, Inorg Chem, 54 (2015) 2765-2771.
[160] TOPAS, in, Bruker AXS Inc., Karlsruhe, Germany, 1999.
[161] V. Petricek, M. Dusek, L. Palatinus, Crystallographic Computing System JANA2006: General features, Z Krist-Cryst Mater, 229 (2014) 345-352.
[162] W.J. Boettinger, U.R. Kattner, K.-W. Moon, J.H. Perepezko, DTA and heat-flux DSC measurements of alloy melting and freezing, Elsevier Science Ltd, Amsterdam, 2007.
[163] S. Wagner, D.A. Rigney, Binary-Systems Involving Catatectic Reaction Solid 1 <-> Solid 2 + Liquid, Metall Trans, 5 (1974) 2155-2160.
[164] S. Brunie, M. Chevreto, J.-M. Kauffman, Crystallographic Study on Vanadium Sulfides and Selenides - Presentation of two new Monoclinic Compounds V_7Se_8 and V_7S_8, Mater Res Bull, 7 (1972) 253-&.
[165] N.T. Nguyen, B. Howe, J.R. Hash, N. Liebrecht, P. Zschack, D.C. Johnson, Synthesis of a family of $\{[(VSe_2)_n]_{1.06}(TaSe_2)_m\}_z$ compounds, Chem Mater, 19 (2007) 1923-1930.
[166] M.C. Peters, J.W. Doak, J.E. Saal, G.B. Olson, P.W. Voorhees, Using First-Principles Calculations in CALPHAD Models to Determine Carrier Concentration of the Binary PbSe Semiconductor, J Electron Mater, 48 (2019) 1031-1043.
[167] R.F. Brebrick, E. Gubner, PbSe Composition Stability Limits, J. Chem. Phys., 36 (1962) 170-&.
[168] N. Chou, K. Komarek, E. Miller, Retrograde Solubility of PbS, PbSe, and PbTe, T Metall Soc Aime, 245 (1969) 1553-1560.
[169] S. Scherrer, M. Rodot, M. Schneider, P. Manet, Etude de la précipitation du sélénium dans le composé PbSe, J Phys Lett-Paris, 35 (1974) L15-L18.
[170] M. Schneider, J.C. Guillaume, Etude des alliages liquides du systeme plomb-selenium a l'aide de mesures electrochimiques, J Phys Chem Solids, 35 (1974) 471-478.
[171] V. Leute, H. Schmidtke, Untersuchungen zum Diffusionsmechanismus in den quasibinären Halbleiterlegierungen (Pb, Sn)Te und (Pb, Sn)Se, Ber Bunsen Phys Chem, 79 (1975) 1134-1140.
[172] J.C. Lin, R.C. Sharma, Y.A. Chang, The Pb-Se (lead-selenium) system, J Phase Equilib, 17 (1996) 253-260.
[173] R. Nozato, K. Igaki, On the Equilibrium Diagram of the Lead-Selenium System (I), Bulletin of the Naniwa University. Series A, Engineering and natural science, 3 (1955) 125-133.
[174] R. Nozato, K. Igaki, On the Equilibrium Diagram of the Lead-Selenium System (II), Bulletin of the Naniwa University. Series A, Engineering and natural science, 3 (1955) 135-141.

[175] K. Friedrich, A. Leroux, Die Schmelzdiagramme der binären Systeme Cu-Cu_2Se, Ag-Ag_2Se und Pb-PbSe, Zeitschrift für die gesamte Hüttenkunde, 5 (1908) 355-358.

[176] J.N. Greenwood, H.W. Worner, The constitution of dilute alloys of lead with sulphur, selenium, and tellurium., Journal of the Institute of Metals, 65 (1939) 435-445.

[177] H. Pelabon, Sur le séléniure de plomb, Comptes Rendus Hebdomadaires Des Seances De L Academie Des Sciences, 144 (1907) 1159-1161.

[178] E. Pelzel, Die Löslichkeit von Tellur, Selen und Mangan in flüssigem Blei, Metallwissenschaft und Technik, 10 (1956) 717-719.

[179] D. Seidman, I. Cadoff, K. Komarek, E. Miller, Note on the Pb-Se Phase Diagram, T Metall Soc Aime, 221 (1961) 1269-1270.

[180] E. Miller, K.L. Komarek, Retrograde solubility in semiconducting intermetallic compounds. Liquidus curves in the Pb-S, Pb-Se, and Pb-Te systems, T Metall Soc Aime, 236 (1966) 832-840.

[181] D.N. Seidman, The Partial Lead-Selenium (0 to 76 at. % Se) Phase Diagram, T Metall Soc Aime, 236 (1966) 1361-1362.

[182] Y.J. Liu, Z.T. Kang, G. Sheng, L.J. Zhang, J. Wang, Z.H. Long, Phase Equilibria and Thermodynamic Basis for the Cd-Se and Pb-Se Binary Systems, J Electron Mater, 41 (2012) 1915-1923.

[183] H. Holleck, F. Benesovsky, H. Nowotny, Intermetallische Phasen mit β-Wolfram-Struktur (V_3Pb, Nb_3Pb und V_3Cd), Monatsh Chem, 94 (1963) 473-&.

[184] E.M. Savitskii, V.V. Baron, Y.V. Efimov, New Vanadium Compounds with Structures of the Cr_3Si Type, Soviet Physics Doklady, 11 (1967) 988-989.

[185] J.M. Leger, H.T. Hall, Pressure and Temperature Formation of A_3B Compounds II. Nb_3Ge, Nb_3Sn, Nb_3Pb, V-In and V-Pb, Journal of the Less-Common Metals, 34 (1974) 17-24.

[186] J.F. Smith, The Pb−V (Lead-Vanadium) system, Bulletin of Alloy Phase Diagrams, 2 (1981) 209-210.

[187] R.Y. Wang, A Further Study of Superconducting Critical-Temperature of $L1_2$ Type Superconductors, Phys Status Solidi A, 94 (1986) 445-452.

[188] Y. Oka, K. Kosuge, S. Kachi, Order-Disorder Transition of Metal Vacancies in Vanadium-Sulfur System .1. Experimental-Study, J Solid State Chem, 23 (1978) 11-18.

[189] M.C.J. Marker, P. Terzieff, P. Kainzbauer, M. Bobnar, K.W. Richter, H. Ipser, BiMn: Synthesis, separation by centrifugation, and characterization, J Alloy Compd, 741 (2018) 682-688.

[190] K. Hayashi, M. Nakahira, Stability and the equilibrium selenium vapor pressure of the VSe_2 phase, J Solid State Chem, 24 (1978) 153-161.

[191] K. Miyauchi, K. Hayashi, M. Nakahira, Phase-Equilibrium of the VSe_2-V_3Se_4 System and the Thermodynamic Quantities of the V_3Se_4 Phase, Mater Res Bull, 18 (1983) 757-764.

[192] A.A. Babitsyna, V.M. Novotortsev, Interaction of Chromium Selenide Cr_2Se_3 with Certain Copper and Tin Selenides, Zhurnal Neorganicheskoi Khimii, 31 (1986) 1825-1828.

[193] S. Jobic, P. Leboterf, R. Brec, G. Ouvrard, Structural Determination and Magnetic-Properties of a New Mixed-Valence Tin Chromium Selenide: $Cr_2Sn_3Se_7$, J Alloy Compd, 205 (1994) 139-145.

[194] S. Jobic, F. Bodenan, G. Ouvrard, E. Elkaim, J.P. Lauriat, Structural Determination and Magnetic-Properties of a New Orthorhombic Chromium Seleno Stannate, $Cr_2Sn_3Se_7$, J Solid State Chem, 115 (1995) 165-173.

[195] Y. Feutelais, M. Majid, B. Legendre, S.G. Fries, Phase diagram investigation and proposition of a thermodynamic evaluation of the tin-selenium system, J Phase Equilib, 17 (1996) 40-49.

[196] T. Chattopadhyay, J. Pannetier, H.G. Vonschnering, Neutron-Diffraction Study of the Structural Phase-Transition in SnS and SnSe, J Phys Chem Solids, 47 (1986) 879-885.

[197] W. Köster, K. Haug, Das Dreistoffsystem Titan-Vanadin-Zinn, Zeitschrift Fur Metallkunde, 48 (1957) 327-330.

[198] S. Komjathy, The Constitution of Some Vanadium-Base Binary and Ternary Systems and the Ageing Characteristics of Selected Ternary Alloys, Journal of the Less-Common Metals, 3 (1961) 468-488.

[199] F. Jouault, P. Lecocq, Un Nouveau Stannure De Vanadium V_2Sn_3, Comptes Rendus Hebdomadaires Des Seances De L Academie Des Sciences, 260 (1965) 4777-&.

[200] F. Jouault, P. Lecocq, Etude comparee des trois diagrammes V-Sn, Nb-Sn, Ta-Sn, Colloques Internationaux du Centre National de la Recherche Scientifique, 157 (1967) 229-235.

[201] L.V. Marchukova, N.M. Matveyev, I.I. Kornilov, The V-Sn Phase Diagram, Russ Metall+, (1973) 157-160.

[202] H. Okamoto, Sn-V (Tin-Vanadium), J Phase Equilib Diff, 34 (2013) 78-79.

[203] J.F. Smith, The Sn−V (Tin-Vanadium) system, Bulletin of Alloy Phase Diagrams, 2 (1981) 210-214.

[204] T. Studnitzky, B. Onderka, R. Schmid-Fetzer, Phase formation and reaction kinetics in the vanadium-tin system, Zeitschrift Fur Metallkunde, 93 (2002) 48-57.

[205] J.B. Darby, D.B. Jugle, Solubility of Several First-Long-Period Transition Elements in Liquid Tin, T Metall Soc Aime, 245 (1969) 2515-&.

[206] Q. Yue, Y.Q. Liu, M.Y. Chu, J.Y. Shen, Thermodynamic modeling of the Sn-V binary system, Calphad-Computer Coupling of Phase Diagrams and Thermochemistry, 33 (2009) 539-544.

[207] H. Okamoto, T.B. Massalski, Thermodynamically Improbable Phase-Diagram Features, Nato Adv Sci Inst Se, 319 (1994) 155-161.

[208] T. Wölpl, W. Jeitschko, Crystal-Structures of VSn_2, $NbSn_2$ and $CrSn_2$ with Mg_2Cu-Type Structure and NbSnSb with $CuAl_2$-Type Structure, J Alloy Compd, 210 (1994) 185-190.

[209] L. Romaka, M. Konyk, Y. Stadnyk, A. Horyn, V.V. Romaka, R. Serkiz, V. Krayovskyy, Interaction of the components in the V-(Fe, Ni)-Sn ternary systems, Chemistry of metals and alloys, 8 (2015) 75-82.

[210] D.I. Bardos, R.K. Malik, F.X. Spiegel, P.A. Beck, Beta-Manganese Phases in Ternary Systems of Transition Elements with Silicon Germanium or Tin, T Metall Soc Aime, 236 (1966) 40-&.

[211] C.C. Chen, S.W. Chen, C.Y. Kao, Interfacial reactions in the Sn-(Ag)/(Ni,V) couples and phase equilibria of the Sn-Ni-V system at the Sn-Rich corner, J Electron Mater, 35 (2006) 922-928.

[212] A.V. Tkachuk, Y.K. Gorelenko, Y.V. Stadnyk, O.I. Bodak, V-Mn-{Sn,Sb} ternary systems, J Alloy Compd, 317 (2001) 280-283.

[213] M. Enomoto, The Sn-Ti-V System (Tin-Titanium-Vanadium), J Phase Equilib, 12 (1991) 363-371.

[214] Z. Hiroi, H. Hayamizu, T. Yoshida, Y. Muraoka, Y. Okamoto, J. Yamaura, Y. Ueda, Spinodal Decomposition in the TiO_2-VO_2 System, Chem Mater, 25 (2013) 2202-2210.

[215] A.V. Antipov, E.B. Rudnyi, Z.V. Dobrokhotova, Thermodynamic evaluation of the Bi-Se system, Inorg Mater+, 37 (2001) 126-132.

[216] H. Lind, S. Lidin, A general structure model for Bi-Se phases using a superspace formalism, Solid State Sci, 5 (2003) 47-57.

[217] H. Lind, S. Lidin, U. Haussermann, Structure and bonding properties of $(Bi_2Se_3)_m(Bi_2)_n$ stacks by first-principles density functional theory, Phys Rev B, 72 (2005).

[218] A. Chaturvedi, A. Slabon, P. Hu, S.L. Feng, K.K. Zhang, R.R. Prabhakar, C. Kloc, Rapid synthesis of transition metal dichalcogenide few-layer thin crystals by the microwave-induced-plasma assisted method, Journal of Crystal Growth, 450 (2016) 140-147.

[219] K.Z. Du, A. Chaturvedi, X.Z. Wang, Y. Zhao, K.K. Zhang, M.I.B. Utama, P. Hu, H. Jiang, Q.H. Xiong, C. Kloc, Plasma-enhanced microwave solid-state synthesis of cadmium sulfide: reaction mechanism and optical properties, Dalton T, 44 (2015) 13444-13449.

[220] T. Lorenz, J.O. Joswig, G. Seifert, Two-dimensional and tubular structures of misfit compounds: Structural and electronic properties, Beilstein J Nanotech, 5 (2014) 2171-2178.

[221] R.B. Soriano, J.S. Wu, M.G. Kanatzidis, Size as a Parameter to Stabilize New Phases: Rock Salt Phases of $Pb_mSb_{2n}Se_{m+3n}$, Journal of the American Chemical Society, 137 (2015) 9937-9942.

[222] J. Rigoult, C. Guidimorosini, A. Tomas, P. Molinie, An Accurate Refinement of 1T-VSe_2 at Room Temperature, Acta Crystallogr B, 38 (1982) 1557-1559.

[223] M. Kalläne, K. Rossnagel, M. Marczynski-Buhlow, L. Kipp, H.I. Starnberg, S.E. Stoltz, Stabilization of the misfit layer compound $(PbS)_{1.13}TaS_2$ by metal cross substitution, Phys Rev Lett, 100 (2008) 4.

[224] S. Sugai, K. Murase, S. Uchida, S. Tanaka, Investigation of the Charge-Density Waves in 1T-VSe_2 by Raman-Scattering, J Phys-Paris, 42 (1981) 740-742.

[225] D.L. Duong, G. Ryu, A. Hoyer, C.T. Lin, M. Burghard, K. Kern, Correction to Raman Characterization of the Charge Density Wave Phase of 1T-$TiSe_2$: From Bulk to Atomically Thin Layers (vol. 11, pg 1034, 2017), Acs Nano, 11 (2017) 2304-2304.

[226] D.L. Duong, G. Ryu, A. Hoyer, C.T. Lin, M. Burghard, K. Kern, Raman Characterization of the Charge Density Wave Phase of 1T-$TiSe_2$: From Bulk to Atomically Thin Layers, Acs Nano, 11 (2017) 1034-1040.

[227] P. Goli, J. Khan, D. Wickramaratne, R.K. Lake, A.A. Balandin, Charge Density Waves in Exfoliated Films of van der Waals Materials: Evolution of Raman Spectrum in $TiSe_2$, Nano Lett, 12 (2012) 5941-5945.
[228] S.V. Ovsyannikov, V.V. Shchennikov, A. Cantarero, A. Cros, A.N. Titov, Raman spectra of $(PbS)_{1.18}(TiS_2)_2$ misfit compound, Mat Sci Eng a-Struct, 462 (2007) 422-426.
[229] E.U. Donev, J.I. Ziegler, R.F. Haglund, L.C. Feldman, Size effects in the structural phase transition of VO_2 nanoparticles studied by surface-enhanced Raman scattering, J Opt a-Pure Appl Op, 11 (2009).
[230] P. Schilbe, Raman scattering in VO_2, Physica B-Condensed Matter, 316 (2002) 600-602.
[231] S. Lee, I.N. Ivanov, J.K. Keum, H.N. Lee, Epitaxial stabilization and phase instability of VO_2 polymorphs, Sci Rep-Uk, 6 (2016).
[232] P. Shvets, O. Dikaya, K. Maksimova, A. Goikhman, A review of Raman spectroscopy of vanadium oxides, J Raman Spectrosc, 50 (2019) 1226-1244.
[233] J.E. Smith, J.C. Tsang, M.W. Shafer, Raman-Spectra of Several Layer Compounds with Charge-Density Waves, Solid State Commun, 19 (1976) 283-286.
[234] Z. Jin, J.Y. Zhou, M.Z. Xie, H. Ji, Y. Ye, K. Jiang, L.Y. Shang, J.Z. Zhang, Z.G. Hu, J.H. Chu, Strong charge-density-wave order of large-area 2D metallic VSe_2 nanosheets discovered by temperature-dependent Raman spectra, Appl Phys Lett, 116 (2020).
[235] H.T. Liu, L.H. Bao, Z. Zhou, B.Y. Che, R.Z. Zhang, C. Bian, R.S. Ma, L.M. Wu, H.F. Yang, J.J. Li, C.Z. Gu, C.M. Shen, S.X. Du, H.J. Gao, Quasi-2D Transport and Weak Antilocalization Effect in Few-layered VSe_2, Nano Lett, 19 (2019) 4551-4559.
[236] J. Pandey, A. Soni, Electron-phonon interactions and two-phonon modes associated with charge density wave in single crystalline $1T-VSe_2$, Phys. Rev. Research, 2 (2020) 033118.
[237] W. Yu, J. Li, T.S. Herng, Z.S. Wang, X.X. Zhao, X. Chi, W. Fu, I. Abdelwahab, J. Zhou, J.D. Dan, Z.X. Chen, Z. Chen, Z.J. Li, J. Lu, S.J. Pennycook, Y.P. Feng, J. Ding, K.P. Loh, Chemically Exfoliated VSe_2 Monolayers with Room-Temperature Ferromagnetism, Adv Mater, 31 (2019).
[238] H.R. Chandrasekhar, R.G. Humphreys, U. Zwick, M. Cardona, Infrared and Raman spectra of the IV-VI compounds SnS and SnSe, Phys Rev B, 15 (1977) 2177-2183.
[239] P.M. Nikolic, L. Milkovic, P. Mihajlovic, B. Lavrencic, Raman-Scattering in SnSe, Czech. J. Phys., 28 (1978) 456-459.
[240] M. Ludemann, O.D. Gordan, D.R.T. Zahn, M. Beekman, R. Atkins, D.C. Johnson, Raman Spectroscopy Insights into the Size-Induced Structural Transformation in SnSe Nanolayers, Langmuir, 30 (2014) 8209-8214.
[241] X.Z. Li, J. Xia, L. Wang, Y.Y. Gu, H.Q. Cheng, X.M. Meng, Layered SnSe nano-plates with excellent in-plane anisotropic properties of Raman spectrum and photo-response, Nanoscale, 9 (2017) 14558-14564.
[242] X.L. Xu, Q.J. Song, H.F. Wang, P. Li, K. Zhang, Y.L. Wang, K. Yuan, Z.C. Yang, Y. Ye, L. Dai, In-Plane Anisotropies of Polarized Raman Response and Electrical Conductivity in Layered Tin Selenide, Acs Appl Mater Inter, 9 (2017) 12601-12607.

[243] S.V. Ovsyannikov, Y.S. Ponosov, V.V. Shchennikov, V.E. Mogilenskikh, Raman spectra of lead chalcogenide single crystals, Phys Status Solidi C, 1 (2004) 3110-3113.

[244] J. Chen, W.Z. Shen, Raman study of phonon modes and disorder effects in $Pb_{1-x}Sr_xSe$ alloys grown by molecular beam epitaxy, Journal of Applied Physics, 99 (2006).

[245] F.S. Manciu, Y. Sahoo, F. Carreto, P.N. Prasad, Size-dependent Raman and infrared studies of PbSe nanoparticles, J Raman Spectrosc, 39 (2008) 1135-1140.

[246] M.O. Kuzivanov, S.P. Zimin, A.V. Fedorov, A.V. Baranov, Raman scattering in lead selenide films at a low excitation level, Opt Spectrosc+, 119 (2015) 938-942.

[247] M. Samanta, K. Pal, P. Pal, U.V. Waghmare, K. Biswas, Localized Vibrations of Bi Bilayer Leading to Ultralow Lattice Thermal Conductivity and High Thermoelectric Performance in Weak Topological Insulator n-Type BiSe, Journal of the American Chemical Society, 140 (2018) 5866-5872.

[248] J.J. Zhang, G.Q. Huang, Phonon dynamics in $(Bi_2Se_3)_m(Bi_2)_n$ infinitely adaptive series, Solid State Commun, 197 (2014) 34-39.

[249] V. Gnezdilov, Y.G. Pashkevich, H. Berger, E. Pomjakushina, K. Conder, P. Lemmens, Helical fluctuations in the Raman response of the topological insulator Bi_2Se_3, Phys Rev B, 84 (2011).

[250] J. Zhang, Z.P. Peng, A. Soni, Y.Y. Zhao, Y. Xiong, B. Peng, J.B. Wang, M.S. Dresselhaus, Q.H. Xiong, Raman Spectroscopy of Few-Quintuple Layer Topological Insulator Bi_2Se_3 Nanoplatelets, Nano Lett, 11 (2011) 2407-2414.

[251] W. Kiefer, H.J. Bernstein, Cell for Resonance Raman Excitation with Lasers in Liquids, Appl Spectrosc, 25 (1971) 500-+.

[252] W. Kiefer, H.J. Bernstein, Rotating Raman Sample Technique for Colored Crystal Powders - Resonance Raman Effect in Solid $KMnO_4$, Appl Spectrosc, 25 (1971) 609-+.

[253] H.J. Sloane, R.B. Cook, Applications of Rotating Solid Sample Technique in Raman Spectroscopy, Appl Spectrosc, 26 (1972) 589-&.

[254] N. Zimmerer, W. Kiefer, Rotating Surface Scanning Technique for Raman-Spectroscopy, Appl Spectrosc, 28 (1974) 279-281.

[255] J.R. Ferraro, K. Nakamoto, C.W. Brown, Introductory Raman spectroscopy, 2nd ed., Academic Press, Amsterdam ; Boston, 2003.

[256] P. Vandenabeele, Practical Raman spectroscopy : an introduction, in, Wiley,, Chichester, West Sussex, United Kingdom, 2013, pp. 1 online resource.

[257] E.K. Rugut, Numerical simulation of structural, electronic and optical properties of transition metal chalcogenides, in: School of Physics, University of the Witwatersrand, Johannesburg, 2017, pp. 112.

[258] E. Smith, G. Dent, Modern Raman spectroscopy : a practical approach, in, Wiley,, Hoboken, NJ, 2019, pp. 1 online resource.

[259] P.-H. Tan, Raman Spectroscopy of Two-Dimensional Materials, in: Springer Series in Materials Science,, Springer Singapore : Imprint: Springer,, Singapore, 2019, pp. 1 online resource (IX, 261 pages 126 illustrations).

[260] Instrument Presentation (https://www.horiba.com/en_en/ramanspectrometerpresentation/), in, HORIBA Europe GmbH, Oberursel, 2020.

[261] G.V. Kamarchuk, A.V. Khotkevich, V.M. Bagatskii, P. Molinie, A. Leblanc, E. Faulques, Spectroscopy of the electron-phonon interaction in the layered two-dimensional dichalcogenide 1T-VSe_2, Low Temp. Phys., 27 (2001) 56-60.

[262] C.Z. Zhang, Q.Q. Yang, C. Koughia, F. Ye, M. Sanayei, S.J. Wen, S. Kasap, Characterization of vanadium oxide thin films with different stoichiometry using Raman spectroscopy, Thin Solid Films, 620 (2016) 64-69.

[263] K. Shirai, K. Kisoda, M. Hangyo, S. Nakashima, On the Raman shift in misfit layer compounds of metal-dichalcogenides $(MX)(TX_2)$ - An effect of the charge transfer on the intralayer noncentral forces, Solid State Commun, 103 (1997) 131-135.

[264] M. Staiger, V. Bacic, R. Gillen, G. Radovsky, K. Gartsman, R. Tenne, T. Heine, J. Maultzsch, C. Thomsen, Raman spectroscopy of intercalated and misfit layer nanotubes, Phys Rev B, 94 (2016) 10.

[265] M. Hangyo, K. Kisoda, T. Nishio, S. Nakashima, T. Terashima, N. Kojima, Staging and interlayer interaction in the misfit-layer compounds $(RS)_nNbS_2$ (R=La,Ce; n=0.6,1.2) studied by Raman and infrared spectroscopies, Phys Rev B, 50 (1994) 12033-12043.

[266] M. Hangyo, S. Nakashima, Y. Hamada, T. Nishio, Y. Ohno, Raman scattering from the Misfit-Layer Compounds $SnNbS_3$, $PbNbS_3$, and $PbTiS_3$,, Phys Rev B, 48 (1993) 11291-11297.

[267] C. Sourisseau, R. Cavagnat, M. Fouassier, J.L. Tirado, J. Morales, Optical, Raman and Resonance Raman-Spectra and Lattice-Dynamics Calculations of the Misfit Layer Compounds, $(SnS)_{1.17}NbS_2$ and $(PbS)_{1.18}TiS_2$, Chem Phys, 181 (1994) 377-392.

[268] M. Hangyo, T. Nishio, S. Nakashima, Y. Ohno, T. Terashima, N. Kojima, Raman and Infrared-Spectra of Misfit Layer Compounds $MNbS_3$ (M=Sn, Pb, La, Ce), Japanese Journal of Applied Physics Part 1-Regular Papers Short Notes & Review Papers, 32 (1993) 581-583.

[269] C. Sourisseau, R. Cavagnat, J.L. Tirado, A Raman-Study of the Misfit Layer Compounds, $(SnS)_{1.17}NbS_2$ and $(PbS)_{1.18}TiS_2$, J Raman Spectrosc, 23 (1992) 647-651.

[270] M. Hangyo, K. Kisoda, S. Nakashima, A. Meerschaut, J. Rouxel, Stage dependence of phonons in misfit layer compounds $(MS)(NbS_2)_n$ (M=Sn,Pb; n=1,2), Physica B-Condensed Matter, 219-20 (1996) 481-483.

[271] K. Kisoda, M. Hangyo, S. Nakashima, K. Suzuki, T. Enoki, Y. Ohno, Raman scattering from Misfit Layer Compounds $(RS)_XTaS_2$ (R = La,Ce,Sm or Gd; S = sulphur; x =1.2, J Phys-Condens Mat, 7 (1995) 5383-5393.

[272] D. Berner, H. Leihenseder, K. Widder, H.P. Geserich, V.M. Burlakov, B.N. Mavrin, V.N. Denisov, R. Roesky, P. Gressier, A. Meerschaut, $(LaSe)_{1.14}(NbSe_2)_2$ - a metal-insulator quantum well crystal?, J Phys-Condens Mat, 9 (1997) 10545-10553.

[273] K. Kisoda, M. Hangyo, S. Nakashima, T. Terashima, N. Kojima, Charge transfer and phonons in misfit layer compounds $(RS)_xNbS_2$ (R = rare earth; x = 1.2), Physica B-Condensed Matter, 219-20 (1996) 565-567.

[274] L.K. Vodopyanov, L.A. Falkovski, J. Irvin, S. Himenis, Raman-Scattering of Light in a Degenerate (Pb, Sn) Se Semiconductor, Jetp Lett+, 53 (1991) 586-590.

[275] K.S. Upadhyaya, M. Yadav, G.K. Upadhyaya, Lattice dynamics of IV-VI ionic semiconductors: An application to lead chalcogenides, Phys Status Solidi B, 229 (2002) 1129-1138.

[276] J.Y. Yang, W.K. Wang, Y. Liu, H.F. Du, W. Ning, G.L. Zheng, C.M. Jin, Y.Y. Han, N. Wang, Z.R. Yang, M.L. Tian, Y.H. Zhang, Thickness dependence of the charge-density-wave transition temperature in VSe_2, Appl Phys Lett, 105 (2014).

[277] S. Barua, M.C. Hatnean, M.R. Lees, G. Balakrishnan, Signatures of the Kondo effect in VSe_2, Sci Rep-Uk, 7 (2017).

[278] K. Xu, P.Z. Chen, X.L. Li, C.Z. Wu, Y.Q. Guo, J.Y. Zhao, X.J. Wu, Y. Xie, Ultrathin Nanosheets of Vanadium Diselenide: A Metallic Two-Dimensional Material with Ferromagnetic Charge-Density-Wave Behavior, Angew Chem Int Edit, 52 (2013) 10477-10481.

[279] A. Pasztor, A. Scarfato, C. Barreteau, E. Giannini, C. Renner, Dimensional crossover of the charge density wave transition in thin exfoliated VSe_2, 2d Mater, 4 (2017).

[280] K. Sato, H. Hinode, M. Wakihara, M. Taniguchi, Homogeneity range of $Sn_xMo_6S_{8-y}$ at 1000 °C and measurement of superconducting critical temperature T_c, Mater Res Bull, 23 (1988) 993-999.

[281] C.F. Gardinier, L.L.Y. Chang, Phase Relationships in Systems Mo-Sn-S, W-Sn-S and Mo-W-S, Journal of the Less-Common Metals, 61 (1978) 221-229.

[282] Bi-Mo-S Isothermal Section of Ternary Phase Diagram: Datasheet from "PAULING FILE Multinaries Edition – 2012" in SpringerMaterials (https://materials.springer.com/isp/phase-diagram/docs/c_0978947), in: P. Villars, H. Okamoto (Eds.), Springer-Verlag Berlin Heidelberg & Material Phases Data System (MPDS), Switzerland & National Institute for Materials Science (NIMS), Japan.

[283] Bi-Mo-S Isothermal Section of Ternary Phase Diagram: Datasheet from "PAULING FILE Multinaries Edition – 2012" in SpringerMaterials (https://materials.springer.com/isp/phase-diagram/docs/c_0978944), in: P. Villars, H. Okamoto (Eds.), Springer-Verlag Berlin Heidelberg & Material Phases Data System (MPDS), Switzerland & National Institute for Materials Science (NIMS), Japan.

[284] Bi-Mo-S Isothermal Section of Ternary Phase Diagram: Datasheet from "PAULING FILE Multinaries Edition – 2012" in SpringerMaterials (https://materials.springer.com/isp/phase-diagram/docs/c_0978945), in: P. Villars, H. Okamoto (Eds.), Springer-Verlag Berlin Heidelberg & Material Phases Data System (MPDS), Switzerland & National Institute for Materials Science (NIMS), Japan.

[285] V.E. Fedorov, A.V. Mishchenko, Z.M. Logvinenko, S.D. Kirik, Stoichiometry of Ternary Molybdenum Sulfide $PbMo_6S_8$, Inorg Mater+, 18 (1982) 17-22.

[286] J. Hauck, Phase relations and stoichiometry of superconducting $Pb_xMo_6S_{8-y}$, Mater Res Bull, 12 (1977) 1015-1019.

[287] G. Krabbes, H. Oppermann, The Phase-Diagram of the Pb-Mo-S System at 1250-K and Some Properties of the Superconducting Pbmo6s8, Cryst Res Technol, 16 (1981) 777-784.

[288] G. Krabbes, H. Oppermann, Darstellung der supraleitenden ternären Phase $PbMo_6S_8$ durch chemischen Transport, Z Anorg Allg Chem, 481 (1981) 13-21.

[289] S. Yamamoto, M. Wakihara, M. Taniguchi, Phase relations in the Pb-Mo-S ternary system at 1000 °C and the superconductivity of $Pb_xMo_6S_{8-y}$, Mater Res Bull, 20 (1985) 1493-1500.

[290] R. Horyn, Phase-Relations in the Pb-Mo-Se Ternary-System at 1323-K and the Superconductivity of the Alloys, Journal of the Less-Common Metals, 98 (1984) 71-77.

[291] T. Ohtani, M. Date, K. Muroi, J. Kaneyasu, Phase study of chevrel compounds of $Pb_xMo_6Se_{8-y}$ and $Cd_xMo_6Se_{8-y}$, Solid State Ion., 141 (2001) 407-410.

[292] G.G. Shabunina, E.V. Amerikova, T.G. Aminov, Study of Bi_2X_3 Interaction with Cr_2X_3 Where (X=S,Te), Zhurnal Neorganicheskoi Khimii, 39 (1994) 998-1000.

[293] G.G. Shabunina, E.V. Kireeva, T.G. Aminov, The interaction of Bi_2Se_3 and Cr_2Se_3, Zhurnal Neorganicheskoi Khimii, 41 (1996) 1565-1567.

[294] E.V. Amerikova, G.G. Shabunina, T.G. Aminov, Sb_2S_3-Cr_2S_3 System, Zhurnal Neorganicheskoi Khimii, 35 (1990) 1613-1616.

[295] G.G. Shabunina, E.V. Amerikova, T.G. Aminov, V.M. Novotortsev, Study of Sb_2X_3 Interaction with Cr_2X_3 Where (X=S,Te), Zhurnal Neorganicheskoi Khimii, 40 (1995) 154-156.

[296] G.G. Shabunina, T.G. Aminov, Study of interaction in the Sb-Cr-Se ternary system, Zhurnal Neorganicheskoi Khimii, 41 (1996) 1912-1915.